

The physics and chemistry of photon-dominated clouds in NGC 3603

Inaugural-Dissertation

zur
Erlangung des Doktorgrades
der Mathematisch-Naturwissenschaftlichen Fakultät
der Universität zu Köln



vorgelegt von
Zoltán Sándor Makai
aus Budapest

Köln 2014

Erster Gutachter: Prof. Dr. Jürgen Stutzki (Universität zu Köln)
Zweiter Gutachter: PD. Dr. Markus Röllig (Universität zu Köln)

Tag der mündlichen Prüfung: 14. Oktober 2014.

For Andi

and

*for the memory of my parents
Mom (†2008) and Dad (†2013)*

“The nitrogen in our DNA, the calcium in our teeth, the iron in our blood, the carbon in our apple pies were made in the interiors of collapsing stars. Therefore, in order to make an apple pie from scratch, you must first create the universe. We are made of starstuff.”

Carl Edward Sagan

“Not only is the Universe stranger than we think, it is stranger than we can think.”

Werner Heisenberg

“A sok tudás nem tanít meg a helyes gondolkodásra”

Herakleitosz

Contents

Abstract	1
Kurzzusammenfassung	2
1 Introduction	5
1.1 Motivation	6
2 Theoretical background	11
2.1 Spectral features	11
2.1.1 Rotational lines	11
2.1.2 Fine- and hyperfine-structures	12
2.2 Einstein-coefficients and critical density	12
2.3 Radiative transfer	15
2.4 Optical depth and column density calculation	16
2.5 Photon-Dominated Regions (PDRs)	18
2.5.1 Energy balance	19
Heating	19
Cooling	21
2.6 Chemistry in the ISM	22
2.6.1 Gas phase chemistry	22
2.6.2 Grain surface chemistry	23

3	Observations by the Herschel Space Observatory	25
3.1	The Herschel Space Observatory	25
3.1.1	HIFI	26
	Observing modes with HIFI	26
3.1.2	PACS	29
	Observing modes with PACS	30
3.1.3	SPIRE	30
3.2	The WADI key-project	32
3.2.1	The target source: NGC 3603	32
4	Data reduction	39
4.1	HIPE	39
4.1.1	HIFI pipeline processes	40
4.1.2	PACS pipeline processes	40
4.2	CLASS	41
4.3	Summary	44
5	Complementary data	47
5.1	SEST data	47
5.2	NANTEN2 data	49
5.3	PACS and SPIRE data (Hi-GAL survey)	50
6	Observational results	55
6.1	Integrated intensity maps	55
6.1.1	HIFI OTF-maps	55
6.1.2	PACS-maps	57
	Line spectroscopy	57
	Range spectroscopy	58
6.2	Velocity structure and line shapes	60
6.2.1	Position-velocity diagrams	60
	OTF observations	60
	Cut observations	62
6.2.2	Channel maps	65

6.2.3	Line profiles and intensities	66
	OTF observations (C1, C2 and C3)	67
	Cut observations	71
	Point observations	74
6.2.4	Kinematic distance	78
6.3	Excitation temperature	79
6.4	Derivation of column densities	79
6.4.1	Column densities along C1, C2 and C3 (OTF-map)	81
	H ₂ column density	81
6.4.2	Column densities from cut observations	83
6.4.3	Column densities from point observations	83
	Abundances	85
6.5	Mass calculations	89
6.5.1	Total and virial gas masses	89
6.5.2	Jeans mass	91
6.6	Summary	93
7	Model results	95
7.1	Theory	95
7.1.1	The RADEX code	96
7.1.2	The KOSMA- τ PDR model	97
7.2	Results	99
7.2.1	RADEX	100
7.2.2	KOSMA- τ	101
7.3	Summary	107
8	Interpretation and discussion	109
8.1	Gas motions	109
8.1.1	Signatures of turbulence	109
8.1.2	Footprints of rotation/torsion	112
8.1.3	Internal cavity in MM2?	114
8.2	Cloud (in)stability	115

8.3	Embedded sources	117
8.4	Density and UV-field with the KOSMA- τ model	119
8.5	Density and temperature with the RADEX	120
8.6	The I(^{12}CO)/I(^{13}CO) ratio	122
8.7	Chemical stratification/structure of NGC 3603	124
8.7.1	Chemical abundances in NGC 3603	126
8.7.2	H ₂ formation and destruction	129
	Summary	132
	References	143
A	Summary of HIFI data	155
B	Summary of PACS data	159
C	Comparison of Herschel and NANTEN2 intensity maps	161
D	Line fits of the observed species from the OTF-map observations	167
E	Line fits of the observed species from the cut observations	179
E.1	1342201675 (o-H ₂ O — MM1)	179
E.2	1342201676 (o-H ₂ O — MM2)	180
E.3	1342201750 (^{12}CO — MM1)	181
E.4	1342201752 (^{12}CO — MM2)	182
E.5	1342201809 (^{13}CO — MM1)	184
E.6	1342201810 (^{13}CO — MM2)	185
E.7	1342201818 ($^{12}\text{C}^+$ — MM1)	186
E.8	1342201819 ($^{12}\text{C}^+$ — MM2)	188
F	Line fits of the observed species from the point observations	191
G	Velocity channel maps	195
H	Line shapes and their distributions in MM1 and MM2	199

I	Integrated intensity maps of the observed species from PACS observations	207
J	The derived physical parameters for Herschel observations	213
K	Energy level diagrams of the observed species	227
L	Beam size correction	235
M	Example scripts	239
	List of Figures	251
	List of Tables	257
	Acknowledgements	259
	Erklärung	263
	Curriculum vitae	264

Abstract

High-mass star-formation in the interstellar medium is one of the main open questions in astronomy: high-mass stars are rare, evolve fast and are frequently obscured or located in dense clusters. Most of our knowledge stems from simulations, not from direct observations.

Stars are born within molecular clouds due to the perturbations of local physical and chemical processes. To investigate these perturbations, we observed one of the most prominent HII region, NGC 3603, in our Galaxy. This molecular cloud complex embraces an open cluster, with massive and hot stars, which provides strong stellar winds and radiation field. These phenomena heavily interact with the neighbouring environment and govern the local physics and chemistry.

To investigate these effects and their influence, we received spectroscopy data of molecules, ions and atoms via Herschel Space Observatory. Data of ground-based telescopes were also used as complementary data.

The observational results showed that the observed clouds have gas components with different temperatures as well as vigorous gas movements. Different models were used to fit the observations. We found that the observed line intensities and abundances match with the model predictions and the model results are independent from the cloud geometry.

All the results we obtain, give the opportunity to characterize the physical conditions and chemical processes within NGC 3603. Based on our observations and our model calculations, we concluded that the observed molecular clouds (or part of them) are probably in gravitationally unstable stage. Hence, the star-formation process within NGC 3603 is still ongoing. This scenario is in agreement with previous studies. It is also likely, that the observed clouds do not rotate as a rigid rotor but have a torsional geometry. On the other hand, due to observational facts (e.g., large beam size, distance of NGC 3603), we were only be able to make statements about the chemistry/chemical stratification within certain limits.

Kurzzusammenfassung

Die Entstehung massereicher Sterne ist eine der großen offenen Fragen moderner Astronomie. Massereiche Sterne sind selten, entwickeln sich schnell und sind oft tief in Staub eingebettet oder in dichten Sternhaufen zu finden. Der größte Teil unseres Wissens über massive Sternentstehung stammt daher aus Simulationen und nicht aus direkten Beobachtungen.

Lokale Störungen des physikalischen und chemischen Zustandes regen die Bildung von Sternen in Molekülwolken an. Um diese Störungen zu untersuchen beobachteten wir eine der prominentesten HII Regionen innerhalb unserer Milchstraße, NGC 3603. Dieser Molekülwolkenkomplex umgibt einen offenen Sternhaufen heißer massereicher Sterne die starke Sternwinde und intensive Strahlung produzieren.

Um deren Einfluß auf die Sternentstehung zu untersuchen, verwendeten wir spektroskopische Beobachtungen des *Herschel Weltraumteleskops* von Molekülen, Ionen und Atomen. Zusätzlich dazu haben wir komplementäre Daten bodengestützter Teleskope verwendet.

Die Daten zeigen, daß die beobachteten Molekülwolken Gaskomponenten mit verschiedenen Temperaturen beherbergen, die teilweise starke Strömungsgeschwindigkeiten aufweisen.

Unsere Ergebnisse erlauben uns die physikalischen und chemischen Zustandsbedingungen innerhalb NGC 3603 zu charakterisieren. Basierend auf unseren Beobachtungen und unseren Modellrechnungen schließen wir, daß die beobachteten Molekülwolken (bzw. Teile von ihnen) gravitativ instabil sind. Folglich ist von einer anhaltenden Sternentstehung in NGC 3603 auszugehen. Diese Annahme wird auch von früheren Studien unterstützt. Es ist weiterhin wahrscheinlich, daß die beobachteten Wolken nicht starr rotieren, sondern eher eine torsionsartige Geometrie aufweisen. Die große Entfernung von NGC 3603 sowie der endlich große Teleskopbeam erlauben uns nur eingeschränkte Aussagen über die chemische Schichtung des lokalen Gases zu treffen.

Introduction

The history of observational radio astronomy goes back to the first third of 20th century (1930's) when Karl Jansky was employed by the Bell Telephone Laboratory as an engineer and investigated statics of an antenna. He detected an unknown periodic signal from the sky. He realized that the detected radiation originates from the Milky Way, more precisely from the Sagittarius constellation¹ (Jansky, 1933), in the direction of the center of our Galaxy. He also stated that the signals are probably emitted by the interstellar gas and dust, which is called interstellar medium (ISM).

A disadvantage of ground-based telescopes that operate in the radio regime is, that the Earth's atmosphere acts as a filter which absorbs a specific frequency range toward the shorter wavelengths (to far-infrared and sub-millimeter regimes) from the sky (Fig. 1.1). Therefore, telescopes operating at this wavelength regimes are mounted at high elevations and dry locations [e.g. NANTEN2² telescope or ALMA³ (altitude \sim 5000 m at Atacama desert, Chile)]. Alternatively, telescopes are also placed above the atmospheric water [e.g. Stratospheric Observatory for Infrared Astronomy (SOFIA)] or even above the atmosphere [Herschel Space Observatory (HSO)].

These highly sophisticated instruments allow us to make on an in-depth study and investigation of the radiation emitted by molecules, ions and atoms that play important roles in the physics and chemistry of the ISM.

¹At that time, Jansky did not know that the source of the detected signal is the Sagittarius-A itself.

²NANTEN means "southern sky" in Japanese

³Atacama Large Millimeter/submillimeter Array

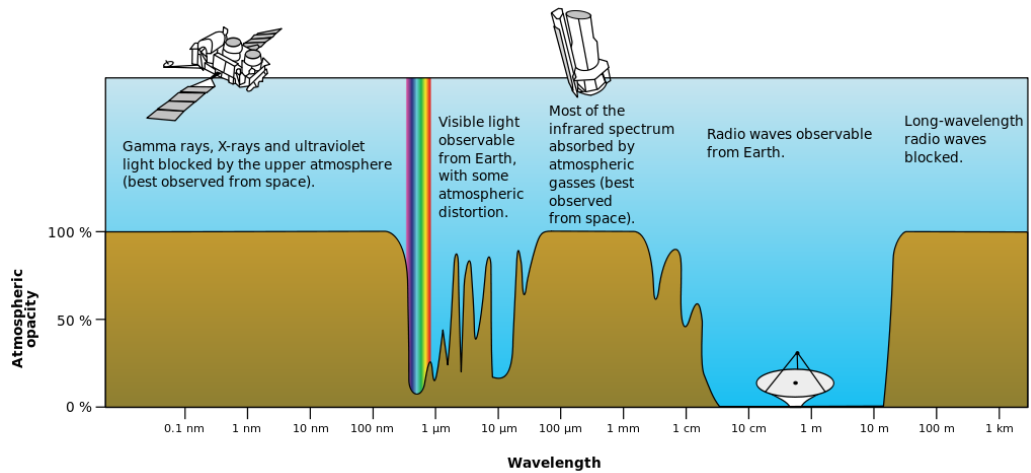


Figure 1.1: *The Earth's atmospheric transmission. Copyright: NASA.*

1.1 Motivation

Our fundamental intention is to understand the main physical conditions and chemical processes in the ISM. One of the open problems in astronomy is the high-mass star-formation. Stars are formed by collapse of cold and dense cores of molecular clouds that are probably fragmented from their parental molecular cloud. The fragmentations are caused by perturbations.

The method that we use to study the perturbations is to observe molecules, atoms and ions which are sensitive to these changes, and serve as tracers of their environment and its conditions that are dominant there. To study and understand the star-formation mechanism, we choose NGC 3603 which is one of the most luminous and prominent HII regions in our Galaxy, located in the Carina constellation (Fig. 1.2) visible only from the southern hemisphere. This object, which is a cloud complex, contains a massive star cluster that provides strong stellar winds and radiation fields which strongly interact with the adjacent environment.

The radiation heats up the surface of the closely located molecular clouds. That warm and thin (compared to the size of the whole molecular cloud) transitional layer⁴, which is called Photon-Dominated Region (PDR⁵), is an extraordinary astrophysical laboratory where the local physical and chem-

⁴We need to keep in mind, that the structure of the molecular clouds can be described by a fractal-Brownian-motion (fBm) [Stutzki et al. \(1998\)](#). Assuming that the three dimensional structure of a cloud can be described by an fBm structure, the volume is dominated by the cloud surface (the surface grows in proportion with the volume) and therefore, this "thin surface layer" makes up a good fraction of the molecular material ([Stutzki, 1999](#)).

⁵This thin layer is also referred as Photo-dissociation Region. I shall use abbreviation PDR as Photon-Dominated Region.

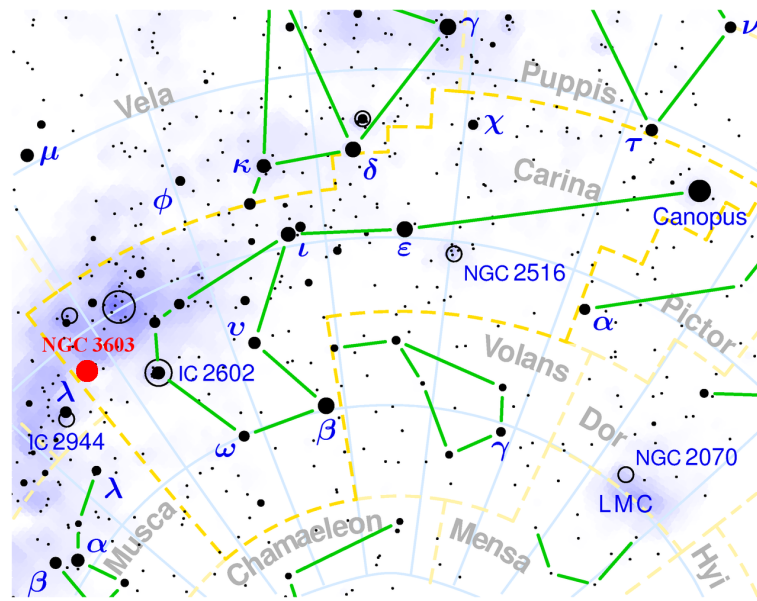


Figure 1.2: The position of NGC 3603 (filled red circle) in the Carina constellation on the southern hemisphere. Copyright: wikipedia.org

ical conditions are influenced and dominated by photons with defined energy range ($6 \leq h\nu \leq 13.6 \text{ eV}$)⁶.

As mentioned earlier, we need to investigate the different physical conditions and chemical processes through a group of carefully selected species (molecules, atoms and ions) that are sensible for the various densities and temperatures.

The footprints of these physical and chemical changes are manifested by either emissions or absorptions of the observed molecules, atoms and ions. Due to the complexity of the interstellar medium (including PDRs), we selected a few specific questions to better understand the physics and chemistry of the ISM.

- **What is the distribution of dust temperature and how is $N(\text{H}_2)$ distributed around the central cluster?**

Molecular hydrogen is the most abundant molecule in the interstellar medium. Because it efficiently forms on dust grain surfaces (within a certain dust temperature), dust is very important. It acts as catalysts for many chemical reactions [even though dust is much less abundant than gas (gas-to-dust mass ratio is ~ 100)]. Thus, the investigation of the dust and $N(\text{H}_2)$ distribution may lead to study the formation of molecular hydrogen.

- **Are the observed molecular clouds at the gravitationally stable or unstable stage?**

⁶The 6 and 13.6 eV are the ionization potential of dust and hydrogen, respectively.

As I mentioned, stars are born in cold and dense cores which are deeply embedded in their host molecular clouds. These cores are created by fragmentation. For the existence of fragmentations, the molecular cloud has to be energetically unstable (the cloud is not in *virial equilibrium*) which means that the thermal (or kinetic) energy and the gravitational potential energy compete with each other. The comparison of the observational data to the virial theorem provides us an insight into the stability of an observed cloud (more precisely stability of any system), hence we can deduce whether the star-formation is still an ongoing process or not.

- **Are there any observable signatures of systematic gas motions and/or enhanced turbulent?**

Turbulence is a relevant trigger of star formation. Gas motions within a molecular cloud happen on large (Brunt et al., 2009) and small scales (Nakamura & Li, 2008; Wang et al., 2010). For example, shock fronts, which are pressure-driven waves that propagates into their neighbouring gas faster than the local sound speed, trigger the star formations. Therefore, the observations of the signatures of turbulence (e.g. broad line widths) could help to identify the existence of turbulence. The study of the velocity structure of the observed molecular cloud may give an insight to the dominant and/or turbulent gas motions.

- **Is there any observable influence of prominent embedded infrared sources on the physics and chemistry of the observed molecular clouds?**

Photons within a certain energy range ($6\text{ eV} \leq h\nu \leq 13.6\text{ eV}$) are playing important role in the chemical and thermal balance of the PDRs. The birth places of these FUV-photons are high mass stars (O- and early B-type stars⁷) which could exist either outside or inside of a molecular cloud.

The local physics and chemistry may be governed by the embedded hot stars, hence the investigation of their adjacent environment could help to characterize the physics and chemistry inside the observed molecular cloud.

- **Are the model predictions of line intensities and densities, and observations in good agreement?**

We can prove our theoretical knowledge about the physical and chemical processes in the ISM with comparisons of observational data and model computations. Numerous models are exist with various assumptions about geometry, physics and chemistry. To un-

⁷The stars are classified based on their spectral characteristics and temperature. In the Morgan–Keenen system, stars are denoted by letters from O, B, . . . M, L; from the hottest to the coolest, respectively.

derstand and give a well detailed description of the ISM is a heroic contention due to its complexity, hence it is beneficial to widen the statistical sample as much as possible to approximate the realness.

- **Is there any observable chemical stratification? Are the observed abundances comparable with model predictions?**

We presume that NGC 3603 contains PDRs [e.g. [Röllig et al. \(2011\)](#)] which gives us an exceptional opportunity to study and compare the observations with the theoretical predictions. PDRs are consist of different layers where the physical conditions and chemical reactions are governed by the decreasing FUV-field strength as a function of cloud depth. Hence, the physical conditions and efficient chemical processes vary in the different layers. The investigation of chemical stratification may allow us to deduce the cloud structure.

Keeping these questions in mind, I shall present detailed study of dense gas tracers [Carbon Monosulfide⁸ (CS) and Formyl ion (HCO⁺)], diffuse gas tracers [Ethyne radical(C₂H) and Methylidyne radical(CH)], shock tracer [Water (H₂O)], important cooling lines (atomic and ionized oxygen [OI]⁹ and [OIII], atomic and ionized carbon [CI] and [CII] . . .) and the most abundant (after H₂) Carbon Monoxide (¹²CO) lines (and its isotopologues, ¹³CO and C¹⁸O) to help characterize the main physical conditions, and chemical processes in the prominent star-forming region NGC 3603.

⁸For the nomenclature of molecules, ions and atoms I follow the book [Tielens \(2005\)](#).

⁹The transitions denoted with square bracket (e.g. [CII]) signify forbidden transitions which means no lines can be measured in earthly laboratories.

Theoretical background

We receive information about the physical conditions of the ISM via spectral line features. These features (either could be line emission or absorption) reflect the physical conditions (density, temperature, pressure) in the molecular clouds. In this chapter, I briefly introduce the physical background necessary for the following chapters. Further and well detailed discussions of the theoretical background can be found in numerous books [for example, [Draine \(2011\)](#); [Herzberg \(1991, 2010\)](#); [Rybicki & Lightman \(2004\)](#); [Tielens \(2005\)](#); [Wilson et al. \(2009\)](#)].

2.1 Spectral features

We mostly receive information from the physical and chemical conditions of the ISM via line emissions (or absorption). To be able to observe this astrophysical phenomena, a quantum-mechanical energy state of the emitter or absorber needs to be excited. The observed photon frequency (ν) corresponds to the energy difference between two states ($\Delta E = h\nu$). Because we observe emission from rotational lines, fine- and hyperfine-structures, I provide a very short introduction to the phenomenon that produce these lines.

2.1.1 Rotational lines

The spectral line features are results from quantum-mechanical molecular rotational transitions. Quantum mechanics allows rotating molecules to possess only discrete quanta of angular momentum (due to the selection rules). The rotational energy is proportional to $J(J + 1)$ which means that the rotational transition frequency is related to J ($\nu \sim J$). Note, that

molecules without permanent electric dipole moment cannot have pure rotational transitions and I shall use the notation system $J \rightarrow J - 1$ for rotational transitions¹.

2.1.2 Fine- and hyperfine-structures

As an electron orbits around the nucleus (or nuclei in molecules) the magnetic field of nucleus (or nuclei) interact with the magnetic moment generated by the electron's spin (due its intrinsic angular momentum). This connection slightly shifts the electron's energy levels which can be detected as a split of the energy levels. This small ($\sim 10^{-2}$ eV) splitting of a spectral line is called fine-structure split which is, again, a result of the interaction between a particle's orbit and its spin.

It is possible that the fine-structure lines are further divided due to another quantum-mechanical effects. Not only the electrons but also the nucleus (or nuclei) possesses a spin, hence a magnetic moment, too. The magnetic moment of the nucleus (or nuclei) interacts with the previously mentioned electromagnetic fields and splits the fine-structure lines into energy levels with even smaller energy difference than fine-structure levels ($\sim 10^{-6}$ eV). This split is called hyperfine-structure.

2.2 Einstein-coefficients and critical density

As a first approximation, we assume a two-level system and these levels are occupied by n_u and n_l number of particles where the subscripts denote the energy levels (*upper* and *lower*)². Under certain conditions, transitions between these two levels are possible with different probabilities. These probabilities are described by the Einstein-coefficients:

Spontaneous emission coefficient (A_{ul} [s^{-1}]) It gives the probability of spontaneous emission of a photon due to the transition from level u to l . The number of radiative transitions per second per unit volume is $A_{ul}n_u$.

Absorption coefficient (B_{lu} [$s^{-1} \text{ erg}^{-1} \text{ cm}^2 \text{ sr}$]) The probability of absorption of a photon (with frequency ν) by a particle that transits from level

¹For example, the rotational transition from the first excited state to the ground state of carbon monoxide is nominated as $^{12}\text{CO} (1 \rightarrow 0)$.

²The energy difference between the upper and lower levels is: $E_u - E_l = h\nu$.

l to u . The number of transitions per second per unit volume per unit mean intensity³ is $B_{lu}n_lI_\nu$.

Induced emission coefficient (B_{ul} [$\text{s}^{-1} \text{ erg}^{-1} \text{ cm}^2 \text{ sr}$]) The probability of stimulated emission of a photon (with frequency ν) by a particle that transits from level u to l . The number of radiative transitions per second per unit volume is $B_{ul}n_uI_\nu$.

These coefficients are connected to each other and the relationship can be written as:

$$\frac{B_{lu}}{B_{ul}} = \frac{g_u}{g_l} \quad \text{and} \quad A_{ul} = \frac{8\pi h\nu^3}{c^3} B_{ul} \quad (2.1)$$

where h is the Planck-constant ($h \approx 6.63 \times 10^{-34} \text{ m}^2 \text{ kg s}^{-1}$), $c \approx 3 \times 10^8 \text{ m s}^{-1}$ is the speed of light in vacuum, g_u and g_l are the statistical weights of upper and lower energy levels, respectively. In local thermodynamic equilibrium (LTE), the populations of the upper and lower energy levels (n_u and n_l) are described by the Boltzman–distribution (with a temperature⁴ that characterizes the population ratio) and proportional to the statistical weights of the energy levels:

$$\frac{n_u}{n_l} = \frac{g_u}{g_l} e^{-h\nu/kT} \quad (2.2)$$

where k is the Boltzmann-constant ($k \approx 1.38 \times 10^{-23} \text{ m}^2 \text{ kg s}^{-2} \text{ K}^{-1}$).

Collisional processes

In the interstellar medium, besides radiation, collisional excitations (and de-excitations) are important cooling and heating processes in the ISM. To get some impression about the prevailing excitation mechanisms (radiation or collisions), the interstellar gas density needs to be investigated. For this, we introduce the collision rates C_{lu} and C_{ul} for the lower and the upper energy levels, respectively:

$$C_{ij} = \langle \sigma_{ij}v \rangle \quad [\text{cm}^3 \text{ s}^{-1}] \quad (2.3)$$

where σ_{ij} is the collisional cross section and v is the relative velocity of collisional partners. The number of collisional transitions per second per

³We assume that a radiation field is exist with a mean intensity I which is described by the Planck-function (assuming thermodynamic equilibrium).

⁴The temperature is either the kinetic temperature (T_{kin}) if collisions dominate (LTE) or the radiation temperature (T_{rad}) if radiation dominates.

unit volume are $n_l C_{lu}$ and $n_u C_{ul}$. In statistical equilibrium the number of upward and downward transitions are equal:

$$n_l B_{lu} I_\nu + n_l C_{lu} = n_u A_{ul} + n_u B_{ul} I_\nu + n_u C_{ul} \quad (2.4)$$

Thus, the ratio of level population

$$\frac{n_u}{n_l} = \frac{B_{lu} I_\nu + C_{lu}}{A_{ul} + B_{ul} I_\nu + C_{ul}} \quad (2.5)$$

If we assume that the collisional excitation and de-excitation processes are dominant, and take into account that the level population follows the Boltzmann-distribution (in LTE), Eq. (2.5) becomes

$$\frac{n_u}{n_l} = \frac{C_{lu}}{C_{ul}} = \frac{g_u}{g_l} e^{-h\nu/kT} \quad (2.6)$$

If we use the relationships $B_{ul} = (c^3/8\pi h\nu^3) A_{ul}$, $B_{lu} = B_{ul}(g_u/g_l)$ and $C_{lu} = C_{ul}(g_u/g_l) \exp(-h\nu/kT)$, Eq. (2.5) can be written as:

$$\frac{n_u}{n_l} = \frac{g_u}{g_l} e^{-h\nu/kT} \frac{K I_\nu (e^{-h\nu/kT})^{-1} + (C_{ul}/A_{ul})}{1 + K I_\nu + (C_{ul}/A_{ul})} \quad (2.7)$$

where $K = c^3/8\pi h\nu^3$. Using Eq. (2.3) we can write:

$$\frac{n}{n_{\text{crit}}} = \frac{C_{ul}}{A_{ul}} \quad \text{where} \quad n_{\text{crit}} \equiv \frac{A_{ul}}{C_{ul}} \approx \frac{A_{ul}}{\langle \sigma v \rangle} \quad [\text{cm}^{-3}] \quad (2.8)$$

The density value where the importance of collisional and radiative de-excitations are equal is called critical density. The critical density varies species by species and is different for each transition. If the gas density is larger than the critical density ($n \gg n_{\text{crit}}$), collisions are the dominant excitation mechanism and the level population is described by the Boltzmann-distribution. In this case, the excitation temperature is equal to the kinetic temperature of the gas ($T_{\text{ex}} = T_{\text{kin}}$).

However, considering optical depth effect, critical density can be changed by a factor $\beta(\tau)$. The factor $\beta(\tau)$ originates from the escape probability theory which describes the chance that a photon formed at optical depth τ in a molecular cloud can leave/escape the cloud before being absorbed, and the critical density can be written as:

$$n_{\text{crit}} = \frac{A_{ul}}{C_{ul}} \beta(\tau_{ul}) \quad [\text{cm}^{-3}] \quad (2.9)$$

More detailed description of the connections between the gas and its critical density can be found, for example, in [Wilson et al. \(2009\)](#) or e.g. discussion for optically thick case in [Mihalas \(1978\)](#); [Scoville & Solomon \(1974\)](#); [Stutzki & Winnewisser \(1985\)](#).

2.3 Radiative transfer

Radiative transfer describing how radiation propagates in the ISM (considering scattering by dust and gas, and emission and absorption processes). The basic equation of radiative transfer is:

$$\frac{dI_\nu}{ds} = -\kappa_\nu I_\nu + \epsilon_\nu \quad (2.10)$$

where I_ν is the specific intensity per unit time, surface, and solid angle in the frequency range of $[\nu, \nu + d\nu]$, ds is the path length (or an infinitesimal step along the line of sight), κ_ν and ϵ_ν are the absorption and emission coefficient, respectively. They can be written as:

$$\epsilon_\nu = \frac{h\nu}{4\pi} n_u A_{ul} \phi(\nu) \quad (2.11a)$$

$$\kappa_\nu = \frac{h\nu}{c} (n_l B_{lu} - n_u B_{ul}) \phi(\nu) \quad (2.11b)$$

where $\phi(\nu)$ is the normalized line profile function ($\int \phi(\nu) d\nu = 1$) giving the probability of emitted photon is in the range of $[\nu, \nu + d\nu]$. Defining optical depth ($d\tau_\nu = -\kappa_\nu ds$) and source function ($S_\nu = \epsilon_\nu / \kappa_\nu$) the Eq. (2.10) can be rewritten as:

$$\frac{dI_\nu}{d\tau_\nu} = -I_\nu + S_\nu \quad (2.12)$$

The general solution of this equation is:

$$I_\nu(\tau_\nu) = I_\nu(0)e^{-\tau_\nu} + \int_0^{\tau_\nu} S_\nu(\tau'_\nu) e^{(\tau'_\nu - \tau_\nu)} d\tau'_\nu \quad (2.13)$$

It gives information about the background radiation (first part) and the radiation which is emitted and absorbed by the medium (second part). Assuming thermal equilibrium [$dI_\nu/ds = 0$, ([Wilson et al., 2009](#))], the distribution of intensity is described by the Planck–function B_ν with a formal excitation temperature (T_{ex}), and we can write:

$$I_\nu = S_\nu = \frac{\epsilon_\nu}{\kappa_\nu} = B_\nu(T) = \frac{2h\nu^3}{c^2} \frac{1}{e^{h\nu/kT_{\text{ex}}} - 1} \quad (2.14)$$

If we assume a homogeneous medium, the solution of Eq. (2.13):

$$I_\nu(\tau_\nu) = I_\nu(0)e^{-\tau_\nu} + S_\nu(\tau_\nu)(1 - e^{-\tau_\nu}) \quad (2.15)$$

In radio astronomy, the received emission is often described in terms of the brightness temperature ($T_B = I_\nu c^2 / 2k\nu^2$). Hence the solution of radiative equation can be written using the brightness temperature:

$$T_B(\tau_\nu) = T_B(0)e^{-\tau_\nu} + T_{\text{ex}}(\tau_\nu)(1 - e^{-\tau_\nu}) \quad (2.16)$$

where $T_B(0)$ is the temperature of the background. If the detected emission is optically thick ($\tau_\nu \gg 1$), we observe the excitation temperature but in case of optically thin emission ($\tau_\nu \ll 1$) only $T_B = \tau_\nu T_{\text{ex}}$ is defined.

2.4 Optical depth and column density calculation

In practice, we receive emitted photons not only from the observed source. Spectral-line data often contain continuum sources (either from the target source or from nearby sources in the field of view). In a case where we are interested about spectral lines, the continuum level needs to be subtracted from the data set. Well detailed methods for continuum subtraction can be found in e.g. [Wilson et al. \(2009\)](#). With this, Eq. (2.16) can be written as:

$$J_\nu(T_B) = f[J_\nu(T_{\text{ex}}) - J_\nu(T_{\text{bg}})](1 - e^{-\tau_\nu}) \quad (2.17)$$

where $J_\nu(T) = (h\nu/k)[\exp(h\nu/kT) - 1]^{-1}$ is the normalized Planck–intensity and f is the filling factor (which is a fraction of the telescope beam occupied by the observed source). The term T_{bg} denotes the temperature of the cosmic background radiation with a value 2.725 K ([Fixsen, 2009](#)).

Using the relationship between the Einstein–coefficients, the definitions of the emission and absorption coefficients (2.11a) and (2.11b), and the definition of the optical depth, τ_ν can be written as (for a given transition):

$$\tau_\nu = N_u A_{ul} \frac{c^2}{8\pi\nu^2} \frac{g_u}{g_l} (1 - e^{-h\nu/kT_{\text{ex}}}) \quad (2.18)$$

where $N_u = \int n_u ds$ is the column density of the upper level.

Considering optically thin emission [$J_\nu(T_{ex}) \gg J_\nu(T_{bg})$ and $T_B \Delta v \approx T_{ex} \int \tau dv$ where Δv is the line width at half maximum in km s^{-1}], the column density of a rotational level J can be calculated via the integration over the observed line profile:

$$N_J = \frac{8\pi k_B \nu^2}{c^3 h A_{ul}} \int \frac{T_B}{\text{K km s}^{-1}} dv \quad [\text{cm}^{-2}] \quad (2.19)$$

In the optically thick case, we have to take into account the optical depth effect, therefore we have to correct Eq. (2.19) by a factor of $\tau/[1 - \exp(-\tau)]$ (Goldsmith & Langer, 1999).

The optical thickness of an observed rotational transition can be deduced from the integrated optical depth using line center opacity (τ_{ν_0}), which can be determined from Eq. (2.17) (assuming $f = 1$ and T_{ex} is known):

$$\tau_{\nu_0} = -\ln \left[1 - \left(\frac{T_{B,\nu_0}}{T_{ex} - T_{bg}} \right) \right] \quad (2.20)$$

If the observed line radiation profile follows the Gaussian velocity distribution, the optical depth can be determined (Ossenkopf et al., 2013):

$$\int \tau dv = \frac{1}{2} \sqrt{\frac{\pi}{\ln 2}} \Delta v \times \tau_{\nu_0} \quad (2.21)$$

where Δv is the line width (FWHM).

For hyperfine lines, we need to take into account all hyperfine components at a given rotational level and the column density of a rotational level (J) can be derived (Simon, 1997):

$$N_J = \frac{8\pi \nu^3}{c^3} \cdot \frac{\tau_{total}}{A_{ul}} \cdot \frac{\frac{1}{2} \sqrt{\frac{\pi}{\ln 2}} \Delta v}{\exp\left(\frac{h\nu}{kT_{ex}}\right) - 1} \quad [\text{cm}^{-2}] \quad (2.22)$$

where τ_{total} is the optical depth of a rotational transition (including all hyperfine components at that given rotational level). In LTE, a level population is following the Boltzmann–distribution and the total column density is the sum of the individual column densities of the levels, thus:

$$N_{tot} = \sum_{J=0}^{\infty} N_J = N_0 \sum_{J=0}^{\infty} (g_J e^{-E_J/kT_{ex}}) = N_J \frac{Q(T_{ex})}{g_J e^{-E_J/kT_{ex}}} \quad [\text{cm}^{-2}] \quad (2.23)$$

where $Q(T_{ex}) = \sum_{J=0}^{\infty} (g_J e^{-E_J/kT_{ex}})$ is the partition function. Equation (2.23) gives the total column density based on one observed transition.

When several rotational transitions are observed, a useful diagnostic tool for the determination of column density and temperature is the rotation diagram. Equation (2.23) can be written as:

$$\frac{N_J}{g_J} = \frac{N_{\text{tot}}}{Q(T_{\text{kin}})} e^{-E_J/kT_{\text{kin}}} \longrightarrow \ln\left(\frac{N_J}{g_J}\right) = \ln\left(\frac{N_{\text{tot}}}{Q(T_{\text{kin}})}\right) - \frac{E_J}{kT_{\text{kin}}} \quad (2.24)$$

Now, if we plot the logarithm of the ratio of the column density and statistical weight of a given level as a function of the energy of that level (in Kelvin), it gives a linear relationship. The slope provides the temperature (more precisely $1/T$) and the intersection with the ordinate gives the column density. This method is useful, for example, to determine which temperature describes the population distribution in LTE or estimates the optical depth.

2.5 Photon-Dominated Regions (PDRs)

The warm surface of molecular clouds is called **Photon-Dominated Region** (PDR). This is a region where the chemical and physical conditions are dominated by the local photon density. FUV-photons with energies between 6 eV and 13.6 eV, provided by hot and young stars (O, B and Wolf-Rayet stars) or by the ambient interstellar radiation field (ISRF), play an important role in the thermal and chemical balance of interstellar gas (Hollenbach & Tielens, 1999). In PDRs, different heating and cooling processes are present e.g., photo-electric emissions from dust grains and cooling by fine-structure emissions of [CII], and [OI] (Kaufman et al., 1999; Röllig et al., 2007; Sternberg & Dalgarno, 1995). PDRs contain layered structure because interstellar dust shields species from FUV-photons, hence chemical stratifications are produced by the progressively weaker FUV-field (Ossenkopf et al., 2007).

A schematic representation of a PDR is shown in Fig. 2.1. The surface part of a PDR (relative to the position of the UV radiation source) has a thin transient region in which most species are ionized, and is called ionization front. Behind this front, the ionized atoms become neutral and the FUV-photons can penetrate into the cloud. Thus, there is still strong enough radiation (therefore high temperature and strong heating) to be able to dissociate hydrogen. The FUV radiation is absorbed by dust grains and PAHs (Polycyclic Aromatic Hydrocarbons). The absorption energy is used to heat the grains and excite PAHs. This part of a PDR emits continuum emission in FIR and the PAH lines in infrared wavelengths (Bakes & Tielens, 1994; Weingartner & Draine, 2001). The gas is heated by photo-electrons (Section 2.5.1) which heat the neutral gas (Tielens & Hollenbach,

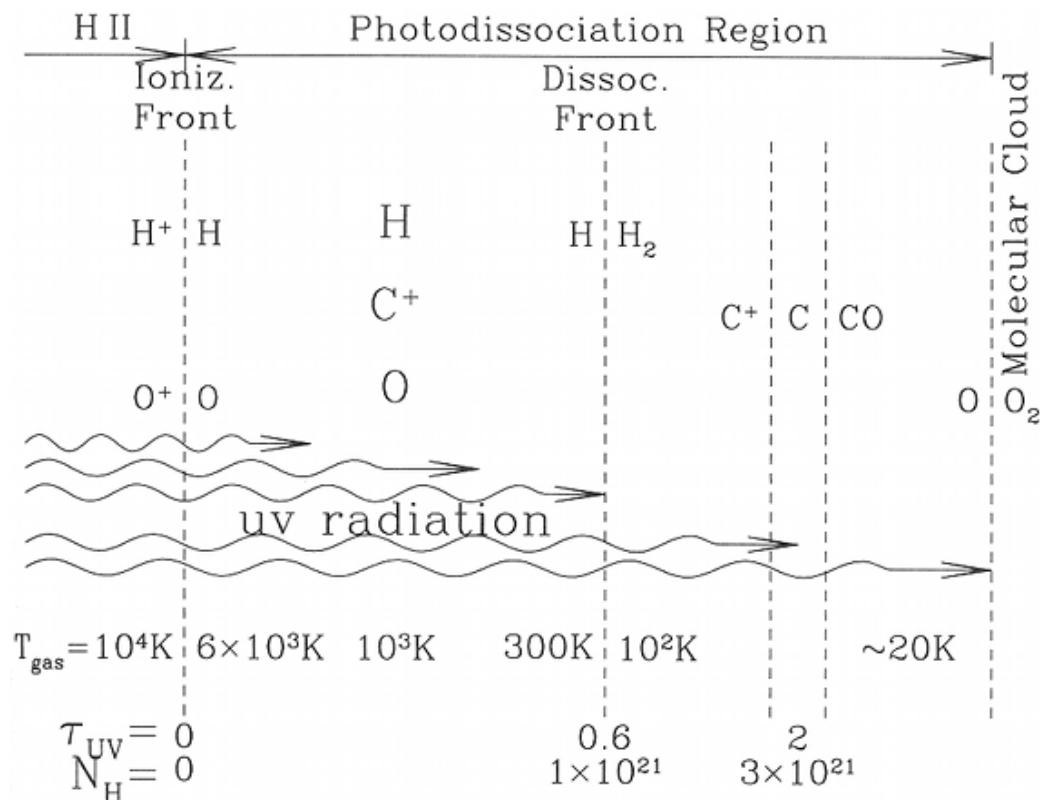


Figure 2.1: A schematic figure about the structure of a PDR (Draine, 2011).

1985; Watson, 1972; Wolfire et al., 1995). Deeper in PDRs another thin region exists, it is called dissociation front. In this front, the molecular hydrogen (H₂) starts to be dominant rather than atomic hydrogen (H). Slightly deeper in the cloud, ionized carbon recombines to produce atomic carbon and ¹²CO.

2.5.1 Energy balance

Heating

Photoelectric heating on grains and PAHs The photoelectric heating (PE-heating, hereafter) process is the dominant heating process in the ISM (Fig. 2.2). In this process, an electron can be ejected from the grain surface when an FUV-photon collides with a dust grain. The kinetic energy of the electron heats up the ambient gas. The efficiency of PE-heating is reduced for highly ionized grains. If the FUV radiation field is attenuated, and the grains are mainly neutral, the PE-heating is more efficient.

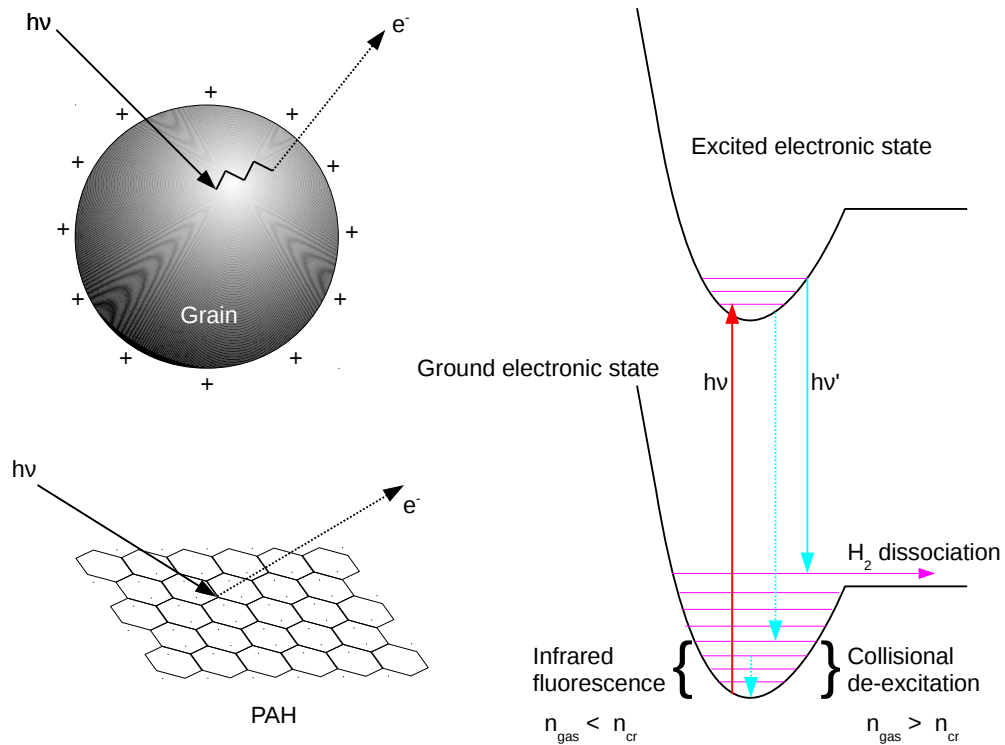


Figure 2.2: A basic figure on how the photoelectric heating works on dust grains and PAHs (left panel) and a schematic diagram of the photo-pumping of H_2 (right panel).

Photo-pumping of H_2 In this case, an absorbed FUV-photon electronically excites H_2 which decays back to an excited vibrational level in the ground electronic state (or if the gas density is low enough [$n < n_{\text{cr}} \sim 10^4 \text{ cm}^{-3}$, (Martin & Mandy, 1995; Martin et al., 1996)] to the ground vibrational state producing infrared emission, Fig. 2.2). If the gas density is large ($n > n_{\text{cr}} \sim 10^4 \text{ cm}^{-3}$) another de-excitation mechanism becomes important which is responsible for the gas heating, namely collisions with hydrogen.

Nevertheless, it is also possible that the photon fluoresces back to the vibrational continuum level in the ground electronic state. In that case, the molecular hydrogen is destroyed by photo-dissociation. If the molecular hydrogen column density is large enough, which means optically thick lines, all of those photons are absorbed by H_2 in the outer part of the molecular cloud that could cause UV fluorescence photo-dissociation. This effect is the so-called *self-shielding* of H_2 . Because the rate of photo-dissociation of molecular hydrogen depends on the column density, the H/H_2 transient region is very thin and sharp.

Dust–gas heating Usually the dust and gas do not have the same temperature ($T_{\text{dust}} \neq T_{\text{gas}}$), and are not in thermodynamic equilibrium⁵. If $T_{\text{dust}} > T_{\text{gas}}$, the gas atoms leap from the grain surface and put energy into the dust environment, thus the gas can be heated up. On the other hand, if $T_{\text{dust}} < T_{\text{gas}}$ (in, for example, PDRs or the diffuse ISM), this process becomes a gas cooling mechanism.

Cosmic–ray heating It is a dominant source of gas heating at the dense part of PDRs, far from the ionization front, where the ambient FUV radiation field is almost completely attenuated. In a localized place in the interstellar medium, where high cosmic–ray ionization occurs, cosmic rays with low energy [~ 100 MeV, (Tielens, 2005)] could play a dominant role in gas heating⁶.

Cooling

The photo-dissociation regions are mainly cooled by emission of collisionally excited far–infrared fine-structure lines [e.g., [OI] at $\lambda = 63 \mu\text{m}$ and $\lambda = 146 \mu\text{m}$, [CII] at $\lambda = 158 \mu\text{m}$ which are also useful as a diagnostic tool for the temperatures and densities of emitting regions (Liseau et al., 2006)] and by rotational transition lines (e.g., ^{12}CO , OH, H_2O). The relative dominance of these lines depends on the chemical composition of the gas phase (Tielens & Hollenbach, 1985) and physical parameters such as the density. For example, in a low density region [$n \ll n_{\text{cr}}([\text{CII}]) \sim 3 \times 10^3 \text{ cm}^{-3}$, (Mookerjee et al., 2011)] [CII] emission dominates the cooling (Abel et al., 2005; Abel, 2006; Heiles, 1994; Kaufman et al., 2006). On the other hand, [OI] ($^3\text{P}_1 \rightarrow ^3\text{P}_2$) is an important cooling line at high densities [because this line has a high critical density $n_{\text{cr}} \approx 5 \times 10^5 \text{ cm}^{-3}$, (Mookerjee et al., 2011; Röllig et al., 2006)]. Additionally, PDRs could be cooled by collisionally excited infrared ro-vibrational lines of molecular hydrogen. Also, if the density is high enough, then another cooling process becomes important, namely the collisions with cooler dust grains (Burke & Hollenbach, 1983).

⁵In dark clouds, where no UV photons are entering, and under high density conditions dust and gas are in equilibrium.

⁶There are another heating mechanisms which could be important under certain circumstances (e.g., photo-dissociation of H_2 , photo-ionization of C, X-ray heating, turbulent and shock heating, gravitational heating.)

2.6 Chemistry in the ISM

The interstellar chemistry was impelled by the discoveries of atoms, ions and molecules in the ISM⁷. In the ISM, two kinds of chemistry can be distinguished: gas-phase and grain-surface chemistry. The chemical reactions are (mainly) governed by photons, electrons and collisions of different types of molecules and atoms. To be able to model the observations, different models have been developed which take into consideration the simplified geometry of a cloud (spherical or plan-parallel approach) and the main chemical reaction types in both gas-phase and grain-surface chemistry. I introduce only the important chemical reaction types because a short description of the models that I applied will be described in Chapter 7.

2.6.1 Gas phase chemistry

Photodissociation: $AB + h\nu \longrightarrow A + B$. The chemistry in PDRs is mainly driven by FUV photons which can destroy the molecules (dissociate them). This procedure is important if the molecular cloud is located in the vicinity of OB stars.

Neutral-neutral: $A + B \longrightarrow C + D$. Another important reaction type is the neutral-neutral chemical reaction which is relatively slow. It is because this reaction needs additional energy to overcome the activation barrier of the neutral species.

Ion-neutral: $A^+ + B \longrightarrow C^+ + D$. Because the reactant is an ion, which means higher energetic state, these reactions have no activation barrier, or at least it is very low, therefore this reaction can be faster at low temperatures than neutral-neutral reaction.

Dissociative electron recombination: $A^+ + e^- \longrightarrow C + D$. This type of reaction could be important in those parts of clouds where the electron density is high enough (for example, at or close to the ionization front in PDRs).

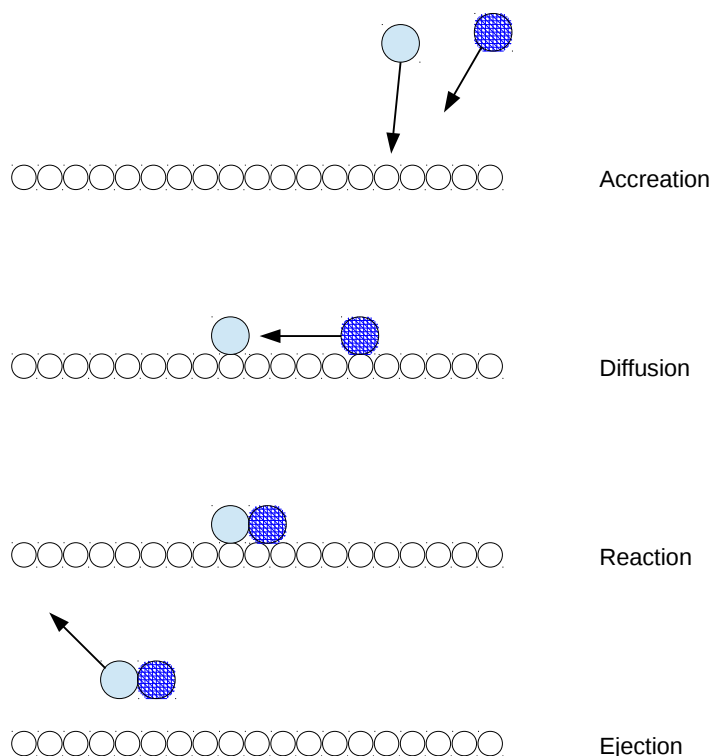


Figure 2.3: A schematic figure on the possible reaction types of two species on grain surface (Tielens, 2005).

2.6.2 Grain surface chemistry

Even if the chemistry and the chemical structure of a molecular cloud mainly depends on the abundance of hydrogen and the gas-phase heavy elements (Sternberg & Dalgarno, 1995), the dust grains play an important role in chemistry as well. The time scale for a process on the grain surface is set by the accretion rate. The accretion rates can be expressed as (Tielens, 2005):

$$k_{\text{ac}} = v\sigma_d n_d S(T, T_d) \quad (2.25)$$

where v is the velocity of species, σ_d is the grain cross section, n_d is the density of grains, and $S(T, T_d)$ is the sticking coefficient which depends on the temperature of gas and dust. The surface atom which is bonded to the surface only by a weak van der Waals force is physically adsorbed (physisorbed). Because of this weak bond, that kind of surface atoms have a high mobility on the surface. On the other hand, it is possible for

⁷Nowadays, around 200 species have been detected in the interstellar medium (see, for example, at <http://www.astro.uni-koeln.de/cdms/molecules>).

some species to stick to the grain surface with much stronger bond. This is called chemisorption because the bonding to the grain surface is a strong covalent bond. Therefore, chemisorbed species have a very low mobility and they cannot easily move on the surface⁸. The mobility is an important “parameter”. If there are two species with high mobility (which means they have high probability to meet each other) on the grain surface, then the reactions between these species are driven mainly by collisions. This is called Langmuir–Hinshelwood mechanism. Another mechanism, called Eley–Rideal mechanism, occurs when a gas–phase element hits directly an immobile atom on the grain surface.

The temperature of the dust grain is also important because, if it is high enough, only chemisorption is relevant, because the probability of the evaporation of physisorbed atoms increases with the dust temperature.

⁸The chemisorbed hydrogen moves on the grain surface via a quantum tunnelling effect, while species heavier than hydrogen can only move on the grain surface via thermal hopping.

Observations by the Herschel Space Observatory

In this chapter, I give a brief description about the space mission Herschel Space Observatory (Section 3.1). After that, I shortly describe which instruments we used for taking scientific data (Sections 3.1.1 and 3.1.2), what kind of observing modes are possible, and which of them were used by us (Sections 3.1.1 and 3.1.2). The data I present in the thesis are part of the WADI-program (Section 3.2) and the one of target sources of this key-project was NGC 3603 (Section 3.2.1).

3.1 The Herschel Space Observatory

The Herschel Space Observatory [(Pilbratt et al., 2010), hereafter Herschel], has the largest single mirror in space so far and carried three instruments [Photodetector Array Camera and Spectrometer (*PACS*), (Poglitsch et al., 2010); Heterodyne Instrument for the Far Infrared (*HIFI*), (de Graauw et al., 2010) and Spectral and Photometric Imaging REceiver (*SPIRE*) (Griffin et al., 2010)] covering a spectral range from the FIR to sub-millimetre (submm). Because molecule rotational transitions are in the submm and FIR regimes and most of the desired species are observed by the instruments HIFI and PACS, I shall give a short introduction of these instruments. On the other hand, I also investigated the combination of SPIRE and PACS data (using *SPIRE PACS Parallel Observing Mode*) to study the dust and UV field distribution (Section 5.3). Therefore, I give a very short introduction about SPIRE, too (Section 3.1.3).

Table 3.1: *The main parameters of the Herschel Space Observatory*

S/C type:	Three-axis stabilised
Operation:	3 hrs ground contact period/day
Dimensions:	7.5 m × 4.0 m (height × diameter)
Telescope diameter:	3.5 m
Total mass:	3170 kg
Solar array power:	1500 W
Average data rate to instruments:	130 kbps
Absolute pointing error:	2.45'' (pointing)/2.54'' (scanning)
Relative pointing error:	0.24'' (pointing)/0.88'' (scanning)
Spatial relative pointing error:	2.44''
Cryogenic lifetime from launch:	at least 3.5 years

3.1.1 HIFI

HIFI can be used for spectroscopy from high to very high spectral resolution (1 – 0.125 MHz) in a wavelength range of $\sim 625 - 240$ (480 – 1250 GHz) and 213 – 157 (1410 – 1910 GHz) μm . These ranges are split into 7 mixer bands each with vertical and horizontal polarizations. HIFI has four spectrometers: two Wide Band Acousto–Optical Spectrometers (*WBS*) and two High Resolution Autocorrelation Spectrometers (*HRS*) that can be used in both polarizations. HIFI uses heterodyne technique¹ which means the signal from the sky (ν_{sky}) is mixed with a signal from a local oscillator (ν_{LO}). The intermediate frequency (ν_{IF}) is the difference of the sky and LO frequencies: $\nu_{IF} = \nu_{LO} - \nu_{sky}$. Because HIFI works as a *double sideband* (*DSB*) receiver both signals [$\nu_{LO} + \nu_{sky}$ (upper sideband, USB) and $\nu_{LO} - \nu_{sky}$ (lower sideband, LSB)] are detected at the same time (Roelfsema et al., 2012).

Observing modes with HIFI

Basically, four kinds of observations are possible with HIFI: position, dual beam and frequency switch, and load chop. The selection of the observing modes depends on, for example, the properties of a target source (e.g. how extended the source is). The possible observing modes with HIFI are:

1. **Single point:** with one position on the sky

¹Many books can give more detailed description about the different heterodyne techniques, e.g. Hall et al. (1981); Kroger (1967); Menzies (1976); Nahin (2001); Schultz (2004) and Wadley (1959).

- Position switch (PS)
 - Dual beam switch (DBS)
 - Frequency switch (FS)
 - Load chop (LC)
2. **Maps:** to observe extended sources
 - On-the-fly (OTF) with position switch
 - OTF with frequency switch
 - Raster with dual beam switch
 3. **Spectral scans:** for line surveys with one position on the sky
 - Dual beam switch
 - Frequency switch
 - Load chop

We received single point observations with dual beam switch mode and OTF maps, thus I give a short description about these observational methods.

DBS, single point observation. In this case, the beam is moved by the secondary (or internal) mirror between the ON and OFF reference positions. For OFF measurements, if it is possible, we observe the blank sky with no emission to correct the observed spectra for the background sky noise and for calibration of the instrument itself. This method is efficient because the OFF position is relatively close to the ON position ($< 3'$), hence the telescope and internal mirror movements are short which increases the efficiency of the observation (more time on source). Also, because of the small motions of the telescope and the secondary mirror (Fig. 3.1), this observing method provides good quality data without standing waves due to the dual chop motions. Because the chopper mirror changes the path of the incoming light, some standing wave could still exist. But if we have the source on both ON and OFF positions (due to the telescope movement) the standing waves can be eliminated or minimized. This leads to stable baselines and good intensity calibration.

On-the-fly (OTF) map. This is the most time efficient observing method with HIFI (basically, the total time of the observing time can be used on the source). The telescope scans the source in rows and every second row has an opposite scan direction (Fig. 3.2). During the scans, there are data readouts at regular time intervals. The default time interval of the readouts is Nyquist-sampled. It means, that the data readouts places at shorter scanning distance than half beam size (HFBS) at the observational frequency. For example, the sampling sizes in case of band 1a is $18''_4$ for

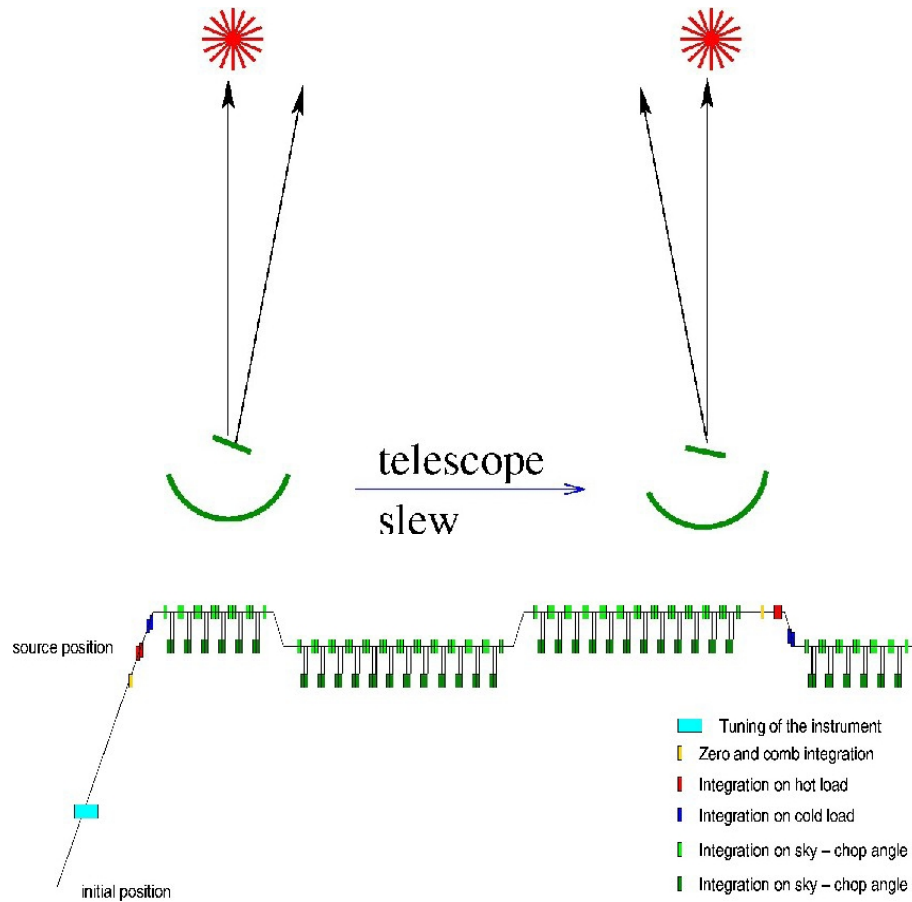


Figure 3.1: *Top:* The light paths from the source. *Bottom:* schematic figure on the dual beam switch observing mode (Jackson et al., 2007).

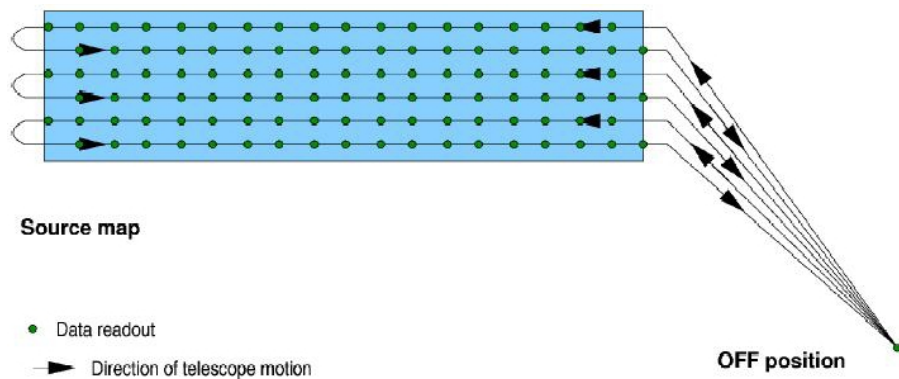


Figure 3.2: Schematic figure on the on-the-fly observing mode. The green dots show the readouts (Jackson et al., 2007).

Nyquist- and is $22''$ for half-beam sampling (Schieder, 2010). This leads to no loss of spatial information and data with no aliasing. After a certain period, OFF measurements are also included for blank sky subtraction.

3.1.2 PACS

The PACS instrument has two modes: imaging dual-band photometry and integral-field spectroscopy (Poglitsch et al., 2010). To be able to investigate the different transitions of important cooling lines, we used PACS due to its capability to observe at shorter wavelengths than HIFI ($\lesssim 157 \mu\text{m}$). Because we only used the spectroscopy part, I give a more detailed description of the spectrometer.

The spectrometer has a wavelength range of $51 \mu\text{m}$ to $220 \mu\text{m}$ which is divided into two channels: blue ($51 - 105 \mu\text{m}$) and red ($102 - 220 \mu\text{m}$). The spectrometer also has different “units”: the basic unit of detector is called as a *pixel*, and a *module* which has 16 pixels in 25 columns. The total field of view (FOV) is $47'' \times 47''$ which is assured by 5×5 spatial pixels (*spaxels*). The spaxels are the basic unit of the integral field of PACS. The individual spaxels cover an area of $9.4'' \times 9.4''$. Figure 3.3 shows how the spaxels cover the given observed field and how the *image slicer* does work: it redistributes the 2D FOV into 1×25 slices as shown in Fig. 3.3. The advantage of the combination of the spectral and spatial resolutions is the efficiency of the observation of weak lines. The real footprint of the spaxels on the sky can be seen on Fig. 3.4. The real distribution of the spaxels depends on the position angle of the pointing. In cases of nod A and B, there is also a small shift ($\sim 2''$) between each spaxel because of the optical distortions between the chopper ON and OFF positions.

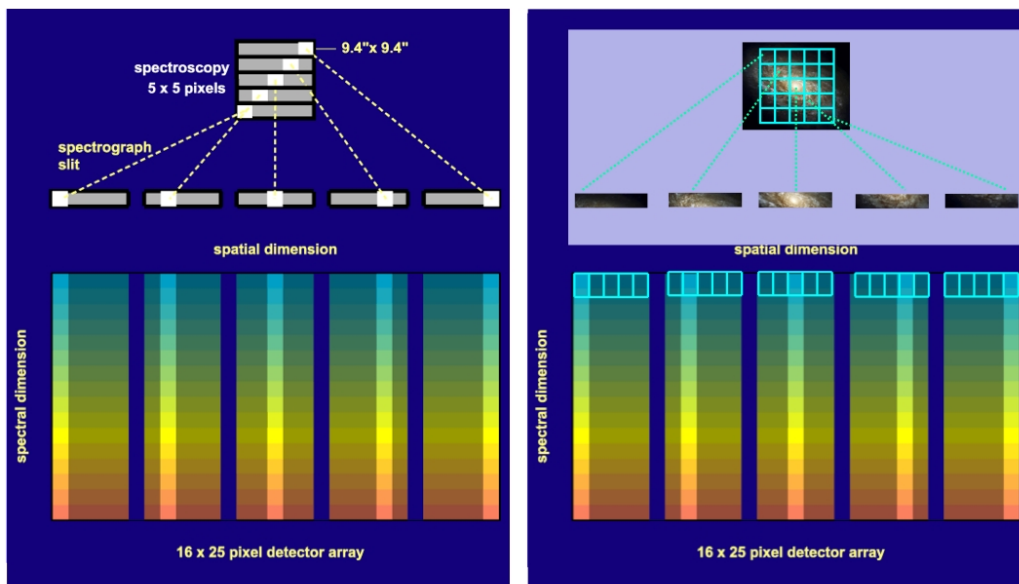


Figure 3.3: How the integral-field spectrometer works: each spaxel is projected into the detector arrays [Altieri & Vavrek \(2011\)](#).

Observing modes with PACS

There are two main observing modes:

1. Line spectroscopy

- Chopping/nodding spectroscopy
- Unchopped grating scan

2. Range spectroscopy

- Chopping/nodding spectroscopy
- Unchopped grating scan

We used line spectroscopy with chop/nod mode and range spectroscopy with unchopped grating scan mode. Thus, a short description about these observing modes will be given.

Line spectroscopy with chop/nod mode. This observing technique is ideal for faint lines with faint or bright continuum. We can select the combination of the wavelength range in which we want to observe: first (102–210 μm) and second (71–105 μm) order, or first and third (51–73 μm) order. This is available for range spectroscopy, too. It is also possible to change the chopper throw between 1.5', 3' or 6' ("small", "medium" and "large", respectively). These values correspond to the rotation of the footprint on the source observation (in both nod positions). In the example shown on Fig. 3.4, the observing sequence is going from the top left (green signs \rightarrow nod A–OFF) to the bottom right (purple signs \rightarrow nod B–OFF). In this case, we had one nod cycle which means the whole nod sequence looks like A-A-B-B: nod A–OFF \rightarrow nod A–ON \rightarrow nod B–ON \rightarrow nod B–OFF. Such a sequence can be repeated, if needed, to observe fainter lines.

Range spectroscopy with unchopped grating scan. In this mode, the observations of one line or several line features are possible, too, like in case of line spectroscopy. This mode allows the observers to define a wavelength range or the full range (SED mode). The other similarity with line spectroscopy is the different chopper throws (except in map mode where only one throw is available, namely the "large"). The unchopped grating scan can be done with Nyquist-sampling or with high-sampling density.

3.1.3 SPIRE

This instrument has an imaging Fourier–transform spectrometer (FTS) and a three–band imaging photometer. The photometer (which provides a

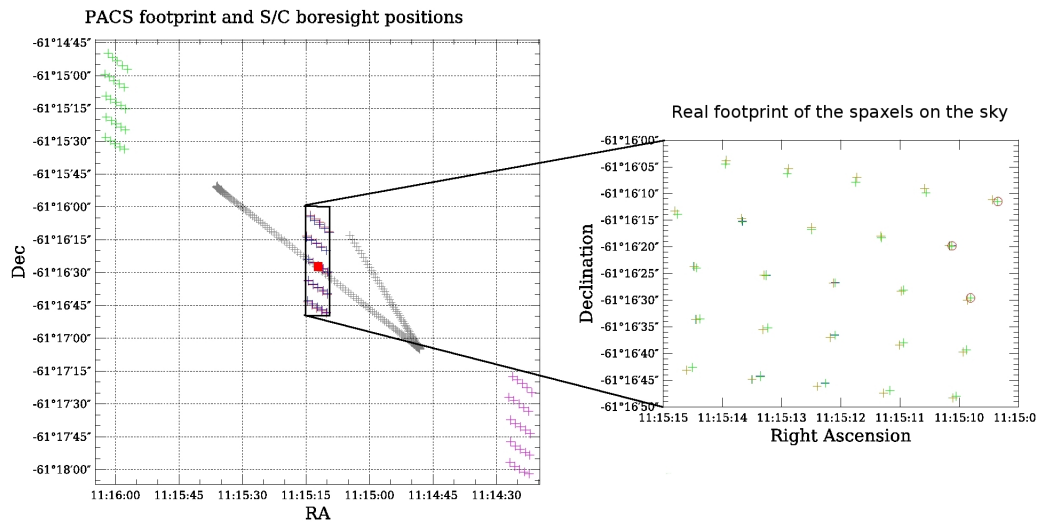


Figure 3.4: An example of the real footprints on the sky. **Left plot:** the PACS footprints (ON and OFF positions are included) and the Herschel boresight (grey crosses). The red square indicates the position of the source. The green and purple crosses mark the OFF positions (nod A and nod B, respectively), while the red and blue crosses show the ON position (nod A + nod B). **Right plot:** the enlargement of the ON position which shows the real footprint on the sky. The red circles show the sequence direction of the numbering of the spaxels: the top right-most represents the 0, 0 spaxel, then, as we go down, 0, 1 and 0, 2 etc. The left-most at the bottom is the 4, 4 spaxel.

broad-band photometry with $\lambda/\Delta\lambda \sim 3$) uses three bands with approximate center wavelengths of 250, 350 and 500 μm . These bands are called PSW, PMW and PLW respectively and have different layout of photometer arrays [more detailed descriptions about SPIRE can be found in, for example, Griffin et al. (2010)]. To investigate the distribution of dust and UV field strength in NGC 3603, I used a Level-2² public photometry data set from SPIRE PACS parallel observing mode³. The observational ID I used was 1342203064 which is a line scan with fast scan speed (60''/s) and covers a large map (120' \times 120') about the surrounding area of NGC 3603. On the other hand, I focused only on a very small fraction of the whole map which is included NGC 3603.

²More information about SPIRE pipeline steps can be found at <http://herschel.esac.esa.int/twiki/bin/view/Public/SpireCalibrationWeb?template=viewprint>

³http://herschel.esac.esa.int/Docs/PMODE/html/parallel_om.html

3.2 The WADI key–project

The physical and chemical processes in molecular clouds are strongly interconnected; the density and temperature of interstellar material define the possible chemical reactions. The surroundings of young and massive stars are heavily influenced by UV radiation emitted by these stars and that radiation and possibly strong stellar winds govern the local physical, and chemical conditions.

The Herschel guaranteed time key–project “The Warm And Dense ISM” [WADI, PI: PD. Dr. Volker Ossenkopf, (Ossenkopf et al., 2010a, 2011)] investigated these interactions via observations of different molecular clouds (concentrating on the thin interaction zones, the so–called PDRs; Section 2.5). The observations are focused on three basic scientific topics, namely the chemistry, dynamics and energy balance of molecular clouds, e.g., what kind of physical processes and conditions can trigger star formation in molecular clouds?; how the UV radiation field interacts with molecular clouds (and/or how the strong stellar wind, provided by hot and young massive stars, influences the interstellar gas in their environment)? The key-project is also interested about the chemistry: which reactions dominate and could lead to the formation of more complex molecules?

Observing light hydrides (e.g., CH, NH etc.) and deriving column densities can help to improve chemical models. Also, the observed carbon species (^{12}CO , ^{13}CO , $^{12}\text{C}^+$) could allow us to determine abundance ratios that can lead to a better understanding of carbon fractionation which is still not clear. Because Herschel has a very good velocity resolution, the investigation of detected emission lines can help to study the velocity structures of an observed molecular cloud. Investigation of the physics of energy balance can be done, for example, by comparison of cooling line intensities ([OI], [CII]). In this thesis, I shall concentrate the center part of a molecular cloud complex and shortly describe it in Section 3.2.1 then give summaries of the observations (Tab. 3.2 and 3.3, and Appendices A and B).

3.2.1 The target source: NGC 3603

With a total bolometric luminosity of $L_{\text{bol}} > 10^7 L_{\odot}$ (Stolte et al., 2004), NGC 3603 is 100 times more luminous than the Orion Nebula and one of the most prominent HII regions in our Galaxy. It is located in the Carina spiral arm (the coordinates⁴ of NGC 3603 are: $\alpha_{\text{J2000}} = 11^{\text{h}}15^{\text{m}}09^{\text{s}}.1$ and $\delta_{\text{J2000}} = -61^{\circ}16'17''$) with a distance of about 7–8 kpc (Melena et al., 2008), and a total gas mass of $\sim 4 \times 10^5 M_{\odot}$ (Grabelsky et al., 1988). It has

⁴From SIMBAD: <http://cdsweb.u-strasbg.fr/>

a massive [the total cluster mass is $\geq 4000 M_{\odot}$, (Brandner et al., 2000)] and young [the average age is $\sim 2.5 \pm 2$ Myr, Clayton (1990)] star cluster with a relatively low foreground extinction [$A_V \sim 4 \dots 5^m$, (Nürnberger & Petr-Gotzens, 2002)]. The cluster has about a dozen O–type stars with masses up to $120 M_{\odot}$ within one cubic light-year (Drissen et al., 1995) and probably three Wolf-Rayet stars (Moffat et al., 1985; Walborn, 1973), providing a very strong UV radiation field and stellar winds.

Because of these conditions, NGC 3603 is an ideal place to study high mass star-formation as well as PDRs [see more in Hollenbach & Tielens (1999); Röllig et al. (2007)]. It is a relatively well studied region almost throughout the whole electromagnetic spectrum (Balick et al., 1980; Clayton, 1986; Corcoran et al., 2000; Harayama et al., 2008; Lebouteiller et al., 2007; Moffat et al., 2002; Mücke et al., 2002; Persi et al., 1985; Sagar et al., 2001; Spezzi et al., 2011; Stevens et al., 2002). Although this giant star forming region is extended and has about a dozen smaller molecular clouds (these small clouds are often called clumps), I focused only on the two closest to the central star cluster in the southwest and southeast (Fig. 3.5). These clumps are denoted as MM1 and MM2 in Nürnberger et al. (2002), respectively. Both MM1 and MM2 also contain pillar-like structures which are visible in the Hubble Space Telescope (HST) images (Brandner et al., 2000).

Table 3.2: Summary of the observed molecules (HIFI). The red letters indicate non-detections. The velocity resolution is 0.7 km s^{-1} .

Obsid	Molecule	Transition	Frequency [GHz]	Beam ["]
1342201692 (MM1 + MM2)	CH	$1_{3/2} \rightarrow 1_{1/2}, F = 2^- \rightarrow 1^+$	536.761	43.5
		$1_{3/2} \rightarrow 1_{1/2}, F = 1^- \rightarrow 1^+$	536.782	
		$1_{3/2} \rightarrow 1_{1/2}, F = 1^- \rightarrow 0^+$	536.796	
	C ₂ H	$6_{13/2} \rightarrow 5_{11/2}, F = 6 \rightarrow 5^a$	523.972	
		$6_{11/2} \rightarrow 5_{9/2}, F = 5 \rightarrow 4^b$	524.034	
		HCO ⁺	$6 \rightarrow 5$	
CS	$11 \rightarrow 10$	538.689		
1342201675 (MM1–peak)	o-H ₂ O	$1_{10} \rightarrow 1_{01}$	556.936	37.7
	o-NH ₃	$1_0 \rightarrow 0_0$	572.498	
1342201676 (MM2–pillar)	o-H ₂ O	$1_{10} \rightarrow 1_{01}$	556.936	
	o-NH ₃	$1_0 \rightarrow 0_0$	572.498	
1342201750 ^c	¹² CO	$9 \rightarrow 8$	1036.912	22.5
1342201752 ^d	¹² CO	$9 \rightarrow 8$	1036.912	
1342201809 ^c	¹³ CO	$10 \rightarrow 9$	1101.350	20.8
1342201810 ^d	¹³ CO	$10 \rightarrow 9$	1101.350	
1342201818 ^c	¹² C ⁺	$^2P_{3/2} \rightarrow ^2P_{1/2}$	1900.537	12.2
1342201819 ^d	¹² C ⁺	$^2P_{3/2} \rightarrow ^2P_{1/2}$	1900.537	
1342223427 (MM2–pillar)	NH	$1_2 \rightarrow 0_1$	~ 974.5	
	p-H ₂ O	$2_{02} \rightarrow 1_{11}$	987.927	
	C ¹⁸ O	$9 \rightarrow 8$	987.560	
	H ₃ O ⁺	$0_0^- \rightarrow 1_0^+$	984.709	
1342223428 (MM1–IF)	NH	$1_2 \rightarrow 0_1$	~ 974.5	
	OH ⁺	$1_2 \rightarrow 0_1$	~ 971.8	
	H ₃ O ⁺	$0_0^- \rightarrow 1_0^+$	984.709	
1342223429 (MM2–peak)	NH	$1_2 \rightarrow 0_1$	~ 974.5	22.5
	p-H ₂ O	$2_{02} \rightarrow 1_{11}$	987.927	
	C ¹⁸ O	$9 \rightarrow 8$	987.560	
	H ₃ O ⁺	$0_0^- \rightarrow 1_0^+$	984.709	
1342223430 (MM1–IF)	NH	$1_2 \rightarrow 0_1$	~ 974.5	
	p-H ₂ O	$2_{02} \rightarrow 1_{11}$	987.927	
	C ¹⁸ O	$9 \rightarrow 8$	987.560	
1342225899 (MM2–peak)	H ₃ O ⁺	$0_0^- \rightarrow 1_0^+$	984.709	
	OH ⁺	$1_2 \rightarrow 0_1$	~ 971.8	
	NH	$1_2 \rightarrow 0_1$	~ 974.5	
1342225900 (MM2–pillar)	OH ⁺	$1_2 \rightarrow 0_1$	~ 971.8	
	H ₃ O ⁺	$0_0^- \rightarrow 1_0^+$	984.709	
	NH	$1_2 \rightarrow 0_1$	~ 974.5	

^a Blend of $F = 7 \rightarrow 6$ and $F = 6 \rightarrow 5$ (separated by 0.5926 MHz)^b Blend of $F = 6 \rightarrow 5$ and $F = 5 \rightarrow 4$ (separated by 0.623 MHz)^c MM1–peak^d MM2–pillar

Table 3.3: Summary of the observed molecules (PACS). The * marks unidentified lines. The first three observations are line spectroscopies while the second three are range spectroscopies.

Obsid	Channels	Molecule	Transition	Wavelength [micron]
1342214681 (MM1-peak)	Blue	[NIII]	$^2P_{3/2} \rightarrow ^2P_{1/2}$	57.343
		[OI]	$^3P_1 \rightarrow ^3P_2$	63.184
1342214684 (MM2-pillar)	Blue	[NIII]	$^2P_{3/2} \rightarrow ^2P_{1/2}$	57.343
		[OI]	$^3P_1 \rightarrow ^3P_2$	63.184
1342214687 (MM2-peak)	Blue	[OI]	$^3P_1 \rightarrow ^3P_2$	63.184
		[OI]	$^3P_1 \rightarrow ^3P_2$	63.184
		*	*	72.850
1342214682 (MM1-peak)	Red	[OIII]	$^3P_1 \rightarrow ^3P_0$	88.356
		[OI]	$^3P_0 \rightarrow ^3P_1$	145.535
		[CII]	$^2P_{3/2} \rightarrow ^2P_{1/2}$	157.741
		^{12}CO	$16 \rightarrow 15$	162.820
		^{12}CO	$15 \rightarrow 14$	173.630
		^{12}CO	$14 \rightarrow 13$	186.010
1342214685 (MM2-pillar)	Red	^{12}CO	$13 \rightarrow 12$	200.270
		[OI]	$^3P_1 \rightarrow ^3P_2$	63.184
		*	*	72.850
		[OIII]	$^3P_1 \rightarrow ^3P_0$	88.356
		[OI]	$^3P_0 \rightarrow ^3P_1$	145.535
		[CII]	$^2P_{3/2} \rightarrow ^2P_{1/2}$	157.741
1342214688 (MM2-peak)	Red	^{12}CO	$16 \rightarrow 15$	162.820
		^{12}CO	$15 \rightarrow 14$	173.630
		^{12}CO	$14 \rightarrow 13$	186.010
		^{12}CO	$13 \rightarrow 12$	200.270
		*	*	122.500
		[NII]	$^3P_2 \rightarrow ^3P_1$	121.898
1342214688 (MM2-peak)	Red	[OI]	$^3P_0 \rightarrow ^3P_1$	145.535
		[CII]	$^2P_{3/2} \rightarrow ^2P_{1/2}$	157.741
		^{12}CO	$16 \rightarrow 15$	162.820
		^{12}CO	$15 \rightarrow 14$	173.630
		^{12}CO	$14 \rightarrow 13$	186.010
		^{12}CO	$13 \rightarrow 12$	200.270

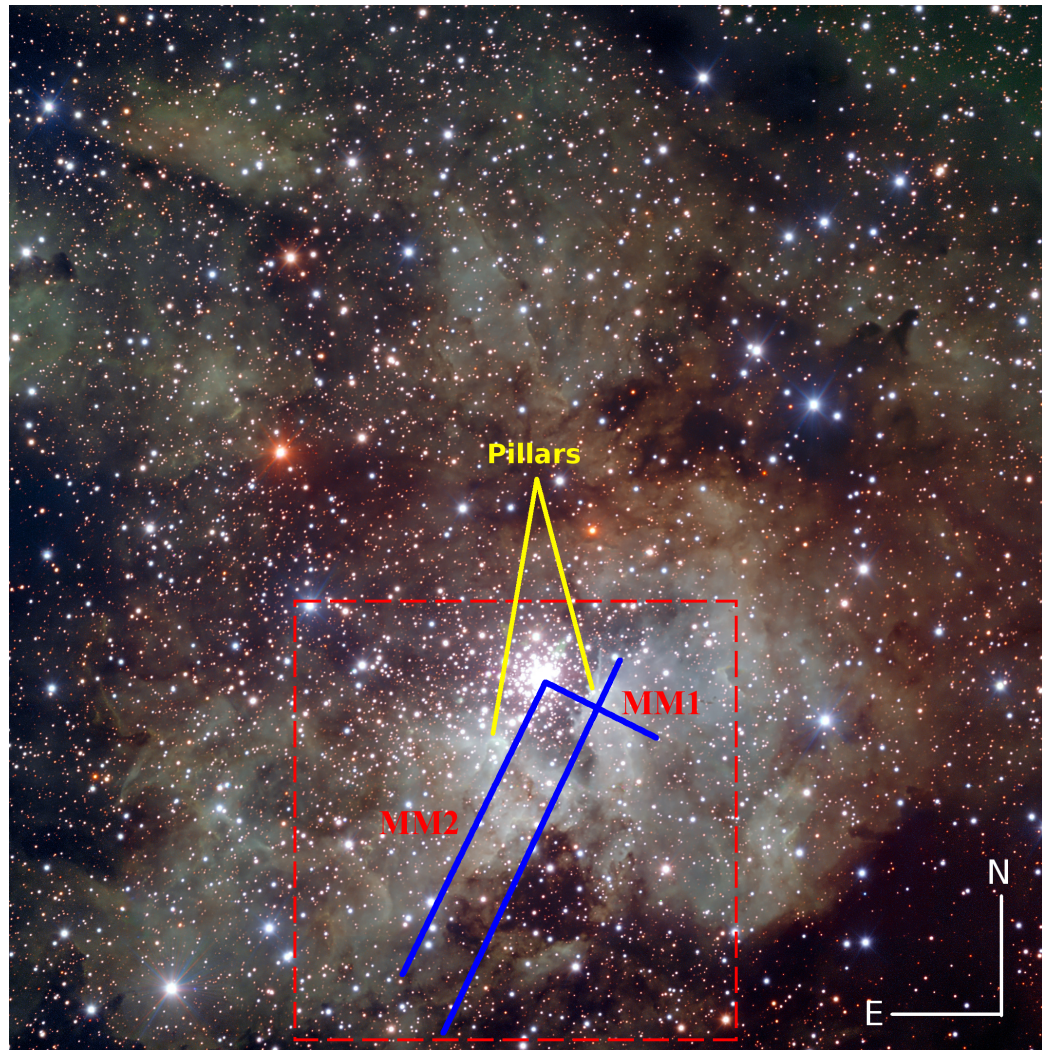


Figure 3.5: This ESO image was taken by the *Very Large Telescope*, VLT, using FORS1 (FOcal Reducer and Spectrograph) instrument with three near-infrared color-filters (V, R, and I). The field of view is $6'.8 \times 6'.8$. The red dashed lines show the area mapped with HIFI, blue lines represent cuts where I did deeper integrations. The two molecular clumps I investigated are also marked.

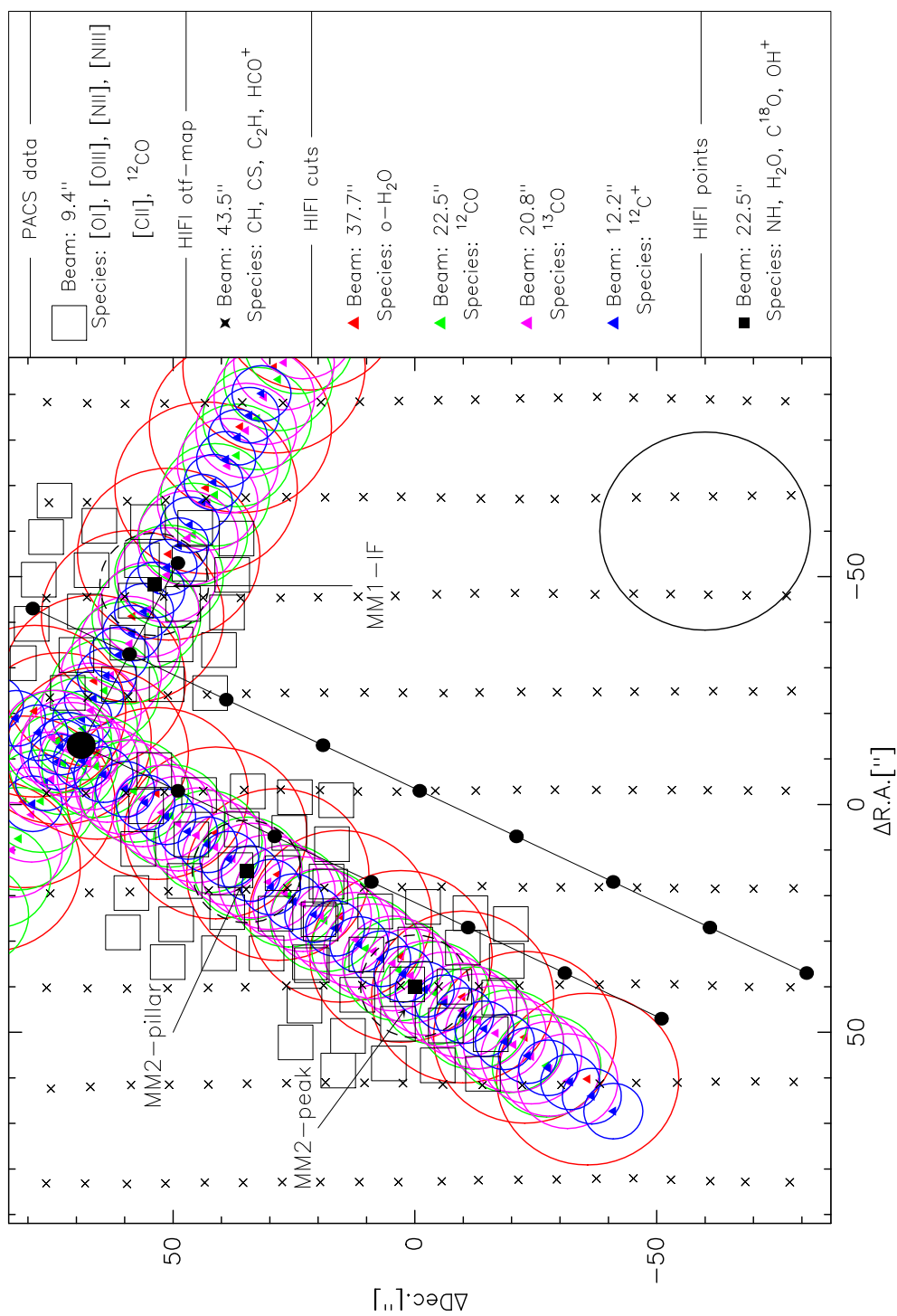


Figure 3.6: Visualization of all the Herschel observations. The big filled circle marks the central OB cluster. The solid lines and the smaller dots along the lines represent the cuts and the locations where I did more detailed analysis of the observed spectra (Section 6.1.1). The label of the PACS-observations are also showed (Section 6.1.2).

Data reduction

In this chapter, I briefly introduce the basic procedures that we used to receive good quality data products. The Herschel Space Observatory provides raw data that needed to be processed to obtain data that can be used for scientific interpretation. For this, I set the **Herschel Interactive Processing Environment** [HIPE¹ (Ott, 2010), Section 4.1] for the basic data reduction steps². I then converted the data into **Continuum and Line Analysis Single-dish Software** [CLASS³, (Bardeau et al., 2006; Pety, 2005)] readable format and did further data reduction steps (baseline subtraction, line fitting etc.) in CLASS (Section 4.2). At this moment, it is not possible to convert PACS data to CLASS, therefore I did all PACS data reduction steps with HIPE.

4.1 HIPE

The observations, provided by Herschel, are automatically pipeline processed (Section 4.1.1). This pipeline creates numerous data products (scientific, auxiliary, calibration, quality and more⁴). The pipelined data is stored at the **Herschel Science Archive** (HSA)⁵ and downloadable via either HSA or HIPE. Even if the data are already pipelined, a re-pipeline process is possible.

¹The latest HIPE version: http://herschel.esac.esa.int/HIPE_download.shtml

²More information about HIPE and data processing can be found at, for example, http://herschel.esac.esa.int/Data_Processing.shtml

³<http://iram.fr/IRAMFR/GILDAS/>

⁴More detailed description about the data products can be found at http://herschel.esac.esa.int/Data_Products.shtml

⁵http://herschel.esac.esa.int/Science_Archive.shtml

4.1.1 HIFI pipeline processes

The pipeline data products can be split into five stages/levels (in both cases HIFI and PACS):

1. *Level-0 data product*: in this level the data is taken from Herschel and only corrected for minor errors (e.g., check LO settings and pointing, check the observation time between WBS and HRS). Usually the data are in readout counts versus pixel numbers.
2. *Level-0.5 data product*: Instrument effects (e.g., non-linearities) are removed from the data and have been frequency calibrated.
3. *Level-1 data product*: The frequency and intensity calibration are applied based on calibration scans. This is the last stage where automatic processing of data is reliable (or “safe”). The output data of pipeline processes have been, for example, velocity corrected and the intensity scale is transformed to Kelvin unit.
4. *Level-2 data product*: The result of this pipeline step is checked for correct temperature and frequency (or velocity, if desired) scale. This product can be used for scientific analysis. On the other hand, additional steps need to be done by hand (e.g., baseline subtractions, stitching sub-bands, remove spurs and/or standing waves and so on).
5. *Level-2.5 data product*: This level does not exist in all observing modes (for instance for point observations). But in cases of maps rotated cubes are created, if needed. Also de-convolution is done in cases of spectral scans.

4.1.2 PACS pipeline processes

The pipeline stages/levels of PACS that are similar to HIFI:

1. *Level-0 data product*: data is directly from the satellite and only corrected for minor errors (e.g., check LO settings and pointing). Usually the data are in readout counts versus pixel numbers.
2. *Level-0.5 data product*: Instrument effects (e.g., non-linearities) are removed and no interaction is needed from the user.
3. *Level-1 data product*: there are more reduction and user interaction may need.

4. *Level-2 data product*: This product can be used for scientific analysis because it is completely reduced but interaction is required.
5. *Level-2.5 data product*: It does exist in few observing modes and additional steps are done (for example, range spectroscopy may need a combination of ON and OFF positions).

The pipeline steps and processes are depending on the observation mode. We obtained chop/nod line spectroscopy and range spectroscopy with unchopped grating scan (Section 3.1.2) and we used different pipeline scripts for them. Major user interactions were not needed in pipeline processes. The baseline subtraction (usually 2nd or 3rd order polynomial were used for baseline) and line fitting were done (I used Gaussian-model) spaxel by spaxel by a jython script written by me (script M.3 and Fig. 4.1). I also wrote a jython script (script M.4) to create plots which show the distribution of spaxels on the sky and integrated flux maps (Fig. 4.3).

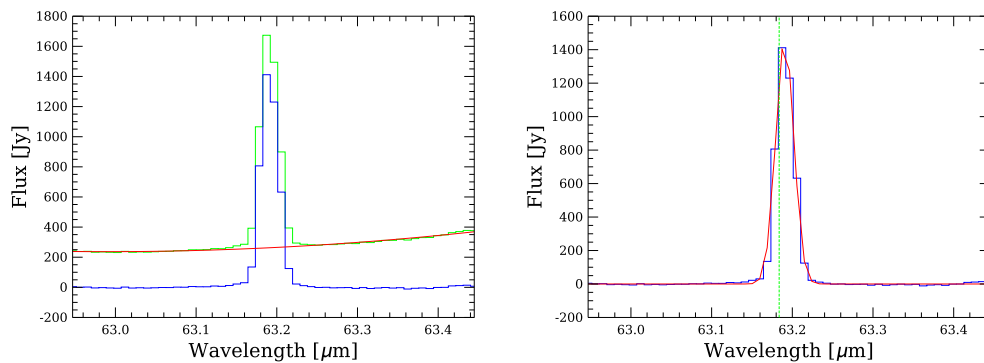


Figure 4.1: An example of baseline subtraction and Gaussian-fitting. The panels show the same spaxel. **Left panel:** the observed [OI] line (green), the fitted second order polynom (red) and the baseline subtracted spectrum (blue) can be seen. **Right panel:** the baseline corrected spectrum (blue) with Gaussian-fit (red line). The green vertical dashed line represents the theoretical rest wavelength of the observed line.

4.2 CLASS

After some preliminary processes (re-pipeline from Level –1 through to Level –2 with HIPE version 4.0, stitching subbands) of HIFI observations, I converted the data to FITS-files which can be used for further analysis in CLASS. To get better S/N ratio, I averaged the H and V polarizations (at each position). Because the final Level –2 data is scaled in T'_A , after resampling the spectra to a given velocity resolution (Tab. 3.2), I scaled the data

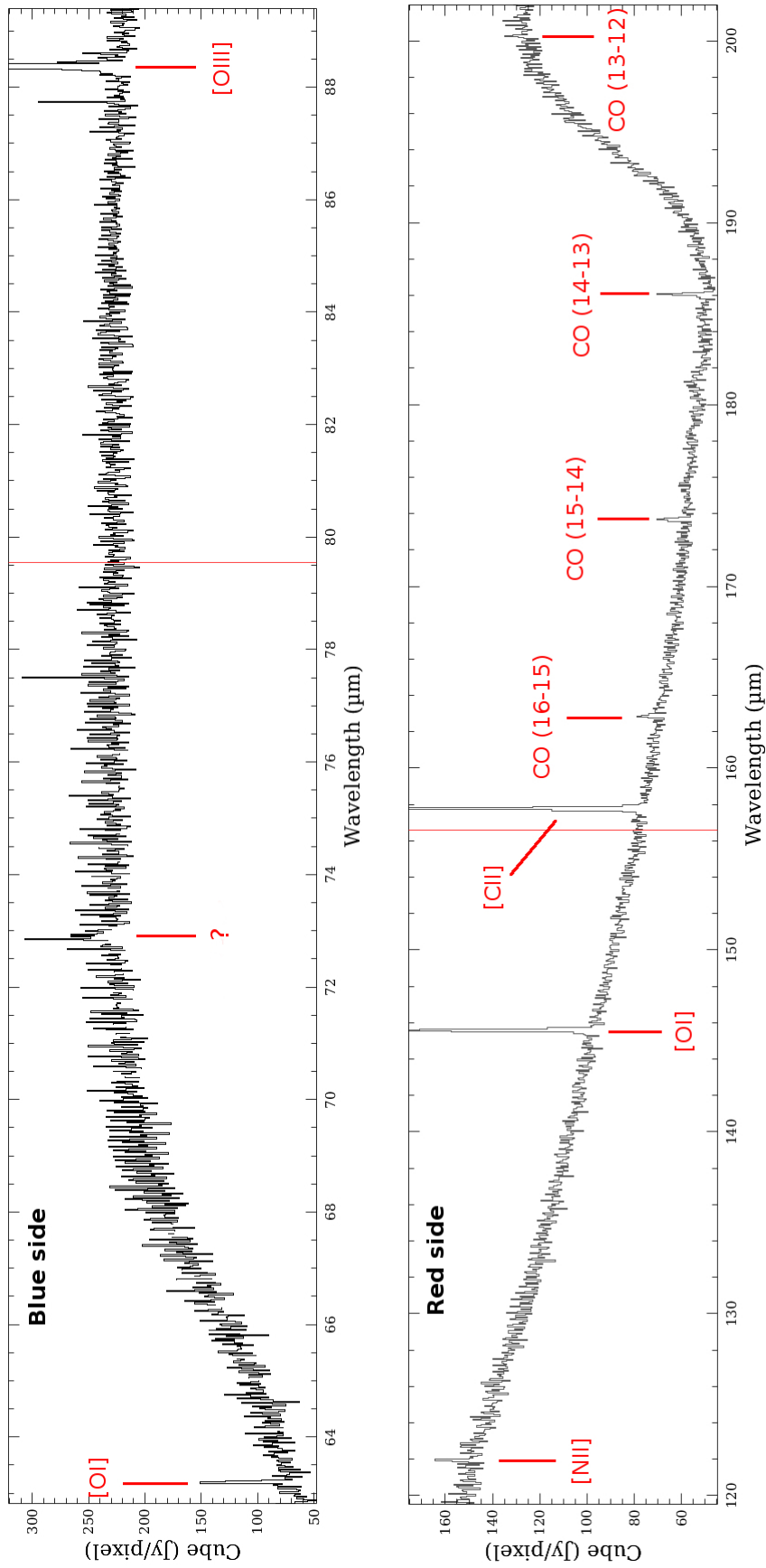


Figure 4.2: Observed lines in PACS range spectroscopy. The plots do not show the whole wavelength ranges (they are zoomed for better visibility) and are from arbitrarily chosen spaxel. The faint vertical red lines mark the central wavelength.

Table 4.1: *Observational parameters for HIFI.*

ObsID	Species	# Points	Spacing ["]	Time ^a [s]	T _{sys} [K]
1342201692	CH, C ₂ H, HCO ⁺ , CS	20 × 9	9.6 × 18.5	584.1	126
1342201675	o-H ₂ O, o-NH ₃	10	16	142.6	161
1342201676	o-H ₂ O, o-NH ₃	10	16	142.6	161
1342201750	¹² CO	18	9.6	579	53.1
1342201752	¹² CO	14	9.6	579	41.2
1342201809	¹³ CO	16	9.6	165.8	716
1342201810	¹³ CO	30	9.6	166.3	716
1342201818	¹² C ⁺	20	5.4	118	2755
1342201819	¹² C ⁺	30	5.4	177.6	2755
1342223427	NH, p-H ₂ O, C ¹⁸ O	1	–	917.3	621
1342223428	NH, OH ⁺	1	–	590.4	617
1342223429	NH, p-H ₂ O, C ¹⁸ O	1	–	917.3	621
1342223430	NH, p-H ₂ O, C ¹⁸ O	1	–	917.3	621
1342225899	NH, OH ⁺	1	–	478.9	617
1342225900	NH, OH ⁺	1	–	590.4	617

^aON–source integration time

to T_{mb} . For this, I divided⁶ T'_A by the main beam efficiency: $T_{mb} = T'_A / \eta_{mb}$ where $\eta_{mb} = 0.76$ with accuracy of 2% (Roelfsema et al., 2012). Baseline correction was applied for all spectra [usually the polynomial order was $\sim 2 - 4$ but in two cases (observational IDs 1342201818 and 1342201819), due to the bad quality baselines, I applied higher order (8)].

To determine physical parameters of the observed lines (peak and integrated intensities, linewidth etc.), I adopted different methods (based on line profiles). Spectra with symmetrical shape and one velocity component were fitted by a Gaussian. When a second velocity component (or a broad wing) appeared, I used a second Gaussian-model to fit it. It is also possible to determine the physical parameters using the “moments–method” [e.g. van der Tak et al. (2013)]. On the other hand, after few tests, I decided to use Gaussian fits because the moment–method gave inconsistent results.

For lines with hyperfine splitting it is possible to use a built–in *hfs–method* in CLASS which can fit up to 40 hyperfine components. This method works well if the velocity components have the same width and do not overlap. C₂H fulfilled these conditions. Because all hyperfine components of CH had two velocity components, the *hfs–fitting* method was not able to fit the lines well. To get around this problem, I used a script (script M.2) which can fit more than one velocity components in hyperfine pattern. The script is based on the Eq. (2.20) and gives the total optical depth, line width,

⁶This is correct only before HIPE 5.1 version

line velocity and a very rough estimation of excitation temperature. I also investigated the spatial and velocity distribution of the observed species. Therefore, position–velocity diagrams (PV–diagrams) and integrated intensity maps were created by CLASS. All of the HIFI OTF–maps, I present in this thesis, were also re-gridded (with spacing of $10''$) to previous ^{12}CO , and [C I] observations from [Röllig et al. \(2011\)](#).

4.3 Summary

The HIFI spectra were re-pipelined from raw data (Level–1) to a data that can be used for scientific analysis (Level–2.5). After the re-pipeline process, I converted our data products to CLASS readable FITS-file by HIPE. The further data reduction steps and processes (baseline subtractions, line fitting, creating integrated intensity maps and PV-diagrams) were done by different GILDAS packages (CLASS, GREG1-3, etc.).

In cases of PACS data, after the re-pipeline processes, I analysed and visualized the data within HIPE by different jython scripts written by me.

In the next chapter, I shall present the complementary data I used about NGC 3603.

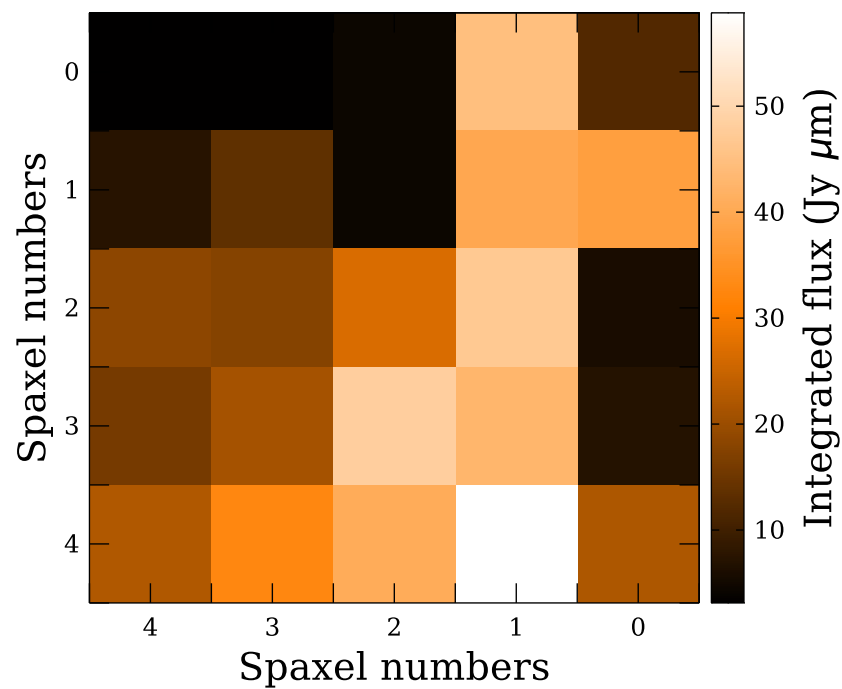
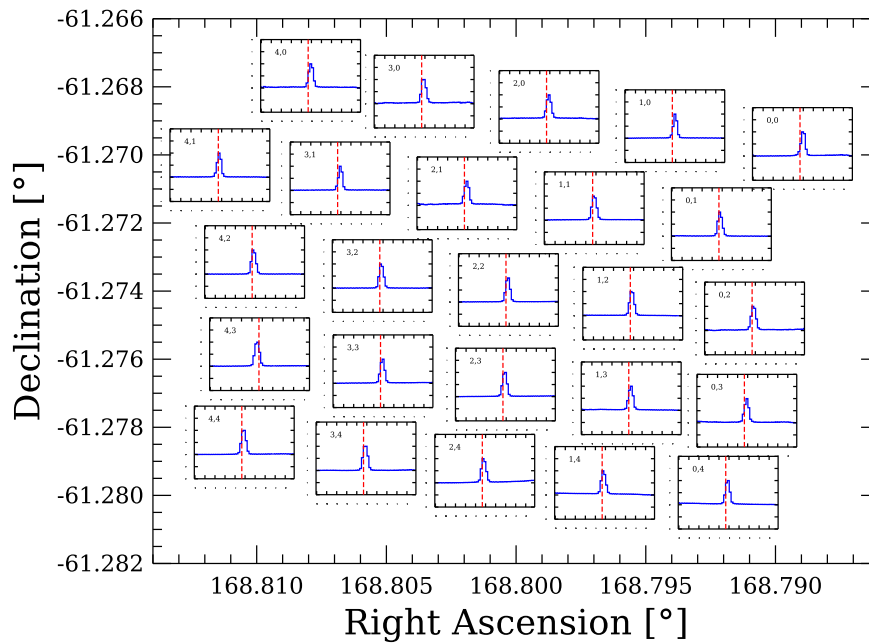


Figure 4.3: *Upper panel:* Distribution of spaxels correspond to the footprint on the sky. The red dashed lines mark the rest wavelength of the line while the small numbers at the upper left corner of sub-plots indicate the spaxel coordinates. The spectra are normalized for the better visibility. *Lower panel:* An example output map from our script [integrated flux map of [OI] ($63\ \mu\text{m}$) line].

Complementary data

5.1 SEST¹ data

Nürnberg *et al.* (2002) presented large scale maps (size: $5.8' \times 16.7'$) of low- J transitions of the high density tracer CS ($2 \rightarrow 1$ and $3 \rightarrow 2$) and a smaller map of $C^{18}O$ ($2 \rightarrow 1$), observed by SEST. From those maps, it is evident that the molecular gas is farther extended to both the north and south from the OB cluster. More than a dozen clumps were detected in CS ($3 \rightarrow 2$ and $2 \rightarrow 1$) (see Fig. 5.1). Other maps [e.g. ^{12}CO ($1 \rightarrow 0$) from Melnick (1989)] also show extended emission to the south from the central cluster. Based on Nürnberg *et al.* (2002), it seems that the velocity structure is the same in almost all clumps and the emission lines are composed of two components in five clumps, including MM2. They also suggest that the pillars, seen in the optical regime (Brandner *et al.*, 2000), are located in front of the OB cluster due to the velocity drift they found on position-velocity diagrams. That velocity pattern can appear when a photo evaporated gas is blown toward the observer (Pound, 1998). In addition, there is a “halo” around the central cluster with a radius of $\sim 25''$ which has been shown as a wind-driven cavity (Balick *et al.*, 1980; Clayton, 1986, 1990). Calculating from CS ($3 \rightarrow 2$) observations the radii of MM1 and MM2 gave < 0.4 and 1.0 pc, respectively. The lower limit of the hydrogen column density in MM1 is $> 0.1 \times 10^{22} \text{ cm}^{-2}$ and $4.0 \times 10^{22} \text{ cm}^{-2}$ in MM2. There is also an indication that the northern part of the whole complex (including MM1 and MM2) has different excitation conditions or higher opacities than the southern region. The different type of masers in the clumps suggest that massive star formation is still an ongoing process.

¹Swedish-ESO Submillimetre Telescope

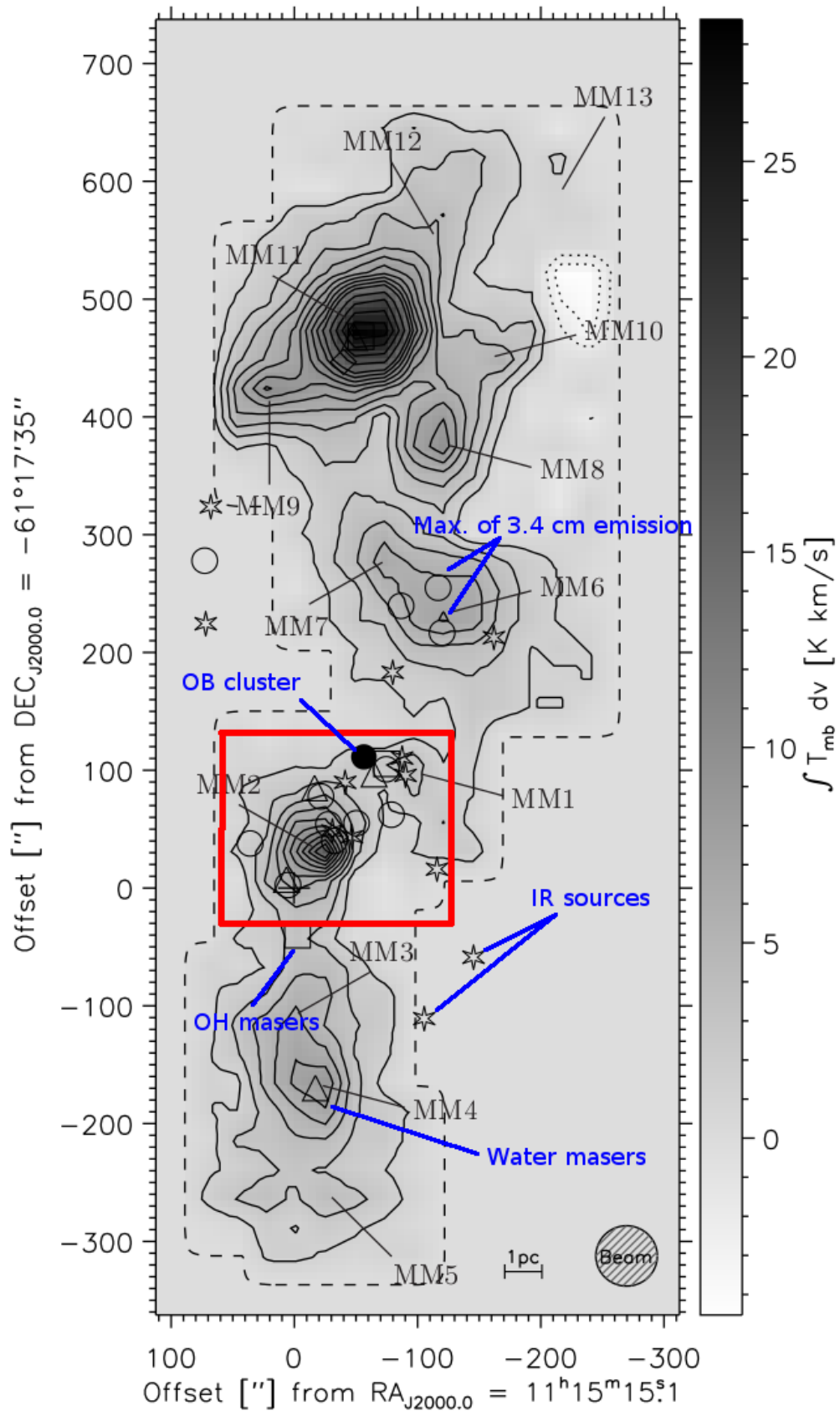


Figure 5.1: *CS* ($2 \rightarrow 1$) integrated intensity map from [Nürnberger et al. \(2002\)](#). The red square marks the area we observed with HIFI and PACS.

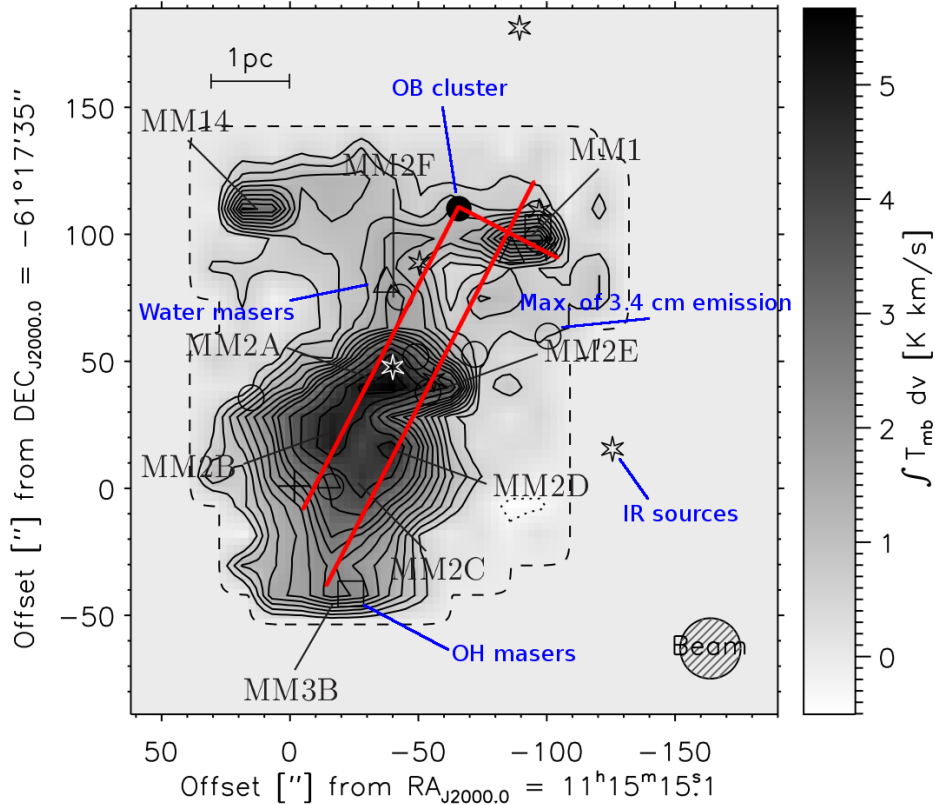


Figure 5.2: $C^{18}O$ ($2 \rightarrow 1$) integrated intensity map from Nürnberg et al. (2002). The overplotted red lines show the cuts observed with HIFI. In Nürnberg et al. (2002) MM2 is dissociated on smaller cores (MM2A–MM2F) but in this thesis I refer to MM2 as one molecular clump (including all smaller cores).

5.2 NANTEN2 data

Fully sampled $200'' \times 200''$ maps of NGC 3603 in rotational transitions of ^{12}CO ($4 \rightarrow 3$ and $7 \rightarrow 6$) and fine-structure transitions of [C I] ($1 \rightarrow 0$ and $2 \rightarrow 1$) were taken by Röllig et al. (2011). These species were observed with the NANTEN2 telescope in Pampa La Bola, Chile. On these maps, MM1 is visible in both ^{12}CO transitions and at the [C I] ($2 \rightarrow 1$) transition (Fig. 5.3). There was no evidence for C-CO layering although the pillars in HST observations and the clearly visible interface from Spitzer data suggest an edge-on PDR structure. Röllig et al. (2011) found similar kinematic behaviour as Nürnberg et al. (2002), namely a velocity shift to the southwest. They also studied the transient region between the ionized and the molecular gas toward MM1 and MM2. To derive the excitation temperatures of these two clumps they assumed LTE and the ratio of optically thin ([C I]) and thick lines (^{12}CO). The line ratios of atomic carbon gave temper-

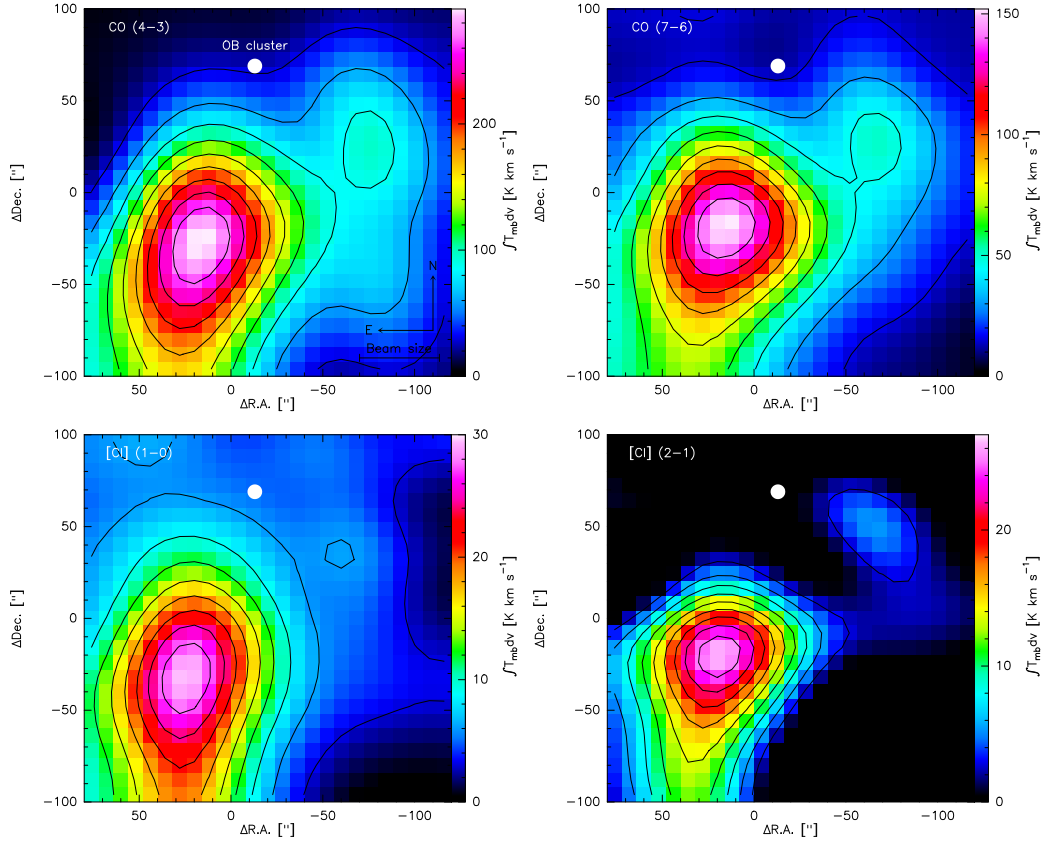


Figure 5.3: Integrated intensity maps from [Röllig et al. \(2011\)](#). The maps are convolved to $43''5$. The contours are from 10% to 90% of peak values.

atures between 40–60 K for MM2 and 42 K for MM1. Based on the optically thick ^{12}CO line ratios, the temperatures are in range of 52 – 62 K in MM2 and 51 K in MM1. The derived H_2 column densities, using C^{18}O data from [Nürnberger et al. \(2002\)](#) (Section 5.1), are $\sim 1 - 5 \times 10^{22} \text{ cm}^{-2}$ in MM2 and $\sim 0.8 - 1.5 \times 10^{22} \text{ cm}^{-2}$ in MM1. To calculate the gas column density and gas temperature, the escape probability method ([Stutzki & Winnewisser, 1985](#)) was adopted. The resulting gas temperatures (42 – 65 K) are in good agreement with the previous values. The column densities of ^{12}CO and atomic carbon is in order of 10^{17} cm^{-2} while the calculated gas density is $10^3 - 10^4 \text{ cm}^{-3}$. The filling corrected molecular hydrogen column densities are $0.9 \times 10^{22} \text{ cm}^{-2}$ and $2.5 \times 10^{22} \text{ cm}^{-2}$ in MM1 and MM2, respectively. It seems, based on the calculations, that the gas is gravitationally bound.

5.3 PACS and SPIRE data (Hi-GAL survey)

The PACS (70 μm and 160 μm) and SPIRE photometric data (250 μm , 350 μm and 500 μm) were taken from the Herschel archive (obsIDs:

1342203065, 1342203064, 1342203081 and 1342203082). These photometric data are public and are from the Hi-GAL survey (Molinari et al., 2010). The SPIRE data were reduced with the standard pipeline and version HIPE10.0.2751. Because the maps have high angular resolution, the presented maps include some white pixels (lower panel of Fig. 5.4). On the other hand, this has no influence on the data because we only focus on the middle part of the whole map where the central OB cluster and the investigated clumps (MM1 and MM2) can be found. The PACS data were reduced with Scanamorphos² (Roussel, 2013), version 2013 March.

Column density and temperature maps were made by a pixel-to-pixel simultaneous fit of temperature and column density (SED fit), assuming a constant temperature for each pixel and an optically thin dust emission. The 70 micron map was not used for the SED fitting (it traces warm gas), and all maps are on a resolution of 36'' with spacing of 14''. The UV-flux was determined assuming that the total flux at 70 μm and 160 μm represents the re-emitted FUV-photons (the map resolution is 14''). The methods, to obtain all of these maps, are well described in e.g. Roccatagliata et al. (2013) and Russeil et al. (2013).

It is noticeable from the upper panel of Fig. 5.4 that $N(\text{H}_2)$ is negligible around the central OB cluster which is in agreement with the scenario of a wind-blown cavity. In MM1, the peak value of hydrogen column density is $N(\text{H}_2) = 2.7 \times 10^{22} \text{ cm}^{-2}$ which is $\sim 60\%$ less than in the bigger MM2 ($N(\text{H}_2) = 6.9 \times 10^{22} \text{ cm}^{-2}$). $N(\text{H}_2)$ is more widely distributed in MM2 and is significant farther from the ionization source as it is tracing the colder molecular material existing in the deeper part. The distribution of dust temperature (lower panel of Fig. 5.4) shows that most of the warm dust ($T_d \gtrsim 40 \text{ K}$) can be found between the observed clumps and at the southeastern edge of MM1, probably tracing the surface of the molecular cloud. These effects are visible on the lower panel of Fig. 5.4 where the distribution of $N(\text{H}_2)$ is over plotted on the dust temperature map. It is also visible that MM1 has warmer dust components ($36 \lesssim T_d \lesssim 40 \text{ K}$) while MM2 contains colder grains ($30 \lesssim T_d \lesssim 36 \text{ K}$). These dust temperatures are in good agreement with previous grain temperature calculations, for example 35 K from Röllig et al. (2011) and 37 K from Wang & Chen (2010).

²<http://www2.iap.fr/users/roussel/herschel/>

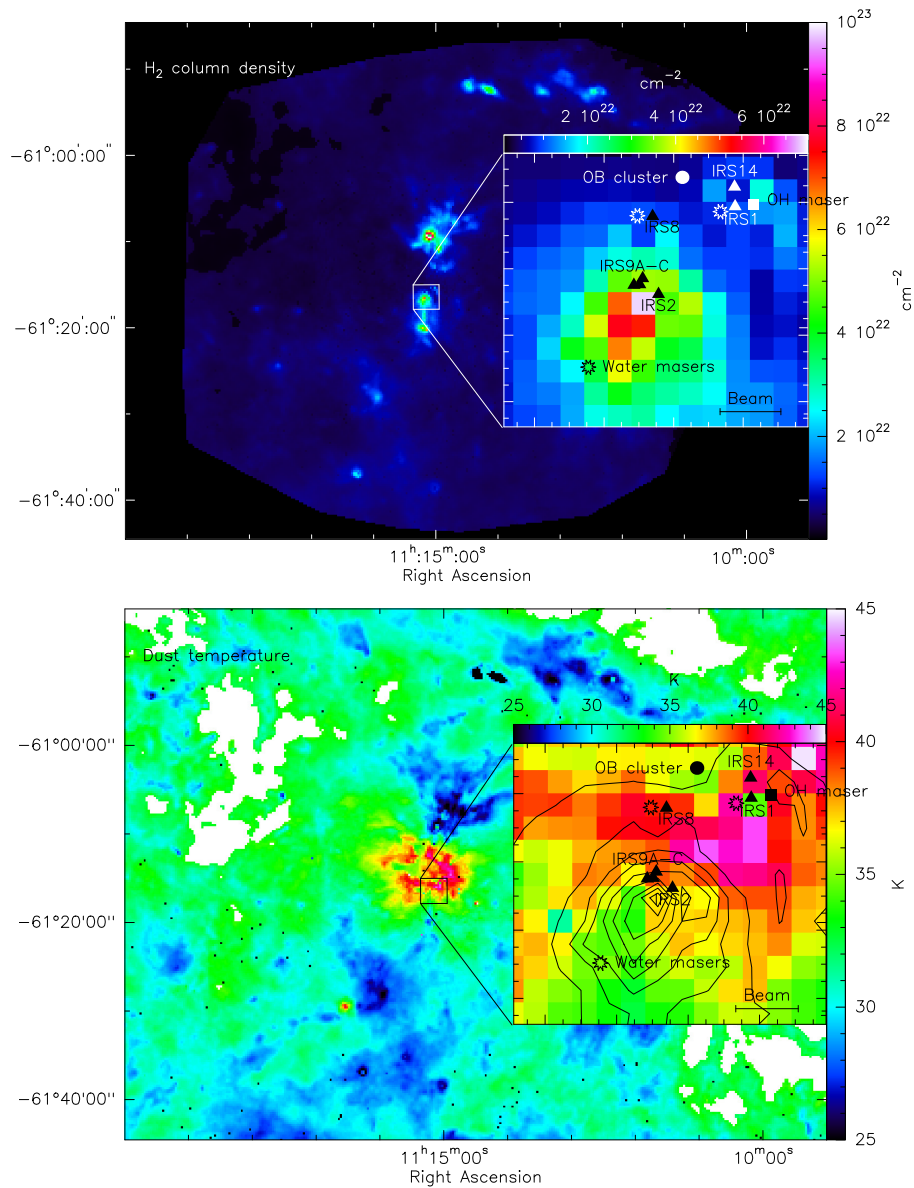


Figure 5.4: *Upper panel:* H_2 column density map created from public data (see text). The area which is investigated in this thesis is presented in the magnified plot. In that plot, the considerable infrared sources [from Nürnberg & Stanke (2003)] are also marked with filled triangles (the different colors only for the better visibility), and the masers (OH and water) are presented, too [also from Nürnberg & Stanke (2003)]. The central cluster is marked by filled circle. *Lower panel:* Dust temperature map from public data. The markers are the same as before. The contours (from 10% to 90% of peak value) show the spatial distribution of $N(H_2)$.

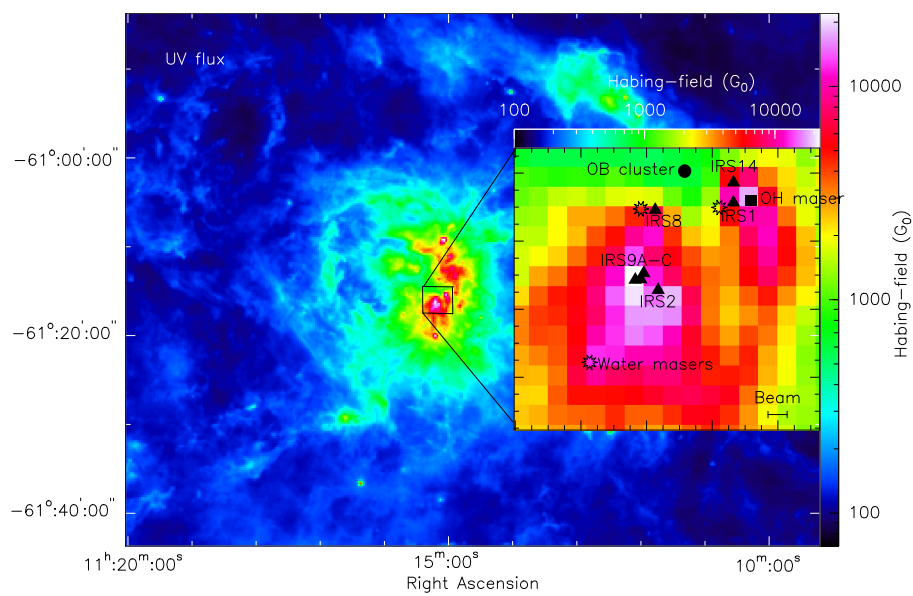


Figure 5.5: UV-flux map from public data. The markers are the same as before.

Observational results

After the basic data reduction steps (e.g. baseline subtraction) and investigation of some previous observational data, I focused on the data analysis of the observed celestial source NGC 3603. I shall present the results based on the integrated intensity maps (Section 6.1), velocity structures and line profiles (Section 6.2), excitation conditions (Section 6.3), column densities (Section 6.4) and masses (Section 6.5) of the observed species.

6.1 Integrated intensity maps

6.1.1 HIFI OTF-maps

To investigate the spatial distribution of different gas tracers in NGC 3603, I compared the integrated intensity distributions of the observed light hydrides and CS (Fig. 6.1), Herschel observations with warm and cold dust and mid- J ^{12}CO , and fine structure lines of [C I] (the map comparisons can be found in Appendix C). The results of the comparisons are the following:

MM1

The smaller clump is significantly emerges from the background field based on the observed integrated intensities. An exception is the CH which, it seems, is not considerable in MM1. It only shows a weak limb between the two observed clumps. The two dense gas tracers HCO^+ and CS are represented by relatively compact emission, while C_2H shows an elongated, diffuse distribution and its intensity peak is “deeper” in the cloud than CS and/or HCO^+ . This indicates that the observed C_2H traces the outskirts and less dense part of the molecular cloud which is influenced by the strong stellar wind from the central ionization source. Contrarily, the

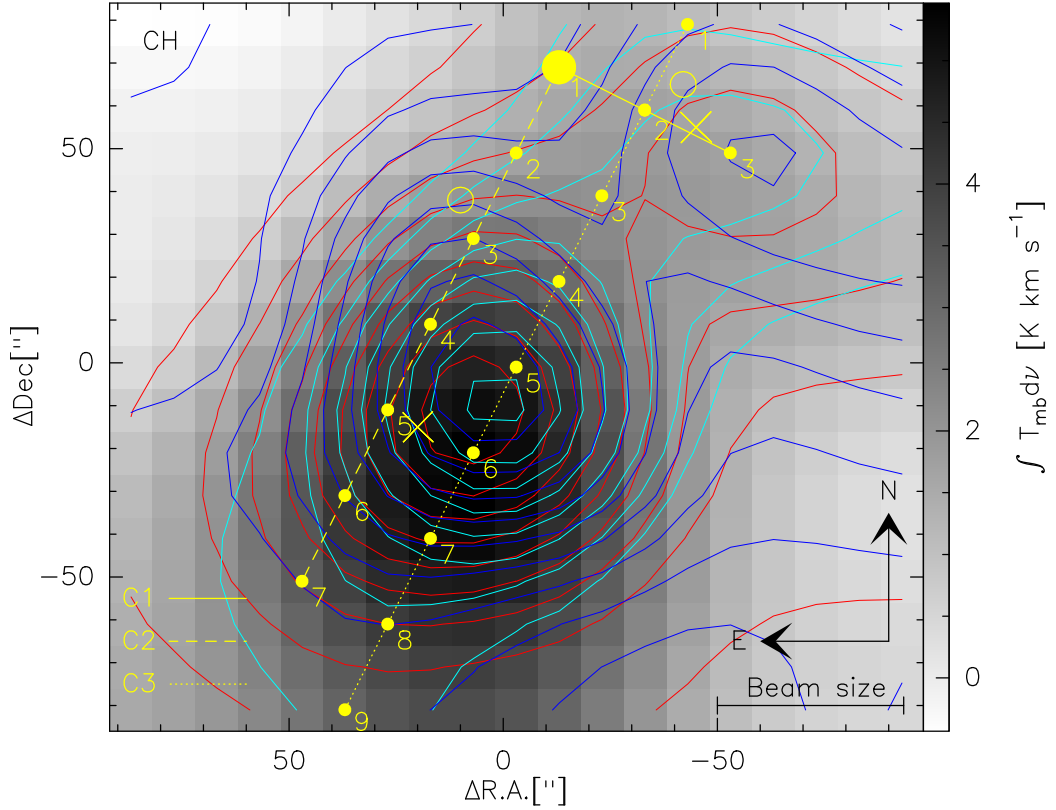


Figure 6.1: Integrated intensity map of CH [integration range is $-12 - -25$ km s^{-1} (including all three observed hyperfine components)] with overplotted contours. Red, cyan and blue contours represent HCO^+ , CS and C_2H (sum of both observed hyperfine components), respectively. The three different cuts, I used for deeper investigations, are marked with different line types (only on this figure). The small yellow dots are separated by $22''$ and represent places where I did detailed investigation along the cuts (for the more easily tracing, I labelled the places with numbers and I shall refer to these points in the text and on other plots based on these numbers). The beam size ($43''.5$) of the OTF-maps is also marked on this figure. **For all of the gray-scaled OTF-maps in this thesis:** the big yellow filled circle marks the central OB cluster. Yellow crosses show the peaks of CS ($2 \rightarrow 1$) in MM1 and MM2 from [Nürnberger et al. \(2002\)](#). The positions of the two pillar-like structures are marked by yellow circles. The size of the maps is $192'' \times 166.5''$ and the 0,0 positions corresponds to $\alpha_{\text{J2000}} = 11^{\text{h}}15^{\text{m}}08^{\text{s}}.85$ and $\delta_{\text{J2000}} = -61^{\circ}16'50''$.

CS and HCO⁺ probably represent more compact and small cores inside MM1 and they are positioned in the deeper layers.

MM2

All molecules show compact spatial distribution in MM2 except CH which is fairly diffuse and its intensity peak position is the farthest from the central star cluster ($\sim 20''$ to the south from CS and HCO⁺ peaks). CH and HCO⁺ are quite strong compared to CS, and C₂H in terms of integrated intensity values (Fig. C.1 and C.2). The intensity peak of C₂H, in contrast to MM1, is positioned closest to the central OB cluster.

The integrated intensity peak distributions suggest that the moderately dense gas tracer C₂H [due its low dipole moment (Tucker et al., 1974; Pety et al., 2005)] is concentrated close to the ionization front where the density is small compare to the deep part of the molecular cloud. The position of the dense gas tracers (CS and HCO⁺) implies small cores deeper inside MM2. The shift of CH may be caused by stellar wind from the central OB cluster and/or some embedded young hot stars. Another reason for the extended observation of CH can be chemistry based, i.e. strong existence of unobserved intermediate key-species (CH⁺_{*n*=1...5} and CH_{*n*=2...4}) of CH chemical network that may lead to the CH formation, and/or presence of immediate chemical channel between C and H.

6.1.2 PACS-maps

I also investigated atomic and ionized cooling lines and created integrated intensity maps from both line and range spectroscopies. We covered MM1 with one full PACS footprint (MM1-IF) while MM2 is covered by two footprints (MM2-pillar¹ and MM2-peak) except [NIII] where we have only one footprint in MM2 (MM2-pillar). Most of the generated integrated intensity maps can be found in Appendix I.

Line spectroscopy

[OI]

We observed the fine structure line $^3P_1 \rightarrow ^3P_2$ of [OI] (63 μm) at all three positions (MM1-IF, MM2-pillar and MM2-peak). In MM1-IF, I found a sharp transition of integrated intensity which is seemingly perpendicular on the direction to the central OB cluster (upper panel of Fig. 6.2). This border is probably an indication for the cavity wall around the central cluster.

In MM2, the intensity peak is concentrated around position 4 in C2 where

¹Please note that I may also refer to this position as MM2-IF but technically it will mean the same position.

prominent infrared sources heat their neighbouring environments. Furthermore, in both MM1 and MM2, the intensity distribution is elongated to the south and coincides with the position of pillars visible in the optical regime. This is in agreement with the scenario that the cooling lines [OI], [OIII] and high- J ^{12}CO are good tracers of pillars (Schneider et al., 2012).

[NIII]

We have line spectroscopy observation of [NIII] in MM1-IF and MM2-pillar (bottom panel of Fig. 6.2). The intensity peak of [NIII] is slightly farther from the central cluster than [OI] and, in addition, its intensity is more widely spread out in both observed clumps which is an implication for the presence of the optically thin diffuse gas.

Range spectroscopy

[OI], [OIII]

The detected [OI] line ($^3\text{P}_1 \rightarrow ^3\text{P}_2$ at $63\ \mu\text{m}$) is quite weak in both clumps (Fig. 1.1). The line intensity distribution does not follow the pillar-like structures. The distribution of [OI] is concentrated in MM1-IF and MM2-pillar. The other fine structure line of [OI] ($^3\text{P}_1 \rightarrow ^3\text{P}_0$ at $145\ \mu\text{m}$) is stronger in both clumps. Its intensity distribution nicely correlates with the pillar in MM1 but this is hardly visible in MM2 (upper panel of Fig. 1.2). The intensity peak is close to the aforementioned embedded infrared sources.

The [OIII] ($^3\text{P}_1 \rightarrow ^3\text{P}_0$ at $88\ \mu\text{m}$) line is much stronger than the [OI] lines and its line intensity is more widely distributed suggesting the existence of diffuse material (lower panel of Fig. 1.2).

[NII]

We were only be able to detect the [NII] line at the MM2-peak position (upper panel of Fig. 1.3). The line is quite weak and its integrated emission is diffusely distributed.

^{12}CO

We have detected four high- J transitions of carbon monoxide ($13 \rightarrow 12$, $14 \rightarrow 13$, $15 \rightarrow 14$ and $16 \rightarrow 15$). All of them have roughly the same elongated distribution and follow the pillar-like structures in MM1 and MM2 (lower panel of Fig. 1.3 and 1.4, and the upper panel of Fig. 1.5). Again, this is in good agreement with the previous scenario which suggest that high- J ^{12}CO lines can be used as a tracer of pillars.

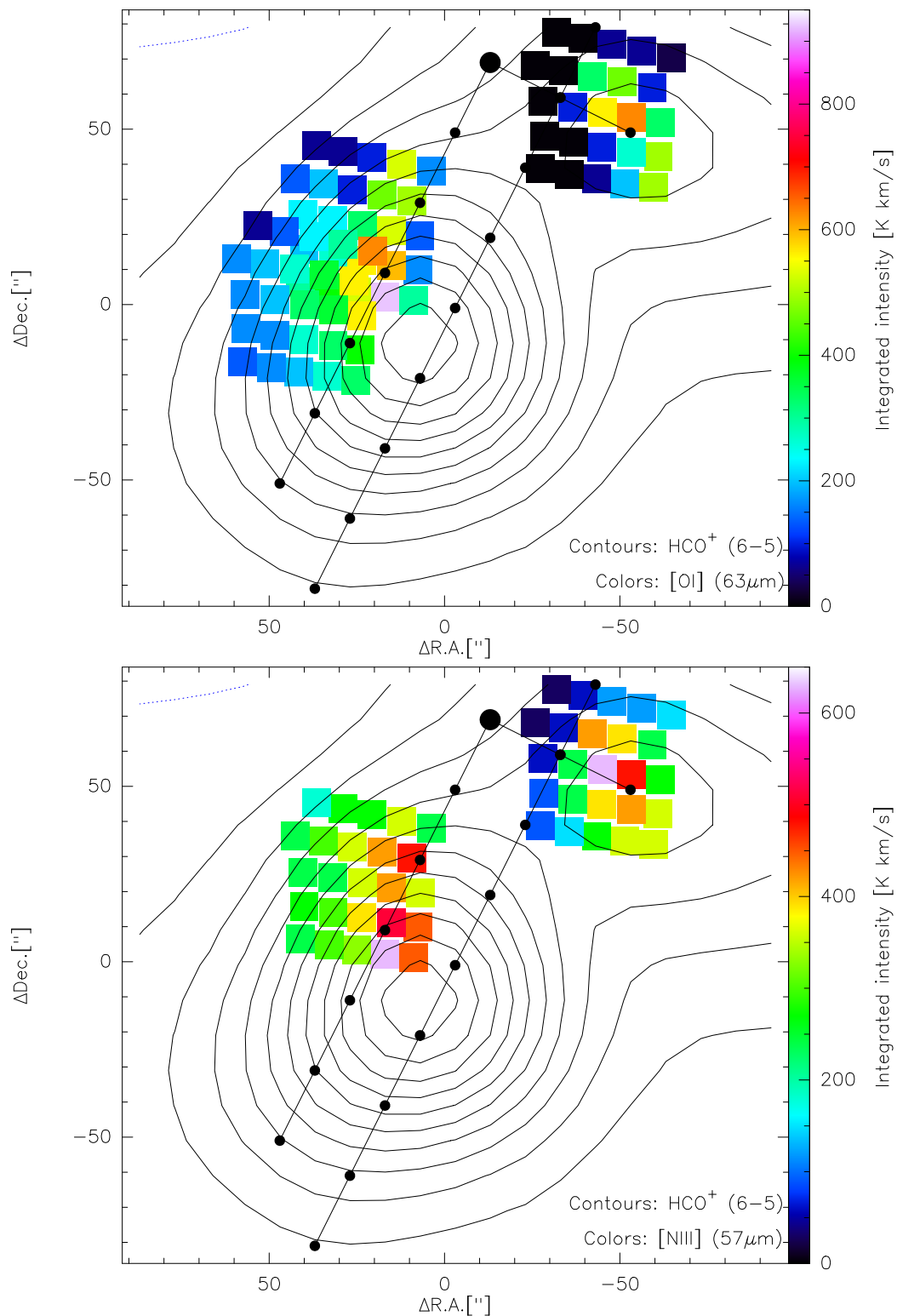


Figure 6.2: Integrated intensity maps of $[OI]$ (top panel) and $[NIII]$ (bottom panel) from line spectroscopy over plotted to HCO^+ ($6 \rightarrow 5$) contours. The black filled circle represents the central OB cluster. Solid lines mark C1 (shortest line), C2 and C3 (longest line).

[CII]

The observed [CII] (158 μm) transition is weak and coincides with the pillar position in MM1. In MM2, the line becomes strong and shows an elongated distribution to the east. This bright limb is at the same position where an identified shock front exists [more in Chapter 8 or in Nürnbergger & Stanke (2003)].

6.2 Velocity structure and line shapes

To study the velocity structure of MM1 and MM2 in NGC 3603, I created position–velocity (PV) diagrams and velocity channel maps² based on the OTF and cut observations.

As I already mentioned in Section 5.2, a detailed investigation of different phases of the interstellar medium such as ionized gas, molecular gas and the transient region in between was done using individual spectra along two cuts toward MM1 and MM2 in Röllig et al. (2011). To receive information about the kinematic structure of the observed molecular cloud and investigate the gas movements in between, and to be able to compare it with previous observations, I created three cuts: one with three positions toward MM1, one with seven positions toward MM2 and one with nine positions also toward MM2, and I shall refer them as C1, C2, and C3, respectively (Fig. 6.1).

6.2.1 Position–velocity diagrams

OTF observations

C1 The gas dense tracers (CS and HCO⁺) show similar intensity distribution along this cut. Based on the PV–diagrams, it seems that CS is composed of two velocity components in C1. These two components are separated by $\sim 1.5 - 2 \text{ km s}^{-1}$ (the velocity resolution of the observations is 0.7 km s^{-1}). HCO⁺ is composed of only one velocity component but its velocity is gently decreasing as we go deeper into the smaller clump. Interestingly, the velocity drop of HCO⁺ (as a function of cloud depth) covers the velocity range of the two components of CS. This might indicate that HCO⁺ is composed of two velocity components, which are not distinguishable. We also have to take into account the very low S/N in case of CS line which makes the observation of the second velocity component arguable. The intensity distributions of diffuse gas tracers (CH and C₂H) are also

²I use figures in this section only for illustration, all of the other channel maps can be found in Appendix G.

quite similar. The hyperfine components [CH ($F = 2 \rightarrow 1$), C₂H ($F = 6 \rightarrow 5$ and $F = 5 \rightarrow 4$)] show one velocity component but their central velocities are shifted with roughly the same values ($\sim 2 \text{ km s}^{-1}$), as in cases of dense gas tracers, as we go farther from the central cluster. The lower hyperfine component of C₂H is slightly wider than the observed higher transition. The intensity peak of $F = 6 \rightarrow 5$ is positioned slightly closer to the central OB cluster (offset $0''$) than the lower one ($F = 5 \rightarrow 4$). This is probably due to a temperature gradient that we expect close to the cloud surface which is influenced by stellar wind and strong FUV radiation. The intensity peak of the main (strongest) hyperfine component of CH ($F = 2 \rightarrow 1$) is deeply shifted into MM1. CH is mainly forming in the surface of the molecular clouds where the density is low and the temperature is high. Therefore, the observed CH intensity distribution in MM1 is probably the result of a temperature gradient and/or strong stellar wind which causes the weak but visible velocity drifts (for all lines).

C2 Along C2, HCO⁺ is composed of two velocity components (~ 12 and $\sim 14.5 \text{ km s}^{-1}$) which roughly coincide with the CS line components (middle panel of the left column on Fig. 6.3). The intensity distributions of the dense gas tracers are well correlated. The peak positions are practically at the same distance from the central OB cluster which is located at offset $0''$. A central line velocity shift is not detected.

The intensity distributions of the diffuse gas tracers (middle panel of the right column on Fig. 6.3) occupy a wide velocity range in C2. The strongest hyperfine component of CH is observable between $\sim 10 - 18 \text{ km s}^{-1}$. This broad velocity range embraces at least two velocity components for CH that are separated by $\sim 2 - 3 \text{ km s}^{-1}$. The higher hyperfine transition of C₂H ($F = 6 \rightarrow 5$) possesses three velocity components in total. Two of them are close to each other in terms of both velocity (at ~ 13.5 and $\sim 14.5 \text{ km s}^{-1}$) and distance from the central cluster (projected separation is $\sim 16''$). The third velocity component is well isolated from these two velocity components (at $\sim 17.5 - 18 \text{ km s}^{-1}$) and lies closest to the ionization source out of the three velocity components of C₂H ($F = 6 \rightarrow 5$). The intensity distribution of the lower transition ($F = 5 \rightarrow 4$) is strongly asymmetric indicating the existence of another component. On the whole, CH peaks in deeper parts of MM2 than C₂H (like in C1) and the aforementioned velocity gradient (or regressive velocity trend as a function of cloud depth) is also visible.

C3 The longest cut through MM2 is tangentially to MM1. The weak velocity component of HCO⁺ at $\sim 14 \text{ km s}^{-1}$ (position $\sim 15''$) represents the edge of MM1 (bottom panel of the left column on Fig. 6.3). The intensity distribution of HCO⁺ is asymmetric and covers the velocity range of

$\sim 10 - 16 \text{ km s}^{-1}$. This wide line width may indicate the presence of another velocity component next to the main component or can be a sign of random gas motions. CS is composed of one component that associates well with the HCO^+ main velocity component. CS and HCO^+ have similar intensity distribution at higher velocities. A velocity trend along the cut is not visible.

In contrast to C1 and C2, the two hyperfine components of C_2H peak at the same depth of the cloud along C3 and they are nicely correlated (bottom panel of the right column on Fig. 6.3). There is no obvious sign of a second velocity component. However, there is a tentative second peak at $\sim 17 \text{ km s}^{-1}$ which might be a sign for a broad (but weak) wing. The intensity distribution of CH suggests the presence of another velocity component next to the main line. This speculated weak component is well followed by the lower hyperfine component of C_2H ($F = 5 \rightarrow 4$). The CH intensity peak, like before in cases of C1 and C2, is at great depth in MM2 just “behind” the peaks of C_2H .

Cut observations

We possess different Herschel cut-observations³ (1 OTF-line) toward NGC 3603. In total, there are four cut observations (with various number of grid points) in both MM1 and MM2 (Fig. 3.6). The observed species are: $\text{o-H}_2\text{O}$, ^{12}CO , ^{13}CO and $^{12}\text{C}^+$ (Tab. 3.2).

MM1 The $\text{o-H}_2\text{O}$ shows diffuse intensity distribution (between velocities $6 - 19 \text{ km s}^{-1}$) and its peak ($\sim 12 \text{ km s}^{-1}$) is deep inside MM1 (left panel in the first row of Fig. 6.4). This could indicate that the ortho–water line traces the dense but moderately warm gas. However, there is a faint emission limb at $\sim 11 \text{ km s}^{-1}$ between the central cluster and the ionization front and, additionally, broad faint blue, and red wings can be identified (if they are not noise). The existence of a shock front could be an explanation for this projection since the water is a good shock tracer. The wings are probably manifestation of outflows.

The ^{12}CO ($9 \rightarrow 8$) emission strongly correlates with water emission in MM1 suggesting that they both traces the same moderately warm gas (considering that its peak is barely closer to the ionization front than water). The intensity distribution shows a strong velocity trend as we go far from the central star cluster indicating the presence of strong stellar winds. This effect was noted in the case of OTF observations in the previous section. This trend is also visible in case of the ortho–water but the velocity gradient is slightly less. The emission of ^{12}CO is wide in terms of velocity,

³Please note that these Herschel cut observations are not identical with the cuts that I generated from the OTF observations (C1, C2 and C3).

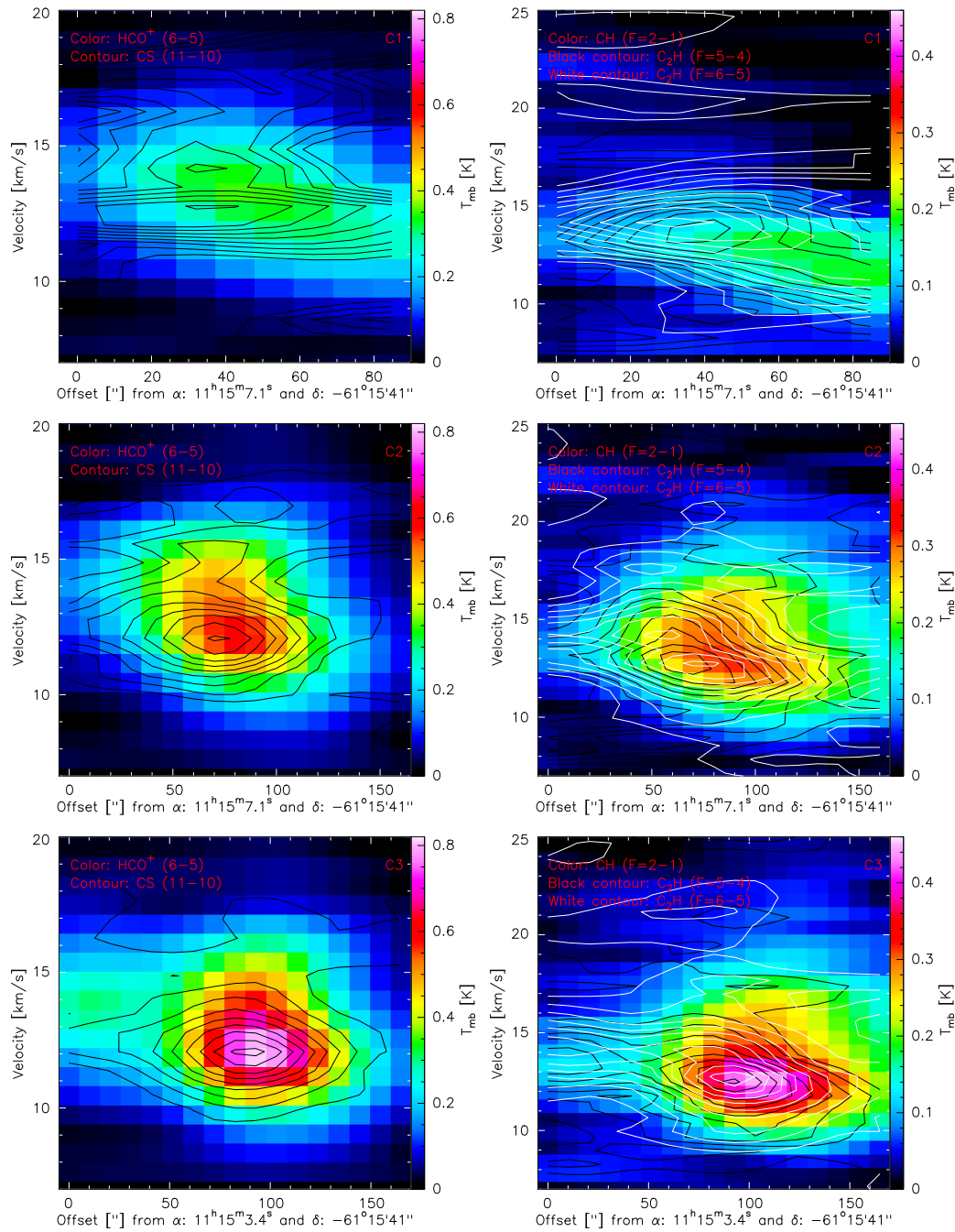


Figure 6.3: PV-diagrams of the observed molecules. All contours are from 10% to 90% of the peak values. **Left column:** the CS intensity peak values: 0.05 K, 0.1 K and 0.16 K from the top to the bottom. **Right column:** the C₂H ($F = 5 \rightarrow 4$) intensity peak values (black contours): 0.12 K, 0.11 K and 0.16 K (from the top to the bottom); the C₂H ($F = 6 \rightarrow 5$) intensity peak values (white contours): 0.14 K, 0.15 K and 0.2 K (from the top to the bottom).

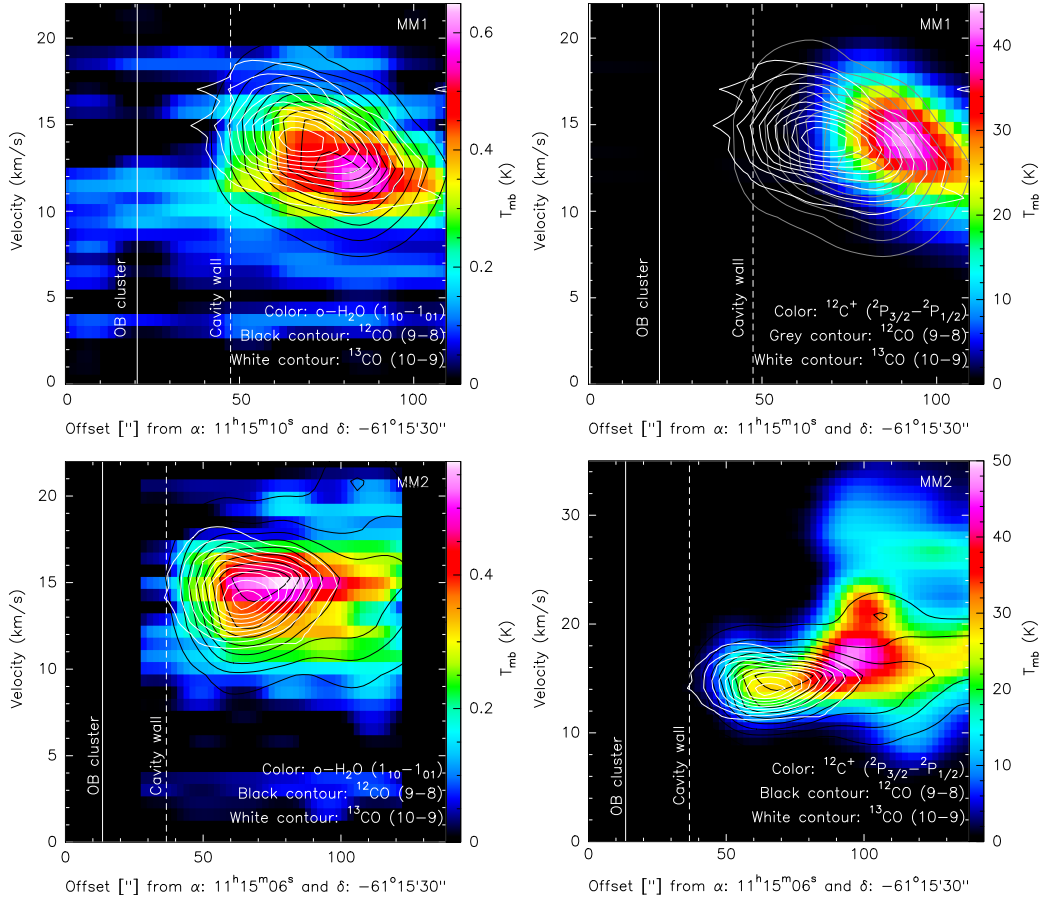


Figure 6.4: Pv -diagrams from the Herschel cut observations for MM1 (top row) and MM2 (bottom row). For all plots: the contours are from 10% to 90% of the peak values: 10.35 K and 11 K for ^{12}CO , 2.61 K and 3 K for ^{13}CO , 45 K and 50 K for $^{12}\text{C}^+$ in MM1 and MM2, respectively.

with a peak at $\sim 13 \text{ km s}^{-1}$. One possible explanation is that the line is composed of two velocity components. On the other hand, the line is fairly symmetric, therefore either the line consist of two components which are very close to each other and have Gaussian-shape or the large width is a signature of turbulence.

The ^{13}CO ($10 \rightarrow 9$) emission peak is positioned slightly closer to the ionization front than ^{12}CO ($9 \rightarrow 8$). Because ^{13}CO ($10 \rightarrow 9$) needs higher temperatures to be excited than ^{12}CO ($9 \rightarrow 8$), this is expected. The emission of ^{13}CO is mostly symmetric except in the less denser part of MM1 and shows a weaker velocity gradient as the depth is increasing.

$^{12}\text{C}^+$ ($^2\text{P}_{3/2} \rightarrow ^2\text{P}_{1/2}$) emission has the strongest negative velocity gradient of all the observed species (right panel in the first row of Fig. 6.4) and composed of only one velocity component. Its intensity peak (at $\sim 14 \text{ km s}^{-1}$) is located the farthest from the central OB cluster compared to the other species. This may indicate, that $^{12}\text{C}^+$ originates from diffuse gas.

MM2 Water emission has a satellite line at $\sim 12 \text{ km s}^{-1}$ (which could be a broad wing on the blue side of the main line) while the main emission line is at $\sim 15 \text{ km s}^{-1}$. Both velocity components stretch deeply inside MM2 (left panel in the second row of Fig. 6.4).

The ^{12}CO emission matches with the ortho–water emission. Its peak is at the same velocity and almost at the same projected distance from central star cluster. The intensity distribution of carbon monoxide is prolonged similar to the water emission. The line is remarkably wide ($\sim 7 \text{ km s}^{-1}$) but multiple velocity components, if there are any, are not distinguishable. Nevertheless, this broad line width could be a footprint of turbulent gas motion within MM2.

The emission of ^{13}CO shows a compact distribution. The intensity peak is slightly blue shifted and a little closer to the ionization front compared to ^{12}CO and o– H_2O . The lines are also relatively wide ($\sim 6 - 7 \text{ km s}^{-1}$) indicating presence of turbulent gas motions.

The ionized carbon shows complex and interesting velocity distribution in MM2. A faint limb appears at $\sim 14 \text{ km s}^{-1}$ at the projected depth of $\sim 65''$ which is well correlated with ^{12}CO and ^{13}CO emission. As we go farther from the ionization front, the main emission line becomes strong at $\sim 16 \text{ km s}^{-1}$ and noticeably wider at $\sim 90'' - 100''$. At the same depth, a second component appears at a velocity of $\sim 21 - 22 \text{ km s}^{-1}$ that is also traced by ^{12}CO . Slightly deeper in MM2, a weaker emission line becomes visible at $\sim 26 - 27 \text{ km s}^{-1}$ which is connected to the $21 - 22 \text{ km s}^{-1}$ component, creating a ring-like structure. This ring structure probably indicates that an internally generated bubble or small cavity is exists.

6.2.2 Channel maps

With channel maps we can investigate the velocity structure on larger spatial scale, namely the intensity distributions of the observed species in the entire complex (or at least in the total field of view). The channel maps I present in this section are created from the OTF observations.

HCO^+ shows a compact intensity distribution between $\sim 11.8 - 13.2 \text{ km s}^{-1}$, especially in MM2 (Fig. 6.5). At lower and higher velocities, the intensity distribution is elongated. This may indicate that the observed dense core is located close to the cavity wall and influenced by strong stellar winds. The intensity peaks appear at 11.8 and 13.2 km s^{-1} in MM2 and MM1, respectively which suggest that the observed clumps are moving by slightly different velocities.

The other dense gas tracer CS, like HCO^+ , demonstrates compact spatial intensity distribution in MM2 (upper panel of Fig. G.2). While the bigger clump is significantly visible in velocity range $\sim 10 - 15 \text{ km s}^{-1}$, MM1 is only visible, as a separated clump, between $\sim 14.5 - 18.5 \text{ km s}^{-1}$.

The observed clumps MM1 and MM2 are well represented in cases of both

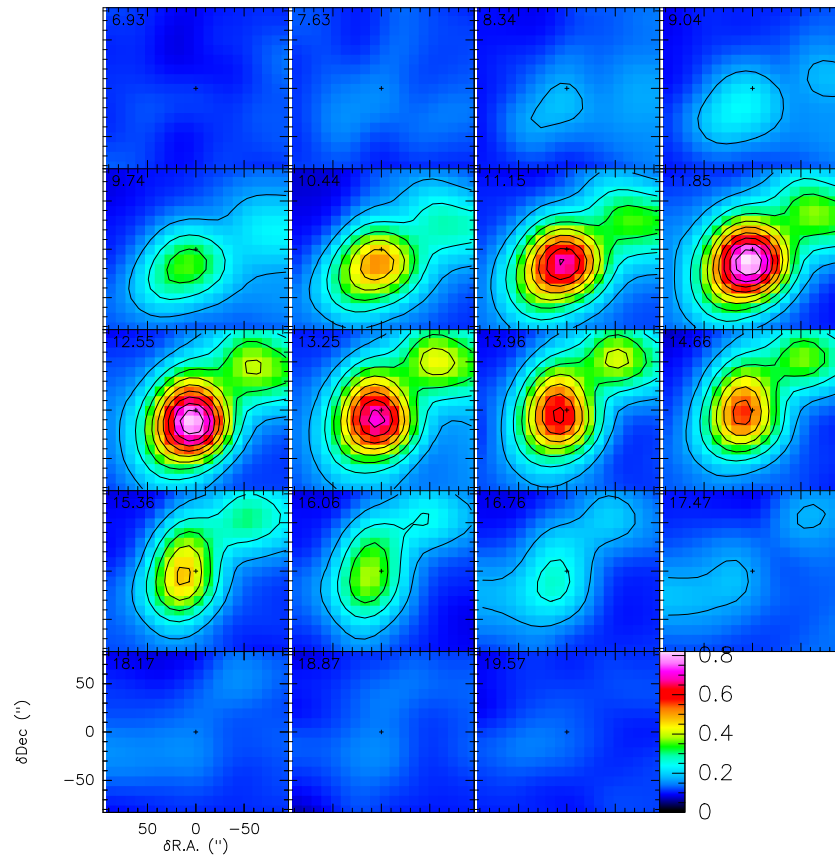


Figure 6.5: Velocity channel map of HCO^+ ($6 \rightarrow 5$) as an example. The covered velocity range is 7 to 20 km s^{-1} , the velocity resolution is 0.7 km s^{-1} and the contours are from 10% to 90% of the peak value (0.82 K). The north is up and east is left.

hyperfine components of C_2H (lower panel of Fig. G.2 and upper panel of Fig. G.3). A strong intensity fluctuation is visible in both MM1 and MM2 at different velocities (especially at the lower hyperfine transition).

The intensity distribution of diffuse gas tracer CH (lower panel of Fig. G.3) is elongated in MM1 and MM2 pointing off from the central ionization source, which could improve the theory that the less dense (outer part) layer has been blown away by strong stellar winds.

6.2.3 Line profiles and intensities

The investigation of line profiles allows us to study the large scale kinematics of the observed gas in the interstellar medium. For example, the observed line broadening can be the results of: the natural (Lorentzian line profile), collisional or pressure (also Lorentzian, but wider, line profile) and thermal or Doppler (Gaussian line profile) broadening. The natural

broadening can hardly be observed (directly) but the broadening caused by collisions can be observed especially in high density region. The thermal broadening strongly depends on the temperature. If turbulent gas motions is presented (turbulence is everywhere in the ISM, particularly in star forming regions), the Doppler width becomes more wider. At the end, the observed lines are the combination of all these effects⁴ (Voigt profile, a convolution of the Lorentzian profile with the Doppler profile).

OTF observations (C1, C2 and C3)

We compared line shapes of HCO^+ with ^{12}CO lines and CS with [CI] lines (Fig. 6.6). C1 and C2 have the same start point (the OB cluster itself), while C3 is starting “above” MM1 and going through both clumps, and the intermediate space in between (Fig. 6.1).

C1 HCO^+ is observed in all positions. It is composed of only one velocity component. The lines have symmetric line shape. The ^{12}CO ($4 \rightarrow 3$) line shows up significantly only in the deeper part of MM1. On the red side of the main lower transition line, a broad wing or a second component appears. The higher rotational line ($7 \rightarrow 6$) is detected tentatively even far from the central cluster (position 1 in C1).

Because of the very low S/N, the fine-structure lines of atomic carbon are at about the detection limit (together with CS) in C1.

C2 Until the first three positions, the dense tracer HCO^+ and the ^{12}CO lines have roughly the same central velocity. From position 4 – 5, HCO^+ consist of two velocity components. The velocity difference between these two components is $\sim 3 - 3.5 \text{ km s}^{-1}$. The ^{12}CO lines also consist of two components from the same depth of MM2 along C2. The line shape of the lower rotational transition ($4 \rightarrow 3$) matches well with the HCO^+ line shape along the whole length of C2. However, the line width of the upper transition ($7 \rightarrow 6$) is strongly increasing from position 5 due to the presence of another velocity component(s).

The other dense gas tracer CS and the [CI] lines are clearly visible from position 3 in C2. The CS line shows a weak second component between positions 3 – 6. [CI] ($^3\text{P}_1 \rightarrow ^3\text{P}_0$) is also composed of two velocity components and is very broad compared to CS and [CI] ($^3\text{P}_2 \rightarrow ^3\text{P}_1$) line. CS, together with [CI] ($^3\text{P}_2 \rightarrow ^3\text{P}_1$), is not detected at the last position in C2.

⁴Note that the final line shape is also depends on, for example, the optical depths.

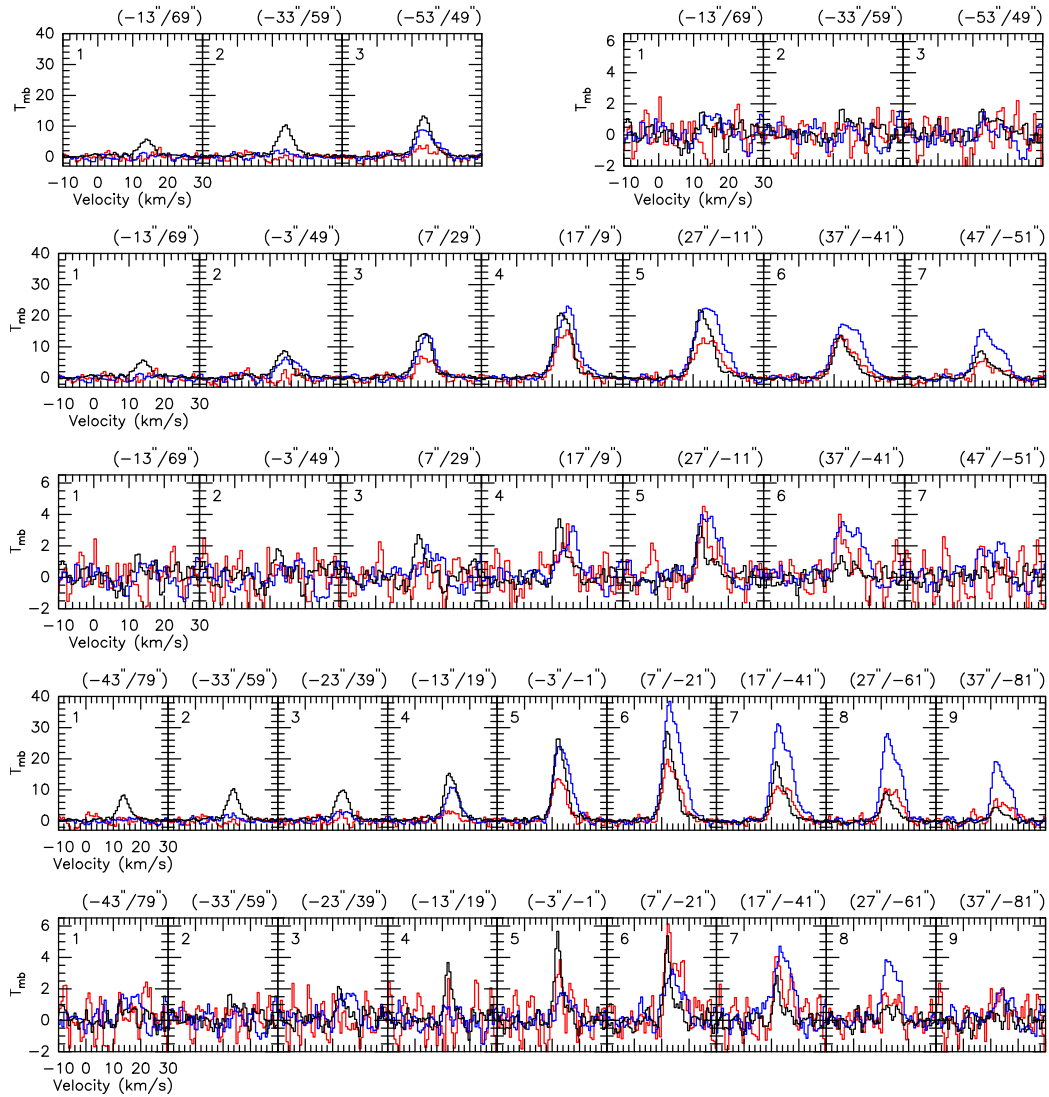


Figure 6.6: Comparison of line profiles along C1 (the first row from the top), C2 (the second and the third rows) and C3 (the fourth and the fifth rows). The left side of the first row, and the second and the fourth rows show line shapes of HCO^+ ($6 \rightarrow 5$) line (black), ^{12}CO ($4 \rightarrow 3$) line (blue) and ^{12}CO ($7 \rightarrow 6$) line (red). The right part of the first row, and the third and the fifth rows show line shapes of CS ($11 \rightarrow 10$) line (black), $[\text{Cl}]$ ($^3\text{P}_2 \rightarrow ^3\text{P}_1$) line (red) and $[\text{Cl}]$ ($^3\text{P}_1 \rightarrow ^3\text{P}_0$) line (blue). The numbers above each panel show the offset coordinates from 0,0 position, while the numbers in the boxes indicate the equally spaced points along the cuts where we did deeper investigation of the observed molecules. In cases of C1 and C2, the OB cluster is at position 1, for C3 the closest position to the cluster is at position 2. The intensities of HCO^+ and of CS are scaled up by 36 and 50, respectively.

C3 In the longest cut, the ^{12}CO lines are clearly visible from position 4. At the edge of MM1 (position 2) and between the observed clumps (position 1 and 3) we find no signal from these lines. On the other hand, the dense gas tracer HCO^+ is clearly detected. From position 4, the HCO^+ and ^{12}CO lines are composed of two velocity components and the velocity separation of these velocity components are remarkably constant along C3. The lines are well correlated in terms of velocity. The velocity separation of the two components, just like in C2, is continually increasing as a function of depth (from ~ 2.6 to $\sim 4.7 \text{ km s}^{-1}$).

The CS line is above the detection limit from position 3 and 8. The atomic carbon lines are shifted a little deeper into MM2 along C3 relative to CS. From position 5, these lines consist of two velocity components that are nicely observable.

Study of line intensities

To determine the peak and integrated intensities of the individual lines, I performed Gaussian fits for rotational transitions of CS and HCO^+ . In cases, where the observed lines are composed of two velocity components, I fitted two Gaussian function simultaneously.

For the correct CH lines fitting, I take into account the theoretical ratios of the relative intensities [$5 : 1 : 2$ for $F = 2^- \rightarrow 1^+ : F = 1^- \rightarrow 1^+ : F = 1^- \rightarrow 0^+$, respectively (Davidson et al., 2001)] and give the velocity shifts of each component (in km s^{-1}) with respect to the strongest $F = 2^- \rightarrow 1^+$ component (left panel of Fig. 6.7).

For the two hyperfine components of the C_2H molecule with a theoretical line ratio of $6.5 : 5.5$ ($F = 6 \rightarrow 5 : F = 5 \rightarrow 4$, respectively), the CLASS built-in hfs-fitting method was used (right panel of Fig. 6.7) because the observed lines are likely composed of one component.

All line fits can be seen in Appendix D and the determined physical parameters are in Tab. J.1 and J.2. The integrated intensity distributions of the observed molecules along the cuts (C1, C2 and C3) can be seen on Fig. 6.8).

C1 It seems, that the maximum of the integrated intensities of CS and C^{18}O ($2 \rightarrow 1$) lines are peaked closer to the central cluster (position 1) than the other species (top panel on Fig. 6.8). However, I have take into account that CS and the atomic carbon lines were observed very tentatively at that position. Thus, their peak position is doubtful. All the other species are peaked deeper in MM1 (position 3).

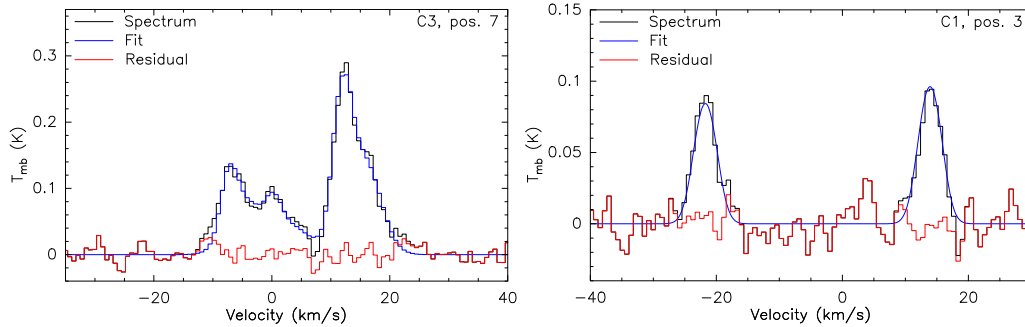


Figure 6.7: Examples for hyperfine fitting by the script *M.2* (left panel) and by the CLASS built-in hfs-fitting method (right panel). Black lines mark the original spectra. Blue lines represent the fitted model while red histograms show the residual.

C2 From the dense gas tracers, CS is peaked closer to the central UV source (position 1) than HCO^+ (middle panel on Fig. 6.8). But this is expected because the CS ($11 \rightarrow 10$) needs higher temperature to be excited than HCO^+ ($6 \rightarrow 5$). The intensity peak of the diffuse gas tracers CH and C_2H appear at the same depth of MM2 (along C2) but their intensities slightly decrease as a function of distance from the central OB cluster. This is consistent with the scenario that they trace the outer and diffuse part of the observed molecular cloud. The peaks of atomic carbon lines and the ^{12}CO lines from Röllig et al. (2011) are shifted far from the central cluster. It seems, that their intensity peaks are at the same position but I have to consider the beam size effect, namely with our beam size ($43''.5$) we cannot entirely resolve MM2 (spatially).

C3 It can be seen from the bottom panel on Fig. 6.8, that there is a small intensity bump at position 2 in most of the cases of the observed species. That little intensity component is equivalent with the edge (or probably with the ionization front/cavity wall) of MM1. The atomic carbon and ^{12}CO lines do not produce that intensity jump, most likely because ^{12}CO and [C] trace gas at high values of A_V .

Similarly to C2, the CS ($11 \rightarrow 10$) line peaks slightly closer to the surface of MM2 (along C3) than the HCO^+ ($6 \rightarrow 5$) transition. The diffuse gas tracers CH and C_2H possess broad intensity distributions along the cut. CH is broader which may suggest that C_2H traces a layer underneath the surface layer where CH is present.

In this cut, I also cannot distinguish the intensity peak positions of ^{12}CO and [C] lines. On the other hand, both ^{12}CO line intensities are peaked deeply inside MM2 (along C3) and show a strong increment. This edgy intensity distribution suggests the presence of small clumps composed of carbon monoxide.

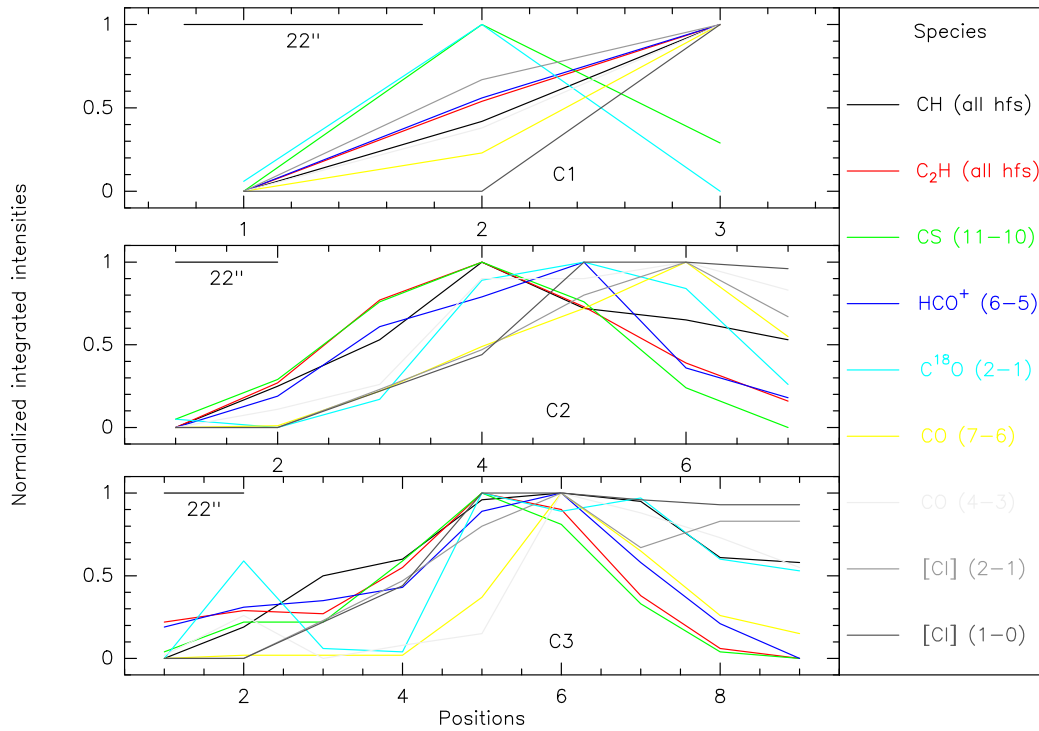


Figure 6.8: Normalized integrated intensities of the observed species along C1, C2 and C3. The $C^{18}O$ data is from [Nürnberger et al. \(2002\)](#) while the $[Cl]$ and ^{12}CO data are from [Röllig et al. \(2011\)](#). In cases of CH and C_2H the hyperfine components are included.

Cut observations

In case of the Herschel cut observations, at many positions, the lines were composed of not only one velocity component but two or even more. As for the OTF observations, I fitted the observed emission lines with Gaussian models to derive physical parameters. The line fits can be seen in Appendix E while the derived parameters from line fits can be found in the Tab. J.3. Figures 6.9 and 6.10 are presented as examples of the lines shapes and their distribution in both MM1 and MM2. In cases of other observed lines, the similar figures can be found in the Appendix H.

MM1 Just behind the ionization front, $o\text{-H}_2\text{O}$ ($1_{10} \rightarrow 1_{01}$) emission becomes stronger and it is composed of more than one velocity component. The intensity peak is located deeply inside in MM1.

^{12}CO ($9 \rightarrow 8$) emerges from the continuum at around the ionization front. The emission line is wide and composed of two velocity components and/or the broad line is the signature of turbulent gas motions.

The intensity peak of ^{13}CO ($10 \rightarrow 9$) appears slightly closer to the ionization front in accordance with the results of our previous investigations. A

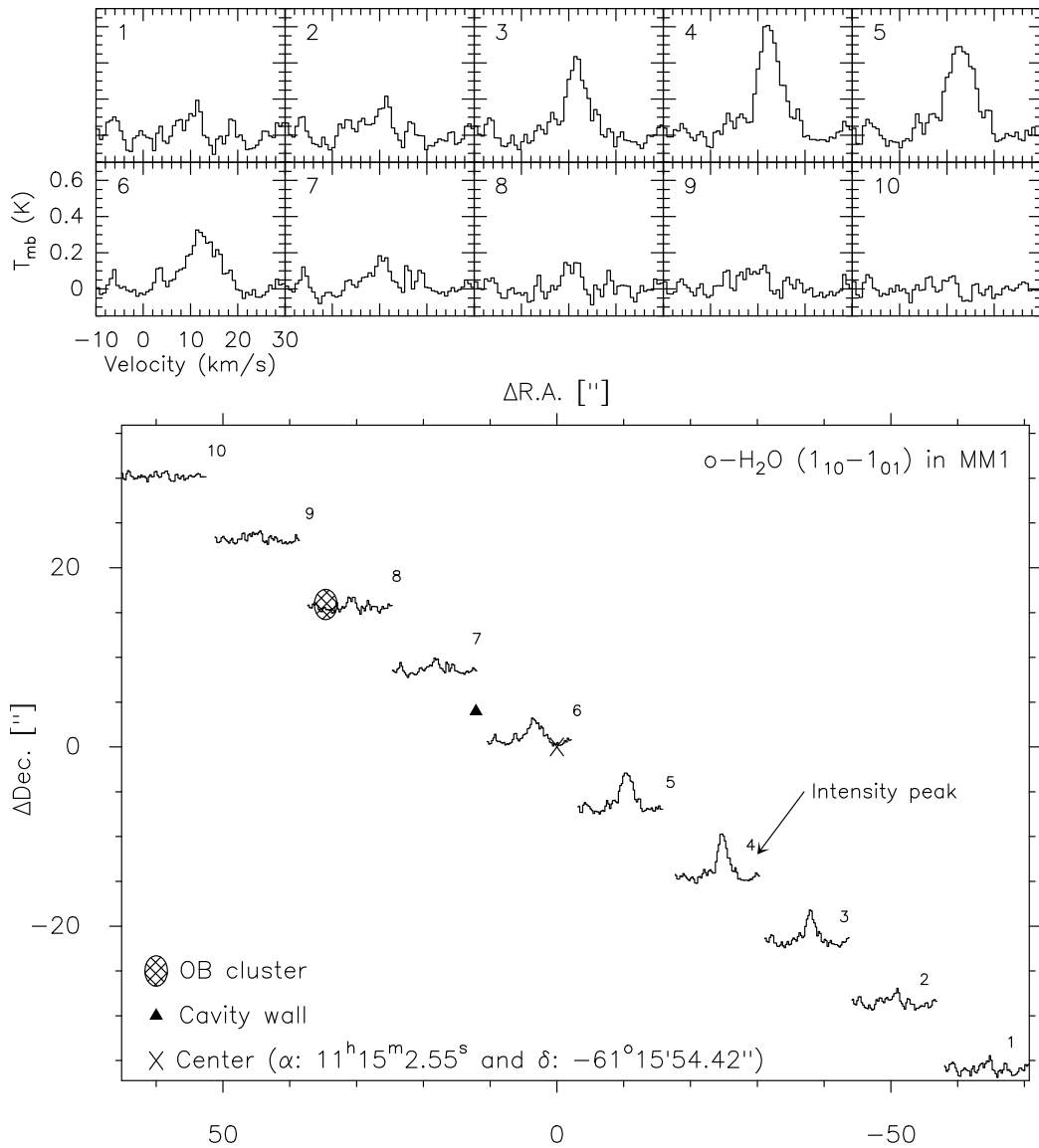


Figure 6.9: Top panel: the ortho-water line shapes in MM1. The numbers in the boxes mark the position numbers. **Bottom panel:** the “distribution” of $o\text{-H}_2\text{O}$ along the cut in MM1. The bottom most-right spectrum is the first and, implicitly, the upper most-left spectrum is the last one, and this sequence is the same for the plots in MM1.

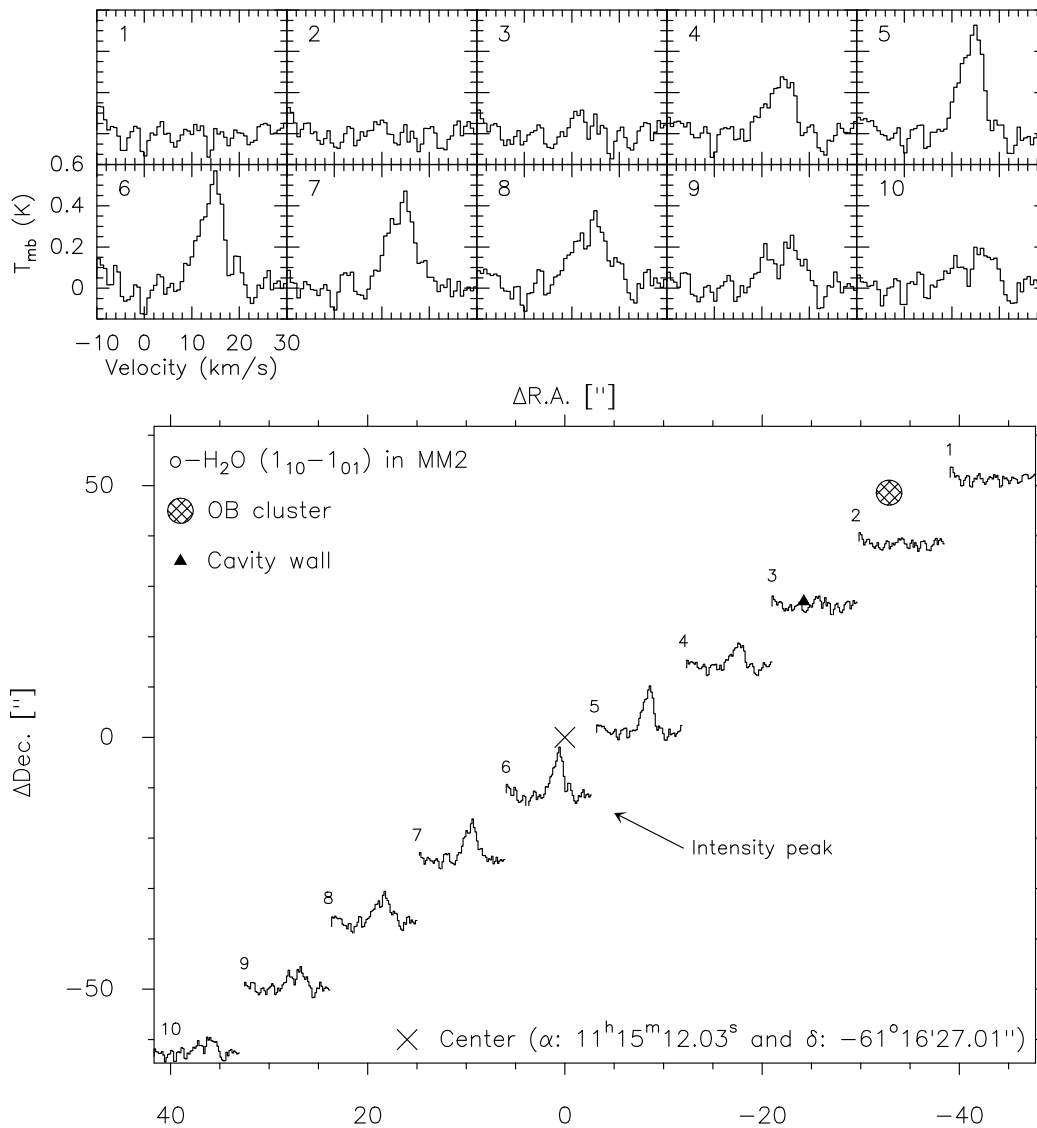


Figure 6.10: The line shapes and distribution of ortho-water in MM2. The top most right spectrum is the first and the bottom most left spectrum is the last one, and this sequence is the same for the plots in MM2.

second velocity component is recognizable but with lower strength than the main emission line, hence the line shape is not symmetric.

The ionized carbon $^{12}\text{C}^+$ ($^2\text{P}_{3/2} \rightarrow ^2\text{P}_{1/2}$) is markedly increasing after the ionization front. Its intensity peak is located relatively deep inside the clump. Very deep inside MM1, a broad wing appears on the blue side of the main line that might be a sign for outflow.

MM2 Just like in MM1, the water line significantly appears only behind the ionization front in MM2. It is obvious that the line consists of two velocity components (at least) and these components are well separated from position ~ 8 far away from the central OB cluster.

In the bigger clump, ^{12}CO has its intensity peak closer to the ionization front than the observed water line. The emission line shows an asymmetric line shape because of a second velocity component. That component appears on the “blue side”, while there is another velocity component on the “red side” of the main emission line. All these can be interpreted as the effects of turbulent gas motions.

Even if the ^{13}CO lines have smaller line widths than, for example, ^{12}CO line, the emission line is probably composed of two velocity components but not at each position.

The $^{12}\text{C}^+$ line presents very complex line profiles after position 19 (which is the intensity peak). Before that, a second velocity components already appeared. At position 18, another strong emission line appears at $\sim 30 \text{ km s}^{-1}$. From positions 21 – 22, probably wings are also visible. The complex line shape indicates that complicated gas motions exist inside MM2, while the component at $\sim 30 \text{ km s}^{-1}$ traces the “rear wall” of the newly discovered internal bubble (Section 6.2.1).

Point observations

We also performed pointed observations at three different positions: MM1-IF, MM2-pillar and MM2-peak. We detected the NH ($1_2 \rightarrow 0_1$) hyperfine component(s) at $\sim 974.5 \text{ GHz}$ (MM1-IF and MM2-pillar), the OH $^+$ ($1_2 \rightarrow 0_1$) hyperfine transition(s) at $\sim 971.8 \text{ GHz}$ (MM1-IF and M2-pillar), the p-H $_2\text{O}$ ($2_{02} \rightarrow 1_{11}$) line at 987.927 GHz (MM1-IF and MM2-pillar) and C ^{18}O ($9 \rightarrow 8$) at 987.56 GHz (MM1-IF, MM2-pillar and MM2-peak).

In case of the OH $^+$ line, first, because we have a significantly strong absorption line just next to the desired emission line, I removed that absorption feature⁵ by fitting a Gaussian and subtracting it. Using the residual, I was able to correctly fit the hyperfine components with the built-in hfs-fitting

⁵The line central velocities of both the emission and absorption lines are separated well (~ 14 and $\sim -19 \text{ km s}^{-1}$, respectively). On the other hand, these velocities are close enough to each other to assume that the absorption could be local to NGC 3603.

method of CLASS. The result line fit of the hfs-fitting method and the theoretical positions of the hyperfine components on the averaged spectrum can be seen on Fig. 6.11⁶.

MM1-IF The observed NH line is relatively wide ($\sim 7 \text{ km s}^{-1}$) but this may be caused by the fact that we observed more than one hyperfine components which are blended. The detection of NH at or close to the cloud surface nicely coincides with the predictions, namely the NH should appear in the diffuse, hot part of the PDRs, e.g. Wagenblast et al. (1993). Similarly to NH, OH^+ is also detected but, in contrast to NH, its line width is smaller ($\sim 4 \text{ km s}^{-1}$) indicating that OH^+ comes from a deeper layer which is less influenced by stellar wind. The visibility of the OH^+ emission also agrees with previous studies that predict this molecule as a warm and diffuse gas tracer of a moderately thick molecular cloud (de Almeida & Singh, 1981). However, the presence of OH^+ could also indicate the existence of a shock front (de Almeida, 1990).

Next to the main emission line, a weak but detectable broad wing was observed in the case of para-water (upper panel of Fig. 6.12). It is possible that this observed broad wing is a signature of a shock front that propagates into the cloud. Besides the broad wings, the main emission line is strong and composed of one velocity component.

The C^{18}O line is visible with a single velocity component and strong emission. Because it has a low dipole moment (~ 0.1 Debye), it can easily be thermalized (Kainulainen et al., 2006). Thus, higher rotational transitions can also be easily excited, hence the strong existence of C^{18}O ($9 \rightarrow 8$) at the hot surface layer of the molecular cloud is expected.

MM2-pillar The observed NH line is much weaker at the interface of MM2 than at MM1. The reasons could be, e.g., the lower amount of diffuse gas and/or the temperature is not high enough to significantly form NH. The OH^+ line is also weaker (it is close to the detection limit) than in MM1. Corresponding to NH, the main reasons for the weak detection is probably a lower temperature or the less diffuse gas.

At the interface of MM2, I also observed a wing in case of the para-water. Very likely this wing is a footprint of the shock front caused by the strong stellar winds from the central OB cluster.

The C^{18}O line has no wing(s) or other velocity components.

MM2-peak Far from the central star cluster, we have no observations of NH and OH^+ . Similarly to MM2-pillar, the reason(s) for the non-detection

⁶The plots I represent in this section are only examples. Similar figures can be found in Appendix F.

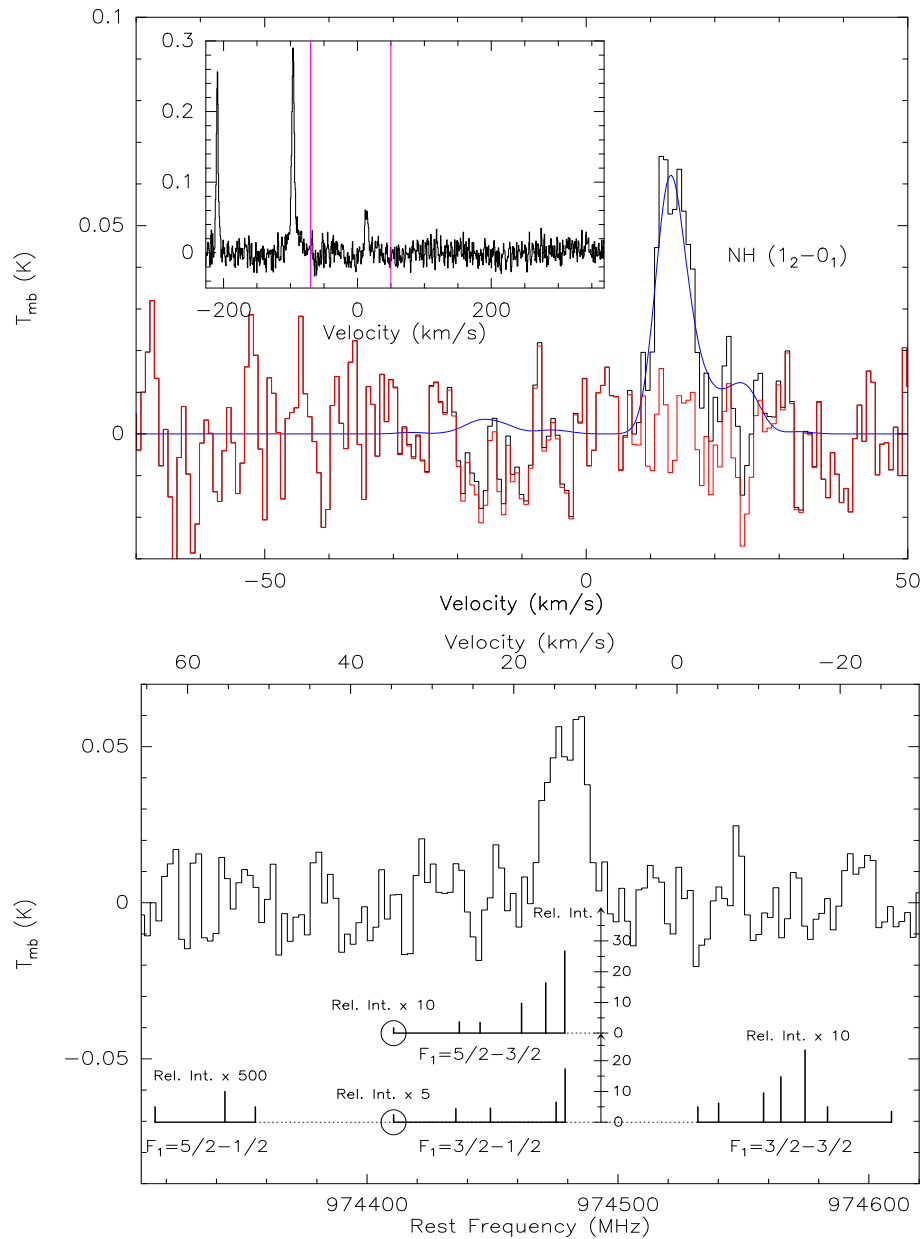


Figure 6.11: Upper panel: The fitted hyperfine components of averaged NH spectrum in MM1-IF. The black line represents the original spectrum, the blue line shows the hfs-fit and the red line marks the residual spectrum. The small box inside the main plot shows the whole LSB spectrum. The magenta lines indicate the window/velocity range of the main plot. The other lines are $C^{18}O$ and $p\text{-H}_2O$ (from USB) from left to right, respectively. **Lower panel:** Theoretical positions of the observed hyperfine components of the NH. The hyperfine groups caused by magnetic dipole interaction are marked. The line strengths are indicated in % of the total line strength. The line strengths of groups $F_1 = 5/2 \rightarrow 1/2$ and $F_1 = 3/2 \rightarrow 3/2$ are scaled up by 500 and 10, respectively. The left hyperfine components of groups $F_1 = 5/2 \rightarrow 3/2$ and $F_1 = 3/2 \rightarrow 1/2$ are scaled up by 10 and 5, respectively.

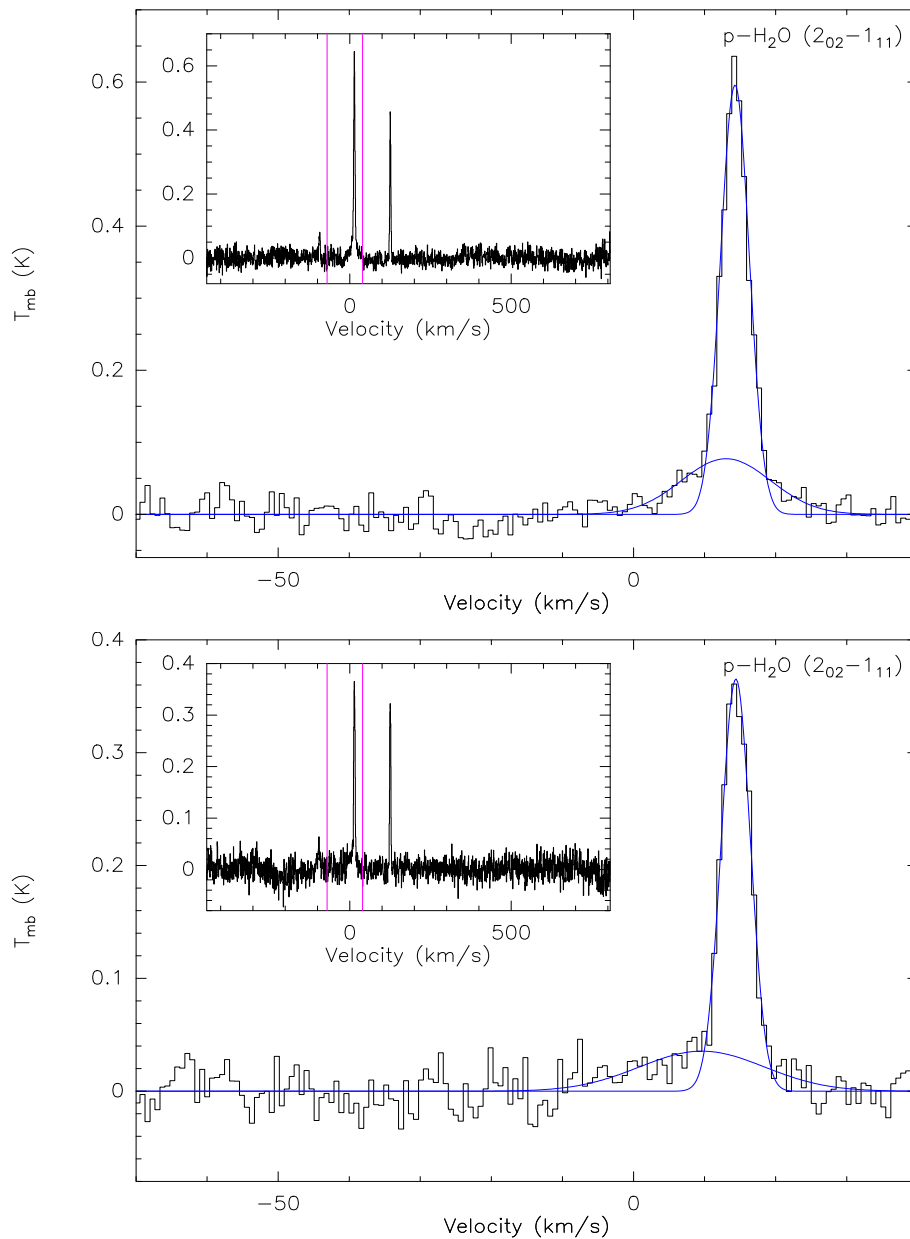


Figure 6.12: Upper panel: The fitted line components of the observed p - H_2O spectrum in MM1-IF (1342223430). The wings were fitted by another Gaussian line. The meanings of colors and small box are the same as before. In the smaller plot, the weak line on the left side of p - H_2O is NH (from LSB) while C^{18}O is visible on the right hand side (from USB). **Lower panel:** The fitted line components of the observed p - H_2O spectrum in MM2-pillar (1342223427).

could be the less amount of diffuse gas and/or slow chemical reactions (due to the lower temperature).

We detected p-H₂O and, it seems, that the main emission line has a second component or a broad wing (it is hard to distinguish based on our observations) on the red side of the main line. In addition, the emission strength is about the third of the strength that we detected at MM2 interface. This decreased intensities (C¹⁸O line is also much weaker) are probably, again, a temperature effect.

6.2.4 Kinematic distance

Using CO and HI observations, the rotation curve of our Galaxy was used [e.g. [Clemens \(1985\)](#)] to establish the distance of molecular clouds ([Roman-Duval et al., 2009](#)). I derived the kinematic distance of NGC 3603 (d) assuming that it fits the galactic rotational curve ($\Theta(R)$). The radial velocity can be written at the position of the molecular cloud [Maciel \(1995\)](#):

$$V_{\text{LSR}} = R_0 \left(\frac{\Theta(R)}{R} - \frac{\Theta_0}{R_0} \right) \sin l \cos b \quad (6.1)$$

where $R_0 = 8.5$ kpc is the galacto-centric distance, $\Theta_0 = 220$ km s⁻¹ is the linear velocity at Sun's position, $l = 291.6253$ and $b = -0.5313$ are the galactic coordinates of NGC 3603, and R is the projected galacto-centric distance which can be written as [Maciel \(1995\)](#); [Stark & Brand \(1989\)](#):

$$R^2 = R_0^2 + d^2 \cos^2 b - 2R_0 \cos b \cos l d \quad (6.2)$$

Rearranging Eq. (6.1):

$$\frac{\Theta(R)}{R} = \frac{V_{\text{LSR}}}{R_0 \sin l \cos b} + \frac{\Theta_0}{R_0} \approx 24.04 \pm 0.04 \text{ km s}^{-1} \text{ kpc}^{-1} \quad (6.3)$$

where the mean $V_{\text{LSR}} = 14.52 \pm 0.32$ km s⁻¹ (which includes all determined velocities of the observed species from Herschel observations) and $\Theta(R) \sim 220$ km s⁻¹ (from the rotational curve), thus $R \approx 9.15 \pm 0.002$ kpc. The solution of Eq. (6.2):

$$d = \frac{-2R_0 \cos b \cos l \pm \sqrt{4R_0^2 \cos^2 b \cos^2 l + 4 \cos^2 b (R^2 - R_0^2)}}{-2 \cos^2 b} \quad (6.4)$$

The result is $d \approx 7.30 \pm 0.05$ kpc which is in good agreement with the previous determination from [Nürnberg et al. \(2002\)](#)⁷.

⁷Note that the calculation is based on all clumps (about a dozen molecular clumps). If I take the V_{LSR} values only of CS ($2 \rightarrow 1$ and $3 \rightarrow 2$) for MM1 and MM2 from [Nürnberg et al. \(2002\)](#), then the result is practically the same.

6.3 Excitation temperature

To calculate the total column densities of the observed molecules, we need information about the excitation temperature. Assuming LTE, one excitation temperature can substitute all excitation temperatures of each level.

Based on previous NANTEN2 observations of ^{12}CO and [C] (Section 5.2), the average excitation temperatures are 51 K and 54.8 K in MM1 and MM2, respectively. Röllig et al. (2011) also performed escape probability calculation to derive volume and column densities, and gas temperature. From those calculations, the result values are 54 K and ~ 48 K in MM1 and MM2, respectively⁸. Based on these derivations, I assumed $T_{\text{ex}} = 50$ K.

To check how reliable this assumption is, I convolved the NANTEN2 data to beam size $43''5$. The averaged excitation temperatures are 47.5 K and 51.5 K in MM1 and MM2, respectively. The differences between these values and the assumed 50 K are 5% and 3% in MM1 and MM2, respectively. Thus, $T_{\text{ex}} = 50$ K is a reasonable approach.

Because I want to model the observed line intensities at two positions (MM1-IF and MM2-IF; Section 7.2), I also used the ^{12}CO ($9 \rightarrow 8$ (assume that it is optically thick) and ^{13}CO ($10 \rightarrow 9$) line intensities (which is optically thin) to derive the excitation temperature:

$$T_{\text{ex}} = \frac{T_{\text{mb}}(^{12}\text{CO})}{1 - \exp(-\tau)} - T_{\text{bg}} \quad (6.5)$$

where $T_{\text{bg}} = 2.725$ K is the temperature of the background radiation field and τ is the optical depth of ^{13}CO which can be determined by:

$$\tau(^{13}\text{CO}) = -\ln \left[1 - \frac{T_{\text{mb}}(^{13}\text{CO})}{T_{\text{mb}}(^{12}\text{CO})} \right] \quad (6.6)$$

The received excitation temperatures are 50.3 K and 56.2 K for MM1-IF and MM2-IF, respectively. These values are in good agreement with the assumed 50 K within $< 1\%$ and $\sim 12\%$ (Tab. 6.1), hence $T_{\text{ex}} = 50$ K is still a good approach.

6.4 Derivation of column densities

Before I apply our assumption on the excitation temperatures to calculate column densities, I studied the total column densities as a function of excitation temperature and the ratios of N_{tot} at given T_{ex} (Fig. 6.13). I found

⁸The difference between the excitation temperatures derived from optically thick ^{12}CO intensity ratio ($I_{\text{CO}(7-6)}/I_{\text{CO}(4-3)}$) and escape probability is mainly caused by the different beam filling assumptions [more in Röllig et al. (2011)].

Table 6.1: The derived excitation temperatures (in Kelvin) with different methods (see text for more) in MM1 and MM2.

	T_{ex}^a	T_{ex}^b	T_{ex}^c	T_{ex}^d
MM1	51.0 (2) ^e	54.0 (8)	47.5 (5)	50.3 (< 1)
MM2	54.8 (~ 10)	~ 48.0 (4)	51.5 (3)	56.2 (~ 12)

^a Based on optically thick ^{12}CO line intensity ratios ($I_{\text{CO}(7-6)}/I_{\text{CO}(4-3)}$) from Röllig et al. (2011).

^b Using escape probability calculations from Röllig et al. (2011).

^c Using optically thick ^{12}CO line intensity ratios convolved to beam size $43''5$.

^d Based on our observations of ^{12}CO ($9 \rightarrow 8$) and ^{13}CO ($10 \rightarrow 9$).

^e The discrepancies from the assumed $T_{\text{ex}} = 50$ K in percent.

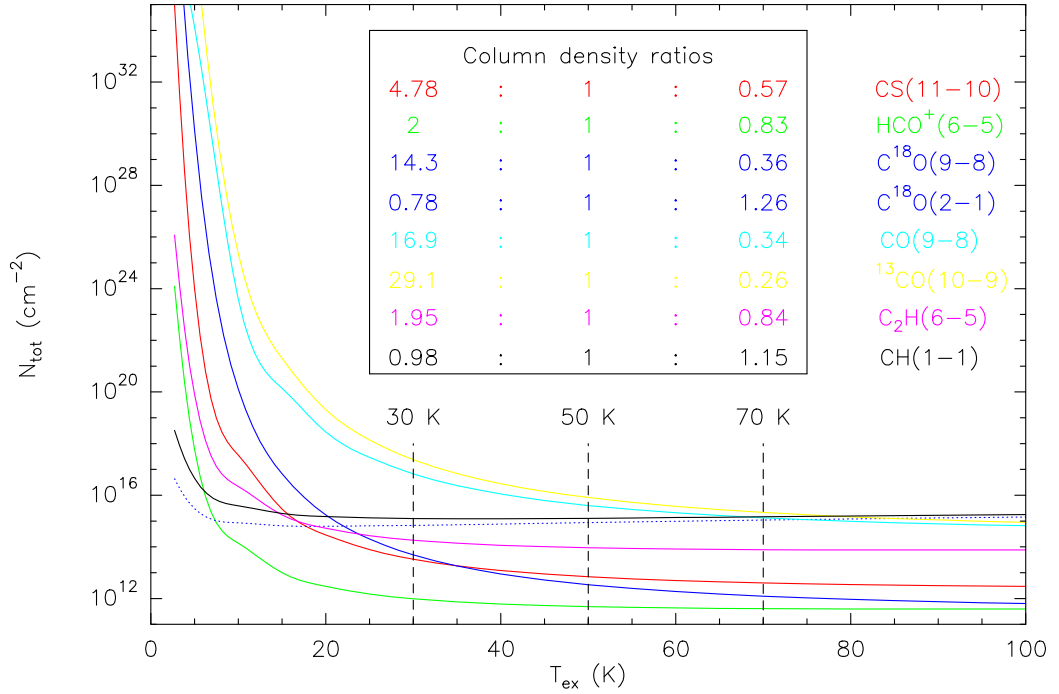


Figure 6.13: Dependency of the total column densities (derived from the observed transitions) from the excitation temperature. I assumed $\int T_{\text{mb}} dv = 1 \text{ K km s}^{-1}$ for all lines. The column density ratios are denoted in the smaller box at 30, 50 and 70 K.

in few cases [C^{18}O ($9 \rightarrow 8$), ^{12}CO ($9 \rightarrow 8$) and ^{13}CO ($10 \rightarrow 9$)], if the real excitation temperature was less than 50 K, N_{tot} would strongly be underestimated.

With these conditions and using Eq. (2.19), I determined the column densities for the observed rotational transitions (N_j). The total column density (N_{tot}) is a sum of column densities of all levels, hence I need the partition function [$Q(T)$] at a given temperature. The partition functions can

be found for many species in, e.g. CDMS. With the partition functions and performing a polynomial interpolation method using *Mathematica*⁹, I derived the partition functions for all observed species at $T = 50$ K.

6.4.1 Column densities along C1, C2 and C3 (OTF-map)

The hyperfine-fitting method can also be used to determine the optical depth [Hily-Blant \(2006\)](#). To derive the column density of a given rotational transition of the observed light hydrides (CH and C₂H), I used Eq. (2.22). In addition to the light hydrides, we also observed linear molecules (CS and HCO⁺). Because I only have one rotational transition of the observed species, I used Eq. (2.20) to derive the line optical depths (assuming $T_{\text{ex}} = 50$ K). Based on those calculations, the observed linear molecules are optically thin. Therefore, I derived the total column densities assume LTE and optically thin emission.

The total column densities as a function of distance from the central ionization source along C1, C2 and C3 are shown in Fig. 6.14. The plot shows that CS is positioned closer to the ionization front than HCO⁺ in C2 and C3 which may suggest that we see a dense CS core surrounded by HCO⁺. The column density distribution of CH is fairly constant from position 3 in C3. This is in accordance with the scenario that CH is a diffuse gas tracer and widespread (C₂H has similar behaviour in C2).

H₂ column density

Assuming that C¹⁸O is optically thin, I used the integrated line intensities of C¹⁸O ($2 \rightarrow 1$) from [Nürberger et al. \(2002\)](#) to determine $N(\text{H}_2)$. Adopting the isotope ratio of 500 and $^{12}\text{CO}/\text{H}_2 = 8.5 \times 10^{-5}$ ($\text{C}^{18}\text{O}/\text{H}_2 = 1.7 \times 10^{-7}$) from [Frerking et al. \(1982\)](#) and using the total column density of C¹⁸O, I calculated the hydrogen column density via:

$$N(\text{H}_2) = \frac{N_{\text{tot}}(\text{C}^{18}\text{O})}{1.7 \times 10^{-7}} \quad [\text{cm}^{-2}] \quad (6.7)$$

As I mentioned in Section 5.3, I also used PACS and SPIRE data to derive H₂ column density. Because the original maps have smaller beam sizes, I convolved the data to the beam size of HIFI maps (43''5). I found small discrepancies (which probably caused by beam dilution effect) between the H₂ column densities calculated by these two different methods (Fig. 6.15). Therefore, for further calculations (i.e. abundances), I used the average values of $N(\text{H}_2)$.

⁹<http://www.wolfram.com/mathematica/>

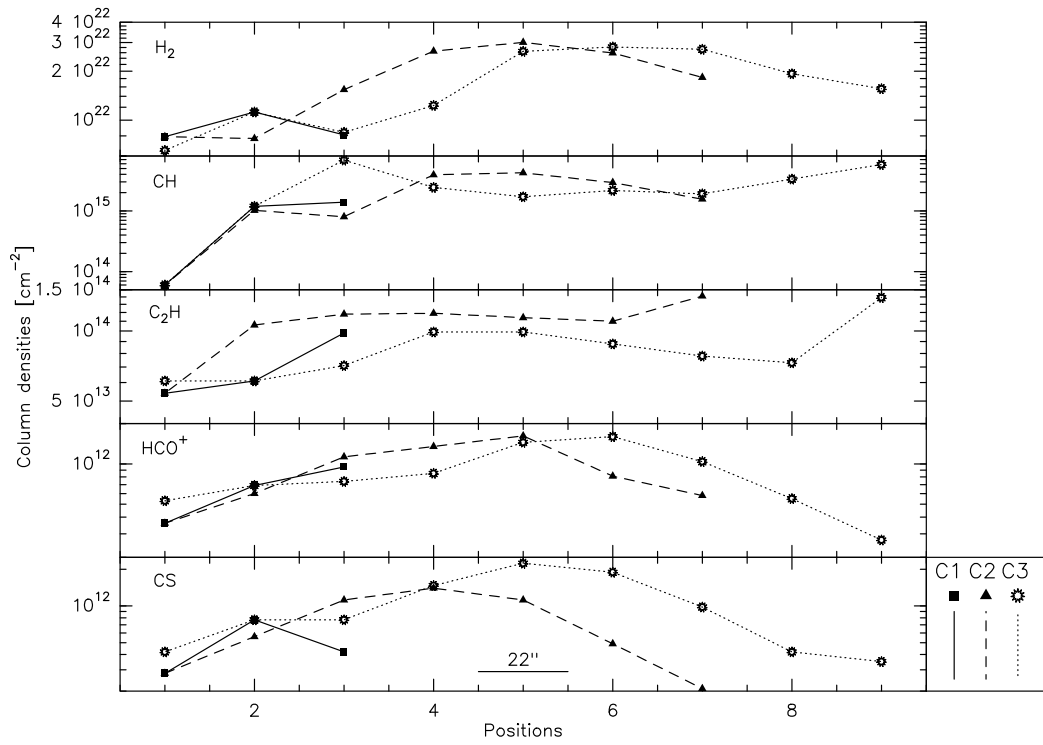


Figure 6.14: The derived total column densities along C1, C2 and C3.

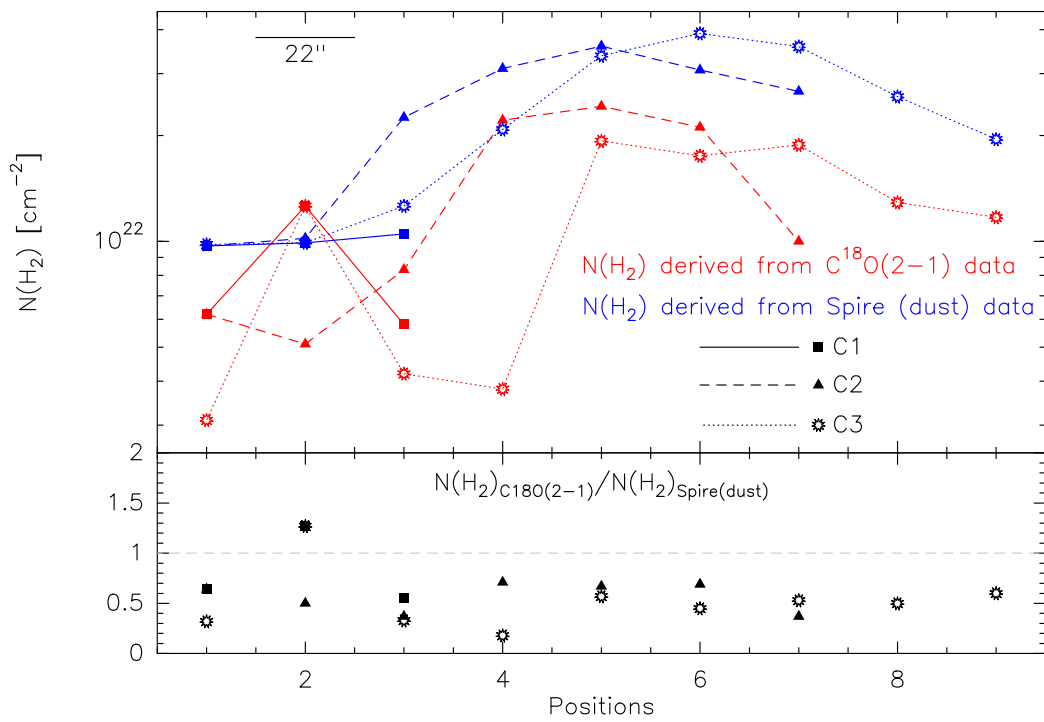


Figure 6.15: Comparison of H_2 column densities derived by different methods (see text).

The results of the column density calculation can be found in Tab. 6.3. The comparison of the derived column densities are on Fig. 6.14. The column density of molecular hydrogen increases from position 2 and 3 in C2 and C3, respectively. This is in good agreement with the existence of a wind-blown cavity around the central OB cluster.

6.4.2 Column densities from cut observations

Based on the optical depth calculations (assuming $T_{\text{ex}} = 50$ K), o-H₂O, ¹²CO (9 → 8) and ¹³CO (10 → 9) are optically thin at all positions. Even if the lower transitions of ¹²CO become optically thick easily, it is possible that transition (9 → 8) is optically thin. It is also possible to determine $N_{\text{tot}}(^{12}\text{CO})$ with rotational-diagram. In LTE, if we plot $\ln(N_u/g_u)$ as a function of E_u/k the slope of the resulting line gives the *rotational temperature*¹⁰. The intersection with the y-axis provides the approximate total column density. Because I have previous observations of ¹²CO (NANTEN2, lower- J lines) and PACS (high- J lines), I was able to combine all these data to create the rotational diagram. The complementary and PACS data were taken with different beam sizes, therefore I convolved all these data to a beam size of 43''5. In total, I have 7 rotational transitions of ¹²CO [(4 → 3), (7 → 6), (9 → 8) and from (13 → 12) to (16 → 15)]. The rotational diagrams can be seen on Fig. 6.16. The calculated column densities are in the order of $10^{16} - 10^{17} \text{ cm}^{-2}$ for the moderately warm and $10^{14} - 10^{15} \text{ cm}^{-2}$ for the warmer ¹²CO components while ¹²C⁺ has column density $\sim 10^{17} - 10^{18} \text{ cm}^{-2}$. The results are shown in Tab. J.4.

6.4.3 Column densities from point observations

The column density of a rotational transition is weighted by the statistical weight (g_{rot}) of that rotational level. The statistical weight of a given rotational transition can be determined by taking into account all multiplets. For calculations of column densities of a given rotational transition I need to determine the rate of spontaneous emission using Eq. (2.1)¹¹.

For the NH ($N = 1 \rightarrow 0$) transition, because $S = 1$, $I_{\text{H}} = 1/2$ and $I_{\text{N}} = 1$, the statistical weight can be determined:

¹⁰For pure rotational transitions often $T_{\text{ex}} = T_{\text{rot}}$. If all levels are thermalized, then the received temperature is equal to the kinetic temperature (Goldsmith & Langer, 1999).

¹¹To have the correct dimension of A_{ul} [s^{-1}], electric dipole moment needs to be converted from Debye to CGS unit: 1 Debye = 1×10^{-18} statC·cm = $1 \times 10^{-18} \text{ g}^{1/2} \text{ cm}^{5/2} \text{ s}^{-1}$.

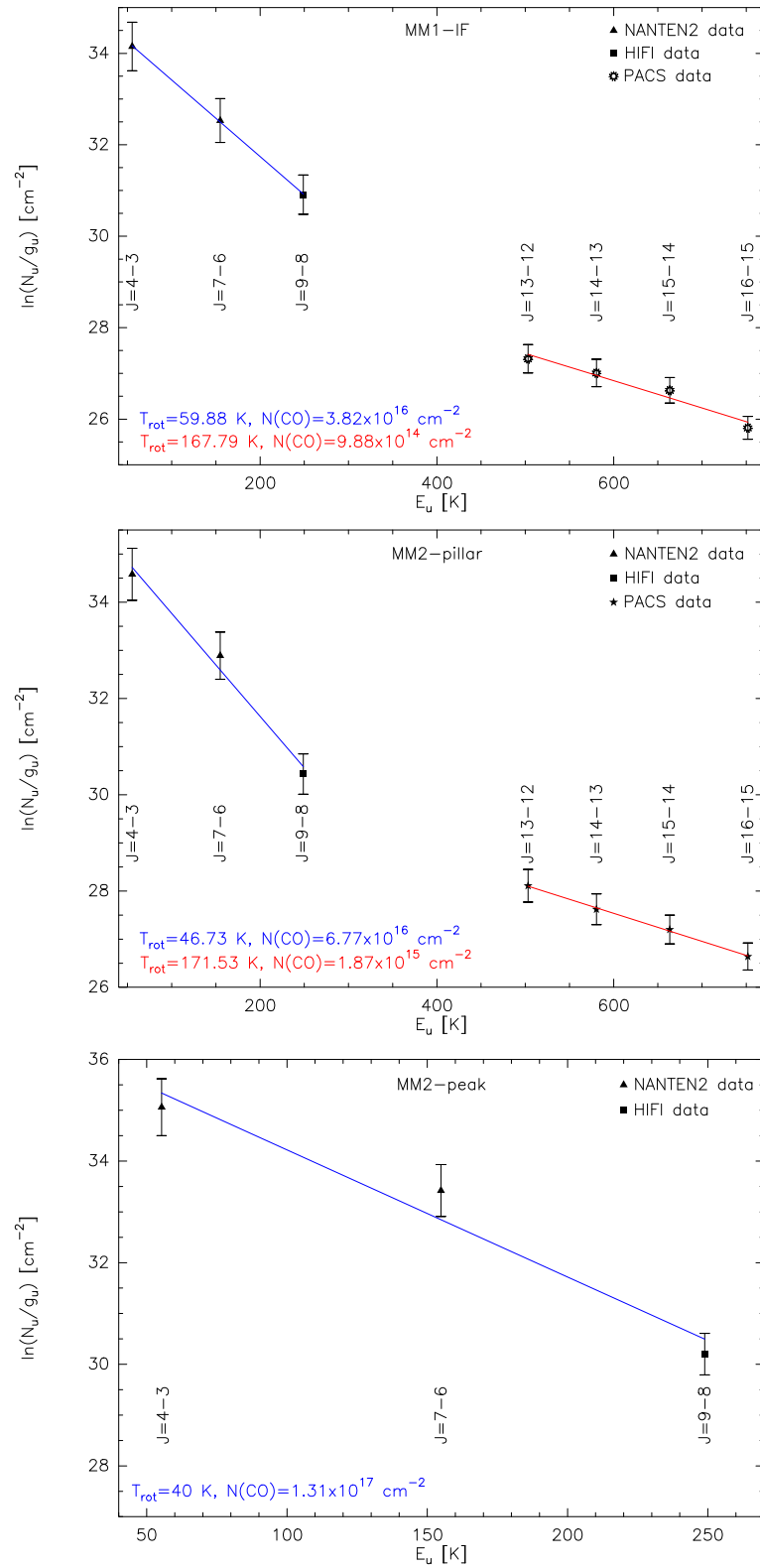


Figure 6.16: Rotational diagrams of ^{12}CO transitions from the interface of MM1 and MM2 (top and middle panels) and from the deeper part of MM2 (bottom panel) where we have no observations of high-J lines.

$$\begin{aligned}
g_{\text{rot}} &= \sum_{J=|N-S|}^{|N+S|} \sum_{F_1=|J-I_H|}^{|J+I_H|} \sum_{F=|F_1-I_N|}^{|F_1+I_N|} g_F = (2J+1)(2I_H+1)(2I_N+1) \\
&= (2N+1)(2S+1)(2I_H+1)(2I_N+1) = 18(2N+1) = 54
\end{aligned} \tag{6.8}$$

As shown in Section 6.4.1, the hyperfine fitting method is a possibility to derive the total optical depth for a whole rotational level. The calculated total optical depth is ~ 0.1 which suggests optically thin line. In case of OH^+ ($N = 1 \rightarrow 0$), because $S = 1$ and $I_H = 1/2$, the statistical weight can be calculated [similarly to Eq. (6.8)]:

$$g_{\text{rot}} = \sum_{J=|N-S|}^{|N+S|} \sum_{F_1=|J-I_H|}^{|J+I_H|} g_{F_1} = (2N+1)(2S+1)(2I_H+1) = 18 \tag{6.9}$$

The determined total optical depth suggests that the rotational transition is marginally optically thick ($\tau_{\text{tot}} = 2.32$) in MM1-IF. The line is more optically thick in MM2-pillar ($\tau_{\text{tot}} = 7.44$).

For the observed para-water $2_{02} \rightarrow 1_{11}$ and C^{18}O ($9 \rightarrow 8$) line I assumed optically thin emission and LTE, thus the total column densities are derived by Eq. (2.23). The results can be found in Tab. 6.2.

Abundances

With the knowledge of hydrogen column density, I was able to calculate and compare the fractional abundances, relative to H_2 , of the observed species along the cuts. The dense gas tracer CS is more abundant at about the cavity wall (in C2) and slightly deeper in MM2 (C3). This may indicate that there is a dense core close to the cavity wall. The HCO^+ shows consistently regressive abundance distribution from the central OB cluster to the deeper part of MM2 (C2 and C3). The abundance of HCO^+ smoothly increases in MM1 as a function of distance from the central star cluster. The same trend can be seen in the case of C_2H except deeply inside MM2 where its abundance slightly rises again. The abundance distribution of CH is remarkably constant from position 2 in C2 and position 4 in C3 which suggest uniform amount of CH in MM2. The results can be seen on Fig. 6.17 and found in Tab. 6.4.

Table 6.2: Results of HIFI point observations for the whole rotational transitions.

Gaussian fitting method												
Region	Molecule	Transition N – N'	$A_{\text{NN}'}$ [s ⁻¹]	g_{N}	E_{N} [K]	$\int T_{\text{mb}} dv$ [K km s ⁻¹]	V [km s ⁻¹]	ΔV [km s ⁻¹]	T_{peak} [K]	N_{tot} [cm ⁻²]		
MM1-IF	p-H ₂ O ^a	2 – 1	5.835×10^{-3}	3	100.8	3.01 ± 0.05	14.3 ± 0.04	4.741 ± 0.096	0.6 ± 0.04	4.51×10^{13}		
	C ¹⁸ O	9 – 8	6.38×10^{-5}	19	237	1.84 ± 0.04	14.4 ± 0.01	3.796 ± 0.085	0.45 ± 0.03	1.17×10^{16}		
MM2-pillar	p-H ₂ O ^a	2 – 1	5.835×10^{-3}	3	100.8	1.89 ± 0.05	14.4 ± 0.06	4.854 ± 0.148	0.37 ± 0.02	2.83×10^{13}		
	C ¹⁸ O	9 – 8	6.38×10^{-5}	19	237	1.52 ± 0.03	14.1 ± 0.05	4.154 ± 0.103	0.345 ± 0.02	9.7×10^{15}		
MM2-peak	p-H ₂ O	2 – 1	5.835×10^{-3}	3	100.8	0.57 ± 0.22	12.9 ± 0.5	4.707 ± 0.768	0.11 ± 0.007	8.54×10^{12}		
	p-H ₂ O 2 nd comp.		5.835×10^{-3}	3	100.8	0.2 ± 0.2	17.9 ± 3.5	6.678 ± 4.224	0.03 ± 0.002	3×10^{12}		
	C ¹⁸ O	9 – 8	6.38×10^{-5}	19	237	0.28 ± 0.04	13.8 ± 0.3	4.2 ± 0.7	0.06 ± 0.004	1.79×10^{15}		

Hyperfine fitting method												
Region	Molecule	Transition N – N'	$A_{\text{NN}'}$ [s ⁻¹]	g_{N}	τ_{tot}	V [km s ⁻¹]	ΔV [km s ⁻¹]	N_{tot} [cm ⁻²]				
MM1-IF	NH ^b	1 – 0	8.31×10^{-3}	54	0.1 ± 0.3	12.7 ± 0.3	4.89 ± 0.65	3.65×10^{12}				
	OH ⁺	1 – 0	1.81×10^{-2}	18	2.32 ± 20.5	13.9 ± 0.3	2.68 ± 1.84	3.03×10^{13}				
MM2-pillar	NH ^b	1 – 0	8.31×10^{-3}	54	0.1 ± 0.4	15.1 ± 0.7	7.72 ± 1.83	5.77×10^{12}				
	OH ⁺	1 – 0	1.81×10^{-2}	18	7.44 ± 6.3	15.8 ± 0.3	2.42 ± 0.69	6.12×10^{13}				
MM2-peak ^c	NH	1 – 0	8.31×10^{-3}	54	–	–	–	–				
	OH ⁺	1 – 0	1.81×10^{-2}	18	–	–	–	–				

^aOnly the main emission line is presented here (no wing).

^bWeighted average spectrum from two different ObsIDs.

^cNo detections of NH and OH⁺.

Table 6.3: The determined total column densities of OTF observations. The $C^{18}O$ column densities are calculated from [Nürnberger et al. \(2002\)](#). The hydrogen column densities are calculated by using Eq. (6.7) (see text).

Cuts	Pos.	Vel. comp.	$N(C^{18}O)$ [10^{15} cm^{-2}]	$N(H_2)$ [10^{22} cm^{-2}]	$N(CH)$ [10^{15} cm^{-2}]	$N(C_2H)$ [10^{14} cm^{-2}]	$N(HCO^+)$ [10^{12} cm^{-2}]	$N(CS)$ [10^{12} cm^{-2}]
C1	1	1	1.05	0.79	0.06	0.54	0.36	0.28
	2	1	2.14	1.12	1.19	0.61	0.69	0.77
	3	1 st 2 nd	0.98	0.81	1.39 –	0.98 –	0.95 –	0.42 0.70
C2	1	1	1.05	0.78	0.06	0.54	0.36	0.28
	2	1	0.88	0.77	1.02	1.06	0.60	0.56
	3	1 st 2 nd	1.42	1.54	0.80 1.50	1.18 –	1.13 –	1.12 –
	4	1 st 2 nd	3.76	2.66	3.93 6.19	1.19 –	1.35 0.30	1.40 0.63
	5	1 st 2 nd	4.11	3.01	4.25 3.11	1.14 –	1.62 0.28	1.12 0.63
	6	1 st 2 nd	3.59	2.59	2.93 1.89	1.10 –	0.81 0.33	0.49 0.28
	7	1 st 2 nd	1.71	1.83	1.56 1.68	1.41 –	0.58 0.17	0.21 0.35
C3	1	1 st 2 nd	0.53	0.65	0.06 –	0.61 –	0.53 –	0.42 0.63
	2	1	2.14	1.12	1.19	0.61	0.69	0.77
	3	1 st 2 nd	0.71	0.84	6.86 6.20	0.71 –	0.74 –	0.77 –
	4	1 st 2 nd	0.65	1.23	2.44 3.31	0.99 –	0.85 0.30	1.47 –
	5	1 st 2 nd	3.28	2.65	1.71 1.04	0.99 –	1.45 0.40	2.24 0.42
	6	1 st 2 nd	2.98	2.82	2.17 3.33	0.88 –	1.60 0.48	1.89 0.49
	7	1 st 2 nd	3.20	2.73	1.91 3.80	0.78 –	1.04 0.36	0.98 0.28
	8	1 st 2 nd	2.19	1.93	3.34 3.88	0.73 –	0.55 0.18	0.42 0.28
	9	1 st 2 nd	2.00	1.56	5.80 5.11	1.39 –	0.27 0.09	0.35 0.42

Table 6.4: *The calculated fractional abundances from OTF observations.*

Cuts	Pos.	Vel. comp.	$X(\text{CH})$ [10^{-7}]	$X(\text{C}_2\text{H})$ [10^{-9}]	$X(\text{HCO}^+)$ [10^{-11}]	$X(\text{CS})$ [10^{-11}]	
C1	1	1	0.08	6.84	4.56	3.54	
	2	1	1.06	5.45	6.16	6.87	
	3	1 st	1.72	12.1	11.7	5.19	
		2 nd	–	–	–	8.64	
C2	1	1	0.08	6.84	4.56	3.54	
	2	1	1.32	13.8	7.79	7.27	
	3	1 st	0.52	7.66	7.34	7.27	
		2 nd	0.97	–	–	–	
	4	1 st	1.48	4.47	5.08	5.26	
		2 nd	2.33	–	1.13	2.37	
	5	1 st	1.41	3.79	5.38	3.72	
		2 nd	1.03	–	0.90	2.09	
	6	1 st	1.13	4.25	3.13	1.89	
		2 nd	0.73	–	1.27	1.08	
	7	1 st	0.85	7.70	3.17	1.15	
		2 nd	0.92	–	0.93	1.91	
	C3	1	1 st	0.09	9.38	8.15	6.46
			2 nd	–	–	–	9.69
2		1	1.06	5.45	6.16	6.87	
3		1 st	8.17	8.45	8.81	9.17	
		2 nd	7.38	–	–	–	
4		1 st	1.98	8.05	6.91	11.95	
		2 nd	0.39	–	2.44	–	
5		1 st	0.65	3.74	5.47	8.45	
		2 nd	1.18	–	1.51	1.58	
6		1 st	0.77	3.12	5.67	6.70	
		2 nd	1.39	–	1.70	1.74	
7		1 st	0.70	2.86	3.81	3.59	
		2 nd	2.01	–	1.32	1.03	
8		1 st	1.73	3.78	2.85	2.18	
		2 nd	3.28	–	0.93	1.45	
9		1 st	3.71	8.91	1.73	2.24	
		2 nd	0.85	–	0.58	2.69	

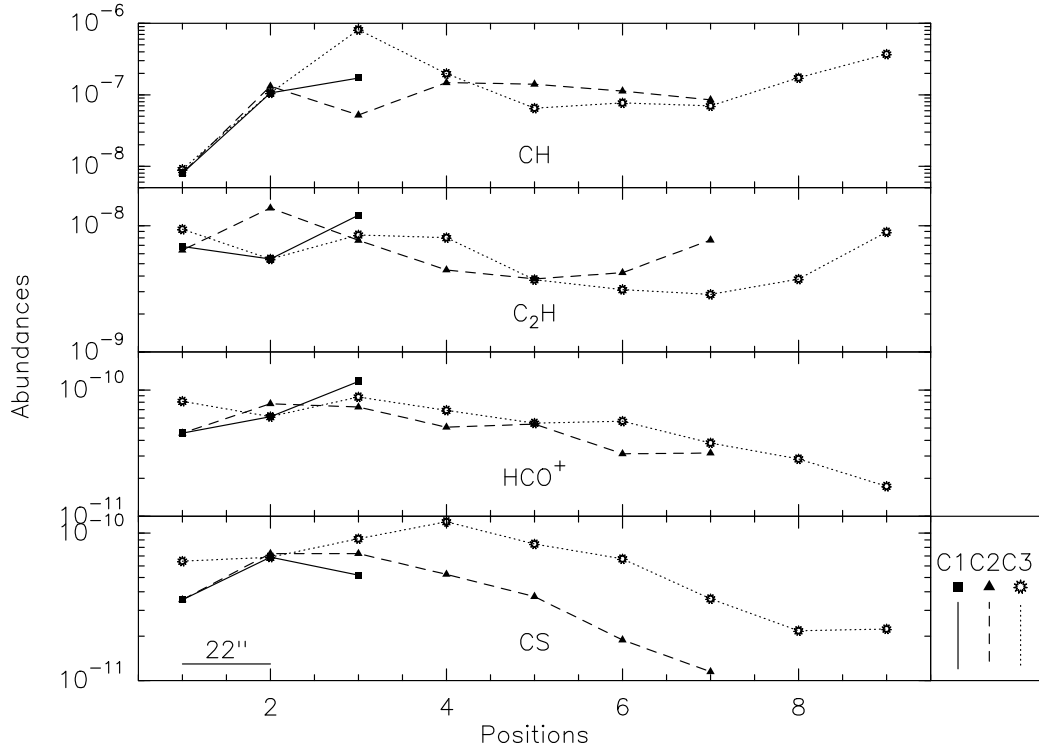


Figure 6.17: The derived fractional abundances along C1, C2 and C3.

6.5 Mass calculations

6.5.1 Total and virial gas masses

I derived the molecular hydrogen mass (M_{H_2}) along C1, C2 and C3 based on the derived H_2 column density. The mass can be calculated via

$$M_{\text{H}_2} = \frac{1}{1.9891 \times 10^{30} \text{ kg}} \left(\mu_{\text{H}_2} m_{\text{H}} \int N(\text{H}_2) dA \right) [M_{\odot}] \quad (6.10)$$

where $\mu_{\text{H}_2} \approx 2.8$ and m_{H} is the mass of hydrogen (1.67×10^{-27} kg). dA is the surface area of the molecular cloud which can be determined by $dA = D^2 d\Omega$ where D is the distance of the observed cloud and $d\Omega$ is the solid angle (I assumed beam filling factor of 1). Note that the gas in the interstellar medium is composed of other elements besides molecular hydrogen (helium and heavier species), thus total gas mass can be derived

$$M_{\text{gas}} = C_{\text{species}} \times M_{\text{H}_2} [M_{\odot}] \quad (6.11)$$

where $C_{\text{species}} = 1.36$ (Sheth et al., 2005; Shibatsuka et al., 2003). I also derived the virial mass of the cloud by

$$M_{\text{vir}} = \frac{5 R \sigma^2}{G} \quad [M_{\odot}] \quad (6.12)$$

where G is the gravitational constant ($G \approx 6.67 \times 10^{-11} \text{ m}^3 \text{ kg}^{-1} \text{ s}^{-2}$) and σ is the velocity dispersion of the cloud. I determined the velocity dispersion via $\sigma = FWHM/\sqrt{8 \ln 2}$ where $FWHM$ is the observed line width (I used HCO^+ line because it is the strongest line from HIFI map observations). R is an effective radius including the area of the cloud ($R = \sqrt{A/\pi}$). Note that the area can only be calculated roughly because the extension of a cloud depends on the observed species. The resulting virial masses are bigger than the values determined by [Nürnberg et al. \(2002\)](#) and [Röllig et al. \(2011\)](#) but the discrepancies are probably due to the different method of virial mass and cloud radius calculation, different beam sizes (they used smaller beam), and smaller line widths. The calculated virial parameters along the cuts suggest that the clumps are not in virial equilibrium ($M_{\text{vir}} > M_{\text{gas}}$). However, assuming that the clumps are in steady state, the clumps are probably still in virial equilibrium (or at least they are predominantly gravitationally bound) but the internal pressure is against the external pressure. This kind of clumps can be called as “pressure–confined clumps” ([Bertoldi & McKee, 1992](#)).

Virial parameter To investigate the importance of the gravitational and kinetic energy of the cloud, I determined the *virial parameter* ([Bertoldi & McKee, 1992](#); [Tatematsu et al., 1993](#)):

$$\alpha_{\text{vir}} = \frac{5 R \sigma^2}{GM_{\text{gas}}} = \frac{M_{\text{vir}}}{M_{\text{gas}}} \quad (6.13)$$

[Bertoldi & McKee \(1992\)](#) found, in cases of pressure–confined clumps, that the virial parameter is proportional to the gas mass, namely $\alpha_{\text{vir}} \approx M^{\epsilon}$ where $\epsilon \approx -0.67$. Figure 6.18 shows the correlation between the virial parameter and the derived total gas mass in both MM1 and MM2. The result ($\epsilon \approx -0.33 \pm 0.24$) is different from the theoretical prediction by $\sim 50\%$. This discrepancy originates from the big deviation of data points. The scattering of data points may be caused by, for example, calculation of velocity dispersion (σ) and the determination of effective radius ($R = \sqrt{A/\pi}$). Because the derivation of the area (A) is strongly dependent on the used species plus $M_{\text{vir}} \propto \sigma^2$ and $M_{\text{vir}} \propto R$, the error could be high at the end. Furthermore, because $M_{\text{gas}} \propto D^2$, the distance calculation can yield to additional error. The calculated parameters are in Tab. 6.6.

Table 6.5: *The results of Jeans mass derivations at different densities and temperatures. The unit of Jeans–mass is in M_{\odot}*

n [cm^{-3}]	T [K]	20	50	100	200	500
10^3		~ 66	~ 259	~ 732	~ 2073	~ 8193
10^4		~ 21	~ 82	~ 232	~ 655	~ 2591
10^5		~ 7	~ 26	~ 73	~ 207	~ 819
10^6		~ 2	~ 8	~ 23	~ 66	~ 259
10^7		~ 1	~ 3	~ 7	~ 21	~ 82

6.5.2 Jeans mass

Star formation needs cold and dense molecular cores. These dense cores come into existence when the gravitational force exceeds the internal (thermal) gas pressure of the parent molecular cloud. The molecular cloud is stable until its gas mass gets to a critical value (which depends on temperature and density). If this critical mass is reached, the contraction of molecular cloud, or part of it, begins. This critical mass is called Jeans mass and it can be derived as

$$M_J = \frac{1}{1.9891 \times 10^{30} \text{ kg}} \left(\frac{5kT}{G\mu m_H} \right)^{3/2} \left(\frac{3}{4\pi\rho_0} \right)^{1/2} [M_{\odot}] \quad (6.14)$$

where $k = 1.38 \times 10^{-23} \text{ kg m}^2 \text{ s}^{-2} \text{ K}^{-1}$ is the Boltzmann-constant, T is the gas temperature in Kelvin, $G \approx 6.67 \times 10^{-11} \text{ kg}^{-1} \text{ m}^3 \text{ s}^{-2}$ is the universal gravitational constant, $\mu = 2$ is the mean molecular weight, $m_H = 1.67 \times 10^{-27} \text{ kg}$ is the mass of hydrogen and $\rho_0 = \mu m_H n(H_2)$ is the density.

For the gas volume density, I combined the previous data from [Röllig et al. \(2011\)](#) ($n \sim 10^3 - 10^4 \text{ cm}^{-3}$) and the assumption that gas has to be very dense ($n \sim 10^7 \text{ cm}^{-3}$) for the appearance of high- J ^{12}CO lines ($J \rightarrow J - 1 \gtrsim 13 \rightarrow 12$). Thus, I computed the Jeans mass at various gas densities ($n \sim 10^3 - 10^7 \text{ cm}^{-3}$) and temperatures (20, 50, 100, 200 and 500 K). The results are in Tab. [6.5](#).

All the deeper parts where the density increases and temperature goes down, the derived Jeans masses are smaller than the derived virial and gas masses. Our results are in agreement with previous studies [e.g. ([Nürnberg et al., 2002](#); [Röllig et al., 2011](#))], namely that the observed molecular clouds, or part of them, are in gravitationally unstable stage which leads to fragmentation and cloud collapse that can trigger star formation.

Table 6.6: *The derived masses and virial parameter along the cuts.*

Cuts	Positions	M_{H_2} [M_{\odot}]	M_{gas} [M_{\odot}]	M_{vir} [M_{\odot}]	α_{vir}
C1	1	329	449	1106	2.47
	2	467	634	1402	2.21
	3	337	459	2539	5.53
C2	1	329	449	1106	2.47
	2	321	436	4272	9.79
	3	641	872	5307	6.08
	4	1108	1507	5381	3.57
	5	1254	1705	4944	2.90
	6	1079	1467	4593	3.13
	7	762	1037	7580	7.31
C3	1	271	368	1411	3.83
	2	467	634	1402	2.21
	3	350	476	1895	3.98
	4	512	697	3727	5.35
	5	1104	1501	3696	2.46
	6	1175	1597	2964	1.86
	7	1137	1547	2301	1.49
	8	804	1093	2007	1.84
	9	650	884	7274	8.23

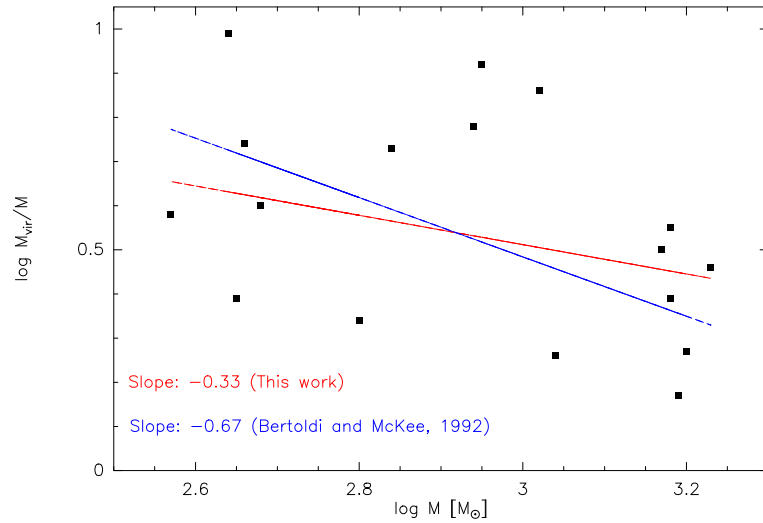


Figure 6.18: *Correlation between the derived virial parameter and gas mass. The filled squares represent the points from C1, C2 and C3. The solid red line is the fit to the data points. The power law index is -0.33 ± 0.24 . The blue line represents the power law index $\epsilon = -0.67$.*

6.6 Summary

The CS ($11 \rightarrow 10$) line is peaked slightly closer to the surface area of the observed clumps than HCO^+ ($6 \rightarrow 5$) transition which is expected if we take into account that: 1) CS needs higher temperature to be excited and 2) the surface area is heated more than the deeper part of the molecular clumps. We likely observed small and dense cores traced by CS which are surrounded by HCO^+ .

The hyperfine components of diffuse gas tracers are also well correlated in both observed clumps. In cases of the diffuse gas tracers, the velocities of the intensity peaks are shifted as a function of the projected cloud depth. This velocity trend is significant and may indicate that the outskirts of the observed clumps are influenced by stellar winds which is supported by the distribution of the CH. C_2H represents the less dense gas and relatively hot material layers which are probably influenced by stellar winds.

The $63\ \mu\text{m}$ and $145\ \mu\text{m}$ [OI] lines nicely follow the pillar-like structures, visible in optical regime, in both MM1 and MM2. In MM1, the [OI] line represents a sharp intensity distribution which probably coincides with the cavity wall.

The [NII] line ($57\ \mu\text{m}$), together with the [OIII] ($88\ \mu\text{m}$) line, is widely spread out in both clumps which suggest the existence of optically thin diffuse gas. All the high- J ^{12}CO lines (from $13 \rightarrow 12$ to $16 \rightarrow 15$) are well correlated with the aforementioned pillar-like structures in MM1 and MM2. The intensity distributions of the $^{12}\text{C}^+$ lines weakly match with the position of pillar in MM1. In MM2, its bright limb coincides with an already identified shock front.

As the intensity distributions of the cooling lines follow the pillars in MM1 and MM2, these observations support the scenario, namely that the cooling lines ([OI], [OIII] and high- J ^{12}CO lines) are expected to be good tracers of pillars.

In both clumps, the water line ($1_{10} \rightarrow 1_{01}$) was detected far from the central cluster indicating that it traces a moderately warm but dense gas layer. The ^{12}CO ($9 \rightarrow 8$) line coincides with the o- H_2O line in both MM1 and MM2, suggesting that these species trace the same moderately warm gas. The broad ^{12}CO and ^{13}CO lines implies the presence of either spectrally unresolved velocity components or turbulent gas motions inside the clumps. The intensity peak of ^{13}CO transition is peaked closer to the cloud surface than ^{12}CO which is probably caused by a temperature gradient. In MM1, the intensity peak of the $^{12}\text{C}^+$ is shifted far from the central UV source. In contrast to MM1, it shows a complex intensity distribution and a ring-like structure in MM2. The ring-like structure indicates a small cavity or bubble inside MM2.

The observed broad wing on the blue side of the para-water line may be a sign of a shock front.

The calculated averaged kinematic distance of NGC 3603 is ~ 7.3 kpc which is in good agreement with previous derivations.

I assumed an excitation temperature of 50 K and I calculated column densities. The derived $N(\text{H}_2)$ in MM1 and MM2 ($\sim 1 - 2 \times 10^{22} \text{ cm}^{-2}$) are in good agreement with previous calculations.

Rotational diagrams were used to derive the rotational temperature (assuming LTE). The gas in MM1 and MM2 is consist of a moderately warm (~ 60 K in MM1 and ~ 50 K in MM2), traced by the transitions of ^{12}CO ($4 \rightarrow 3, 7 \rightarrow 6$ and $9 \rightarrow 8$), and a warmer gas (~ 170 K in both clumps), traced by the transitions of ^{12}CO ($13 \rightarrow 12$ to $16 \rightarrow 15$).

I found that the observed clumps are not in virial equilibrium. The Jeans mass calculations suggest that the observed clumps, or part of them, are in gravitationally unstable stage. This leads to the fragmentation and collapse of the clouds, hence this result in agreement with previous statements, namely the star formation is an ongoing process in MM1 and MM2.

To check the consistency between the observational results and theories, I compared our results with model calculations. In the next chapter, I shall present the model results.

7.1 Theory

To interpret the observed emissions from PDRs, I compared the observational data with model calculations. With this, detailed studies of physical conditions [via radiative transfer codes: e.g. RADEX (van der Tak et al., 2007) and RATRAN (Hogerheijde & van der Tak, 2000) which are non-LTE codes] and chemical properties (via chemical models) of PDRs are possible. There are a number of different models that can be used for investigation of the previously mentioned processes. In PDR models, basically, two setups are used for the cloud geometry¹: a 1-D plane-parallel approach where the modelled gas is illuminated either unidirectionally or isotropically [e.g. Meudon (Goicoechea & Le Bourlot, 2007; Le Petit et al., 2006)] and a spherical approach where the radiation is assumed to be isotropic [e.g. KOSMA- τ (Röllig et al., 2006; Stoerzer et al., 1996)] (Fig. 7.1). For studying the possible chemical reactions and networks in PDRs, two common approaches are used: “time-dependent chemistry” when the chemical reaction time scale is longer than the time scale of radiation field and/or density change. In contrast with time dependent chemistry, in the “steady-state chemistry” chemical reactions have shorter time scale than the time scale of radiation change. A well detailed study and comparison of different PDR models can be found in e.g. Röllig et al. (2007).

In this thesis, I used the RADEX code and the KOSMA- τ PDR model (model results are also available by online²). In the following, I give a very brief introduction of the physical and chemical setups of these models.

¹These simplifications also make the radiative transfer problem easier solvable.

²<http://www.astro.uni-koeln.de/~pdr>

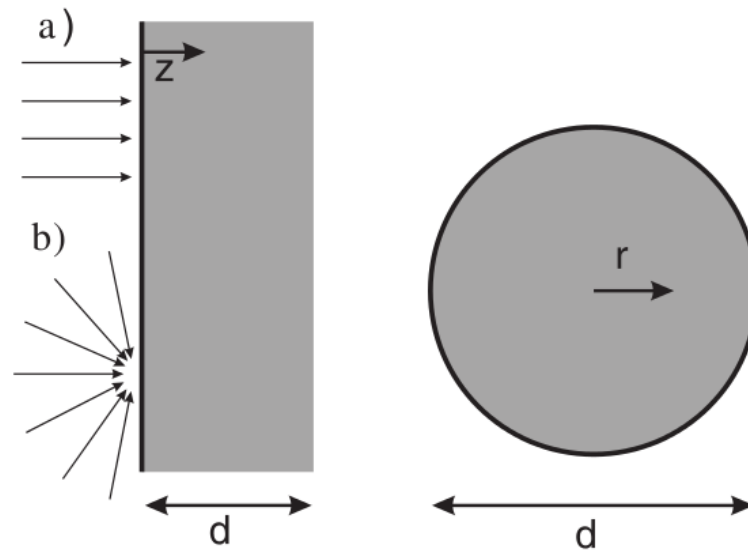


Figure 7.1: *The geometrical simplifications in PDR models from Röllig et al. (2007). Left panel: The 1-D plan-parallel approach where the slab can be radiated unidirectionally (a) or isotropically (b). Right panel: The spherical approach where the radiation field is isotropic.*

7.1.1 The RADEX code

RADEX³ (van der Tak et al., 2007) is a non-LTE code which calculates the atomic and molecular line intensities assuming isothermal and homogeneous medium with no large-scale velocity fields. It uses statistical equilibrium (including both collisional and radiative processes) and escape probability methods (for optical depth effects). The code can be used for any species which have collisional rate coefficients available. For RADEX, these rate coefficients and other spectroscopic data are provided by LAMDA database⁴ (Schöier et al., 2005).

To derive the line intensities, RADEX solves the radiative transfer equation (Section 2.3) while the excitation temperature is defined as in Section 2.3 (Eq. 2.15). The radiative transfer equation can be solved if we know the level population (under LTE conditions). On the other hand, statistical equilibrium can be a good approach for solve the rate equation if LTE cannot be used (for example, the density is too low):

³It is available from <http://www.sron.rug.nl/~vdtak/radex/index.shtml>

⁴<http://www.strw.leidenuniv.nl/~moldata>

$$\frac{dn_i}{dt} = 0 = \underbrace{\sum_{j \neq i}^N n_j P_{ji}}_{\text{formation}} - n_i \underbrace{\sum_{j \neq i}^N P_{ij}}_{\text{destruction}} \quad (7.1)$$

where P_{ij} and P_{ji} are the destruction and formation rate coefficients of level i . The formation rate coefficient includes the specific intensity averaged from all directions which means that Eq. 7.1 involves non-local radiation effects, too.

Assuming that the investigated source has a simple geometry (i.e., homogeneous sphere) the solution of radiative transfer can be simplified with escape probability $[\beta(\tau)]$ which describes the probability that a photon can escape from the place where it was generated. The escape probability can be expressed, assuming homogeneous and spherically symmetric medium, as (Osterbrock & Ferland, 2006; van der Tak et al., 2007):

$$\beta = \frac{1.5}{\tau} \left[1 - \frac{2}{\tau^2} + \left(\frac{2}{\tau} + \frac{2}{\tau^2} \right) e^{-\tau} \right] \quad (7.2)$$

where τ is the optical depth at the line center and it depends on the line width, column density and the level population.

The input parameters (after the name of the molecular data file and the output file name) are: frequency range in GHz (in general, all transitions of a species are taken into account), kinetic temperature in K, the number of collisional partner (the code can handle up to 7 collisional partners simultaneously), the name and density of the collisional partner in cm^{-3} (we can choose other partners, not only H_2 ; e.g., atomic hydrogen or electrons), the temperature of the background radiation field in K, the column density of the molecule in cm^{-2} , and the line width in km s^{-1} .

7.1.2 The KOSMA- τ PDR model

This model, which is an updated version of a PDR model described by Stoerzer et al. (1996), provides: 1) spherical geometry, 2) possibility to put (or remove) new species to (or from) the chemical network and the chemical network will immediately be updated, 3) chemistry of different isotopologues, 4) modelling clumpy clouds (Cubick et al., 2008). Once the chemical and physical structure of the model cloud is “known”, emission line strength is calculated by radiative transfer code (Röllig et al., 2013).

Each clump is characterized by four parameters, namely: n (total gas density at the surface of the cloud in cm^{-3}), M (clump mass in solar mass), χ_D

(FUV intensity in units of the Draine field) and Z (metallicity). The radial density profile of a modelled clump is assumed (Cubick et al., 2008; Röllig & Ossenkopf, 2013):

$$n(r) = n_0 \left(\frac{r}{R_{\text{clump}}} \right)^{-\alpha} \quad (R_{\text{core}} \leq r \leq R_{\text{clump}}) \quad (7.3a)$$

$$n(r) = \text{const.} \quad (0 \leq r \leq R_{\text{core}}) \quad (7.3b)$$

where n_0 is the total number density of hydrogen nucleus at the clump surface ($n_0 = n_H + 2n_{H_2}$), R_{core} is the radius of the inner core which is 20% of the clump radius ($R_{\text{core}} = 0.2R_{\text{clump}}$) and $\alpha = 1.5$ is the power-law index. When assuming a clumpy composition of model clouds, the distribution of the clump mass is expressed as (Cubick et al., 2008; Ossenkopf et al., 2010b):

$$\frac{dN}{dM} = AM^{-\beta} \quad (7.4)$$

where dN is the number of clumps within a mass bin dM , A is a proportionality constant, M is the mass of the clump ($M \propto R_{\text{clump}}$) and β is a power-law index that is related to the fractal structure of ISM (Stutzki et al., 1998). This model uses $\beta = 1.8$ based on the results in Heithausen et al. (1998).

The KOSMA- τ PDR model is using 21 cooling and heating processes. The most important cooling processes are the gas–grain collisions [at high density, see more in Burke & Hollenbach (1983); Stoerzer et al. (1996); Röllig et al. (2006)] and cooling via fine structure lines of [CII], and [OI].

The most important heating processes are the photo-electric heating of grains, collisional de-excitation of H_2^* and H_2 formation heating [at relatively weak FUV radiation ($\chi_D < 10^3$) and low density ($n < 10^4 \text{ cm}^{-3}$)]. The total heating rate can be expressed as (Röllig et al., 2006):

$$\Gamma_{\text{tot}} \approx \Gamma_{\text{pe}}^{\text{net}} + \Gamma_{\text{H}_2}^{\text{net}} + \Gamma_{\text{H}_2\text{-formation}} \quad (7.5)$$

where $\Gamma_{\text{pe}}^{\text{net}} = \Gamma_{\text{pe}} - \Lambda_{e\text{-rec}}$ (the second term is the cooling rate because of electron recombination) and $\Gamma_{\text{H}_2}^{\text{net}} = \Gamma_{\text{H}_2^*} - \Lambda_{\text{H}_2}$ [because hydrogen is not only important in heating processes but, at high temperature, in cooling too (Sternberg & Dalgarno, 1989; Röllig et al., 2006)].

A pure gas-phase steady–state chemistry is assumed in this PDR model [except hydrogen formation on grains (Röllig et al., 2006; Sternberg & Dalgarno, 1995)]. The density change of any given species i can be formulated as

$$\frac{dn_i}{dt} = \overbrace{\sum_j \sum_k n_j n_k R_{jki} + \sum_l n_l \zeta_{li}}^{\text{formation processes}} - n_i \underbrace{\left(\sum_l \zeta_{il} + \sum_l \sum_j n_j R_{ijl} \right)}_{\text{destruction processes}} \quad (7.6)$$

which is the balance equation that has to be solved for the solution of the chemical network. In this differential equation R_{jki} and R_{ijl} are reaction rate coefficients (e.g., for reaction $X_j + X_k \rightarrow X_i + \dots$ where X could be any species), ζ_{li} and ζ_{il} are the rate coefficients of the local photo-reactions (ionization or dissociation caused by either cosmic rays or FUV photons). If $dn_i/dt = 0$, it is called stationary chemical model. The rate coefficients can be obtained via different and numerous databases such as the UMIST⁵ database for astrochemistry (Woodall et al., 2007).

7.2 Results

Because I want to deduce the main and prominent physical conditions of the PDRs in NGC 3603, I had to carefully choose species that I would like to model to be able to receive a complete picture. I selected ^{12}CO , ^{13}CO , C, [CII] and [OI] for the following reasons (very briefly):

CO

Carbon monoxide is, after H_2 , the most abundant species in the gas-phase interstellar medium and it cools down the gas via its rotational transition lines (Fuente et al., 2012). ^{12}CO and ^{13}CO are ubiquitously used as a tracer of O, H_2 (Ripple et al., 2013; Liseau et al., 2010), and globules (Haikala et al., 2006). ^{12}CO can easily be collisionally excited and thermalized (due to its low dipole moment ~ 0.1 Debye), hence it can be used to investigate the kinetic gas temperature (Ridge et al., 2003; San Jose-Garcia et al., 2013). The high rotational lines of ^{12}CO are good PDR tracers (Ossenkopf et al., 2010b; San Jose-Garcia et al., 2013) but can also be used to investigate molecular outflows (Bjerkeli et al., 2013), temperature and density structure of a cloud (Haikala et al., 2006). In contrast to the higher rotational lines, the low- J lines of ^{12}CO and ^{13}CO are widely used to study dense but cold cores (Tachihara et al., 2002; Schneider et al., 2011). ^{13}CO can be used as a tracer of dense part of molecular clouds (Glenn & Hunter, 2001) as well as outflows from cavity walls and extended envelopes (Graves et al., 2010; Yıldız et al., 2012).

⁵<http://ape.jb.man.ac.uk/udfacn/>

[CI], [CII], [OI]

Atomic carbon is an important species in the physical and chemical processes within molecular clouds (Minchin et al., 1994). It is used to investigate the warm and dense gas (Israel et al., 2014), and the surface of FUV illuminated clumps (Hitschfeld et al., 2008). Its abundance ratio with ^{12}CO has widely been investigated so far (Keene et al., 1985; Phillips & Huggins, 1981; Wootten et al., 1982). Interestingly, based on these studies, the $[\text{CI}]/^{12}\text{CO}$ ratio is relatively high (≥ 0.1) suggesting the presence of atomic carbon not only on the surface, but deeper part of the clumps [e.g. Kramer et al. (2008)]. These observational results are in conflict with steady-state chemical models of PDRs which predict high $[\text{CI}]$ abundance close to the surface of a cloud (due to photo-dissociation of ^{12}CO).

The ionized carbon lines are the strongest cooling lines of the interstellar medium (Venemans et al., 2012), even in the less dense PDRs (Abel, 2006; Abel et al., 2005; Heiles, 1994; Kaufman et al., 2006; Matsuhara et al., 1997). Usually, it is optically thin (Abel et al., 2007; Stacey et al., 2010) but not in all cases (Vastel et al., 2003). Due the lower ionization potential compared to hydrogen [11.26 eV, (Vastel et al., 2003)], ionized carbon can exist in both ionized and neutral hydrogen regions (Mizutani et al., 2004) at low visual extinction (Röllig et al., 2006).

Just like $[\text{CII}]$, the $[\text{OI}]$ $63\ \mu\text{m}$ line is also an important and strong cooling line of warm and high density regimes (Röllig et al., 2006). This cooling line is presented in intermediate warm interstellar medium and shocks (Aannestad, 1973) as well as in the deeper part of PDRs (Melnick et al., 1979). This line is easier to detect than the $146\ \mu\text{m}$ line of $[\text{OI}]$ (Abel et al., 2007). The neutral oxygen and ionized carbon are useful diagnostic tools for the estimation of the temperature and density of the emitting regions (Liseau et al., 2006).

I picked the species from the interfaces of MM1 and MM2. These thin layers (compared to the size of the whole molecular cloud) are likely the edge of the HII cavity (located around the central OB cluster), and transient regions between the ionized and molecular gas. The two points coincide with the Herschel point observations of MM1-IF (observational IDs are 1342223428 and 1342223430) and MM2-IF (observational IDs are 1342223429 and 1342225899); see Tab. 3.2 and Fig. 3.6.

7.2.1 RADEX

I modelled our observed line intensities using a two-ensemble non-LTE model. Because the lower transitions of ^{12}CO line can easily be optically thick, I assumed optically thick emissions for transitions ($4 \rightarrow 3$), ($7 \rightarrow 6$) and moderate optical thickness for ($9 \rightarrow 8$), unity beam filling, and, as one of an input parameter, I tuned the background radiation temperature to

Table 7.1: *The best fit results from RADEX code. The $N(^{13}\text{CO})$ column densities are calculated assuming $^{12}\text{C}/^{13}\text{C} = 67$.*

Component	T_{kin} [K]	$n(\text{H}_2)$ [cm^{-3}]	$N(^{12}\text{CO})$ [cm^{-2}]	$N(^{13}\text{CO})$ [cm^{-2}]
MM1-IF				
Mod. warm	30	9×10^4	8×10^{18}	1.2×10^{17}
Warm	520	1.1×10^5	1.0×10^{15}	1.0×10^{15}
	170	1.0×10^7	1.0×10^{15}	
MM2-IF				
Mod. warm	43	9×10^3	6×10^{18}	9.0×10^{16}
Warm	420	3.0×10^5	1.1×10^{15}	1.6×10^{13}
	180	1.0×10^7	1.8×10^{15}	2.7×10^{13}

2.725 K. Figures 7.2 and 7.3 show the best fit results.

The ^{12}CO line intensities are fitted well, while big difference occur between model and observation of ^{13}CO in both cases MM1-IF and MM2-IF. Figure 7.3 represents the best fit results for the fine-structure lines in MM1-IF and MM2-IF. With the moderately warm component (filled blue squares), I was able to reproduce the line intensities of atomic and ionized carbon, and only [C I] (610 μm) emission was slightly underestimated by the model in MM2-IF. The [O I] (145 μm) line is fitted well by assuming warm component [$T = 520$ K and $T = 170$ K (MM1-IF; turquoise and purple squares, respectively); $T = 420$ K and $T = 180$ K (MM2-IF; turquoise and purple squares, respectively)]. The parameters, correspond to the best fit results, can be found in Tab. 7.1.

7.2.2 KOSMA- τ

First, I modelled the observed ^{12}CO line intensities. From the observed transitions, ($4 \rightarrow 3$) and ($7 \rightarrow 6$) are from previous studies (Röllig et al., 2011), ($9 \rightarrow 8$) is HIFI, and the high- J transitions are PACS observations (from $13 \rightarrow 12$ to $16 \rightarrow 15$). I also tried to model ^{13}CO line intensities but I only have one rotational transition ($10 \rightarrow 9$). On the other hand, it is particularly interesting to investigate the abundance ratio of $^{12}\text{C}/^{13}\text{C}$ which reflects the gas temperature (Röllig & Ossenkopf, 2013). Table 7.2 includes the observed line intensities, that I used for modelling, convolved to the beam size $43''5$. I assumed a general 30% error for the data points (Fig. 7.4 to 7.3) due to HIFI and PACS flux uncertainties, unit and beam conversions. Figure 7.4 shows the observed ^{12}CO and ^{13}CO line intensi-

Table 7.2: *Integrated line intensities of the selected lines for KOSMA- τ model. The intensities are convolved to beam size $43''5$.*

Species	Transition	Intensities [K km s^{-1}]	
		MM1-IF	MM2-IF
^{12}CO	4 \rightarrow 3	90.59	138.71
	7 \rightarrow 6	54.33	78.25
	9 \rightarrow 8	17.76	11.00
	13 \rightarrow 12	1.00	2.20
	14 \rightarrow 13	0.85	1.56
	15 \rightarrow 14	0.66	1.17
	16 \rightarrow 15	0.33	0.75
^{13}CO	10 \rightarrow 9	1.33	1.88
C^+	1 \rightarrow 0	3.90	9.57
O	1 \rightarrow 2	4.65	6.28
	0 \rightarrow 1	1.52	3.74
C	1 \rightarrow 0	8.16	15.69
	2 \rightarrow 1	3.25	6.73

ties (filled red and turquoise squares, respectively) and the best fit model results (filled blue and purple squares).

As a first approach, I assumed non-clumpy (one sphere that fills the beam) and clumpy (many different spheres that fill the beam) molecular cloud to fit the observed line intensities. Based on the investigations of the model results (gas volume density, gas mass and FUV-field strength; Tab. 7.3), I concluded that both cases fit the data equally well. This result is probably caused by beam dilution effect.

In both cases, I was able to fit the observed ^{12}CO line intensities with two ensembles: a moderately warm component which occupies a larger fraction of the beam (see beam filling factor f in Tab. 7.3), thus contributes most of the gas mass, and a warmer component with a small fraction of gas mass (because of the minor fraction of full beam size). The model points for ^{13}CO lines were calculated using the elemental abundance ratio $[^{12}\text{C}]/[^{13}\text{C}] = 67$ (Röllig & Ossenkopf, 2013). It is evident from the plots, that the model underestimates the line intensity of the ^{13}CO line with the used elemental ratio.

Figure 7.5 shows the best fit result for the fine-structure lines. The model slightly underestimates [OI] ($63 \mu\text{m}$) and [CI] ($610 \mu\text{m}$) in MM1-IF. In case of MM2-IF, all fine-structure lines were fitted well (within the 30% uncertainty).

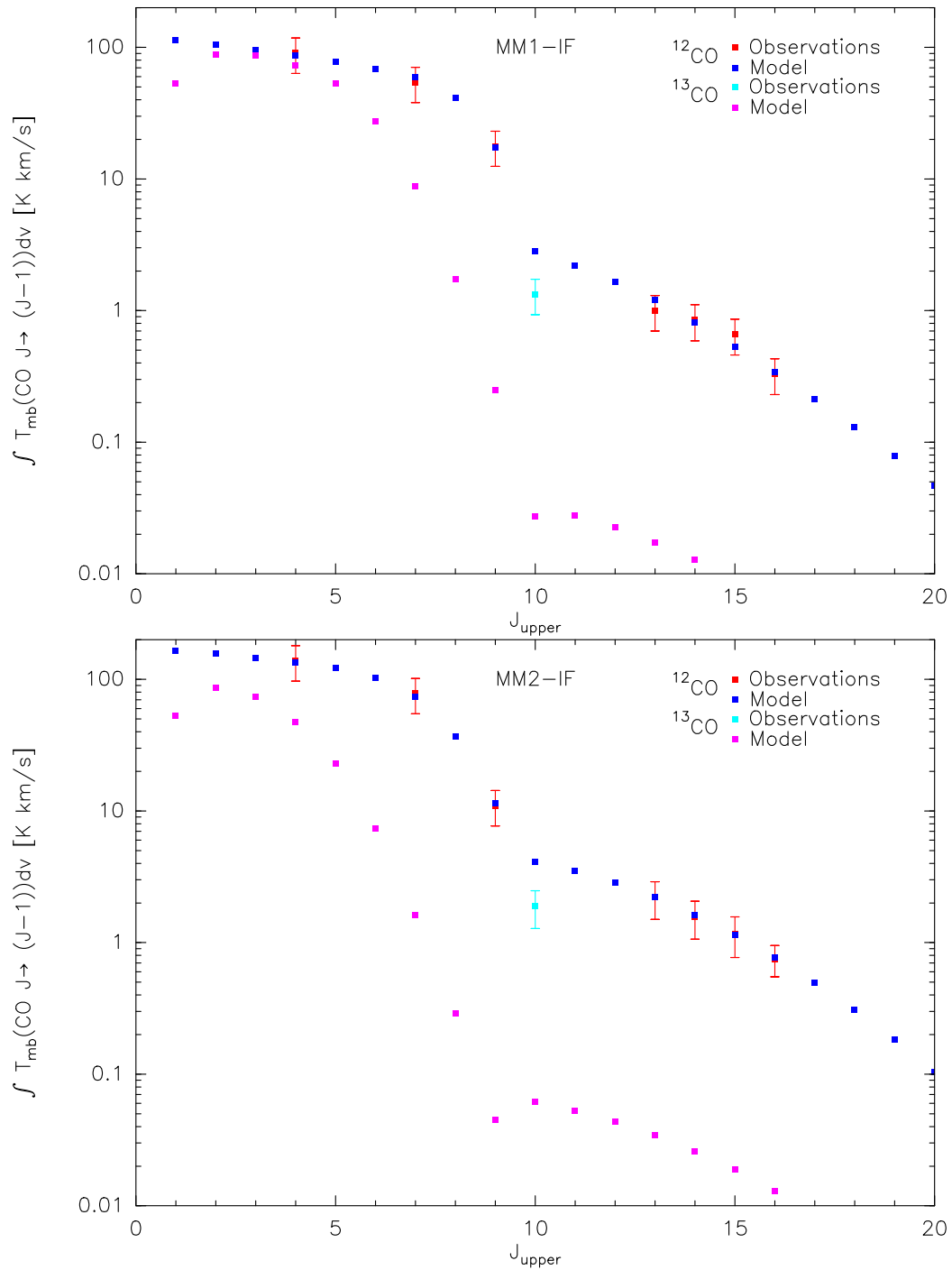


Figure 7.2: The fitted line intensities using RADEX model in MM1-IF and MM2-IF.

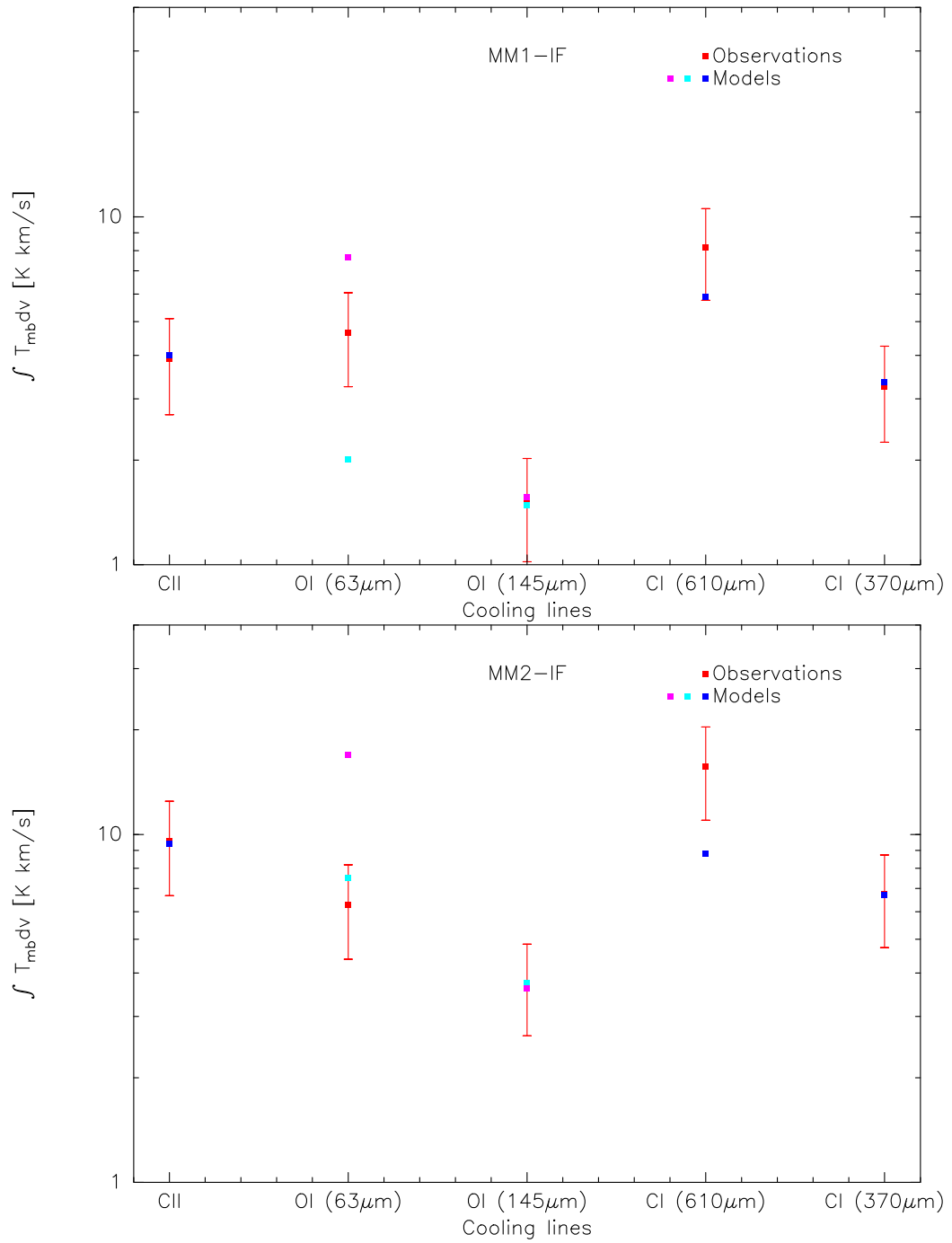


Figure 7.3: The fitted line intensities of cooling lines using RADEX model in MM1-IF and MM2-IF.

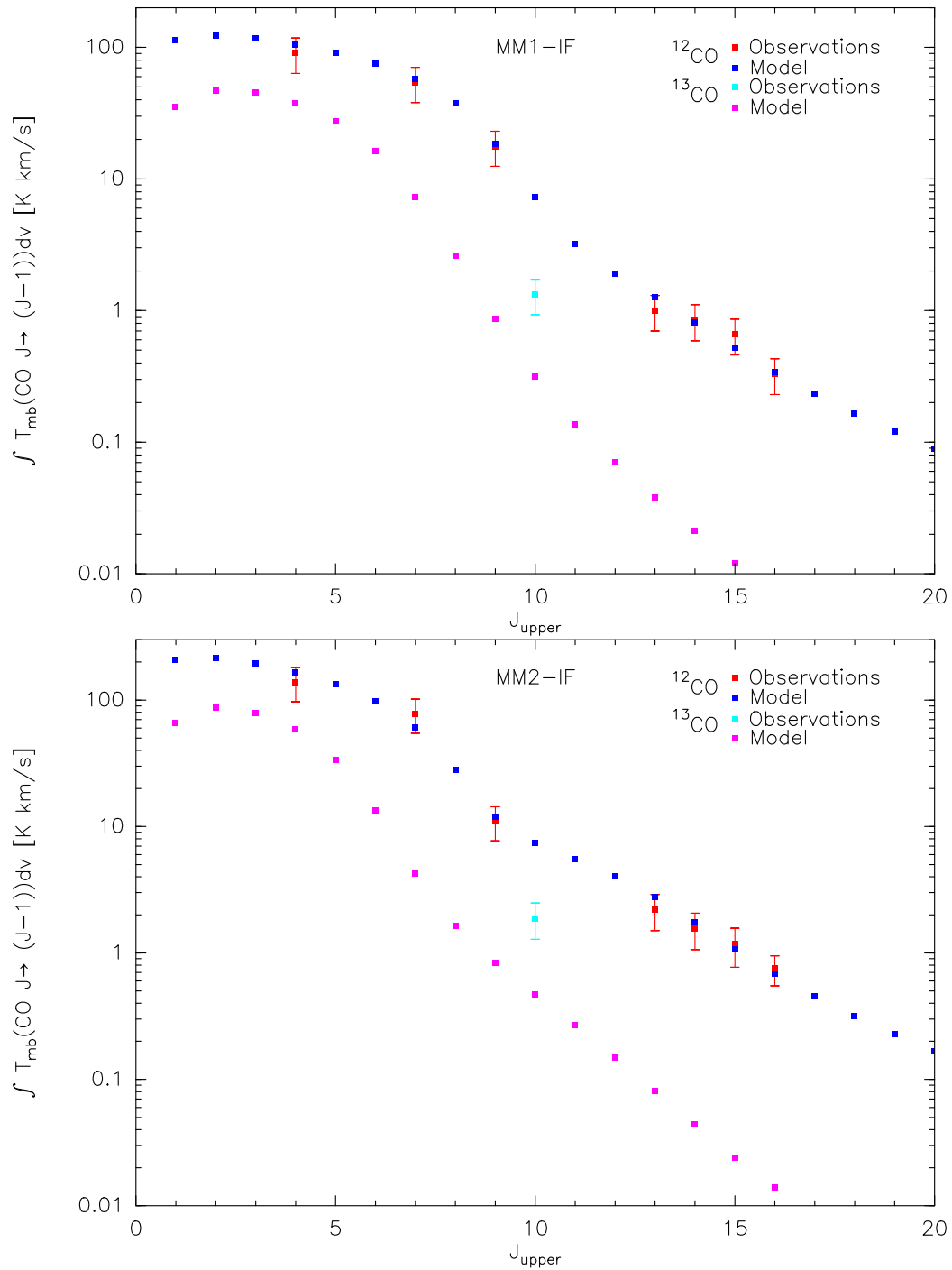


Figure 7.4: The fitted line intensities using $\text{KOSMA-}\tau$ clumpy model in MM1-IF and MM2-IF.

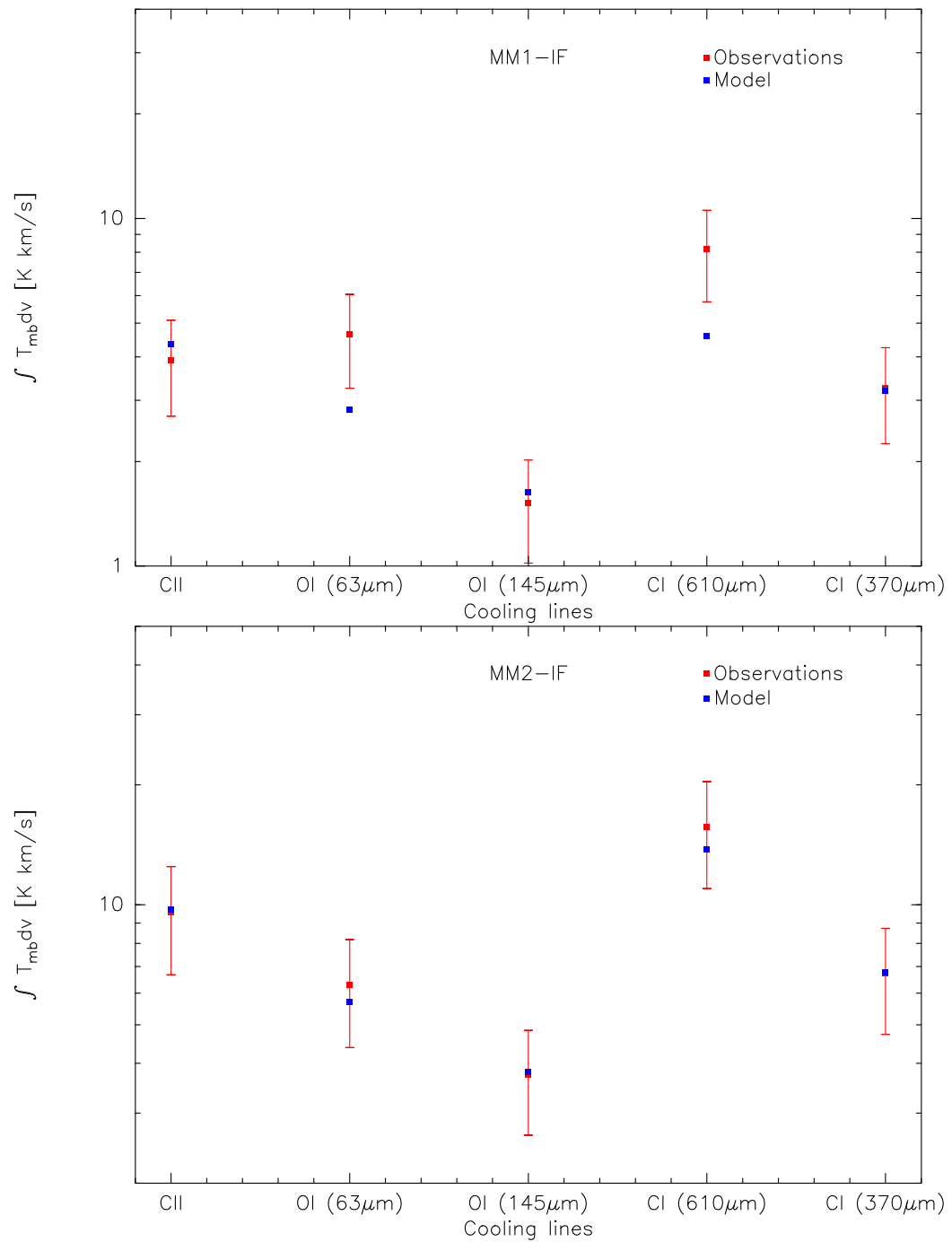


Figure 7.5: The fitted line intensities of cooling lines using *KOSMA-T* clumpy model in MM1-IF and MM2-IF.

Table 7.3: *The output parameters from KOSMA- τ model for MM1-IF and MM2-IF, in both cases of cool and warm components.*

MM1-IF								
Components	Non-clumpy				Clumpy			
	n [cm^{-3}]	M [M_{\odot}]	χ_D	f	$\langle n \rangle$ [cm^{-3}]	M [M_{\odot}]	χ_D	f
Mod. warm	$10^{5.7}$	$10^{3.0}$	$10^{1.2}$	0.76	$10^{5.8}$	$10^{3.2}$	$10^{1.4}$	0.78
Warm	$10^{5.8}$	$10^{2.5}$	$10^{3.5}$	0.01	$10^{5.6}$	$10^{2.3}$	$10^{3.5}$	0.10

MM2-IF								
Components	Non-clumpy				Clumpy			
	n [cm^{-3}]	M [M_{\odot}]	χ_D	f	$\langle n \rangle$ [cm^{-3}]	M [M_{\odot}]	χ_D	f
Mod. warm	$10^{5.0}$	$10^{3.0}$	$10^{1.1}$	0.99	$10^{5.0}$	$10^{3.2}$	$10^{1.0}$	0.61
Warm	$10^{5.8}$	$10^{1.9}$	$10^{3.6}$	0.03	$10^{5.6}$	$10^{2.3}$	$10^{3.4}$	0.26

7.3 Summary

I compared the observed data with theoretical predictions/calculations. For this, I used two models: a non-LTE, radiative modelling with the RADEX code and a PDR modelling with the KOSMA- τ model. For the comparisons, I used ^{12}CO ($4 \rightarrow 3$, $7 \rightarrow 6$, $9 \rightarrow 8$ and from $13 \rightarrow 12$ to $16 \rightarrow 15$), ^{13}CO ($10 \rightarrow 9$), [OI] ($63 \mu\text{m}$ and $145 \mu\text{m}$), [CI] ($610 \mu\text{m}$ and $370 \mu\text{m}$) and [CII] ($158 \mu\text{m}$) lines.

I fitted the observed ^{12}CO lines well with two ensembles (a cool component with an almost unity beam filling and a warm component which occupies only a small fraction of the beam). I fitted the observed ^{13}CO line intensity with the widely used elemental abundance ratio of $[^{12}\text{C}]/[^{13}\text{C}] = 67$ but, with this ratio, the intensity is strongly underestimated. The model was able to fit well the cooling line intensities except [OI] ($63 \mu\text{m}$) and [CI] ($610 \mu\text{m}$) transitions in MM1, where these lines were also slightly underestimated.

I also modelled the observed line intensities with a two-ensemble non-LTE model, using the RADEX code. Likewise with KOSMA- τ , the ^{12}CO and the cooling lines were fitted well [except [OI] ($63 \mu\text{m}$) line]. In case of ^{13}CO line, I received a huge discrepancy (using the same elemental abundance ratio). The result temperature for the moderately warm component is 30 K [with density of $n(\text{H}_2) \approx 10^5 \text{ cm}^{-3}$] in MM1-IF. In case of the warm component, I fitted the lines with a less dense [$n(\text{H}_2) \approx 10^5 \text{ cm}^{-3}$] but very warm ($\sim 500 \text{ K}$) and with a denser [$n(\text{H}_2) \approx 10^7 \text{ cm}^{-3}$] but a bit less warm ($\sim 200 \text{ K}$) gas.

In the next chapter, I shall discuss all of the observational results that I already received and try to describe the prominent physical conditions and chemical processes trusting to our final goal which is to provide a simple but complete picture of NGC 3603.

Interpretation and discussion

In the previous chapters, I presented our observational results based on the large set of data provided by the Herschel Space Observatory. In this chapter, I try to find solutions that can help to explain the observed phenomena and can lead to the better understanding of the physical and chemical conditions in NGC 3603.

8.1 Gas motions

8.1.1 Signatures of turbulence

Taking into account one velocity component, most of the observed lines are relatively broad (the “lower limit” is $\sim 2 \text{ km s}^{-1}$ while the “upper limit” is $\sim 8 \text{ km s}^{-1}$). The line widths are the result of three main effects. The width of lines caused by natural and collisional (“pressure”) broadening are comparable and negligible¹ compare to the third, the thermal effect.

Considering only the thermal broadening, the usual line width that we should observe, at 10 K, is $\Delta v_{\text{th}} \approx 0.3 \text{ km s}^{-1}$ (Larson, 1981). I determined the line widths caused by thermal effect at various temperatures. The thermal line width (along the line of sight) can be calculated in velocity space as

$$\Delta v_{\text{th}} = 2\sqrt{\ln 2} \sqrt{\frac{2kT_{\text{kin}}}{m}} = 1.665 \sqrt{\frac{2kT_{\text{kin}}}{m}} \quad [\text{km s}^{-1}] \quad (8.1)$$

where k is the Boltzmann-constant, T_{kin} is the temperature and m is the mass of molecules, ions or atoms in unit of kg ². The line widths, observed

¹The collisional broadening could be relevant but only in the high density ISM.

²I converted the atomic mass units to kg via $1 \text{ amu} \approx 1.67 \times 10^{-27} \text{ kg}$.

by us, are significantly wider than the thermal broadening (Tab. 8.1). On the other hand, we have to keep in mind that the line thermal widths are strongly depends on the molecular weight, hence the results are valid only for a given particular molecule.

However, besides the thermal effect, another effects could influence the observed line widths. As we investigate a star-forming region that heavily influenced by stellar wind, interacts with expanding bubbles and involves shock fronts, the most likely scenario to explain the remaining line widths is the presence of vivid gas motions³.

To derive the turbulent velocity of the gas at given temperature, I need to consider the instrumental line-broadening too, which is, in case of HIFI, the velocity resolution itself in a given band. The turbulent velocity can be calculated as e.g. Melnick (1978)

$$v_{\text{turb}} = \sqrt{\Delta v_{\text{obs}}^2 - \Delta v_{\text{ins}}^2 - \frac{2kT_{\text{kin}}}{m}} \quad [\text{km s}^{-1}] \quad (8.2)$$

where Δv_{obs} and Δv_{ins} are the observed and the instrumental line widths, respectively. I utilized the averaged values of the observed line widths from Tab. 8.1 for determine v_{turb} . Hence, the results in Tab. 8.2 are the averaged turbulent velocities in the cuts.

One of the main generators of the turbulences are the shock fronts that can be created by expanding HII regions and fast stellar winds (Draine, 2011). Nürnbergger (2003) reported the existence of 6 shock fronts in NGC 3603 (Fig. 8.1). These shock fronts can be characterized by, for example, the dimensionless Mach-number which is the ratio of the moving source (e.g., shock front) and the sound speed in that environment ($\mathcal{M} = v_{\text{sf}}/c_s$). The sound speed can be determined in an isothermal medium (Gusdorf et al., 2008a; Ossenkopf, 2002) by:

$$c_s = \sqrt{\frac{\gamma k T_{\text{kin}}}{\mu}} \quad [\text{m s}^{-1}] \quad (8.3)$$

where γ is the heat capacity, k is the Boltzmann-constant and $\mu = 2.36m_H$ is the mean particle mass. For adiabatic sound speed, the heat capacity is slightly higher than unity, $\gamma = 5/3$ (Gusdorf et al., 2008a). Using $\gamma = 5/3$, I calculated the shock speed as (Helder et al., 2011):

$$v_{\text{SF}} = \sqrt{\frac{kT_{\text{kin}}(\gamma + 1)^2}{2(\gamma - 1)\mu}} \quad [\text{m s}^{-1}] \quad (8.4)$$

³The observed line widths depend on e.g. Zeeman- and Stark-effects too, but these are much more weaker in PDRs.

Table 8.1: *The averaged line widths from C1, C2 and C3 (upper part) and the derived thermal line-broadening at given temperatures (lower part).*

Species	$\langle \Delta v_{\text{obs}} \rangle$ (C1)	$\langle \Delta v_{\text{obs}} \rangle$ (C2)	$\langle \Delta v_{\text{obs}} \rangle$ (C3)		
	[km s ⁻¹]	[km s ⁻¹]	[km s ⁻¹]		
CH	4.46	3.56	4.10		
C ₂ H	3.18	5.29	4.14		
HCO ⁺	4.99	4.40	4.30		
CS	2.61	2.22	2.95		

	T _{kin} [K]				
	20	50	100	200	500
Δv_{th} (CH) [km s ⁻¹]	0.27	0.42	0.59	0.84	1.33
Δv_{th} (C ₂ H) [km s ⁻¹]	0.19	0.30	0.43	0.61	0.99
Δv_{th} (HCO ⁺) [km s ⁻¹]	0.18	0.28	0.40	0.56	0.89
Δv_{th} (CS) [km s ⁻¹]	0.14	0.23	0.32	0.46	0.72

Note: For the thermal line width (Δv_{th}) derivations I used the following mass values:

$$\text{CH} = 13.0187 \text{ amu} \approx 21.61 \times 10^{-27} \text{ kg};$$

$$\text{C}_2\text{H} = 25.02951 \text{ amu} \approx 41.55 \times 10^{-27} \text{ kg};$$

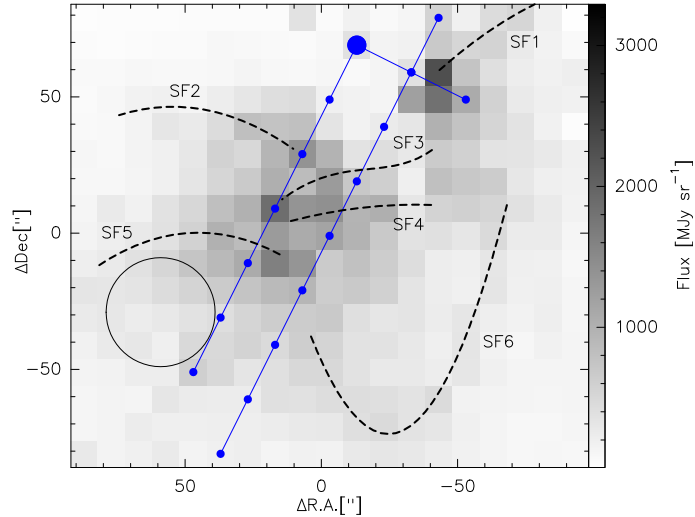
$$\text{HCO}^+ = 29.01811 \text{ amu} \approx 48.17 \times 10^{-27} \text{ kg};$$

$$\text{CS} = 44.0763 \text{ amu} \approx 73.17 \times 10^{-27} \text{ kg}.$$

Table 8.2: *The derived turbulent velocities in km s⁻¹.*

Species	Cuts	T [K]				
		20	50	100	200	500
CH	C1	4.40	4.40	4.39	4.38	4.33
	C2	3.49	3.48	3.47	3.45	3.40
	C3	4.04	4.03	4.02	4.01	3.96
C ₂ H	C1	3.10	3.10	3.09	3.08	3.05
	C2	5.24	5.24	5.24	5.23	5.21
	C3	4.08	4.08	4.07	4.06	4.04
HCO ⁺	C1	4.94	4.94	4.93	4.93	4.91
	C2	4.34	4.34	4.34	4.33	4.31
	C3	4.24	4.24	4.24	4.23	4.21
CS	C1	2.51	2.51	2.51	2.50	2.48
	C2	2.10	2.10	2.10	2.09	2.06
	C3	2.86	2.86	2.86	2.85	2.83

Figure 8.1: The shock fronts on Spitzer $8\mu\text{m}$ map together with the cuts. The positions of shocks are from Nürnberg (2003). The shocks were observed at $11.9\mu\text{m}$ and indicating warm dust with a few 100 K [details in Nürnberg (2003)]. The big circle represent the ring-like structure visible on the PV-diagram of $^{12}\text{C}^+$ (see more in Section 8.1.3).



The result Mach-number is $\mathcal{M} \approx 1.8$ which implies slightly supersonic shock speed. On the other hand, the error budget of this Mach-number is fairly high due to uncertain temperature and large beam size. Line emissions from, for example, ortho- or para-water, or high- J ^{12}CO (Gusdorf et al., 2012) are suitable to investigate shock fronts. However, high- J ^{12}CO lines could trace PDRs (Ossenkopf et al., 2010b; San Jose-Garcia et al., 2013) but can also be used to investigate molecular outflows (Bjerkeli et al., 2013) and temperature, and density structure of a cloud (Haikala et al., 2006). Water lines are also good tracers of warm and dense gas (Omont et al., 2011) and molecular outflows (due to its high dipole moment). If the shock speed is high enough ($\gtrsim 25 \text{ km s}^{-1}$), the grain mantles are sputtering and the amount of silicon monoxide (SiO) is significantly higher in the gas-phase (Gusdorf et al., 2008a,b).

Because I do not have any SiO observations of which could help to identify the footprints of existing shocks, and the beam size is not large enough to spatially resolve the different phenomenon that can exist in NGC 3603 (embedded infrared sources (EIRS), shock fronts, masers and ionization fronts), the detected emission lines can show the combined signatures of the previously mentioned effects.

8.1.2 Footprints of rotation/torsion

Besides the inner turbulent gas motions within the observed molecular clumps, rotational movements or torsion of the clumps are also possible. Based on the channel maps that I created from the OTF observations (Appendix G), I realized rotations of spatial distribution of emissions in MM2.

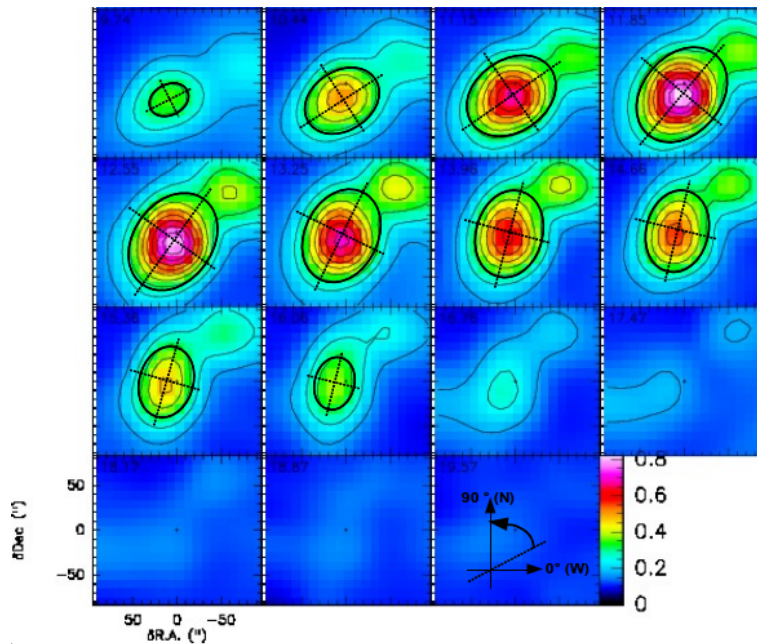


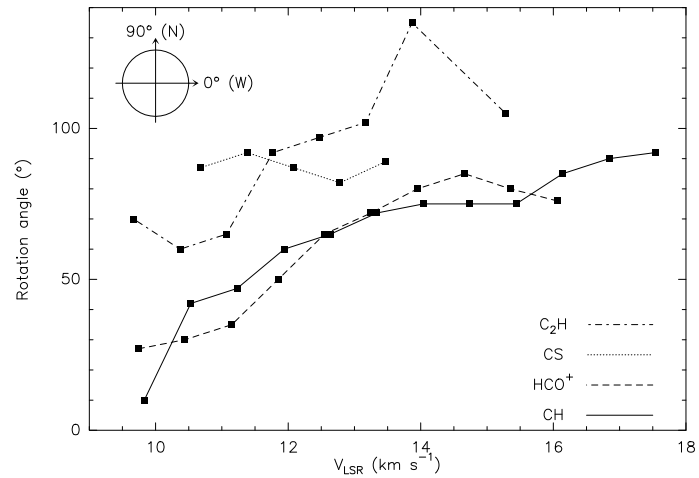
Figure 8.2: An example for visualize the emission rotation in MM2. The channel map shows HCO^+ with the drawn ellipses (see text). The rotation angle of major axis of the ellipses is measured from west to north (see the schematic plot in the last sub-plot where the dashed line represents a major axis of an ellipse).

To quantify these rotations, I draw an ellipse to contours that represent emissions which emerge from the background by at least 30% of the peak emission (Fig. 8.2). Then, I illustrated the rotation angle of major axis of the drawn ellipse as a function of velocities with velocity steps of 0.7 km s^{-1} (Fig. 8.3).

The dense core tracer CS shows a very compact emission distribution through many velocities in velocity channel map (upper panel of Fig. G.2). On the whole, the CS emission does not show significant rotation in MM2 which suggest that the observed CS lines are coming from a very compact and dense core, and that core is not notably influenced by either stellar wind from the central OB cluster or any shock fronts.

The other observed molecules indicate noticeable rotation in MM2 as a function of velocity. HCO^+ is predicted to be a dense gas tracer, together with CS. The possible rotation traced by HCO^+ may be a hint that we observed another core (around the inner CS core) which is located closer to the cloud surface, encompass by the outskirts traced by CH and C_2H , hence it can be influenced by the aforementioned effects. To be able to distinguish between rotation and twirl, I also inspected the PV-diagrams because if there is rotation, it should be manifested on the position-velocity diagrams [e.g. in Brinch et al. (2008)]. Based on the investigation of the

Figure 8.3: *Visualization of emission rotation in MM2, based on the major axis position of an ellipse that fits to data that emerge from the background by minimum 30% of peak value.*



PV-diagrams and channel maps, I conclude that what we see is the curling of MM2 along the line-of-sight instead of rotation, and the channel maps provide information about the cloud geometry.

Nevertheless, I need to consider that, even if rotations of the emission distribution are easily observable, these method is very rough and the error budget of the rotation angles could be high.

8.1.3 Internal cavity in MM2?

Already Clayton (1986) observed a spectra which showed vivid gas movements within NGC 3603. Clayton (1990) reported that the face-side of MM1 is composed by a highly illuminated front that can shield the stellar wind from the deeper part. In contrast, MM2 does not show such a bright rim suggesting that the stellar wind provided by the central cluster can penetrate deeply into MM2 causing complex velocity structure therein.

The most interesting velocity structure has been presented by $^{12}\text{C}^+$ in MM2 (Fig. 6.4). The main velocity component of the ionized carbon is well traced by both the ^{12}CO and ^{13}CO . Relatively far from the central cluster (at projected distance $\sim 100''$) a broad velocity component (or more at velocities ~ 21 and ~ 27 km s⁻¹) appears. These velocity components are seemingly connected to each other creating a ring-like structure and indicating an internal cavity or bubble.

As a first approach, I assumed that this structure is related to the prominent EIRS in MM2 (IRS9 and IRS2, Section 8.3). If I assume that the area, embraced by the ring, is totally spherical then its projected diameter is $\sim 40''$ which corresponds to ~ 1.4 pc at the distance of 7.3 kpc. The analysis of the spatial situations of the HIFI cut observations toward MM2 and the cut C2 reveals that these two slices are not parallel as a function of distance from the central cluster (Fig. 3.6). Bear this in mind, I plot the

position of ring structure and compared its location to the EIRS and shock fronts (Fig. 8.1 and 8.4).

It is obvious from Fig. 8.4 that the ring-like structure is located far away from the EIRS, hence any physical connection is unlikely. In addition, the direct surroundings in which the physics and chemistry are influenced by the IRS9 complex is very small (Section 8.3), confirming the lack of concrete physical association with IRS9.

On the other hand, one of the shocks lies reasonably close to the curve of the “bubble” facing to the OB cluster (SF5 on Fig. 8.1). The shock fronts are detected at $11.9\ \mu\text{m}$ and $18\ \mu\text{m}$ (Nürnberg & Stanke, 2003) and probably trace warm dust and/or highly ionized gas. This observational result is in agreement with previous PACS and SPIRE data that show presence of warm gas roughly at the position of ring-like structure (Fig. 5.4). The SF5 position (together with the other shock fronts) is well traced by the Spitzer $8\ \mu\text{m}$ data (gray-scaled map on Fig. 8.1) which is a good tracer of hot and ionized Polycyclic Aromatic Hydrocarbons (PAHs) (Lebouteiller et al., 2007). However, the cavity-like structure is not visible on the Spitzer map (only the “upper” curve) which may indicate that it is may not a real cavity.

The main ionization energy of PAHs is mostly provided by UV radiation. In case of NGC 3603, this could be, if the FUV-photons penetrate deep inside the cloud, due to clumpy PDR structure. High-energy photons from embedded source are unlikely because no internal source has been detected within the ring-like structure so far. Nevertheless, it is possible that other, significantly strong, effects influence the ionization process of PAHs, like dust extinction or metallicity (Cox & Spaans, 2006).

The other possibility for the explanation of the ring structure visible on the PV-diagram of $^{12}\text{C}^+$, is that we trace the main cloud component at $\sim 13 - 16\ \text{km s}^{-1}$ in $^{12}\text{C}^+$ together with the ionized and shocked gas that is blown away (at $\sim 27\ \text{km s}^{-1}$) from the observer by the strong stellar wind, as in case of M17 (Pérez-Beaupuits et al., 2012).

8.2 Cloud (in)stability

The roots of star formation in molecular clouds are instabilities. As long as the gravitational forces are not exceeding the thermal (kinetic) energies in the molecular cloud, the cloud (or part of it) cannot contract. Cloud contraction leads to formation of dense cores which might be the cradle of the next generations of stars. To analyse the balance between the gravitational force and the internal motions, I derived the virial masses and virial parameters along the cuts C1, C2 and C3 (Section 6.5).

The determined virial masses are bigger than the observed gas masses which suggest that the observed clumps are not in virial equilibrium. However, I also studied the ratio of the virial and total gas masses to be able to investigate the connection between the gravitational and kinetic energies (Section 6.5.1).

Bertoldi & McKee (1992) found that the virial parameter is proportional to the gas mass ($\alpha \approx M^{-0.67}$). This value is close to that has been found, $\alpha \approx M^{-0.61}$, based on ^{13}CO observations (Loren, 1989b). Using our observations, I found a less steep correlation, namely $\alpha \approx M^{-0.33}$. The power-law index is different from the previously mentioned numbers by $\sim 50\%$. Because the virial mass strongly depends on the velocity dispersion of a molecule ($M_{vir} \propto \sigma^2$), the plot of virial parameter versus gas mass is related to a certain part of the molecular cloud traced by the used molecule.

The ambient magnetic field could also play an important role for self-gravitating massive cores which are encompassed by a gas that is compressed by the clump (Bertoldi & McKee, 1992; Loren, 1989a). If a magnetic field is present, then it can support the cloud against cloud collapse⁴, hence the star formation can be slower. For example, early B-type stars possess magnetic field which, as I mentioned earlier, can be important and can influence star formation [e.g. (Maeder & Meynet, 2005)], specially in case of massive stars [$M_* \gtrsim 8M_{\odot}$, Ferrario et al. (2009)].

I used the HCO^+ lines for calculating the velocity dispersion, hence the slope of the fitted line on Fig. 6.18 probably refers to a denser core. This is in agreement with measurements in Orion-bar where the virial parameter was found to be proportional to the gas mass with a power-law index of ~ -0.35 (Tatematsu et al., 1993). They used CS data which is the another dense gas tracer next to HCO^+ and this is also in good agreement with the scenario that the massive clumps are usually not close to the virial equilibrium instead of the smaller ones (Loren, 1989b).

Nonetheless, the core traced by HCO^+ seems to be not in virial equilibrium but, because of our large beam size, I cannot distinguish which part(s) of the observed clumps are really far or close to the virial equilibrium.

The molecular cloud (or part of it) starts to gravitationally collapse if its mass larger than a critical mass, the Jeans-mass. The Jeans-mass depends on the gas temperature and its density. Röllig et al. (2011) calculated the gas density in NGC 3603 (more precisely in MM1 and MM2) as $n \sim 10^3 - 10^4 \text{ cm}^{-3}$. Besides lower density tracers, CH and C_2H , we detected emissions from high rotational transitions of carbon monoxide too ($J_u > 13$). ^{12}CO has low dipole moment (~ 0.1 Debye), hence its low- J lines can easily be collisionally excited and thermalized. Contrariwise, the high- J lines are good tracers of PDRs (Ossenkopf et al., 2010b; San

⁴Cloud rotation can also support a molecular cloud and increase the time of the gravitational collapsing phase.

Jose-Garcia et al., 2013). Therefore, to excite these high rotational lines the gas must be warm and dense (Hollenbach & Tielens, 1997; Stacey et al., 1993) with $T \approx 500$ K, and $n \sim 10^7$ cm⁻³.

Once I use the Jeans–mass, I naively assume that the observed molecular clump has no rotation, turbulence and magnetic field. I furthermore assumed that the density is broadly even, hence no or infinitesimal density gradients exist. If I assume a uniform density, the cloud surface falls inside the cloud during the free-fall time:

$$t_{\text{ff}} = \frac{1}{4} \sqrt{\frac{3\pi}{2G\rho_0}} \quad [\text{s}] \quad (8.5)$$

where $\rho_0 = 2m_H n(H_2)$ is the gas density and G is the gravitational constant (the free–fall time has no dependence on the size and total mass). If I invoke median density $n(H_2) \sim 10^5$ cm⁻³, the derived free-fall time is $\sim 10^5$ year which is slightly higher than the usual values for molecular clouds ($t_{\text{ff}} \sim 10^3 - 10^4$ yr). In the case of non–uniform density, the cloud collapses in shorter time scale (denser and smaller cores collapse faster). But again, magnetic field can support the thermal (kinetic) energy in the battle against gravitation.

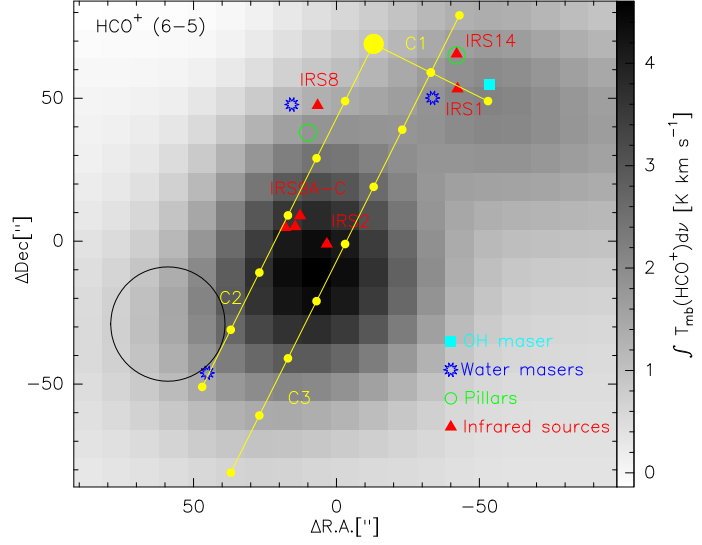
I derived the Jeans–masses at different density and temperature regimes ($n \sim 10^3 - 10^7$ cm⁻³ and $T = 20, 50, 100, 200$ and 500 K, see Tab. 6.5). The results are in good agreement with our predictions, and previous computations, namely that only the outer layers are not or weakly involved in the gravitational collapse phase. The denser and deeper part(s) of the observed clumps are probably in the gravitational contraction phase that leads to star formation inside MM1 and MM2.

8.3 Embedded sources

Based on the calculation in the previous section, I concluded, in conjunction with Röllig et al. (2011), that the star formation is ongoing in MM1 and MM2. Also, as a sign of star formation, prominent embedded infrared sources and masers have been identified in both molecular clumps MM1 and MM2 [Fig. 8.4; Frogel et al. (1977); Nürnberger & Petr-Gotzens (2002); Nürnberger & Stanke (2003); Nürnberger (2003, 2008); Nürnberger et al. (2010); Persi et al. (1985); Vehoff et al. (2010)].

The newly born massive stars (O- and early B-type) are vigorous sources of high-energy photons that can ionize their immediate vicinity by radiation, jets, supernova explosion and stellar winds (Sternberg et al., 2003). To derive the size of the area around the embedded source(s) which is

Figure 8.4: The positions of the embedded infrared sources and masers from Nürnberg & Stanke (2003) plotted on the HCO^+ integrated intensity map. The pillars and cuts are also marked. The big circle represents the ring-like structure visible on the PV-diagram of $^{12}\text{C}^+$ (Section 8.1.3).



probably influenced by those very young and hot stars, I determined the Strömgren-radius (Strömgren, 1939) by

$$R_s = \sqrt[3]{\frac{3L_{Ly}}{4\pi\alpha_H n(H)^2}} \quad [\text{cm}] \quad (8.6)$$

where L_{Ly} is the number of Lyman-photons per second, $n(H) \sim 10^3 \text{ cm}^{-3}$ is density and $\alpha_H = 2.56 \times 10^{-13} T^{-0.85} \text{ cm}^3 \text{ s}^{-1}$ is the recombination rate [e.g. Draine (2011) and Lacki (2013)].

For the calculations, I assumed that the region is spherical and the interstellar medium within the Strömgren-radius is fully ionized and composed of hydrogen. There are two embedded infrared sources have been found in MM1 (IRS1 and IRS14) and four in MM2 (IRS9A-C and IRS2) [e.g. Nürnberg (2003); Nürnberg et al. (2010)]. The most prominent source is IRS9 which consists of three (probably) early B-type stars. From the triplet, IRS9A is the most luminous one ($2.3 \times 10^5 L_\odot$), hence its Strömgren-sphere should be the largest. Thus, I focused on this source.

The derived Lyman-photon number per seconds for IRS9A is $L_{Ly} \sim 10^{40} \text{ s}^{-1}$ (Nürnberg, 2003) which is a low value even for B-type stars. However, this number is only a lower limit. The effective temperature of this source is $\gtrsim 2.2 \times 10^4 \text{ K}$ and putting together all this information, the derived Strömgren-radius is $R_s \sim 0.04 \text{ pc}$. Converting this value to a projected distance (using the calculated distance in Section 6.2.4) from the position of IRS9A, I received $1''$. I concluded that I likely cannot detect any footprints of different chemistry and/or physics governed by these embedded sources. This is true even for the closest position to IRS9 complex (position 4 in C2, Fig. 8.4) where I did deeper analysis of spectra.

8.4 Density and UV-field with the KOSMA- τ model

From the KOSMA- τ model results (Tab. 7.3), the first important output is that the best model fits are independent from the clumpiness. As a consequence, it is not possible to differentiate whether we observe one clump that fills the beam or observe numerous but small clumps within the beam. However, it is implausible that the observed molecular cloud consists of only one big clump based on previous statements (e.g., observations of compact emission from the dense gas tracer CS, that probably trace a small core located inside MM2; a widely spread CH emission which is likely coming from the outer, diffuse layer). Hence, for the further analysis, I assumed that MM1 and MM2 are clumpy.

The observed ^{12}CO lines are fitted well with a two-ensemble model (Fig. 7.4). The “lower- J ” lines ($4 \rightarrow 3$, $7 \rightarrow 6$ and $9 \rightarrow 8$), trace moderately warm gas while the high- J transitions indicate the presence of warm gas. This is in agreement with the scenario, predicted from the rotational diagrams (Fig. 6.16). The derived gas volume densities ($n \sim 10^5 - 10^6 \text{ cm}^{-3}$) are slightly higher than the previously calculated values from Röllig et al. (2011), $n \sim 10^3 - 10^4 \text{ cm}^{-3}$, using escape probabilities. Considering that our observational input parameters are smoothed to the beam size of $43''.5$ and the observed clouds in all likelihood cover larger area on the sky than this beam size (at least MM2), therefore we probably observed bigger amount of gas than Röllig et al. (2011). Thus, the discrepancy, which is in the order of 2, is probably caused by the different beam sizes (they smoothed their data to $38''$). Nonetheless, the higher gas volume density supports the scenario, namely high density and temperature [$n \approx 10^7 \text{ cm}^{-3}$ and $T \approx 500 \text{ K}$, Hollenbach & Tielens (1997) and Stacey et al. (1993)] is needed to excite ^{12}CO with $J_u \geq 13$.

In general, a high UV-radiation field is needed for PDRs to be able to dissociate and ionize molecules and atoms. Röllig et al. (2011) derived a considerably high FUV-field ($\chi_D \sim 3 - 6 \times 10^3$) using HIRES/IRAS far-infrared data. They also found that the FUV-field strength is increasing with distance from the central cluster oppositely to our expectations. On the other hand, the HIRES/IRAS data strongly suffers from beam dilution effect (the minimum beam size was $\sim 35''$).

I also analysed the FUV-field strength via publicly available PACS and SPIRE data ($70 \mu\text{m}$ and $160 \mu\text{m}$ data, Section 5.3), assuming that all the FUV-photons are absorbed and re-emitted in the infrared regime. The beam size is $14''$ which allows us to study the FUV-field in more details (magnified plot on Fig. 5.5). It is important to consider that the FUV-field strength map that we received is a summation of external (from the central OB cluster) and internal (EIRS and masers) FUV-photons. It is visible that

the FUV-peaks coincide with the prominent EIRS suggesting them as the birth place of significant amount of FUV-photons.

The derived peak FUV-intensity from PACS and SPIRE data is roughly an order higher from the HIRES/IRAS result ($\chi_D \sim 1 - 2 \times 10^4$)⁵ probably due to the better spatial resolution.

The KOSMA- τ model can approximate the minimum FUV-field strength that we need for the observed line emission intensities. The line intensities of warm component assume an FUV-field strength of $\chi_D \sim 10^3$ which is in agreement with the value from Röllig et al. (2011) and slightly lower than what I derived from the PACS and SPIRE data but, again, it is probably due to beam dilution effect. For the moderately warm gas, traced by the lower- J lines, we expect lower FUV-field as these lines are produced at deeper and cooler layers where the FUV-field is more attenuated. In agreement with this expectation, the minimum FUV-field that we need to reproduce the line intensities of moderately warm gas is $\chi_D \sim 10^1$.

Because of the beam filling factor, all the computed parameters of the observed molecular clouds are lower limits.

Cooling lines The observed cooling line intensities are fitted well with the KOSMA- τ . In MM1, the intensity of the lower fine structure line of [OI], at $63 \mu\text{m}$ ($^3P_1 \rightarrow ^3P_2$), is slightly underestimated together with the lower fine transition of [Cl] at $610 \mu\text{m}$ ($^3P_1 \rightarrow ^3P_0$). Even with this small discrepancy, the model fits are reasonable.

The critical density of the atomic oxygen fine structure lines is in the order of $\sim 10^5 \text{ cm}^{-3}$ which is close to the gas density we received from the model and slightly higher than the value from Röllig et al. (2011). This might indicate that radiative excitation is the less dominant excitation process. This is supported by [Cl] that has a factor 10 lower critical density ($\sim 10^4 \text{ cm}^{-3}$), thus the collisions could be the significant excitation process.

8.5 Density and temperature with the RADEX

In this case, I assumed unity beam filling ($f = 1$) and fitted the same transitions with a two-ensemble model. The ^{12}CO as well as the cooling lines are fitted well (Fig. 7.2 and 7.3) but in the case of cooling lines the deviation between the observed and modelled points is somewhat higher than in case of KOSMA- τ model.

The volume density of the moderately warm gas component is in the order of $n \sim 10^4 - 10^5 \text{ cm}^{-3}$ in MM2 and MM1, respectively (Tab. 7.1). This value

⁵The FUV-field from PACS and SPIRE data is given in Habing field (G_0). The connection between G_0 and Draine-field (χ_D) is $G_0 \approx 1.7\chi_D$ (Bertoldi & Draine, 1996).

is lower by an order than what I received from the KOSMA- τ model. The small discrepancy is probably caused by beam dilution effect (I assumed unity filling factor).

Besides the volume densities, the kinetic temperatures were also derived. For the moderately warm components, I compute 30 and 43 K which are lower than the temperatures from the rotational diagrams (Fig. 6.16). These weaker temperatures, however, could be roughly correct if we take into account that I assumed local thermodynamic equilibrium for the rotational diagram method.

As I already mentioned, high temperature and density are needed to excite high- J ^{12}CO lines. Therefore, for the warm gas component, I adjust two input settings: one with high density ($n \sim 10^7 \text{ cm}^{-3}$) and the other one with high temperature ($T > 400 \text{ K}$). When these parameters were both high, I was not able to fit the observed line intensities at all. In case of high density, the kinetic gas temperature from the model is sufficiently similar to the results from the rotational diagram method (the differences are only a few Kelvins). If the gas density is $\gtrsim 10^7 \text{ cm}^{-3}$ all transitions are thermalized, hence the rotation temperature is equal to the kinetic temperature. When higher temperatures were assumed, the result gas densities that I received from the model were in the order of $n \sim 10^5 \text{ cm}^{-3}$ which is in very good agreement with previous observations.

It is also difficult to determine which part of the PDRs are observed by the received ^{12}CO transitions. In PDRs, we expect that the higher rotational transitions are the signatures of high temperature (hence they trace the outer layers) while the lower- J lines are tracers of less warm layers (Pérez-Beaupuits et al., 2012), thus they trace the deeper parts of the PDRs. Nevertheless, if the observed molecular cloud is clumpy, no clear chemical and physical stratification should be observed (Stutzki et al., 1988). Therefore, the lower- J ^{12}CO lines probably originate in the moderately warm and less dense part while the high- J lines probably trace the envelopes of the clumps which is located close to the PDR surface (Tauber et al., 1994). Other possibility for the presence of warm ^{12}CO is that additional heating mechanism(s) exist(s), i.e. cosmic-rays (Pellegrini et al., 2009) or shock-fronts and/or turbulence (Habart et al., 2010).

Pressure Because the observed line intensities can equally be fitted well with the aforementioned setups, we cannot determine whether the gas pressure is caused by high temperature or by high density. The pressure ($P/k \sim nT$) can be used as a characterisation of massive star-forming regions (Nagy et al., 2012). Papadopoulos et al. (2012) found that, in general, the pressure in our Galaxy is in the order of $\sim 10^4 \text{ K cm}^{-3}$. On the other hand, the derived densities depend on the $n(H)_{tot}$, hence the error budget of pressure calculations could be high (Greve et al., 2009). In case of NGC 3603, the estimated pressures are in the range of

Table 8.3: *The derived pressures in NGC 3603.*

Source	Component	T [K]	n [cm ⁻³]	P/k [K cm ⁻³]
KOSMA- τ^a				
MM1-IF	Mod. warm	~ 60	$\sim 10^6$	6×10^7
	Warm	~ 170	$\sim 10^6$	1.7×10^8
MM2-IF	Mod. warm	~ 46	$\sim 10^5$	4.6×10^6
	Warm	~ 170	$\sim 10^6$	1.7×10^8
RADEX-code ^b				
MM1-IF	Mod. warm	30	9.0×10^4	2.7×10^6
	Warm	520	1.1×10^5	5.7×10^7
		170	1.0×10^7	1.7×10^9
MM2-IF	Mod. warm	43	9.0×10^3	3.9×10^5
	Warm	420	3.0×10^5	1.3×10^8
		180	1.0×10^7	1.8×10^9

^a The temperatures from the rotational diagram; densities from model calculations.

^b The temperatures and densities are from the model calculations.

$P/k \sim 4 \times 10^5 - 2 \times 10^9$ K cm⁻³ (see Tab. 8.3). The derived pressures are roughly consistent (considering the possibly high error budget) with values from other high-mass star-forming regions, i.e. W49-complex with pressure value up to $\sim 5 \times 10^8$ K cm⁻³ (Nagy et al., 2012) or Sgr B2 with maximum value of 2.4×10^7 K cm⁻³ (de Vicente et al., 1997).

8.6 The I(¹²CO)/I(¹³CO) ratio

The integrated line intensity ratio of ¹²CO and its isotopologue can be used to study the optical depth variation along the line of sight in the observed molecular cloud. Numerous studies of this line intensity ratios have been done for both extragalactic sources and the Milky Way. Helfer & Blitz (1995) reported that the ratio $\mathfrak{R}_{1 \rightarrow 0} = I(^{12}\text{CO})/I(^{13}\text{CO})$ is $\sim 8 - 25$ in NGC 1068 which is in agreement with, for instance, Sage & Isbell (1991) who investigated more than a dozen extragalactic sources and found the line intensity ratio in range between 2.5 and 17.

In the Milky Way, \mathfrak{R} is usually smaller for Giant Molecular Clouds (GMCs) where $\mathfrak{R}_{1 \rightarrow 0} = 3 - 6$ (Wilson & Walker, 1994). On the other hand, much higher ratios have also been found in Galactic diffuse clouds [$\mathfrak{R}_{1 \rightarrow 0} \sim 21$ (Knapp & Bowers, 1988)]. Robert & Pagani (1993) investigated two Bok

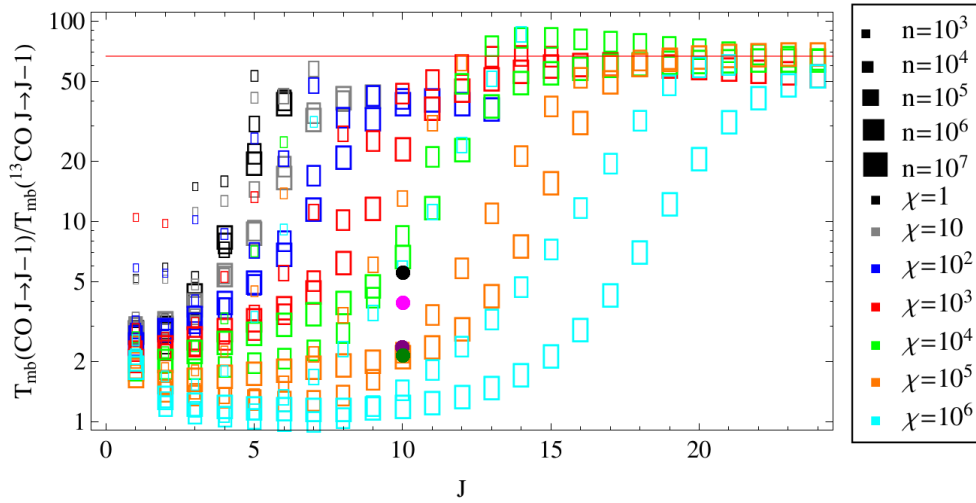


Figure 8.5: The $^{12}\text{CO}/^{13}\text{CO}$ integrated line intensity ratios as a function of rotational quantum numbers from [Röllig & Ossenkopf \(2013\)](#). The filled purple and black circles represent $\mathfrak{R} \sim 3.9$ and 5.6 that needed to fit well the ^{13}CO line intensity with the KOSMA- τ model at $J = 10$. The dark red and dark green circles mark the line ratios of ~ 2.3 and ~ 2.1 from the RADEX code. The red line denotes the elemental ratio $^{12}\text{C}/^{13}\text{C} \approx 67$.

globules⁶ and found $\mathfrak{R}_{1 \rightarrow 0} \sim 3$. These studies showed that the line intensity (and column density⁷) ratios can vary even within our Galaxy.

A remarkable difference between model calculations and observations of ^{12}CO and ^{13}CO line intensities is visible on Fig. 7.4 and 7.2. The KOSMA- τ model line intensity ratio at $J = 10$ fit the observed ^{13}CO line, if the line ratios would be $\mathfrak{R} \sim 3.9$ and 5.6 in MM2-IF and MM1-IF, respectively. In case of the RADEX code, the ratios should be $\mathfrak{R} \sim 2.3$ and 2.1 to be able to fit the observed line intensity at $J = 10$.

From Fig. 8.5, it is visible that these line ratios suggest high UV-field ($\chi_D \sim 10^4 - 10^5$) and gas density ($n \sim 10^5 - 10^6 \text{ cm}^{-3}$). This density regime exactly coincides with the results from the LTE-modelling. The UV-field strength I received from the PACS and SPIRE data ($\chi_D \sim 1 - 2 \times 10^4$) as well as from KOSMA- τ model ($\chi_D \sim 10^3$) seem to be lower than Fig. 8.5 suggests. If we consider these lower values of UV-field strength, the intensity ratio should be between $\sim 7 - 40$. Nonetheless, as we are looking

⁶Bok globules are dark clouds in the interstellar medium where stars can form.

⁷The column density and line intensity ratios are somewhat proportional, however, they are not equal. For example, $N(^{12}\text{C})/N(^{13}\text{C}) = [S(^{13}\text{C})I(^{12}\text{C})]/[\beta(^{12}\text{C})I(^{13}\text{C})]$ where S is the fractional line strength and $\beta = (1 - e^{-\tau})/\tau$ is the escape probability. Similarly, for molecules $N(^{12}\text{C}^{18}\text{O})/N(^{13}\text{C}^{18}\text{O}) = [F I(^{12}\text{C}^{18}\text{O})]/[\beta(^{12}\text{C}^{18}\text{O})I(^{13}\text{C}^{18}\text{O})]$ where F is a correction factor ([Keene et al., 1998](#)). Hence, mostly due to optical depth effect, we cannot make far-reaching conclusions about the column density ratios from the line integrated intensity ratios.

at dense PDRs ($n > 10^3 \text{ cm}^{-3}$) and not diffuse clouds, the intensity ratio should likely be less than $\mathfrak{R} < 20$ (or even $\mathfrak{R} < 10 - 15$).

These low values for the integrated line intensity ratios can be explained by optical depth effect. If both lines were optically thick, the line ratio would be 1. Because \mathfrak{R} is marginally higher than the unity ratio, the ^{12}CO line is probably optically thick⁸ and the ^{13}CO is slightly optically thin. If I take into account the derived gas masses too ($M \sim 10^2 - 10^3 M_{\odot}$), the small line ratios ($\mathfrak{R} \sim 2 - 5.5$) are in agreement with model calculations from [Röllig & Ossenkopf \(2013\)](#) because \mathfrak{R} was the smallest ($\mathfrak{R} \leq 2$) in models with high clump mass and the highest in low mass models⁹.

8.7 Chemical stratification/structure of NGC 3603

Observation of any signatures of chemical stratification of a molecular cloud is a hard contention, even if the molecular cloud is a typical instance of edge-on PDRs. For example, the observation of the distribution of different chemical layers is impossible if the beam size is large and/or the celestial object is far from the observer. Next to the spatial resolution, clumpiness plays also an important role [e.g. [Pérez-Beaupuits et al. \(2012\)](#)]. If a molecular cloud consists of many smaller clumps the FUV-photons can penetrate deeper inside the cloud and illuminate the surfaces of those clumps. As a consequence, the mixture of layers may induce an indistinguishable chemical stratification within the beam.

For a classical edge-on PDRs [NGC 3603 is believed to be an edge-on PDR ([Röllig et al., 2011](#))], we expect a stratification as $\text{C}^+ - \text{C} - \text{CO}$ (high- J to low- J) from the central ionization source. When a molecular cloud is clumpy, no stratification should be observed [Stutzki et al. \(1988\)](#). As already mentioned in Section 7.2.2, due to shock fronts, embedded sources (masers and infrared objects) and strong stellar wind from the central OB cluster, it is very unlikely that NGC 3603 contains only one big clump.

Nevertheless, the combination of derived relative abundances (to H_2), column densities and the distribution of integrated intensities allows us to make a number of statements about the chemical stratifications and the structure of the observed molecular cloud.

In MM1, the line integrated intensity peaks of the high- J rotational lines of ^{12}CO appear close to the ionization source while the lower rotational tran-

⁸It is still possible that the lower- J ^{12}CO lines are optically thick and higher- J transitions ($J_u > 9$) are optically thin, if they are sub-thermally excited.

⁹In their model, the clump mass range was defined from 10^{-2} to 10^3 solar masses.

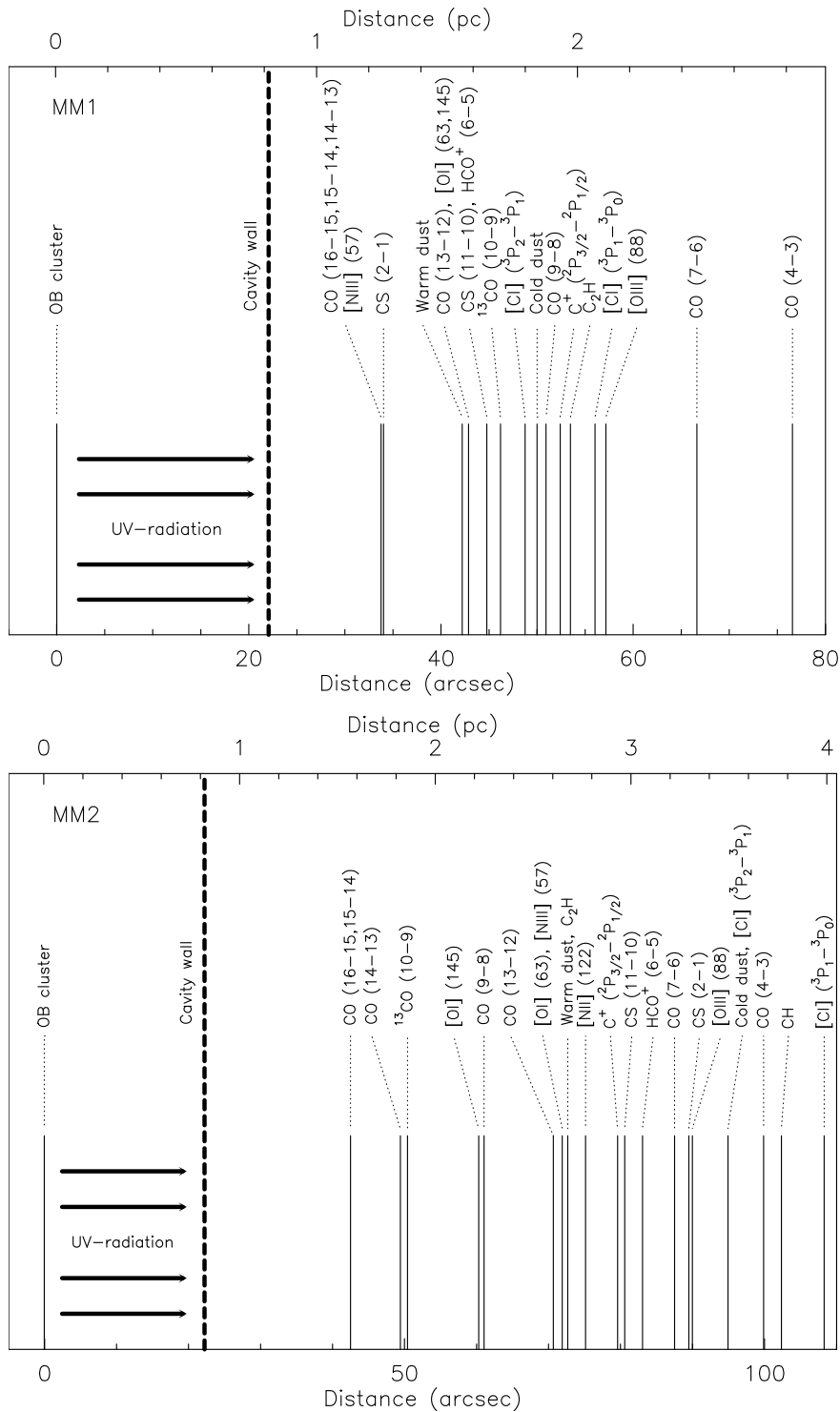


Figure 8.6: The projected distance of the peak integrated line intensities in MM1 (upper panel) and MM2 (lower panel) from the central star cluster. The intensity values are from all Herschel observations (HIFI-OTF, -point, -cuts and PACS). The dashed line roughly represent the border of the wind-driven cavity exists around the OB cluster (from the literature). The projected distances in parsecs were calculated at a distance of 7.3 kpc.

sitions show up at the deeper part¹⁰ of MM1 (upper panel of Fig. 8.6). This trend is also observable in MM2 which indicates a warm layer ($T_{\text{gas}} \gtrsim 170$ K) of carbon monoxide close the cloud surface in both clouds. Deeper, a moderately warm ($T_{\text{gas}} \sim 30 - 50$ K) and dense ^{12}CO layer exists. On the other hand, like Röllig et al. (2011), I did not find clear observational evidence for $\text{C}^+ - \text{C} - \text{CO}$ layering neither in MM1 nor in MM2. The peaks of line intensities are not evenly distributed in MM1. Most of them ($\sim 63\%$) are within ~ 1 parsec, creating a mixture of dense (e.g., CS and HCO^+) and diffuse (e.g., [OIII] and C_2H) gas tracers which affirm our assumption that small and dense cores are co-existing with diffuse gas layer(s) within NGC 3603.

In the bigger cloud (MM2), the intensity peaks are more smoothly dispersed. Because dense core tracers, like CS and HCO^+ , are observed far from the ionization source, those cores might be located deeper but, due to a projection effect, these clumps could also be close to the surface. The detection of CS ($11 \rightarrow 10$) line indicates that those clumps are probably still influenced by FUV-photons¹¹. This is possible if we assume clumpy material, thus FUV-photons can penetrate deeper inside the observed molecular cloud. The penetration of FUV-photons into a cloud strongly depends on the absorption and scattering of dust [e.g., Tielens & Hollenbach (1985) and citations therein] and the geometry of the observed cloud (Hollenbach & Tielens, 1997). As the peaks of dusts are located relatively deep in MM2, it is possible that the photons from the central OB cluster move and interact with their environment even farther inside the cloud. It is because the FUV-photons are not absorbed and/or scattered by dust grains, only at high depth. This is in agreement with Okada et al. (2010) who found in NGC 3603 that the low- J CS emission peaks from Nürnberger et al. (2002), the radio, the MIR and FIR continuum are not well separated from each other. This indicates a co-existence of warm dust, ionized gas and the molecular clumps. But, again, we need to take into account possible geometry/projection effects.

8.7.1 Chemical abundances in NGC 3603

The chemistry in PDRs is heavily dominated and influenced by FUV-photons from an ionization source, thus photo-reactions are the most im-

¹⁰Once we know the celestial coordinates of the central cluster (α_1, δ_1) and of the emission peaks of an observed species (α_2, δ_2), the projected angular distance (γ) can be approximated, for small angular distances, by $\gamma \simeq \sqrt{[(\alpha_1 - \alpha_2) \cos(\delta_1)]^2 + (\delta_1 - \delta_2)^2}$.

¹¹The critical density of this transition ($n_{\text{crit}} \sim 10^9 \text{ cm}^{-3}$) is higher than the gas density in MM1 and MM2. Thus, radiative pumping is the dominant excitation process rather than collisions.

portant chemical processes¹². The strength of the incident FUV-flux is important together with the gas density because the position of the thin transient layer H/H₂ depend on χ_D/n where $n = n_H + 2n_{H_2}$ (Sternberg, 1988; Sternberg & Dalgarno, 1995). The depth where the C⁺–C–CO transient zone appears could depend, for example, on different formation and destruction processes that compete with each other (Röllig & Ossenkopf, 2013), and on grains/PAHs (Röllig et al., 2007).

I applied the KOSMA- τ model to analyse the abundance distributions of different gas tracers as a function of visual extinction at various densities and UV-field strengths (Fig. 8.7)¹³. The models predict similar relative density distribution for CH and C₂H. Close to the surface ($A_v \lesssim 1 - 2$), in the case of less dense gas ($n \sim 10^4 \text{ cm}^{-3}$), their abundances differ by a factor of ~ 100 . This variance decreases when the density and/or the UV-field are higher.

The relative densities from the OTF-map observations are $\sim 10^{-7}$ and $\sim 10^{-9}$ for CH and C₂H, respectively. The difference of the observational abundances is in good agreement with the model calculations at gas density $n \sim 10^4 \text{ cm}^{-3}$, supporting our assumption, namely that CH traces the less dense, FUV-illuminated surface layer where the dust and gas temperatures are $\sim 60 - 150 \text{ K}$ and $\sim 100 - 500 \text{ K}$, respectively. This is a reasonable assumption if we take into account the strong UV-field ($\chi_D \sim 10^3 - 10^4$) provided by the central OB cluster and the average gas density of $\sim 10^4 \text{ cm}^{-3}$ (top right panel on Fig. 8.7). The observed C₂H lines are probably coming from the outer and diffuse layers instead of the deeper and denser part¹⁴.

The CS and HCO⁺ abundances are distributed likewise as they both are dense gas tracers. If we assume that the observed high- J lines are coming from a very dense core ($n \geq 10^5 - 10^6 \text{ cm}^{-3}$) where the UV-field is highly attenuated ($\chi_D = 10^2$), then we need to focus on the bottom left panel on Fig. 8.7. The CS abundance is obtrusively higher than HCO⁺ throughout the cloud in the model calculation (even at the dense part, $A_v \gtrsim 4 - 5$). On the other hand, our observation showed that both dense tracers are equally abundant [$X(\text{CS}) \approx X(\text{HCO}^+) \sim 10^{-11}$] in NGC 3603. One explanation could be that the CS (11 \rightarrow 10) line traces an envelope of dense clumps which are still strongly illuminated by incident FUV-photons, therefore it may be a verification of clumpy cloud structure of NGC 3603. As a direct consequence, the CS molecule is probably efficiently destroyed via photo-

¹²Cosmic rays are also important specially at high depth of a molecular cloud where the FUV-field is strongly attenuated, thus cosmic-ray induced photochemistry is relevant. Besides the photo-reactions, other reactions (e.g., collisions) can also be important depending on a certain physical condition.

¹³We also modelled the dust and gas temperatures with the same parameter grids.

¹⁴The C₂H molecule is believed to be a tracer of both diffuse molecular clouds [e.g. De Beck et al. (2012) and Gerin et al. (2011)] and dense, hot cores [e.g. Huggins et al. (1984)].

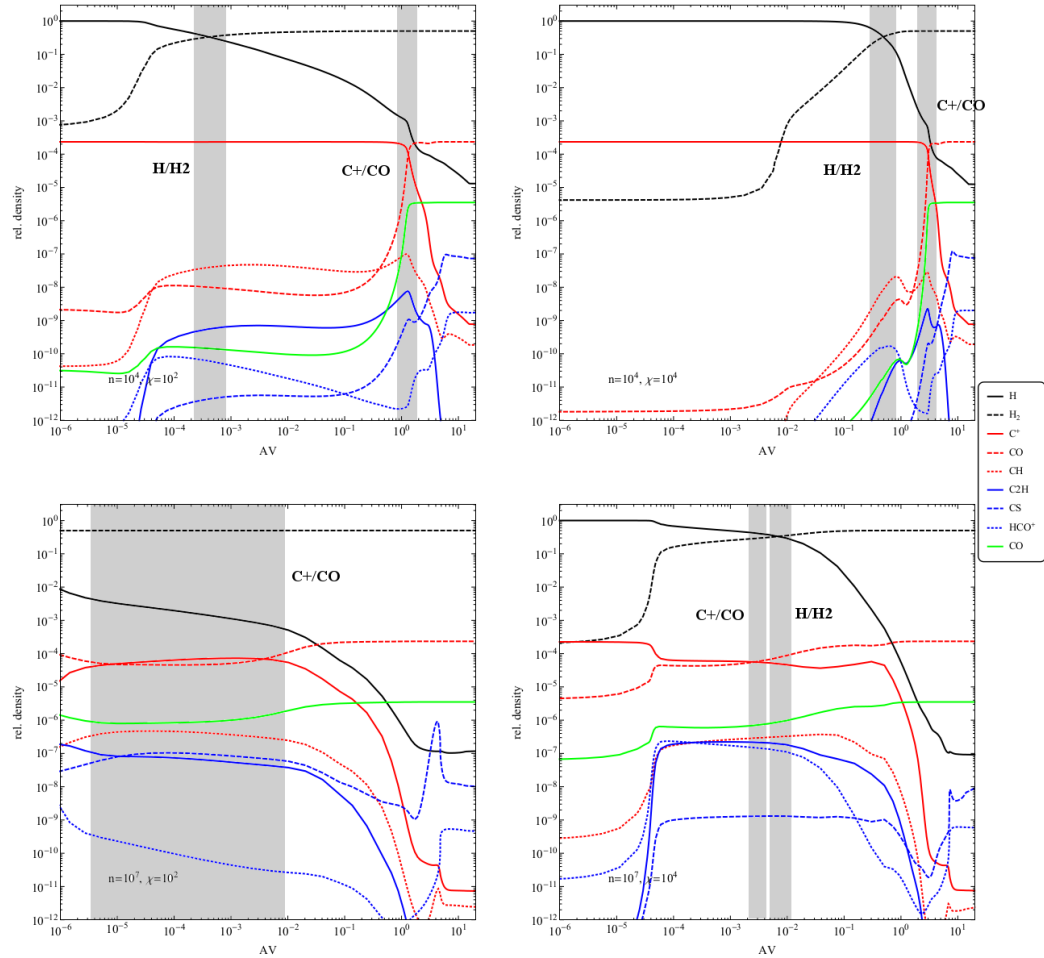


Figure 8.7: Abundances as a function of A_V for few species from KOSMA- τ model. The density values are $n = 10^4 \text{ cm}^{-3}$ and $n = 10^7 \text{ cm}^{-3}$ which correspond to a lower limit of the average density and to an extreme case respectively in NGC 3603. The UV-field strengths are also represent the lower limit ($\chi_D = 10^2$) and an average value ($\chi_D = 10^4$). The gray areas roughly denote the important transition zones H/H_2 and C^+/CO . The ionization source is on the left side, thus the heading of the FUV-photons is from left to right.

dissociation and -ionization ($\text{CS} + h\nu \rightarrow \text{C} + \text{S}$ and $\text{CS} + h\nu \rightarrow \text{CS}^+ + e^-$, respectively) at cloud depth of $A_v \sim 3 - 8$ in NGC 3603. Considering these results, the bottom right panel offers the best description of the abundances of dense gas tracers. Based on the model derivations for high density and FUV-fields ($n = 10^7 \text{ cm}^{-3}$ and $\chi_D = 10^4$), the abundances of CS and HCO^+ can be equally weak ($\sim 10^{-11}$) at visual extinction ~ 7 .

PDR or XDR? Let us focus on the bottom right panel of Fig. 8.7. That sub-plot shows the relative densities if we assume that the FUV-field can penetrate inside the observed molecular cloud, hence the FUV-field is strong and the density is high enough. An interesting effect can be discovered, namely the location of the transient zones H/H₂ and C⁺/CO are swapped in terms of cloud depth viewed from the ionization source. This is possible and not a unique case if we assume an XDR (X-ray Dominated Region) instead of a PDR, where the heating processes¹⁵ and/or the chemistry are dominated by X-rays (Maloney et al., 1996; Sternberg et al., 1997). The sources of high energy X-ray can be, for example, shock fronts, massive stars¹⁶ (Hollenbach & Tielens, 1997). Maloney et al. (1996) studied different numerical models about XDRs and found that the C⁺–CO transitional layer shifts toward the ionization source with the enhancement of gas density.

They plot the abundances of few species as a function of effective ionization parameter (ξ_{eff})¹⁷ and the ratio of local X-ray energy removing rate per particle and gas density (H_X/n), and these two parameters are proportional. In the high density model ($n \sim 10^5 \text{ cm}^{-3}$) the abundance of H₂ was uniformly dominant roughly at the same depth (the position of the transition layer H/H₂ did not changed significantly). In addition, the enhancement of the ¹²CO abundance was faster in the high density regime because the higher temperature increases the formation rate of the main isotope of carbon monoxide, hence the C–CO layer shifts closer to the surface.

Due to the shock fronts and embedded young (and hot) stars¹⁸, it is possible that significant amount of X-rays are produced in the dense clumps within MM1 and MM2. Therefore, I cannot disqualify a scenario where the physics and chemistry of the densest parts of NGC 3603 are dominated by X-rays (and maybe cosmic-rays) rather than FUV-photons from the central OB cluster and from the embedded sources.

8.7.2 H₂ formation and destruction

H₂ formation is assumed to be more efficient on grain–surface than in gas–phase where H₂ formation is slow. Temperature below 20 K is very efficient because all atomic hydrogen can leave the grain surface as H₂ (Cazaux &

¹⁵The main heating process in XDRs is dominated by X-ray induced photoelectrons and the gas-phase process is more important than the photoelectric reactions on dust grains (Maloney et al., 1996).

¹⁶This list is incomplete.

¹⁷This effective ionization rate characterizes the optically thick X-ray illuminated clouds (Maloney et al., 1996) while, in optically thin case, the relevant parameter is the ionization rate, ξ (Tarter et al., 1969).

¹⁸Additional X-ray sources can be, for example, another young and hot stars which are related to the central OB cluster.

Tielens, 2004) and inefficient above ~ 100 K (Röllig et al., 2013). Observations showed that H_2 formation on dust-grains is efficient enough even at high dust temperature up to 75K (Tielens, 2005). New model calculations also indicate that both silicates and carbonaceous grains can be a good substrata for molecular hydrogen formation up to $T \sim 100$ K (Röllig et al., 2013). Therefore, in the temperature regime $T \sim 10 - 75$ K hydrogen atoms can efficiently form on dust grain surface while above ~ 100 K the physisorbed H atoms evaporate before they form H_2 .

The observed dust temperatures in NGC 3603 ($\sim 32 - 42$ K) fit well into the $10 - 75$ K range. The derived dust temperatures are in good agreement with Röllig et al. (2011) and Wang & Chen (2010) (35 and 37 K, respectively), and indicate the formation of hydrogen atoms on the grain surfaces (Sternberg & Dalgarno, 1995):



Figure 5.4 shows that the warmer dust ($T_{\text{dust}} \gtrsim 40$ K) is located close to the wind-driven cavity wall indicating that we see the surface layer which is heated up by either photoelectric-effect or FUV-pumping of molecular hydrogen.

The photoelectric heating efficiency (ϵ) depends on a ratio (γ) of photoionization rate and the electron recombination rate (Hollenbach & Tielens, 1997; Tielens & Hollenbach, 1985). The γ is proportional to the temperature and UV-field strength (Tielens & Hollenbach, 1985):

$$\gamma \approx 3 \times 10^{-5} G_0 n_e^{-1} \sqrt{T} \quad (\text{8.7})$$

where n_e is the electron density. I assumed that the abundance of electrons can be derived from the ionized carbon abundance. The $N(C^+)$ is in the order of 10^{18} cm^{-2} and the $N(H_2)$ is roughly in the order of 10^{22} cm^{-2} . This leads to the electron abundance of 10^{-4} . Using an average gas volume density $\sim 10^5 \text{ cm}^{-3}$, the derived electron density is 10 cm^{-3} [this value is typical for PDRs (Tielens & Hollenbach, 1985; Nagy et al., 2013)]. Adopting a temperature regime $40 - 500$ K, $\gamma \approx 0.2 - 0.7$. If $\gamma < 1$ the photoelectric heating efficiency is high and vice-versa. Thus, the photoelectric heating on grains/PAHs is putatively the dominant heating process close to the surface of NGC 3603.

Figures 5.4 and 6.14 show that the peak of the molecular hydrogen column density is located relatively far behind the HII cavity wall. One explanation could be that the hydrogen has been blown away by strong stellar wind provided by the central cluster. The other reason could be the H_2 self-shielding effect (shielding effect by dust also contributes) which becomes important when the column density of H_2 is higher than $\sim 10^{14}$

cm^{-2} [e.g. [Hollenbach & Tielens \(1997\)](#)]. Due to the self-shielding, the photo-dissociation of H_2 is only relevant at the surface of the cloud¹⁹:



Therefore, the enhancement of $N(\text{H}_2)$ occurs deeper/farther part of NGC 3603 which may explain the increasing column density as a function of distance from the central cluster. Of course, the combination of these processes (stellar wind and self-shielding effects) are also possible.

¹⁹It is also possible to dissociate molecular hydrogen via collision with FUV-pumped hydrogen (H_2^*), however, if we assume that the photoelectric heating is more dominant, then reaction $\text{H}_2^* + \text{H}_2 \rightarrow \text{H} + \text{H} + \text{H}_2$ is probably not relevant.

Summary

In this thesis, I presented a detailed analysis of rotational and hyperfine transitions of different gas tracers, i.e. CH, C₂H, CS and HCO⁺, to characterize the main physical and chemical conditions in one of the most luminous star-forming region, NGC 3603²⁰, which is located in the Carina constellation. After the short theoretical introduction (Chapter 2), in which I briefly introduced the basic and most important physical and chemical processes which could be relevant in PDRs, I acquainted the Herschel Space observatory which was used to receive a large set of data (Chapter 3). The data were taken within one of the key-project, called WADI (PI.: PD. Dr. Volker Ossenkopf; Section 3.2), and comprises OTF-maps, cut and point observations using the HIFI and PACS instruments mounted on board of the Herschel.

In Chapter 4, the data reduction processes were introduced. To obtain high quality data that can be used for scientific interpretation, different software programs were used (HIPE and CLASS; Sections 4.1 and 4.2). A few complementary and/or publicly available data (Chapter 5) allow us to derive different physical parameters independently from our observations. This leads to data comparisons and cross checks, and could help for the interpretation of the reduced data.

In Chapter 6, I derived the main physical parameters (densities, temperatures, velocities) based on integrated intensity maps (Section 6.1), position-velocity diagrams and channel-maps (Section 6.2). The observational data need to be compared with model calculations to be able to compare our theoretical knowledge with the observations. I used both LTE (KOSMA- τ) and non-LTE (RADEX-code) approaches to interpret the ob-

²⁰The NGC 3603 is a molecular cloud complex which consists of about a dozen smaller molecular clouds. In this thesis, I only focused on the two closest molecular clouds to the central OB cluster. One of them, MM1, is smaller and positioned roughly west relative to the central ionization source. The bigger cloud, MM2, is located to the south-east.

servational results (Sections 7.1 and 7.2).

At the beginning of this thesis (Section 1.1), I addressed a few specific questions related to NGC 3603, with the hope to better understand the physics and chemistry in the interstellar medium. In the following, I summarize the main conclusions for those questions.

What is the distribution of dust temperature and how is $N(\text{H}_2)$ distributed around the central cluster?

We used public PACS (70 μm and 160 μm) and SPIRE (250 μm , 350 μm and 500 μm) data from Hi-GAL survey to derive the dust temperatures. These wavelengths are tracers of cool dust except 70 μm , hence it was excluded from the SED-fitting²¹. The determined dust temperatures are in the range $\sim 30 - 40$ K which is in very good agreement with previous observations [35 K from Röllig et al. (2011) and 37 K from Wang & Chen (2010)]. Röllig et al. (2011) also presented a Spitzer 8 μm map which traces the hot PAHs. Comparing that map with the map I possess from the Herschel data, no significant difference appears between the hot and cool dust distributions which suggest the mixture of various temperature components. This may indicate small scale fluctuations of the dust opacity.

The column density of H_2 was derived by SED-fitting. In MM1 and MM2, the calculated $N(\text{H}_2)$ was relatively high ($2 \times 10^{22} \lesssim N(\text{H}_2) \lesssim 1 \times 10^{23} \text{ cm}^{-2}$), the higher column densities are from MM2. The $N(\text{H}_2)$ values were determined using optically thin low rotational transitions of C^{18}O ($2 \rightarrow 1$) from Nürnberger et al. (2002). The final results fall in the same regime, $N(\text{H}_2) \sim 10^{22} \text{ cm}^{-2}$. The comparison of the column density distribution of molecular hydrogen and the dust temperatures derived from the PACS and SPIRE data is shown in Fig. 5.4. It is noticeable from that plot that the peak and most of the $N(\text{H}_2)$ are shifted away from the central ionization source and, it seems, there is a “hydrogen-free” zone around the star cluster. This suggests that the molecular hydrogen has been blown away by strong stellar wind – provided by the hot, young and massive O- and early B-type stars – to the deeper part of the observed molecular clouds from the central OB cluster. This scenario is confirmed by several previous observations [e.g. (Balick et al., 1980; Clayton, 1986, 1990; Nürnberger & Petr-Gotzens, 2002; Vehoff et al., 2010)], showing a cavity/bubble around the central cluster.

As the formation of molecular hydrogen is highly efficient on dust grain surfaces, the grain temperature is an important parameter. Previous calculations showed [e.g. Röllig & Ossenkopf (2013) and Tielens (2005)] that molecular hydrogen can productively form on grains if $T_{\text{dust}} \approx 10 - 100$ K, thus H_2 forms efficiently in MM1 and MM2. As visible from Fig. 5.4, the

²¹Optically thin dust emission and a constant temperature for each pixel were assumed along the line of sight.

warmer dust is located closer to the cavity wall than $N(\text{H}_2)$, therefore it is possible that we see the surface layer traced by dust while the molecular hydrogen is coming from the deeper and cooler molecular part. On the other hand, another scenario can also exist. For example, if the $N(\text{H}_2)$ is high enough ($> 10^{14} \text{ cm}^{-2}$) the H_2 self-shielding effect becomes an important phenomenon. The photo-dissociation of molecular hydrogen could only be a relevant destruction process at the surface of the cloud, because of the shielding-effect. Hence, bigger amount of H_2 may exist in the deeper part.

Are the observed molecular clouds at the gravitationally stable or unstable stage?

After I calculated the column density of molecular hydrogen along the three cuts I defined in MM1 and MM2 (C1, C2 and C3), investigation of gravitational stability of the clouds was done by the derivations and comparisons of total gas, virial and Jeans masses. The average total gas mass is $M_{\text{gas}} \sim 1 \times 10^4 M_{\odot}$ which is lower than the averaged virial mass ($M_{\text{vir}} \sim 4 \times 10^4 M_{\odot}$), and this indicates that the observed clouds are not in virial equilibrium. In general, the relation between the kinetic (thermal) and gravitational energies is one of the most important parameters. To study that parameter, I investigated the virial parameter (Bertoldi & McKee, 1992; Tatematsu et al., 1993) which is the ratio of the virial and total gas masses ($\alpha = M_{\text{vir}}/M_{\text{gas}}$). Previous observations showed that the virial parameter is proportional to the gas mass with values $\alpha \approx M^{-0.67}$ (Bertoldi & McKee, 1992) and $\alpha \approx M^{-0.61}$ (Loren, 1989b). I also found a correlation, however, with a less steep slope ($\alpha \approx M^{-0.33}$).

The dense gas tracer HCO^+ line was used to calculate the velocity dispersion, thus Fig. 6.18 shows the connection between the kinetic and gravitational energies in a dense core within MM1 and MM2. This scenario is in agreement with Tatematsu et al. (1993) who found in the Orion Bar, based on observations of the another dense gas tracer CS, that the virial parameter is proportional to the gas mass with the value $\alpha \approx M^{-0.31}$. It supports the assumption that the massive clumps are not close to the virial equilibrium (Loren, 1989b). On the other hand, we need to keep in mind that, due to the spatially unresolved clouds, it is not possible to state which clumps (or parts of the clouds) are far from the virial equilibrium.

I derived the Jeans masses at different density ($n \sim 10^3 - 10^7 \text{ cm}^{-3}$) and temperature ($T \sim 20 - 500 \text{ K}$)²² regimes and found that the Jeans masses are higher than the virial and total gas masses only in the warmest and less dense layers in MM1 and MM2. This supports the scenario that the dense and cool regions are in a gravitationally unstable stage and star-formation is still ongoing. This result is in agreement with previous studies of NGC

²²We also derived the Jeans masses at relatively high temperature because of the observations of high- J ^{12}CO lines ($J_u > 13$).

3603 [e.g., [Nürnberg et al. \(2002\)](#) and [Röllig et al. \(2011\)](#)].

The usual free-fall time for molecular clouds is ($t_{\text{ff}} \sim 10^3 - 10^4$ yr). Assuming an average gas density $n \sim 10^5 \text{ cm}^{-3}$, the computed free-fall time is $t_{\text{ff}} \sim 10^5$ years which is slightly higher than the usual value. This could be if, for example, the kinetic energy is supported by ambient magnetic field, provided by massive O- and early B-type stars in MM1 and MM2 [e.g. [Nürnberg & Petr-Gotzens \(2002\)](#) and [Nürnberg & Stanke \(2003\)](#)], and cloud rotation. A density gradient can also play an important role because the collapse of the denser and smaller clumps is faster.

Are there any observable signatures of systematic gas motions and/or enhanced turbulent?

Most of the observed averaged line widths, based on the OTF observations, are significantly wider ($\sim 2 - 6 \text{ km s}^{-1}$) than the line widths expected from pure thermal gas motions ($\sim 0.1 - 1 \text{ km s}^{-1}$). Because NGC 3603 is a high-mass star-forming region which consists of several shock fronts, embedded infrared sources, masers and is probably heavily influenced by strong stellar wind, it is likely that the remaining line widths are footprints of turbulent gas motions²³. As I mentioned, NGC 3603 (more precisely MM1 and MM2) incorporates 6 shock fronts (Fig. 8.1) which can be characterized by the ratio of the velocity of the moving source (e.g., shock front) and the local sound speed. The derivation of this ratio, the Mach-number, showed that the shock fronts in MM1 and MM2 is putatively supersonic ($\mathcal{M} \sim 2$). Please note, that the error budget of the Mach-number calculation could be fairly high due to the uncertain temperatures and the large solid angle. Observation of SiO with higher resolution could help in the investigation of shock fronts because if their speed is high enough ($v_{\text{SF}} \geq 25 \text{ km s}^{-1}$) than the grains sputter and the amount of gas-phase SiO is enhanced ([Gusdorf et al., 2008a,b](#)).

The analysis of velocity channel maps is suggested the rotation/torsion of the observed molecular clumps. To quantify the rotation/torsion, I fitted an ellipse to emission which exceeds at least 30% of the peak emission (Fig. 8.2) and studied the rotational angle of the major axis as a function of velocity (Fig. 8.3). The investigation led to the conclusion that the CS line probably originates from a very dense core which is located deeply inside the observed molecular clouds and not influenced by stellar winds and/or shock fronts. The other dense gas tracer HCO^+ , together with the diffuse gas tracers CH and C_2H , are clearly affected by the aforementioned phenomena. Hence, I concluded that either HCO^+ traces the envelope of dense core traced by CS or, due to the clumpiness of MM1 and MM2, HCO^+ traces a dense clump which is located close to the cloud surface, perturbed by stellar winds. The outskirts of the molecular clouds

²³The observed line widths are also affected by the natural, collisional and electromagnetic (i.e. Zeeman and Stark) effects but these are much weaker in PDRs.

are probably traced by CH and C₂H and heavily affected by shock fronts and stellar wind. The detailed analysis of the PV–diagrams could not support the “rotation-theory” of the clouds²⁴. Furthermore, I also investigated the distribution of line-center velocities but did not find any signature of cloud rotation. Thus, I concluded that channel maps and PV–diagrams can be used to receive geometrical information, and MM1 and MM2 are probably curled rather than rotating as a rigid body. Note, that the stellar wind could also be trailed on PV–diagrams. Figures 6.3 and 6.4 provide information, and confirms, that CS is less affected by stellar winds in both MM1 and MM2.

Is there any observable influence of prominent embedded infrared sources on the physics and chemistry of the observed molecular clouds?

Previous studies [e.g. (Nürnberg & Petr-Gotzens, 2002; Nürnberg & Stanke, 2003; Nürnberg, 2003)] found prominent infrared sources (O- and early B-type stars) within MM1 (IRS1 and IRS14) and MM2 (IRS9-complex and IRS2) which are plotted on Fig. 8.4. As the hot and massive stars are vigorous sources of high-energy photons, these stars ionize their adjacent environment, hence influence the physics and chemistry within a certain spatial range. To approximate the size of the sphere where the local physical and chemical conditions are governed by an embedded star, I derived the Strömgren-radius (R_S) in the case of IRS9-A which is believed to be the most luminous ($\sim 2.3 \times 10^5 L_\odot$) from all the IRS-sources in MM1 and MM2, hence its R_S should be the biggest. For the calculations, I take into consideration that the region is spherically symmetric and the gas within R_S is fully ionized and consists of hydrogen only.

Nürnberg & Stanke (2003) found a somewhat low L_{Ly} value ($\sim 10^{40} \text{ s}^{-1}$), hence I kept this as a lower limit, and an effective temperature of $\gtrsim 2 \times 10^4 \text{ K}$ for IRS9-A. Utilizing these parameters and assuming $n(H) \sim 10^3 \text{ cm}^{-3}$, the derived Strömgren-radius is $R_S < 0.1 \text{ pc}$. As L_{Ly} and T_{eff} seem to be sort of low values for an early B-type star, I derived R_S applying values $T_{\text{eff}} \sim 3 \times 10^4 \text{ K}$ and $L_{Ly} \sim 10^{47} - 10^{48}$ photon per second presuming B0-B0.5 stars and solar metallicity (Sternberg et al., 2003). With these assumptions, the Strömgren-radii are $\sim 2.7 - 5.6 \text{ pc}$, corresponding to $76'' - 158''$ (using a distance of 7.3 kpc). Comparing the sizes of the derived Strömgren-radii and of the beam, I concluded that the physics and chemistry (dominated by the embedded sources) are not detectable even at the closest position to IRS9-A (position 4 in the cut C2 on Fig. 8.4).

²⁴If we assume a Keplerian rotation, the line emission distribution should reflect on it on the PV–diagram (Brinch et al., 2008).

Are the model predictions of line intensities and densities, and observations in good agreement?

To compare the observed line intensities of ^{12}CO rotational transitions ($4 \rightarrow 3, 7 \rightarrow 6, 9 \rightarrow 8, 13 \rightarrow 12, 14 \rightarrow 13, 15 \rightarrow 14$ and $16 \rightarrow 15$), of ^{13}CO ($10 \rightarrow 9$) and of various cooling lines (e.g., [OI], [CI] and [CII]) with both LTE (KOSMA- τ) and non-LTE (RADEX) models, I assumed different geometries. Based on the results, the best model fits are independent from the geometry of the molecular cloud in terms of clumpiness. As a consequence, it is indistinguishable that the beam is filled with only one clump or filled by numerous but smaller clumps.

With the KOSMA- τ , the ^{12}CO rotational and cooling lines were fitted by a two-ensemble model (Fig. 7.4). The gas densities were $n \sim 10^5 - 10^6 \text{ cm}^{-3}$ in MM1 and MM2 which are lower than found by Röllig et al. (2011) applying escape probability calculations ($n \sim 10^3 - 10^4 \text{ cm}^{-3}$). The discrepancy is probably originates from beam dilution effects. The $n \sim 10^6 \text{ cm}^{-3}$ is in agreement with the assumption that high temperature ($T \approx 500 \text{ K}$) and density ($n \sim 10^7 \text{ cm}^{-3}$) are needed to excite high- J ^{12}CO lines [e.g. Hollenbach & Tielens (1997) and Stacey et al. (1993)].

Röllig et al. (2011) found a strong UV-field ($\chi_D \sim 10^3$) in MM1 and MM2 from HIRES/IRAS data. I derived the UV-field strength from PACS and SPIRE data ($70 \mu\text{m}$ and $160 \mu\text{m}$), and from KOSMA- τ model. In general, with the enhancement of distance from the ionization source the FUV-field becomes attenuated, thus a reduction of the FUV-field is expected. In conjunction with Röllig et al. (2011), I did not find such a trend in neither MM1 nor MM2. However, as I assumed that all FUV-photons are absorbed by grains and re-emitted in the infrared regime, the resulting FUV-field map (Fig. 5.5) is the composition of the external (from the central OB cluster) and internal (from the embedded sources) FUV-photons where the beam dilution effect is also super-positioned. This can be an explanation for the higher UV-field strength that I derived from the Herschel data ($\chi_D \sim 10^4$). The calculated χ_D by KOSMA- τ was in agreement with previous studies from Röllig et al. (2011) for the warm gas component ($\chi_D \sim 10^3$). To reproduce the emission line intensities of moderately warm gas, a lower FUV-field was sufficient ($\chi_D \sim 10$) which is expected if I assume that that the observed lower- J ^{12}CO lines trace denser and cooler layers where the FUV-photons cannot penetrate efficiently enough. But again, beam filling factor plays an important role and needs to be taken into account.

With the RADEX non-LTE code, the line intensities were well fitted with a two-component model, applying unity beam filling. The resulting volume gas density is slightly lower ($n \sim 10^4 - 10^5 \text{ cm}^{-3}$) than from KOSMA- τ . On the other hand, the lower gas densities likely caused by the fact that, due to the unity beam filling, we probably observed the mixture of dense cores (with small filling factors) and diffuse gas (which dominates the beam). Because the high- J ^{12}CO rotational lines ($J_u \gtrsim 14$) need high temperature ($T \gtrsim 400 \text{ K}$) and high density ($n \gtrsim 10^7 \text{ cm}^{-3}$), I applied these values to

RADEX model and investigated the results. In the case of high density, the output gas temperature is similar to the values that I received from the rotational diagrams. At high temperature, the calculated volume density ($n \sim 10^5 \text{ cm}^{-3}$) was also in good agreement with previous derivations. Because the gas pressure is a good parameter to characterize a star-forming region (Nagy et al., 2012), I estimated the gas pressure based on the derived gas densities and temperatures in MM1 and MM2. The output of these calculations ($P/k \sim 10^5 - 10^9 \text{ K cm}^{-3}$) is roughly consistent²⁵ with pressure values that have been found in other high-mass star-forming regions, i.e. Orion Bar [$P/k \lesssim 10^8 \text{ K cm}^{-3}$, (Nagy et al., 2012)] and Sgr B2 [$P/k \sim 10^7 \text{ K cm}^{-3}$, (de Vicente et al., 1997)].

Notable differences were observed (Fig. 7.4 and 7.2) between the line intensities from modelling and observations in cases of ^{12}CO and ^{13}CO , assuming the elemental ratio $^{12}\text{C}/^{13}\text{C} \approx 67$. From KOSMA- τ , if the line ratios are $\mathfrak{R} \sim 3.9$ and $\mathfrak{R} \sim 5.6$ (for MM2-IF and MM1-IF, respectively), the model is able to fit the observed line intensities at $J = 10$. In case of the RADEX-code, these values are $\mathfrak{R} \sim 2.3$ and $\mathfrak{R} \sim 2.1$. Röllig & Ossenkopf (2013) analysed the distribution of line ratio $\mathfrak{R} = ^{12}\text{CO}(J \rightarrow J - 1)/^{13}\text{CO}(J \rightarrow J - 1)$ as a function of upper rotational state (J_u) at different gas densities and FUV-field strengths (Fig. 8.5). The low line ratios I received imply high density and FUV-field ($n \sim 10^5 - 10^6 \text{ cm}^{-3}$ and $\chi_D \sim 10^4 - 10^5$, respectively). The density regime correlates well with previous values but the UV-field strength is marginally higher than what I received from KOSMA- τ and the Herschel observations. Taking into account that we investigate dense PDRs, the line ratio should be $\mathfrak{R} \lesssim 10 - 15$. I interpreted the low line ratios as an optical depth effect, namely the main carbon-monoxide isotope is optically thick while its rarer isotope is marginally²⁶ optically thin.

Is there any observable chemical stratification? Are the observed abundances comparable with model predictions?

For classical edge-on PDRs $\text{C}^+ - \text{C} - \text{CO}$ layering is expected, however, in case of clumpy molecular cloud this chemical stratification should not be observed (Stutzki et al., 1988). The distribution of the peak line emissions as a function of projected distance from the central OB cluster (Fig. 8.6) might indicate such a layering structure in MM1 and MM2. The high- J ^{12}CO lines are peaked closer to the ionization source than the lower- J lines. Beside this result, I did not find any clear evidence for $\text{C}^+ - \text{C} - \text{CO}$ layering. Because the gas density is lower than the critical density of CS ($11 \rightarrow 10$), the excitation process is probably radiative pumping rather than collision. This and the fact that the peak line emission is far from the OB cluster ($\sim 3 \text{ pc}$) supports the scenario that the observed molecular clouds

²⁵The error budget could be an order of magnitude (Greve et al., 2009).

²⁶If both lines were optically thick, the line ratio would be 1. But the result line ratios only a bit higher than unity.

are clumpy. Thus, FUV-photons can penetrate inside the clouds and illuminate the surface of dense clumps where CS ($11 \rightarrow 10$) may originate. Within one beam size, strong mixture of different gas tracers (i.e. dense and diffuse gas) and dust can be found which is in agreement with [Okada et al. \(2010\)](#) who found, based on low- J CS lines²⁷, radio, MIR and FIR continuum data, a mixture of warm dust and ionized, and molecular gas in NGC 3603. On the other hand, this compound of different species makes it impossible to further conclude about the chemical stratification/structure of NGC 3603.

The relative densities of few species (CS, HCO^+ , CH and C_2H) were modelled with the KOSMA- τ model at different densities and UV-field strengths (Fig. 8.7). For the diffuse gas tracers, CH and C_2H , the model calculations predict similar abundance distribution. The derived abundances (from the OTF observations) in MM1 and MM2 are $\sim 10^{-7}$ and 10^{-9} for CH and C_2H , respectively. This abundance is in agreement with the model predictions. As the CH line is supposed to trace the outskirts of the PDRs (or the diffuse clouds), this result indicates that CH and C_2H traces the less dense ($n \sim 10^4 \text{ cm}^{-3}$) and highly illuminated ($\chi_D \sim 10^4$) outer layer(s) of the PDRs rather than the diffuse gas ($n < 10^3 \text{ cm}^{-3}$) in which MM1 and MM2 are embedded. The derived abundances of dense gas tracers, CS and HCO^+ , are identical ($\sim 10^{-11}$) while the model calculations predict significant differences even at high depth ($A_V \gtrsim 4 - 5$). The underabundance of the CS line indicates an efficient destruction mechanism. For example, photo-dissociation ($\text{CS} + h\nu \rightarrow \text{C} + \text{S}$) and photo-ionization ($\text{CS} + h\nu \rightarrow \text{CS}^+ + e^-$) can destroy CS efficiently if I assume a clumpy geometry. In that case, FUV-photons can penetrate deeper inside the clouds (even to $A_V \sim 3 - 8$) and heavily influence the surface of dense clumps within MM1 and MM2. In the high density and UV-field model ($n = 10^7 \text{ cm}^{-3}$ and $\chi_D = 10^4$), at high depth ($A_V \sim 7$), the abundances of CS and HCO^+ become roughly equal with a value of $\sim 10^{-11}$.

The high density and UV-field model also predicted the shifts of the H/H_2 and C^+/CO transitional layers. [Maloney et al. \(1996\)](#) found similar “behaviour” in case of X-ray Dominated Regions (XDRs). In their studies, essentially, the H/H_2 layer, due to the evenly dominant H_2 abundance, is positioned at the same depth of the clouds. But the C^+/CO layer is significantly shifted toward the ionization source because the abundance of the ^{12}CO is increased steeply. It is caused by the higher temperature which increases the formation rate. As the observed molecular clouds include numerous shock fronts, massive young embedded stars and stars which are probably members of the central OB cluster, significantly high enough X-ray photons can be presented in MM1 and MM2. Nevertheless, I cannot discard neither the scenario that the physics and chemistry in the densest region of MM1 and MM2 ($n \gtrsim 10^6 - 10^7 \text{ cm}^{-3}$) are dominated by FUV-

²⁷The CS ($3 \rightarrow 2, 2 \rightarrow 1$) data are from [Nürnberg et al. \(2002\)](#).

photons (provided by the OB cluster and the embedded sources) nor the assumption that the physical and chemical conditions are governed by the X-ray photons (together with cosmic rays).

The detailed investigations of the two closest molecular clouds (MM1 and MM2) of the high-mass star-forming complex NGC 3603 give the opportunity to characterize the physical conditions and chemical stratification. Most of the observational results I received from the data of the Herschel Space Observatory are in good agreement with previous, ground-based observations and with model calculations. Due to the observational limitations caused by the beam size and the distance of the celestial source, I was only able to establish statements within certain limits.

References

- Aannestad, P. A. 1973, *Astrophysical Journal Supplement Series*, 25, 223
- Abel, N. P. 2006, *Monthly Notices of the Royal Astronomical Society*, 368, 1949
- Abel, N. P., Ferland, G. J., Shaw, G., & van Hoof, P. A. M. 2005, *Astrophysical Journal Supplements*, 161, 65
- Abel, N. P., Sarma, A. P., Troland, T. H., & Ferland, G. J. 2007, *Astrophysical Journal*, 662, 1024
- Altieri, B. & Vavrek, R. 2011, *PACS observer's manual*, 2nd edn., ESAC
- Bakes, E. L. O. & Tielens, A. G. G. M. 1994, *Astrophysical Journal*, 427, 822
- Balick, B., Boeshaar, G. O., & Gull, T. R. 1980, *Astrophysical Journal*, 242, 584
- Bardeau, S., Pety, J., Hily-Blant, P., et al. 2006, *Continuum and Line Analysis Single-dish Software*, Tech. rep., Institut de Radioastronomie Millimétrique
- Bertoldi, F. & Draine, B. T. 1996, *The Astrophysical Journal*, 458, 222
- Bertoldi, F. & McKee, C. F. 1992, *Astrophysical Journal*, 395, 140
- Bjerkeli, P., Liseau, R., Nisini, B., et al. 2013, *Astronomy & Astrophysics*, 552, L8
- Brandner, W., Grebel, E. K., Chu, Y.-H., et al. 2000, *Astronomical Journal*, 119, 292

- Brinch, C., Hogerheijde, M. R., & Richling, S. 2008, *Astronomy & Astrophysics*, 489, 607
- Brunt, C. M., Heyer, M. H., & Mac Low, M.-M. 2009, *Astronomy & Astrophysics*, 504, 883
- Burke, J. R. & Hollenbach, D. J. 1983, *Astrophysical Journal*, 265, 223
- Cazaux, S. & Tielens, A. G. G. M. 2004, *The Astrophysical Journal*, 604, 222
- Clayton, C. A. 1986, *Monthly Notices of the Royal Astronomical Society*, 219, 895
- Clayton, C. A. 1990, *Monthly Notices of the Royal Astronomical Society*, 246, 712
- Clemens, D. P. 1985, *Astrophysical Journal*, 295, 422
- Corcoran, M. F., Moffat, A., Mushotzky, R., et al. 2000, in *Bulletin of the American Astronomical Society*, Vol. 32, American Astronomical Society Meeting Abstracts, 1456
- Cox, N. L. J. & Spaans, M. 2006, *Astronomy & Astrophysics*, 451, 973
- Cubick, M., Stutzki, J., Ossenkopf, V., Kramer, C., & Röllig, M. 2008, *Astronomy & Astrophysics*, 488, 623
- Davidson, S. A., Evenson, K. M., & Brown, J. M. 2001, *The Astrophysical Journal*, 546, 330
- de Almeida, A. A. 1990, *Revista Mexicana de Astronomia y Astrofisica*, 21, 499
- de Almeida, A. A. & Singh, P. D. 1981, *Astronomy & Astrophysics*, 95, 383
- De Beck, E., Lombaert, R., Agúndez, M., et al. 2012, *Astronomy & Astrophysics*, 539, A108
- de Graauw, T., Helmich, F. P., Phillips, T. G., et al. 2010, *Astronomy & Astrophysics*, 518, L6
- de Vicente, P., Martín-Pintado, J., & Wilson, T. L. 1997, *Astronomy & Astrophysics*, 320, 957
- Draine, B. T. 2011, *Princeton Series in Astrophysics*, Vol. 146, *Physics of the Interstellar and Intergalactic Medium* (Princeton University Press)
- Drissen, L., Moffat, A. F. J., Walborn, N. R., & Shara, M. M. 1995, *Astronomical Journal*, 110, 2235

- Ferrario, L., Pringle, J. E., Tout, C. A., & Wickramasinghe, D. T. 2009, *Monthly Notices of the Royal Astronomical Society*, 400, L71
- Fixsen, D. J. 2009, *The Astrophysical Journal*, 707, 916
- Frerking, M. A., Langer, W. D., & Wilson, R. W. 1982, *The Astrophysical Journal*, 262, 590
- Frogel, J. A., Persson, S. E., & Aaronson, M. 1977, *The Astrophysical Journal*, 213, 723
- Fuente, A., Caselli, P., McCoey, C., et al. 2012, *Astronomy & Astrophysics*, 540, A75
- Gerin, M., Kaźmierczak, M., Jastrzebska, M., et al. 2011, *Astronomy & Astrophysics*, 525, A116
- Glenn, J. & Hunter, T. R. 2001, *The Astrophysical Journal Supplement Series*, 135, 177
- Goicoechea, J. R. & Le Bourlot, J. 2007, *Astronomy & Astrophysics*, 467, 1
- Goldsmith, P. F. & Langer, W. D. 1999, *Astrophysical Journal*, 517, 209
- Grabelsky, D. A., Cohen, R. S., Bronfman, L., & Thaddeus, P. 1988, *Astrophysical Journal*, 331, 181
- Graves, S. F., Richer, J. S., Buckle, J. V., et al. 2010, *Monthly Notices of the Royal Astronomical Society*, 409, 1412
- Greve, T. R., Papadopoulos, P. P., Gao, Y., & Radford, S. J. E. 2009, *The Astrophysical Journal*, 692, 1432
- Griffin, M. J., Abergel, A., Abreu, A., et al. 2010, *Astronomy & Astrophysics*, 518, L3
- Gusdorf, A., Anderl, S., Güsten, R., et al. 2012, *Astronomy & Astrophysics*, 542, L19
- Gusdorf, A., Cabrit, S., Flower, D. R., & Pineau Des Forêts, G. 2008a, *Astronomy & Astrophysics*, 482, 809
- Gusdorf, A., Pineau Des Forêts, G., Cabrit, S., & Flower, D. R. 2008b, *Astronomy & Astrophysics*, 490, 695
- Habart, E., Dartois, E., Abergel, A., et al. 2010, *Astronomy & Astrophysics*, 518, L116
- Haikala, L. K., Juvela, M., Harju, J., et al. 2006, *Astronomy & Astrophysics*, 454, L71

- Hall, J. L., Baer, T., Hollberg, L., & Robinson, H. G. 1981, Springer Series in Optical Sciences, Vol. 30, Precision Spectroscopy and Laser Frequency Control Using FM Sideband Heterodyne Techniques (Springer Berlin Heidelberg), 15–24
- Harayama, Y., Eisenhauer, F., & Martins, F. 2008, *Astrophysical Journal*, 675, 1319
- Heiles, C. 1994, *Astrophysical Journal*, 436, 720
- Heithausen, A., Bensch, F., Stutzki, J., Falgarone, E., & Panis, J. F. 1998, *Astronomy & Astrophysics*, 331, L65
- Helder, E. A., Vink, J., & Bassa, C. G. 2011, *The Astrophysical Journal*, 737, 85
- Helfer, T. T. & Blitz, L. 1995, *The Astrophysical Journal*, 450, 90
- Herzberg, G. 1991, *Molecular spectra and Molecular structure III. Electronic spectra and electronic structure of polyatomic molecules* (Malabar: Krieger Publishing Company Inc.)
- Herzberg, G. 2010, *Atomic spectra and atomic structure* (New York: Dover Publications)
- Hily-Blant, P. 2006, *CLASS: Continuum and Line Analysis Single-dish Software*, 1st edn., IRAM
- Hitschfeld, M., Aravena, M., Kramer, C., et al. 2008, *Astronomy & Astrophysics*, 479, 75
- Hogerheijde, M. R. & van der Tak, F. F. S. 2000, *Astronomy & Astrophysics*, 362, 697
- Hollenbach, D. J. & Tielens, A. G. G. M. 1997, *Annual Review of Astronomy & Astrophysics*, 35, 179
- Hollenbach, D. J. & Tielens, A. G. G. M. 1999, *Reviews of Modern Physics*, 71, 173
- Huggins, P. J., Carlson, W. J., & Kinney, A. L. 1984, *Astronomy & Astrophysics*, 133, 347
- Israel, F. P., Guesten, R., Meijerink, R., et al. 2014, ArXiv e-prints
- Jackson, B., Kester, D., Ossenkopf, V., et al. 2007, *HIFI observer's manual*, 1st edn.
- Jansky, K. G. 1933, *Nature*, 132, 66

- Kainulainen, J., Lehtinen, K., & Harju, J. 2006, *Astronomy & Astrophysics*, 447, 597
- Kaufman, M. J., Wolfire, M. G., & Hollenbach, D. J. 2006, *Astrophysical Journal*, 644, 283
- Kaufman, M. J., Wolfire, M. G., Hollenbach, D. J., & Luhman, M. L. 1999, *Astrophysical Journal*, 527, 795
- Keene, J., Blake, G. A., Phillips, T. G., Huggins, P. J., & Beichman, C. A. 1985, *The Astrophysical Journal*, 299, 967
- Keene, J., Schilke, P., Kooi, J., et al. 1998, *Astrophysical Journal Letters*, 494, L107
- Knapp, G. R. & Bowers, P. F. 1988, *The Astrophysical Journal*, 331, 974
- Kramer, C., Cubick, M., Röllig, M., et al. 2008, *Astronomy & Astrophysics*, 477, 547
- Kroger, H. 1967, *Avalanche Mode Photodiodes for Heterodyne Techniques at 1.06 Microns* (Defense Technical Information Center)
- Lacki, B. C. 2013, *Monthly Notices of the Royal Astronomical Society*, 431, 3003
- Larson, R. B. 1981, *Monthly Notices of the Royal Astronomical Society*, 194, 809
- Le Petit, F., Nehmé, C., Le Bourlot, J., & Roueff, E. 2006, *The Astrophysical Journal Supplement Series*, 164, 506
- Lebouteiller, V., Brandl, B., Bernard-Salas, J., Devost, D., & Houck, J. R. 2007, *Astrophysical Journal*, 665, 390
- Liseau, R., Justtanont, K., & Tielens, A. G. G. M. 2006, *Astronomy & Astrophysics*, 446, 561
- Liseau, R., Larsson, B., Bergman, P., et al. 2010, *Astronomy & Astrophysics*, 510, A98
- Loren, R. B. 1989a, *The Astrophysical Journal*, 338, 902
- Loren, R. B. 1989b, *The Astrophysical Journal*, 338, 925
- Maciel, W. J. 1995, *Astrophysics and Space Science*, 229, 203
- Maeder, A. & Meynet, G. 2005, *Astronomy & Astrophysics*, 440, 1041
- Maloney, P. R., Hollenbach, D. J., & Tielens, A. G. G. M. 1996, *The Astrophysical Journal*, 466, 561

- Martin, P. G. & Mandy, M. E. 1995, *Astrophysical Journal Letters*, 455, L89
- Martin, P. G., Schwarz, D. H., & Mandy, M. E. 1996, *Astrophysical Journal*, 461, 265
- Matsuhara, H., Tanaka, M., Yonekura, Y., et al. 1997, *Astrophysical Journal*, 490, 744
- Melena, N. W., Massey, P., Morrell, N. I., & Zangari, A. M. 2008, *Astronomical Journal*, 135, 878
- Melnick, G., Gull, G. E., & Harwit, M. 1979, *Astronomical Journal*, 227, L29
- Melnick, J. 1978, *Astronomy & Astrophysics*, 70, 157
- Melnick, J. 1989, *The Messenger*, 57, 4
- Menzies, R. T. 1976, *Topics in Applied Physics*, Vol. 14, *Laser heterodyne detection techniques* (Springer Berlin Heidelberg), 297–353
- Mihalas, D. 1978, *Stellar atmospheres*, 2nd edn. (San Francisco: Freeman & co.)
- Minchin, N. R., White, G. J., Stutzki, J., & Krause, D. 1994, *Astronomy & Astrophysics*, 291, 250
- Mizutani, M., Onaka, T., & Shibai, H. 2004, *Astronomy & Astrophysics*, 423, 579
- Moffat, A. F. J., Corcoran, M. F., Stevens, I. R., et al. 2002, *Astrophysical Journal*, 573, 191
- Moffat, A. F. J., Seggewiss, W., & Shara, M. M. 1985, *Astrophysical Journal*, 295, 109
- Molinari, S., Swinyard, B., Bally, J., et al. 2010, *The Publications of the Astronomical Society of the Pacific*, 122, 314
- Mookerjea, B., Kramer, C., Buchbender, C., et al. 2011, *Astronomy & Astrophysics*, 532, A152
- Mücke, A., Koribalski, B. S., Moffat, A. F. J., Corcoran, M. F., & Stevens, I. R. 2002, *Astrophysical Journal*, 571, 366
- Nagy, Z., van der Tak, F. F. S., Fuller, G. A., Spaans, M., & Plume, R. 2012, *Astronomy & Astrophysics*, 542, A6
- Nagy, Z., Van der Tak, F. F. S., Ossenkopf, V., et al. 2013, *Astronomy & Astrophysics*, 550, A96

- Nahin, P. J. 2001, *The science of radio with MATLAB and ELECTRONICS WORKBRANCH* (Springer-Verlag New York, Inc.), 297–353
- Nakamura, F. & Li, Z.-Y. 2008, *The Astrophysical Journal*, 687, 354
- Nürnbergger, D. E. A. 2003, *Astronomy & Astrophysics*, 404, 255
- Nürnbergger, D. E. A. 2008, *Journal of Physics Conference Series*, 131, 012025
- Nürnbergger, D. E. A., Bronfman, L., Yorke, H. W., & Zinnecker, H. 2002, *Astronomy & Astrophysics*, 394, 253
- Nürnbergger, D. E. A. & Petr-Gotzens, M. G. 2002, *Astronomy & Astrophysics*, 382, 537
- Nürnbergger, D. E. A. & Stanke, T. 2003, *Astronomy & Astrophysics*, 400, 223
- Nürnbergger, D. E. A., Vehoff, S., Hummel, C. A., & Duschl, W. J. 2010, in *Revista Mexicana de Astronomia y Astrofisica Conference Series*, Vol. 38, *Revista Mexicana de Astronomia y Astrofisica Conference Series*, 71–73
- Okada, Y., Kawada, M., Murakami, N., et al. 2010, *Astronomy & Astrophysics*, 514, A13
- Omont, A., Neri, R., Cox, P., et al. 2011, *Astronomy & Astrophysics*, 530, L3
- Ossenkopf, V. 2002, *Astronomy & Astrophysics*, 391, 295
- Ossenkopf, V., Gerin, M., Rolf, G., et al. 2010a, in *COSPAR Meeting*, Vol. 38, *38th COSPAR Scientific Assembly*, 2478
- Ossenkopf, V., Röllig, M., Cubick, M., & Stutzki, J. 2007, in *Molecules in Space and Laboratory*
- Ossenkopf, V., Röllig, M., Kramer, C., et al. 2011, in *EAS Publications Series*, Vol. 52, *EAS Publications Series*, ed. M. Röllig, R. Simon, V. Ossenkopf, & J. Stutzki, 181–186
- Ossenkopf, V., Röllig, M., Neufeld, D. A., et al. 2013, *Astronomy & Astrophysics*, 550, A57
- Ossenkopf, V., Röllig, M., Simon, R., et al. 2010b, *Astronomy & Astrophysics*, 518, L79
- Osterbrock, D. E. & Ferland, G. J. 2006, *Astrophysics of gaseous nebulae and active galactic nuclei*

- Ott, S. 2010, in *Astronomical Society of the Pacific Conference Series*, Vol. 434, *Astronomical Data Analysis Software and Systems XIX*, ed. Y. Mizumoto, K.-I. Morita, & M. Ohishi, 139
- Pahre, M. A., Ashby, M. L. N., Fazio, G. G., & Willner, S. P. 2004, *The Astrophysical Journal Supplement Series*, 154, 229
- Papadopoulos, P. P., van der Werf, P. P., Xilouris, E. M., et al. 2012, *Monthly Notices of the Royal Astronomical Society*, 426, 2601
- Pellegrini, E. W., Baldwin, J. A., Ferland, G. J., Shaw, G., & Heathcote, S. 2009, *The Astrophysical Journal*, 693, 285
- Pérez-Beaupuits, J. P., Wiesemeyer, H., Ossenkopf, V., et al. 2012, *Astronomy & Astrophysics*, 542, L13
- Persi, P., Ferrari-Toniolo, M., Tapia, M., & Roth, M. 1985, *Astronomy & Astrophysics*, 144, 275
- Pety, J. 2005, in *SF2A-2005: Semaine de l'Astrophysique Française*, ed. F. Casoli, T. Contini, J. M. Hameury, & L. Pagani, 721
- Pety, J., Teyssier, D., Fossé, D., et al. 2005, *Astronomy & Astrophysics*, 435, 885
- Phillips, T. G. & Huggins, P. J. 1981, *Astrophysical Journal*, 251, 533
- Pilbratt, G. L., Riedinger, J. R., Passvogel, T., et al. 2010, *Astronomy & Astrophysics*, 518, L1
- Poglitsch, A., Waelkens, C., Geis, N., et al. 2010, *Astronomy & Astrophysics*, 518, L2
- Pound, M. W. 1998, *Astrophysical Journal Letters*, 493, L113
- Ridge, N. A., Wilson, T. L., Megeath, S. T., Allen, L. E., & Myers, P. C. 2003, *The Astronomical Journal*, 126, 286
- Ripple, F., Heyer, M. H., Gutermuth, R., Snell, R. L., & Brunt, C. M. 2013, *Monthly Notices of the Royal Astronomical Society*, 431, 1296
- Robert, C. & Pagani, L. 1993, *Astronomy & Astrophysics*, 271, 282
- Roccatagliata, V., Preibisch, T., Ratzka, T., & Gaczkowski, B. 2013, *Astronomy & Astrophysics*, 554, A6
- Roelfsema, P. R., Helmich, F. P., Teyssier, D., et al. 2012, *Astronomy & Astrophysics*, 537, A17
- Röllig, M., Abel, N. P., Bell, T., et al. 2007, *Astronomy & Astrophysics*, 467, 187

- Röllig, M., Kramer, C., Rajbahak, C., et al. 2011, *Astronomy & Astrophysics*, 525, A8
- Röllig, M. & Ossenkopf, V. 2013, *Astronomy & Astrophysics*, 550, A56
- Röllig, M., Ossenkopf, V., Jeyakumar, S., Stutzki, J., & Sternberg, A. 2006, *Astronomy & Astrophysics*, 451, 917
- Röllig, M., Szczerba, R., Ossenkopf, V., & Glück, C. 2013, *Astronomy & Astrophysics*, 549, A85
- Roman-Duval, J., Jackson, J. M., Heyer, M., et al. 2009, *The Astrophysical Journal*, 699, 1153
- Roussel, H. 2013, *The Publications of the Astronomical Society of the Pacific*, 125, 1126
- Russeil, D., Schneider, N., Anderson, L. D., et al. 2013, *Astronomy & Astrophysics*, 554, A42
- Rybicki, G. B. & Lightman, A. B. 2004, *Radiative processes in astrophysics* (Weinheim: Wiley-VCH Verlag GmbH & Co. KgaA)
- Sagar, R., Munari, U., & de Boer, K. S. 2001, *Monthly Notices of the Royal Astronomical Society*, 327, 23
- Sage, L. J. & Isbell, D. W. 1991, *Astronomy & Astrophysics*, 247, 320
- San Jose-Garcia, I., Mottram, J. C., Kristensen, L. E., et al. 2013, *ArXiv e-prints*
- Schieder, R. 2010, *Technical note on HIFI mapping modes*
- Schneider, N., Bontemps, S., Simon, R., et al. 2011, *Astronomy & Astrophysics*, 529, A1
- Schneider, N., Güsten, R., Tremblin, P., et al. 2012, *Astronomy & Astrophysics*, 542, L18
- Schöier, F. L., van der Tak, F. F. S., van Dishoeck, E. F., & Black, J. H. 2005, *Astronomy & Astrophysics*, 432, 369
- Schultz, J. 2004, *Fabrication Techniques for Heterodyne Mixer Chips and Devices* (University of Virginia)
- Scoville, N. Z. & Solomon, P. M. 1974, *Astrophysical Journal Letters*, 187, L67
- Sheth, K., Vogel, S. N., Regan, M. W., Thornley, M. D., & Teuben, P. J. 2005, *The Astrophysical Journal*, 632, 217

- Shibatsuka, T., Matsushita, S., Kohno, K., & Kawabe, R. 2003, *Publications of the Astronomical Society of Japan*, 55, 87
- Simon, R. 1997, PhD thesis, University of Cologne
- Spezzi, L., Beccari, G., De Marchi, G., et al. 2011, *Astrophysical Journal*, 731, 1
- Stacey, G. J., Hailey-Dunsheath, S., Ferkinhoff, C., et al. 2010, *Astrophysical Journal*, 724, 957
- Stacey, G. J., Jaffe, D. T., Geis, N., et al. 1993, *Astrophysical Journal*, 404, 219
- Stark, A. A. & Brand, J. 1989, *The Astrophysical Journal*, 339, 763
- Sternberg, A. 1988, *The Astrophysical Journal*, 332, 400
- Sternberg, A. & Dalgarno, A. 1989, *The Astrophysical Journal*, 338, 197
- Sternberg, A. & Dalgarno, A. 1995, *Astrophysical Journal Supplements*, 99, 565
- Sternberg, A., Hoffmann, T. L., & Pauldrach, A. W. A. 2003, *The Astrophysical Journal*, 599, 1333
- Sternberg, A., Yan, M., & Dalgarno, A. 1997, in *IAU Symposium*, Vol. 178, *IAU Symposium*, ed. E. F. van Dishoeck, 141
- Stevens, I. R., Corcoran, M. F., & Moffat, A. F. J. 2002, in *Astronomical Society of the Pacific Conference Series*, Vol. 260, *Interacting Winds from Massive Stars*, ed. A. F. J. Moffat & N. St-Louis, 343
- Stoerzer, H., Stutzki, J., & Sternberg, A. 1996, *Astronomy & Astrophysics*, 310, 592
- Stolte, A., Brandner, W., Brandl, B., Zinnecker, H., & Grebel, E. K. 2004, *Astronomical Journal*, 128, 765
- Strömgren, B. 1939, *The Astrophysical Journal*, 89, 526
- Stutzki, J. 1999, in *The Physics and Chemistry of the Interstellar Medium*, ed. V. Ossenkopf, J. Stutzki, & G. Winnewisser, 203
- Stutzki, J., Bensch, F., Heithausen, A., Ossenkopf, V., & Zielinsky, M. 1998, *Astronomy & Astrophysics*, 336, 697
- Stutzki, J., Stacey, G. J., Genzel, R., et al. 1988, *The Astrophysical Journal*, 332, 379
- Stutzki, J. & Winnewisser, G. 1985, *Astronomy & Astrophysics*, 144, 13

- Tachihara, K., Onishi, T., Mizuno, A., & Fukui, Y. 2002, *Astronomy & Astrophysics*, 385, 909
- Tarter, C. B., Tucker, W. H., & Salpeter, E. E. 1969, *The Astrophysical Journal*, 156, 943
- Tatematsu, K., Umemoto, T., Kameya, O., et al. 1993, *Astrophysical Journal*, 404, 643
- Tauber, J. A., Tielens, A. G. G. M., Meixner, M., & Goldsmith, P. F. 1994, *The Astrophysical Journal*, 422, 136
- Tielens, A. G. G. M. 2005, *The physics and chemistry of the interstellar medium* (Cambridge: Cambridge University Press)
- Tielens, A. G. G. M. & Hollenbach, D. 1985, *Astrophysical Journal*, 291, 722
- Tucker, K. D., Kutner, M. L., & Thaddeus, P. 1974, *Astrophysical Journal Letters*, 193, L115
- van der Tak, F. F. S., Black, J. H., Schöier, F. L., Jansen, D. J., & van Dishoeck, E. F. 2007, *Astronomy & Astrophysics*, 468, 627
- van der Tak, F. F. S., Chavarría, L., Herpin, F., et al. 2013, *Astronomy & Astrophysics*, 554, A83
- Vastel, C., Polehampton, E. T., Baluteau, J.-P., et al. 2003, in *ESA Special Publication, Vol. 511, Exploiting the ISO Data Archive. Infrared Astronomy in the Internet Age*, ed. C. Gry, S. Peschke, J. Matagne, P. Garcia-Lario, R. Lorente, & A. Salama, 225
- Vehoff, S., Hummel, C. A., Monnier, J. D., et al. 2010, *Astronomy & Astrophysics*, 520, A78
- Venemans, B. P., McMahon, R. G., Walter, F., et al. 2012, *Astrophysical Journal Letters*, 751, L25
- Wadley, T. L. 1959, *Heterodyne Techniques in Specialised Radio Instrumentation* (University of the Witwatersrand)
- Wagenblast, R., Williams, D. A., Millar, T. J., & Nejad, L. A. M. 1993, *Monthly Notices of the Royal Astronomical Society*, 260, 420
- Walborn, N. R. 1973, *Astrophysical Journal Letters*, 182, L21
- Wang, J. & Chen, Y. 2010, *Science in China G: Physics and Astronomy*, 53, 271

- Wang, P., Li, Z.-Y., Abel, T., & Nakamura, F. 2010, *The Astrophysical Journal*, 709, 27
- Watson, W. D. 1972, *Astrophysical Journal*, 176, 103
- Weingartner, J. C. & Draine, B. T. 2001, *Astrophysical Journal Supplements*, 134, 263
- Wilson, C. D. & Walker, C. E. 1994, *The Astrophysical Journal*, 432, 148
- Wilson, T. L., Rohlfs, K., & Hüttemeister, S. 2009, *Tools of Radio Astronomy* (Springer-Verlag Berlin Heidelberg)
- Wolfire, M. G., Hollenbach, D., McKee, C. F., Tielens, A. G. G. M., & Bakes, E. L. O. 1995, *Astrophysical Journal*, 443, 152
- Woodall, J., Agúndez, M., Markwick-Kemper, A. J., & Millar, T. J. 2007, *Astronomy & Astrophysics*, 466, 1197
- Wooten, A., Phillips, T. G., Beichman, C. A., & Frerking, M. 1982, *Astrophysical Journal*, 256, L5
- Xilouris, E. M., Tabatabaei, F. S., Boquien, M., et al. 2012, *Astronomy & Astrophysics*, 543, A74
- Yıldız, U. A., Kristensen, L. E., van Dishoeck, E. F., et al. 2012, *Astronomy & Astrophysics*, 542, A86



Summary of HIFI data

OBSID: 1342201692. This is a Nyquist-sampled, position-switched OTF map with reference positions of $\alpha_{J2000} = 11^{\text{h}}15^{\text{m}}08^{\text{s}}85$ and $\delta_{J2000} = -61^{\circ}16'50''0$, observed in July, 2010. In the map each line consists of 11 independent points with an average spacing of $18.6''$, covering in total $204.6''$ (the observed map consists of 9 OTF lines). We used the wide band spectrometer, with full IF range of 4 GHz at 1.1 MHz, in both polarizations H and V, and the observed band was 1a. The covered frequency range in band 1a is 522.5 GHz to 527.1 GHz in LSB and 534.6 GHz to 539.1 GHz in USB. The goal noise was 0.047 K and the system noise temperature is 126 K at 531 GHz in both LSB and USB. The total observing time was 1405 s.

OBSID: 1342201675. It is a cut (1 OTF line) with positions of $\alpha_{J2000} = 11^{\text{h}}15^{\text{m}}02^{\text{s}}55$ and $\delta_{J2000} = -61^{\circ}15'54''42$, observed in July, 2010. The line consists of 9 independent points with an average spacing of $16.0''$, covering in total $144.0''$. We used WBS and the band was 1b with a covered frequency range of 556.6 GHz to 560.7 GHz in LSB and 568.6 GHz to 571.6 GHz in USB. The goal noise is 0.04 K and the system noise temperature is 161 K at 565 GHz at both the upper and lower sideband. The total observing time was 424 s.

OBSID: 1342201676. It is a cut (1 OTF line) with positions of $\alpha_{J2000} = 11^{\text{h}}15^{\text{m}}12^{\text{s}}03$ and $\delta_{J2000} = -61^{\circ}16'27''01$. The line consists of 9 independent points with an average spacing of $16''5$, covering in total $148''5$. We used WBS and the band was 1b with a covered frequency range as one before. The goal noise is 0.04 K and the system noise temperature is 161 K at 565 GHz at both the upper and lower sideband. The total observing time was 414 s.

OBSID: 1342201750. It is a cut (1 OTF line) with positions of $\alpha_{J2000} = 11^{\text{h}}15^{\text{m}}02^{\text{s}}41$ and $\delta_{J2000} = -61^{\circ}15'55''05$, observed in July, 2010. The line consists of 18 independent points with an average spacing of $9''6$, covering in total $172''8$. We used WBS and the band was 4a with a covered

frequency range of 1024.1 GHz to 1027.1 GHz in LSB and 1034.9 GHz to 1037.9 GHz in USB. The goal noise is 1 K and the system noise temperature is 579 K at 1031 GHz at both the upper and lower sideband. The total observing time was 296 s.

OBSID: 1342201752. It is a cut (1 OTF line) with positions of $\alpha_{J2000} = 11^{\text{h}}15^{\text{m}}11^{\text{s}}.93$ and $\delta_{J2000} = -61^{\circ}16'26''.17$, observed in July, 2010. The line consists of 14 independent points with an average spacing of $9''.6$, covering in total $134''.4$. We used WBS and the band was 4a with a covered frequency range as one before. The goal noise is 1 K and the system noise temperature is 579 K at 1031 GHz at both the upper and lower sideband. The total observing time was 279 s.

OBSID: 1342201809. It is a cut (1 OTF line) with positions of $\alpha_{J2000} = 11^{\text{h}}15^{\text{m}}02^{\text{s}}.49$ and $\delta_{J2000} = -61^{\circ}15'54''.72$, observed in August, 2010. The line consists of 16 independent points with an average spacing of $9''.6$, covering in total $153''.6$. We used WBS and the band was 4b with a covered frequency range of 1101.2 GHz to 1103.9 GHz in LSB and 1111.8 GHz to 1114.8 GHz in USB. The goal noise is 0.15 K and the system noise temperature is 716 K at 1108 GHz at both the upper and lower sideband. The total observing time was 454 s.

OBSID: 1342201810. It is a cut (1 OTF line) with positions of $\alpha_{J2000} = 11^{\text{h}}15^{\text{m}}12^{\text{s}}.01$ and $\delta_{J2000} = -61^{\circ}16'26''.95$, observed in August, 2010. The line consists of 30 independent points with an average spacing of $9''.6$, covering in total $288''$. We used WBS and the band was 4b with a covered frequency range as one before. The goal noise is 0.15 K and the system noise temperature is 716 K at 1108 GHz at both the upper and lower sideband. The total observing time was 452 s.

OBSID: 1342201818. This is a cut (1 OTF line) with positions of $\alpha_{J2000} = 11^{\text{h}}15^{\text{m}}02^{\text{s}}.55$ and $\delta_{J2000} = -61^{\circ}15'54''.59$, observed in August, 2010. The line consists of 20 independent points with an average spacing of $5''.4$, covering in total $108''.0$. We used WBS and the band was 7b with a covered frequency range of 1892.6 GHz to 1894.1 GHz in LSB and 1901.1 GHz to 1902.5 GHz in USB. The goal noise is 1 K and the system noise temperature is 2755 K at 1897 GHz at both the upper and lower sideband. The total observing time was 411 s.

OBSID: 1342201819. It is a cut (1 OTF line) with positions of $\alpha_{J2000} = 11^{\text{h}}15^{\text{m}}11^{\text{s}}.99$ and $\delta_{J2000} = -61^{\circ}16'26''.88$, observed in August, 2010. The line consists of 30 independent points with an average spacing of $5''.4$, covering in total $162''.0$. We used WBS and the band was 7b with a covered frequency range as one before. The goal noise is 1 K and the system noise temperature is 2755 K at 1897 GHz at both the upper and lower sideband. The total observing time was 471 s.

OBSID: 1342223427. It is a dual beam switch (DBS) point observation with positions of $\alpha_{J2000} = 11^{\text{h}}15^{\text{m}}10^{\text{s}}.89$ and $\delta_{J2000} = -61^{\circ}16'15''.2$, observed

in July, 2011. We used WBS and the band was 4a with a covered frequency range of 974.4 GHz to 977.4 GHz in LSB and 985.3 GHz to 988.3 GHz in USB. The goal noise is 0.018 K and the system noise temperature is 621 K at 981 GHz at both the upper and lower sideband. The total observing time was 2083 s.

OBSID: 1342223428. It is a dual beam switch (DBS) point observation with positions of $\alpha_{J2000} = 11^{\text{h}}15^{\text{m}}02^{\text{s}}.15$ and $\delta_{J2000} = -61^{\circ}15'56''.1$, observed in July, 2011. We used WBS and the band was 4a with a covered frequency range of 972.2 GHz to 975.2 GHz in LSB and 985.3 GHz to 988.3 GHz in USB. The goal noise is 0.022 K and the system noise temperature is 617 K at 979 GHz at both the upper and lower sideband. The total observing time was 1440 s.

OBSID: 1342223429. It is a dual beam switch (DBS) point observation with positions of $\alpha_{J2000} = 11^{\text{h}}15^{\text{m}}14^{\text{s}}.39$ and $\delta_{J2000} = -61^{\circ}16'50''.0$, observed in July, 2011. We used WBS and the band was 4a with a covered frequency range of 974.4 GHz to 977.4 GHz in LSB and 985.3 GHz to 988.3 GHz in USB. The goal noise is 0.018 K and the system noise temperature is 621 K at 981 GHz at both the upper and lower sideband. The total observing time was 2083 s.

OBSID: 1342223430. It is a dual beam switch (DBS) point observation with positions of $\alpha_{J2000} = 11^{\text{h}}15^{\text{m}}02^{\text{s}}.15$ and $\delta_{J2000} = -61^{\circ}15'56''.1$, observed in July, 2011. We used WBS and the band was 4a with a covered frequency range as one before. The goal noise is 0.022 K and the system noise temperature is 621 K at 981 GHz at both the upper and lower sideband. The total observing time was 2083 s.

OBSID: 1342225899. It is a dual beam switch (DBS) point observation with positions of $\alpha_{J2000} = 11^{\text{h}}15^{\text{m}}14^{\text{s}}.4$ and $\delta_{J2000} = -61^{\circ}16'50''.0$, observed in August, 2011. We used WBS and the band was 4a with a covered frequency range of 972.2 GHz to 975.2 GHz in LSB and 983.1 GHz to 986.1 GHz in USB. The goal noise is 0.025 K and the system noise temperature is 617 K at 979 GHz at both the upper and lower sideband. The total observing time was 1170 s.

OBSID: 1342225900. It is a dual beam switch (DBS) point observation with positions of $\alpha_{J2000} = 11^{\text{h}}15^{\text{m}}10^{\text{s}}.89$ and $\delta_{J2000} = -61^{\circ}16'15''.2$, observed in August, 2011. We used WBS and the band was 4a with a covered frequency range as one before. The goal noise is 0.022 K and the system noise temperature is 617 K at 979 GHz at both the upper and lower sideband. The total observing time was 1440 s.



Summary of PACS data

OBSID: 1342214681. This is a line spectroscopy (pointed, chop/nod) with positions of $\alpha_{J2000} = 11^h15^m01^s47$ and $\delta_{J2000} = -61^\circ15'55''.99$, observed in February, 2011. The covered wavelength range for [OI] 63 micron line is $62.9\ \mu\text{m}$ to $63.4\ \mu\text{m}$, while the continuum rms is 572 mJy and the line rms is $9.22 \times 10^{-18}\ \text{W/m}^2$. The covered wavelength range for [NIII] 57 micron line is $57.1\ \mu\text{m}$ to $57.6\ \mu\text{m}$, while the continuum rms is 730 mJy and the line rms is $15.54 \times 10^{-18}\ \text{W/m}^2$. The total observing time was 1473 s.

OBSID: 1342214684. This is a line spectroscopy (pointed, chop/nod) with positions of $\alpha_{J2000} = 11^h15^m09^s48$ and $\delta_{J2000} = -61^\circ16'30''.57$, observed in February, 2011. The covered wavelength range is the same as one before for both lines. For [OI] 63 micron line the continuum rms is 572 mJy and the line rms is $9.22 \times 10^{-18}\ \text{W/m}^2$. For [NIII] 57 micron line the continuum rms is 730 mJy and the line rms is $15.54 \times 10^{-18}\ \text{W/m}^2$. The total observing time was 996 s.

OBSID: 1342214687. This is a line spectroscopy (pointed, chop/nod) with positions of $\alpha_{J2000} = 11^h15^m09^s85$ and $\delta_{J2000} = -61^\circ16'56''.23$, observed in February, 2011. For [OI] 63 micron line the continuum rms is 572 mJy and the line rms is $9.22 \times 10^{-18}\ \text{W/m}^2$ (the covered wavelength range is the same as before). The total observing time was 568 s.

OBSID: 1342214682, 1342214685 and 1342214688. These are range spectroscopies (pointed, unchopped grating scan) with positions of $\alpha_{J2000} = 11^h15^m02^s49$ and $\delta_{J2000} = -61^\circ15'54''.01$, $\alpha_{J2000} = 11^h15^m10^s77$ and $\delta_{J2000} = -61^\circ16'14''.21$, and $\alpha_{J2000} = 11^h14^m14^s28$ and $\delta_{J2000} = -61^\circ16'48''.99$, respectively (all of them were observed in February, 2011). All information described from here are the same for these three observations. Reference wavelength for the range 107 – 206 micron: $180\ \mu\text{m}$. The covered wavelength range is $106.4\ \mu\text{m}$ to $206.2\ \mu\text{m}$. The continuum rms (at reference wavelength) is 520 mJy, the line rms (at reference wavelength) is $5.2 \times 10^{-18}\ \text{W/m}^2$. The best continuum rms occurs at $132\ \mu\text{m}$ with the

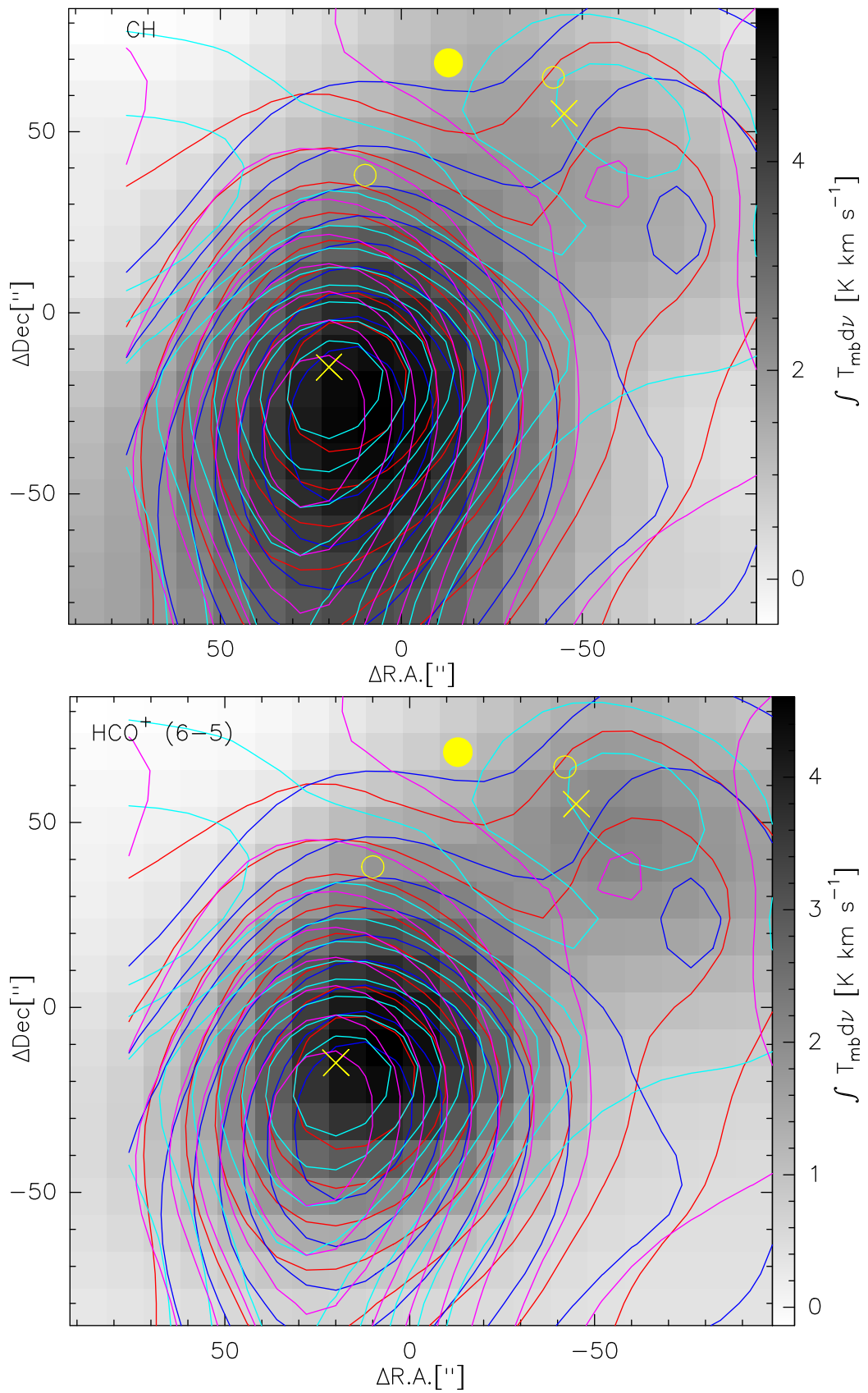
value of 214 mJy, while the best line rms occurs at 138 μm with the value of $4.09 \times 10^{-18} \text{ W/m}^2$. The worst continuum rms occurs at 206.0 μm with the value of 2079 mJy, while the worst line rms occurs at 206 μm with the value of $13.55 \times 10^{-18} \text{ W/m}^2$. Reference wavelength for the range 70–103 micron: 86.5 μm . The covered wavelength range is 53.2 μm to 103.1 μm . The continuum rms (at reference wavelength) is 834 mJy, the line rms (at reference wavelength) is $13 \times 10^{-18} \text{ W/m}^2$. The best continuum rms occurs at 75.5 μm with the value of 569 mJy, while the best line rms occurs at 91.5 μm with the value of $11.18 \times 10^{-18} \text{ W/m}^2$. The worst continuum rms occurs at 103 μm with the value of 116542 mJy, while the worst line rms occurs at 103 μm with the value of $1002.74 \times 10^{-18} \text{ W/m}^2$. The total observing time was 1751 s.



Comparison of Herschel and NANTEN2 intensity maps

Gray-scaled integrated intensity maps (species indicated on the top left corner). For the first four figures: red, blue, cyan and magenta contours represent ^{12}CO ($7 \rightarrow 6$), ^{12}CO ($4 \rightarrow 3$), $[\text{Cl}]$ ($^3\text{P}_2 \rightarrow ^3\text{P}_1$) and ($^3\text{P}_1 \rightarrow ^3\text{P}_0$) NANTEN2 data, respectively (all data are convolved to $43''_5$ beam).

On the upper panel of Fig. C.3 red contours represent Spitzer $8\ \mu\text{m}$ data, blue contours mark SPIRE $500\ \mu\text{m}$ data, while cyan and magenta contours show fine structure lines of $[\text{Cl}]$ ($^3\text{P}_2 \rightarrow ^3\text{P}_1$ and $^3\text{P}_1 \rightarrow ^3\text{P}_0$, respectively) from NANTEN2 telescope. On the lower panel of the same figure, the red and blue contours represent the same data, while cyan and magenta contours show ^{12}CO ($7 \rightarrow 6$) and ^{12}CO ($4 \rightarrow 3$) NANTEN2 data (data sets are convolved to $43''_5$ beam). On Fig. C.4 all contours show the same data as before on the upper panel of Fig. C.3.

**Figure C.1**

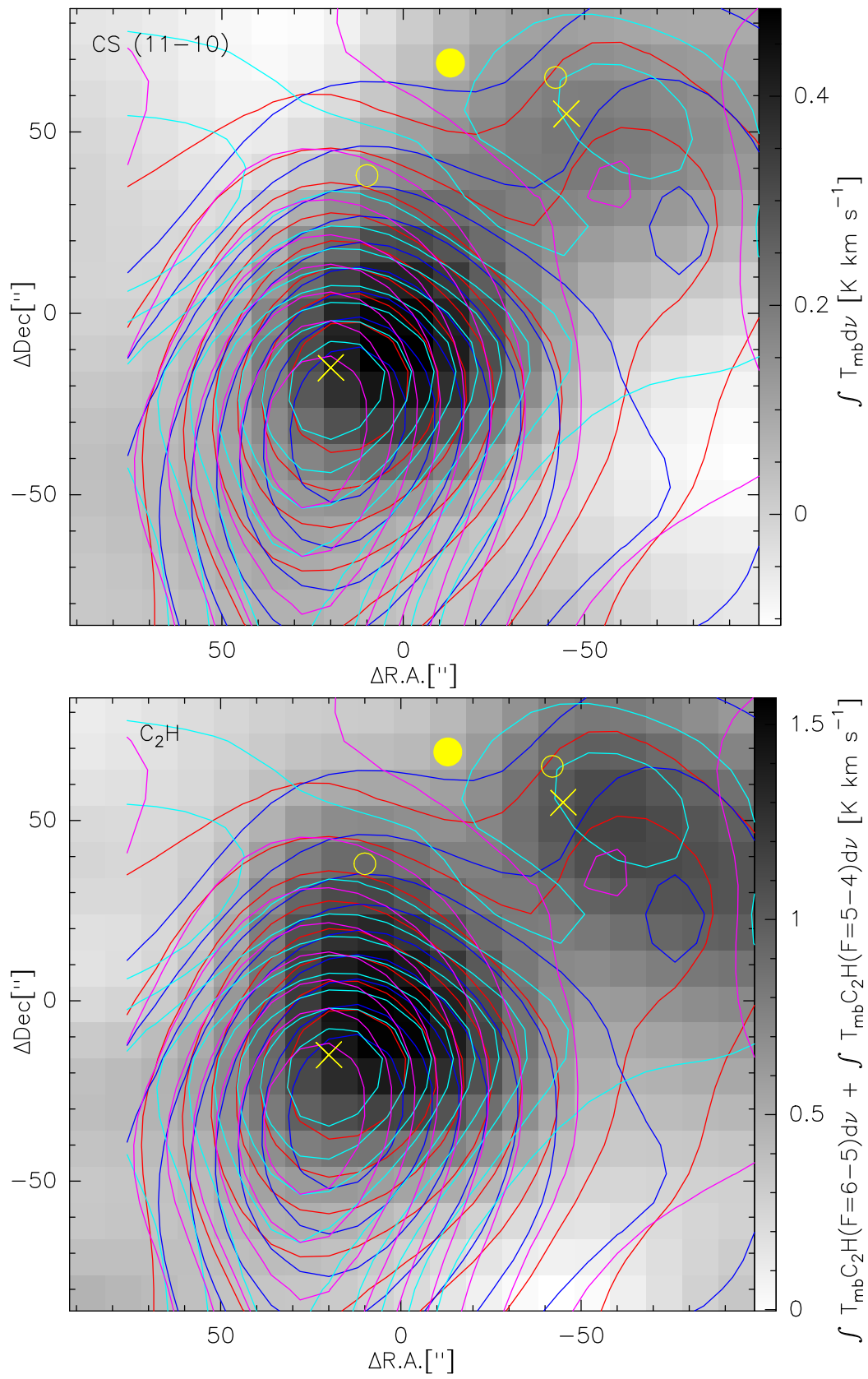
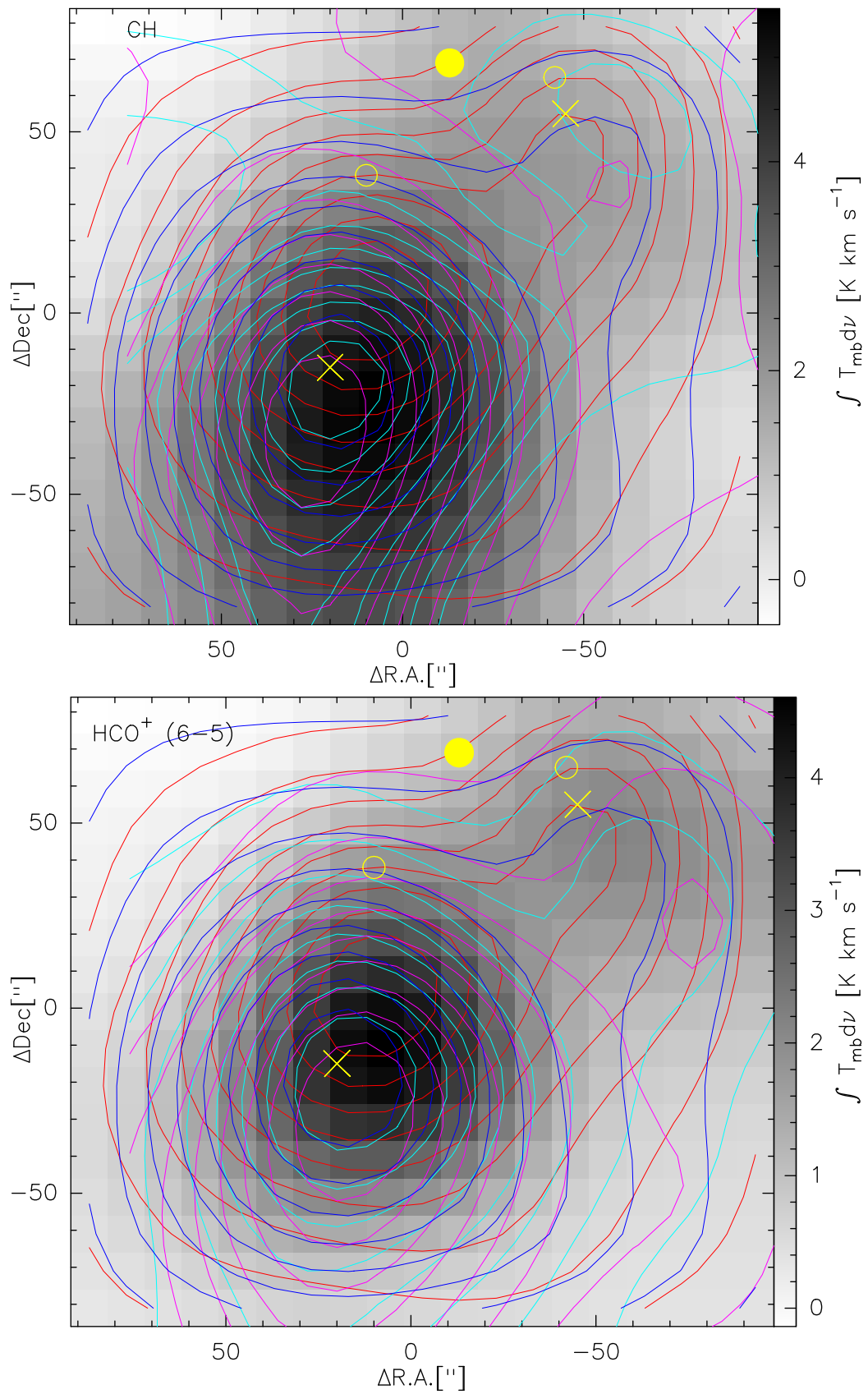


Figure C.2

**Figure C.3**

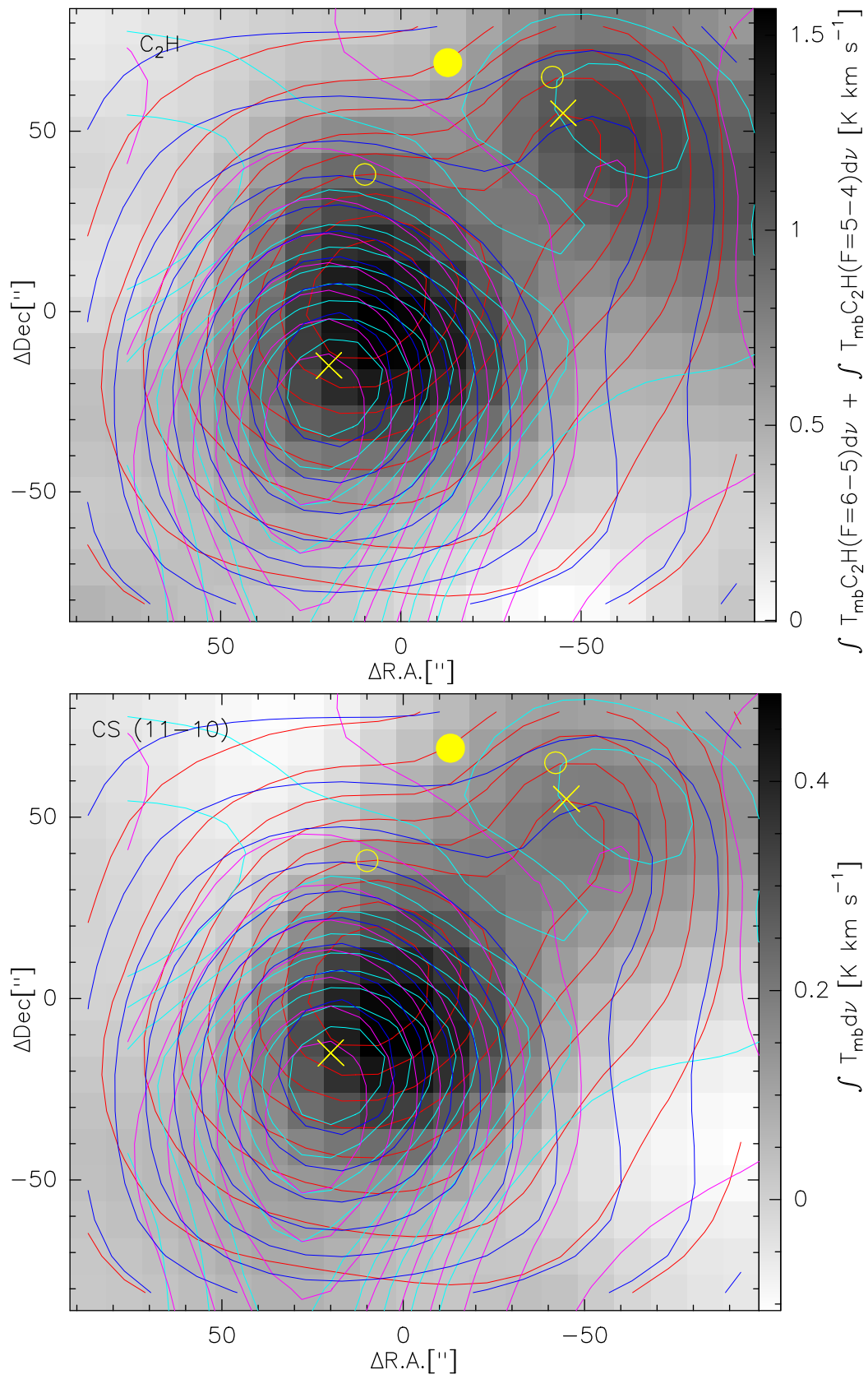


Figure C.4



Line fits of the observed species from the OTF-map observations

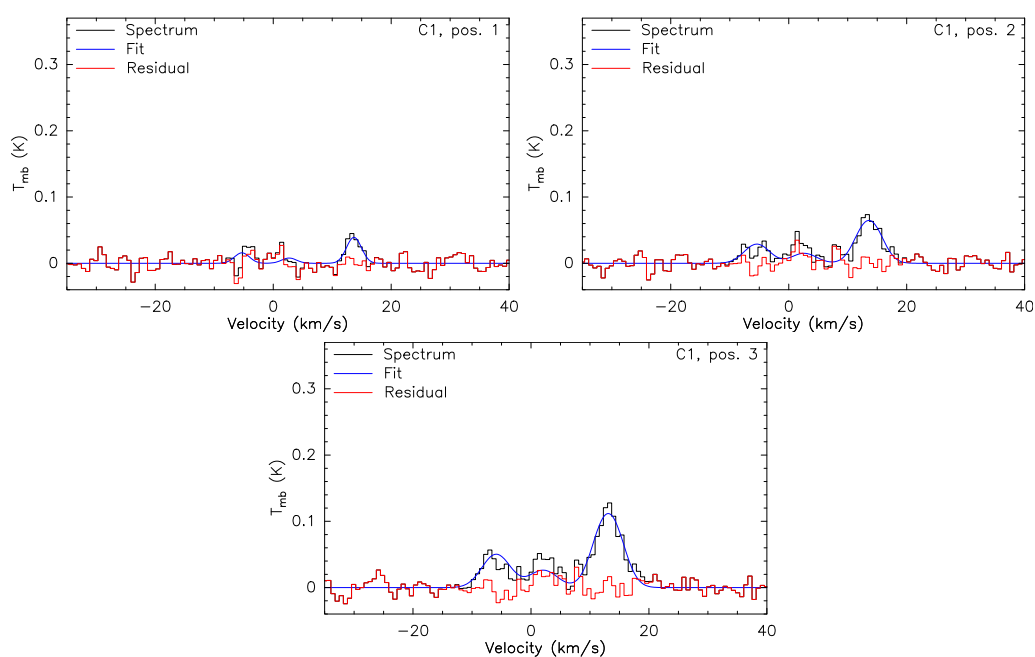


Figure D.1: Line fits of CH in C1 (toward MM1). The cuts and positions are indicated at the top right corner of plots. The notation is the same for all line fit figures.

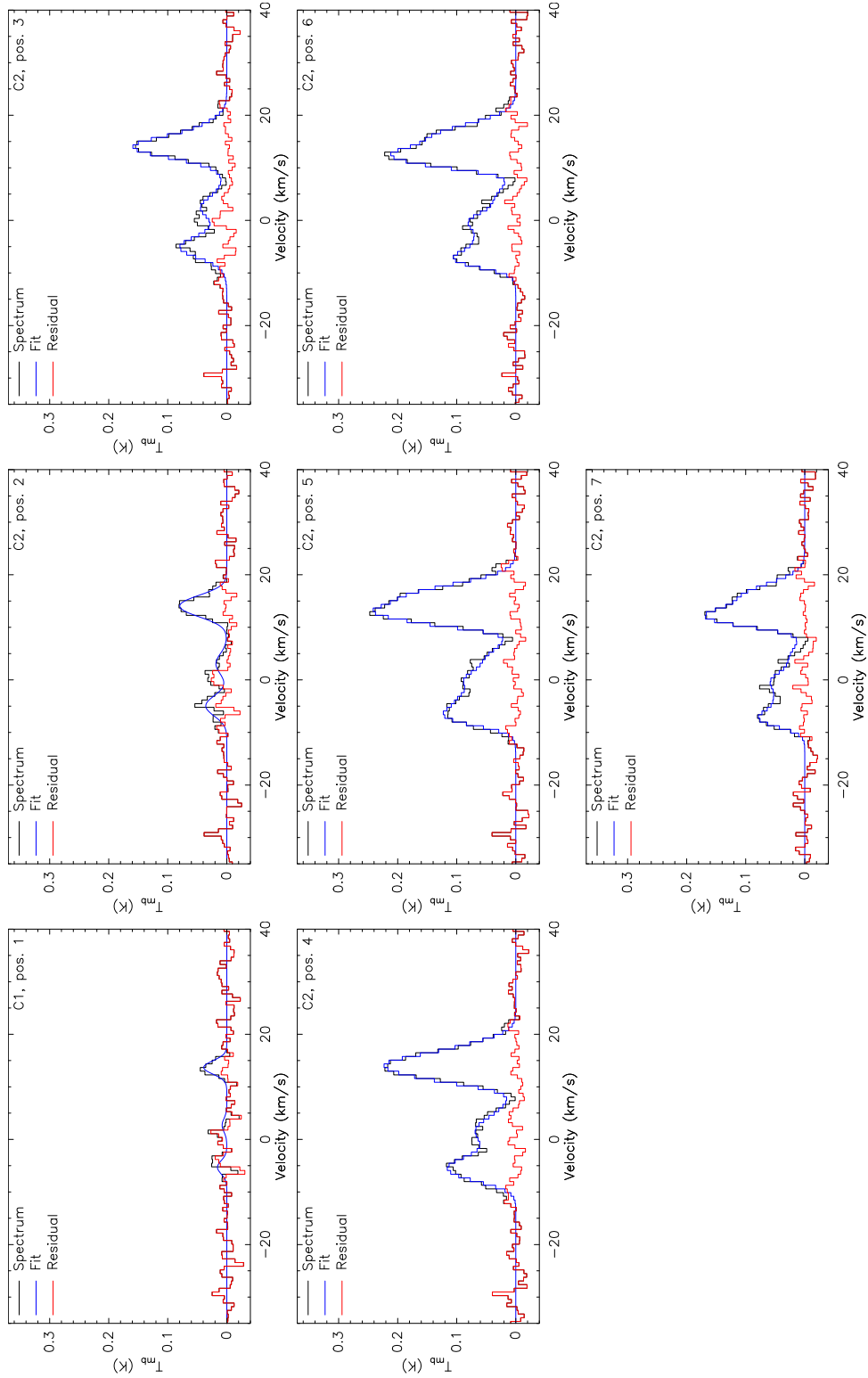


Figure D.2: Line fits of CH in C2 (toward MM2). Note: C1 pos. 1 = C2 pos. 1. Second velocity component appears from position 4.

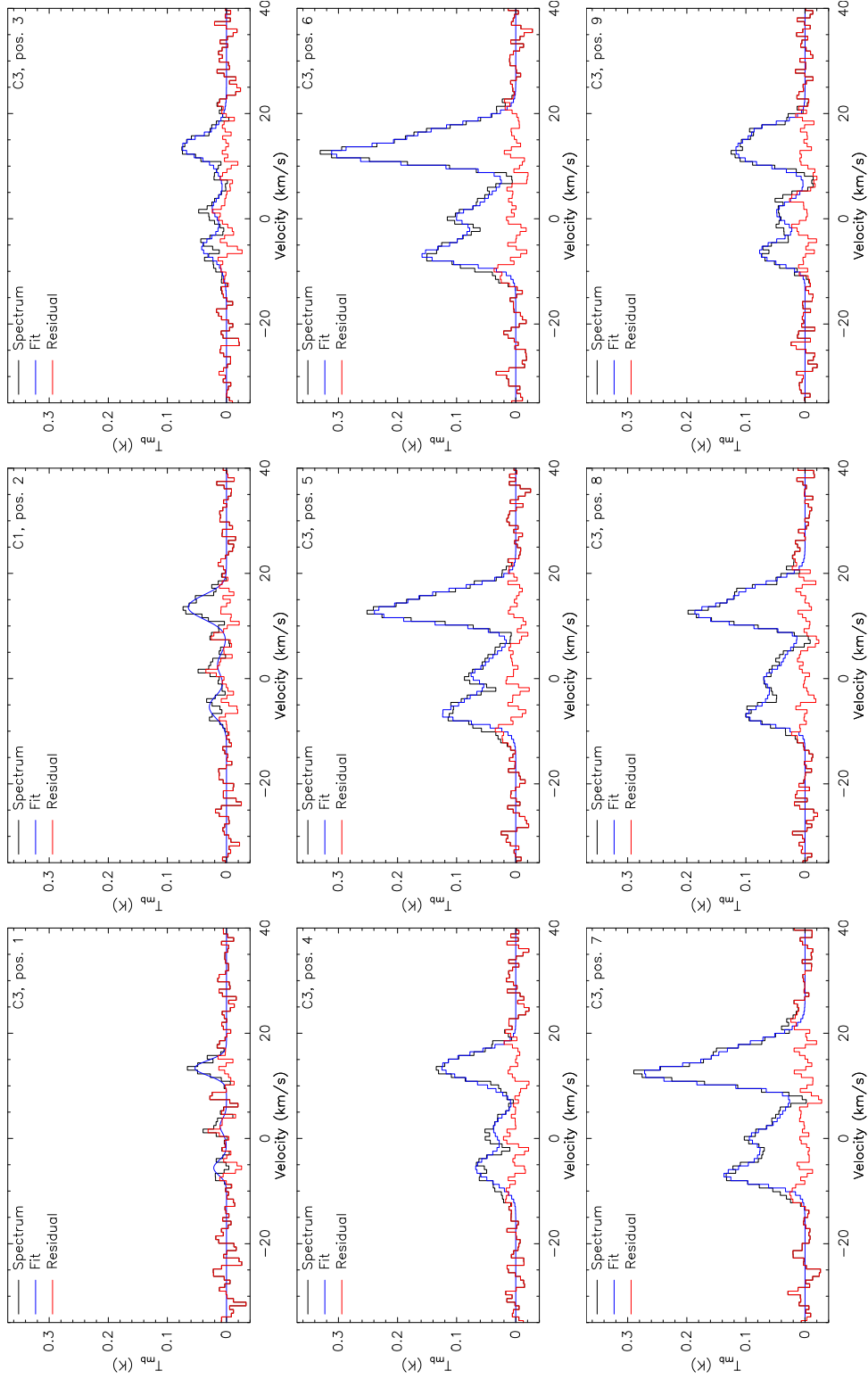


Figure D.3: Line fits of CH in C3 (toward MM2). Note: C1 pos. 2 = C3 pos. 2. Second velocity component appears from position 4.

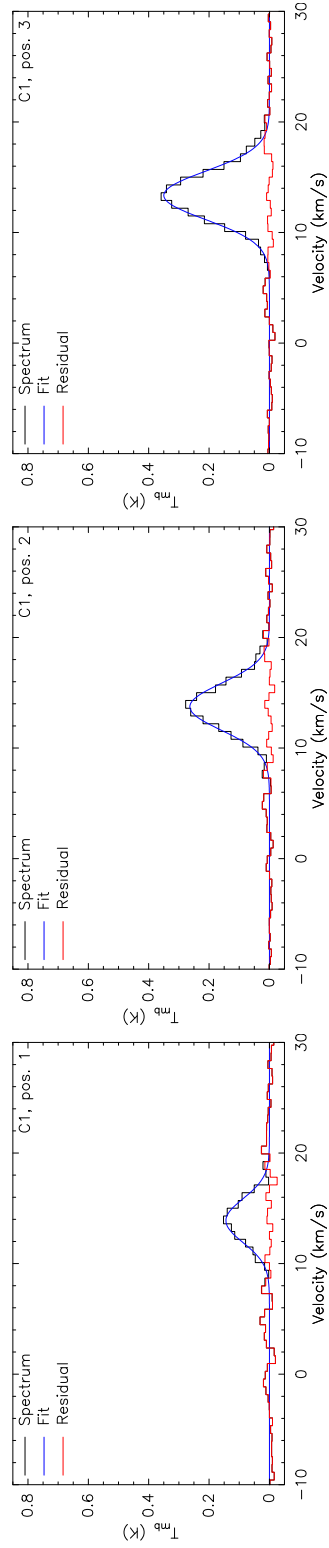


Figure D.4: Line fits of HCO^+ in C1 (toward MM1).

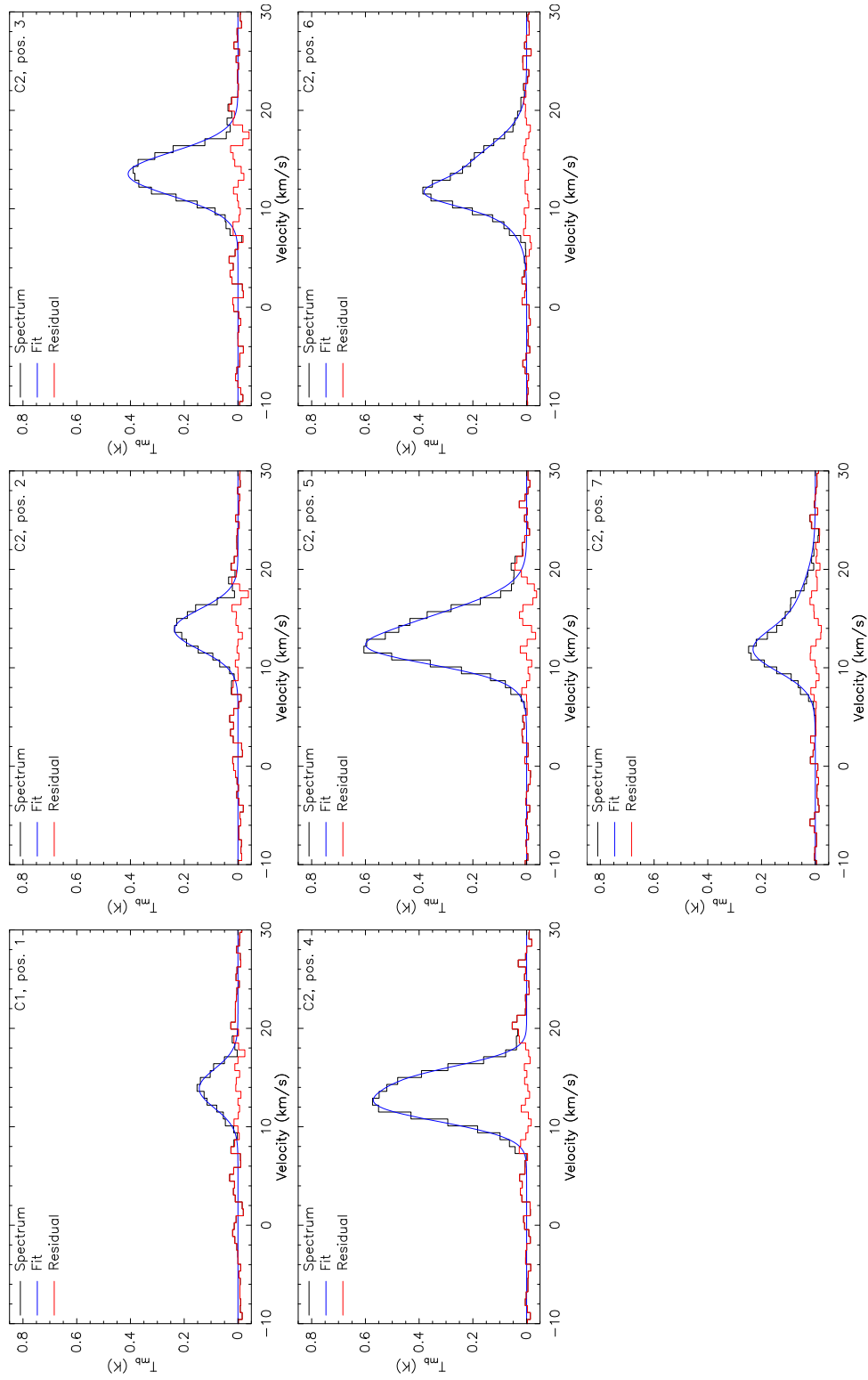


Figure D.5: Line fits of HCO^+ in C2 (toward MM2). Note: C1 pos. 1 = C2 pos. 1. Second velocity component appears from position 4.

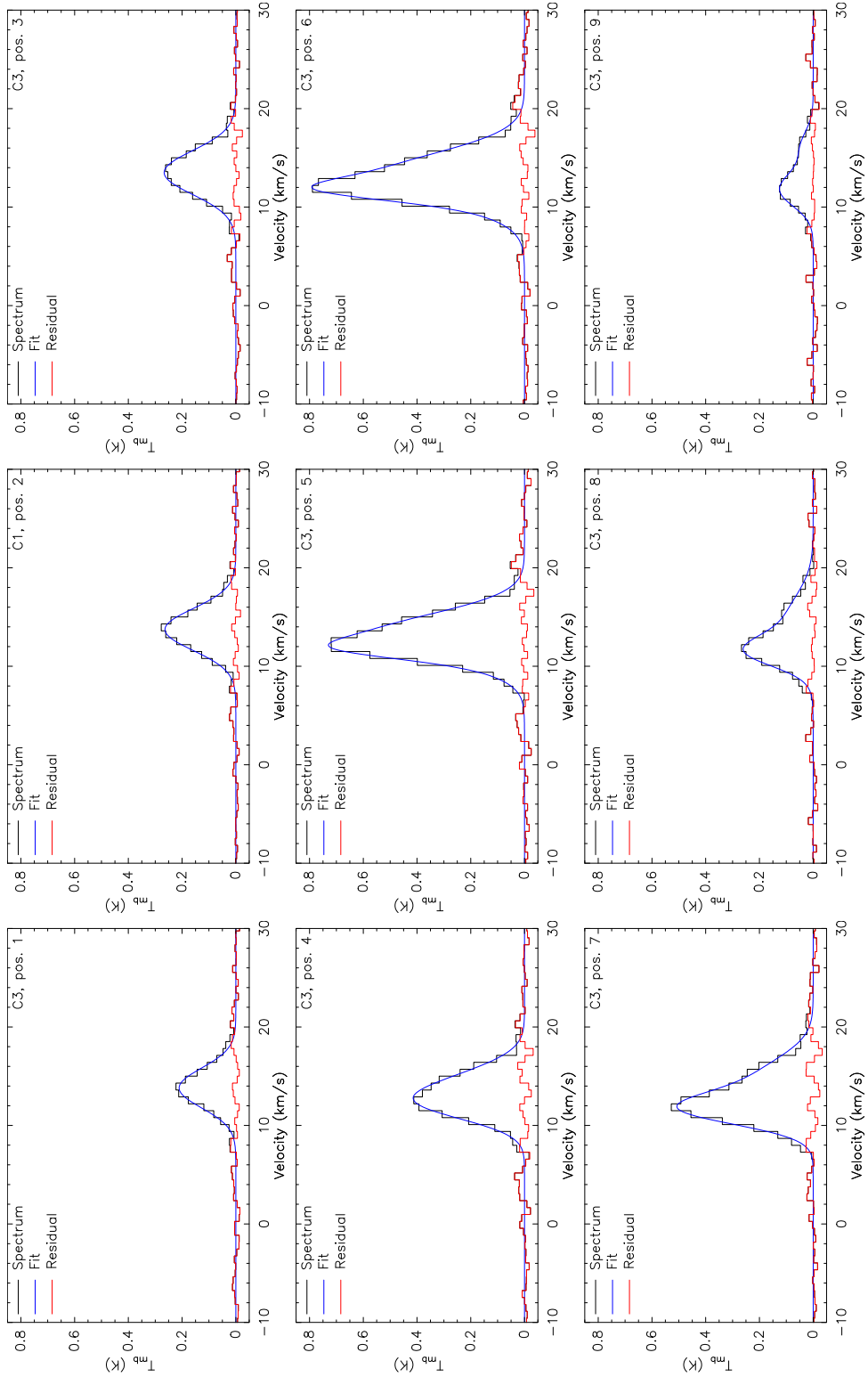


Figure D.6: Line fits of HCO^+ in C3 (toward MM2). Note: C1 pos. 2 = C3 pos. 2. Second velocity component appears from position 4.

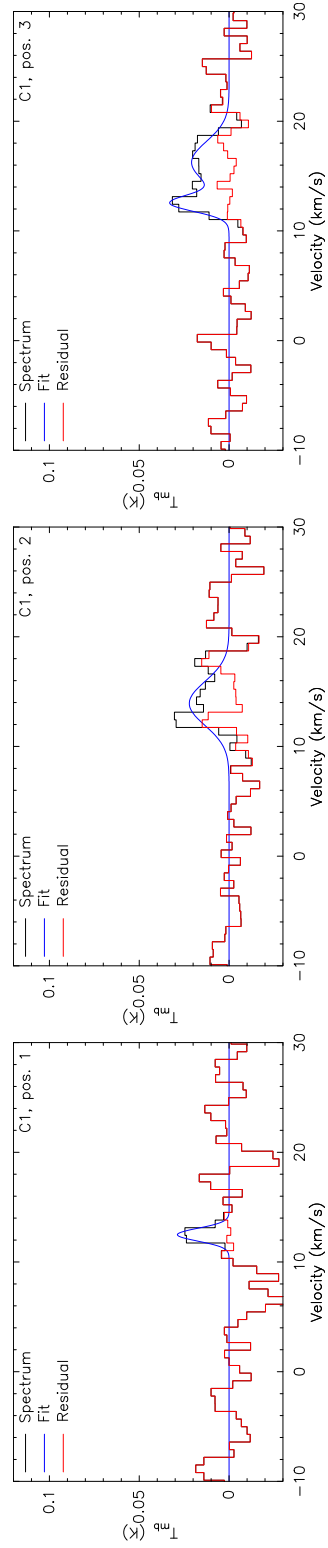


Figure D.7: Line fits of CS in C1 (toward MM1).

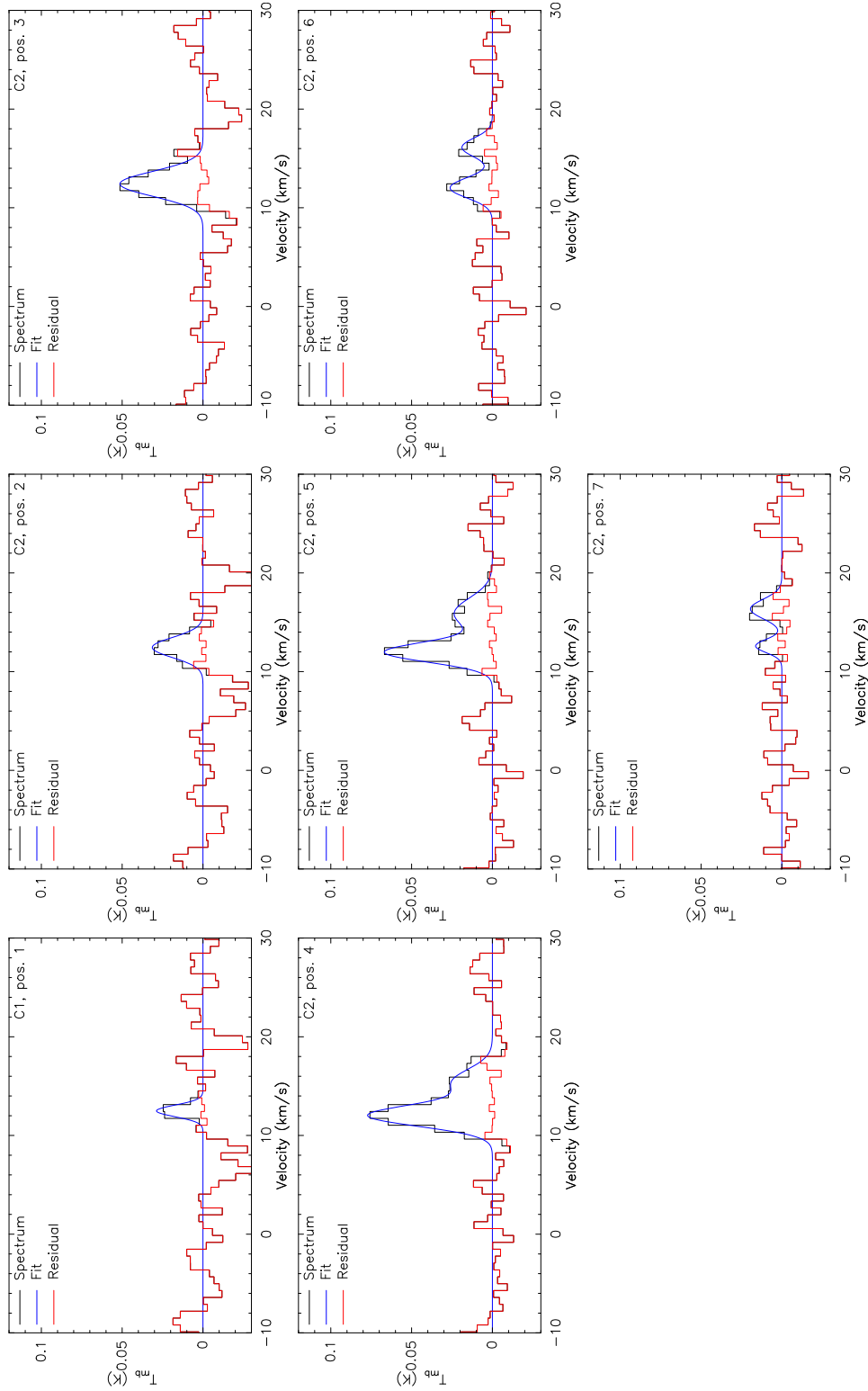


Figure D.8: Line fits of CS in C2 (toward MM2). Note: C1 pos. 1 = C2 pos. 1. Second velocity component appears from position 4.

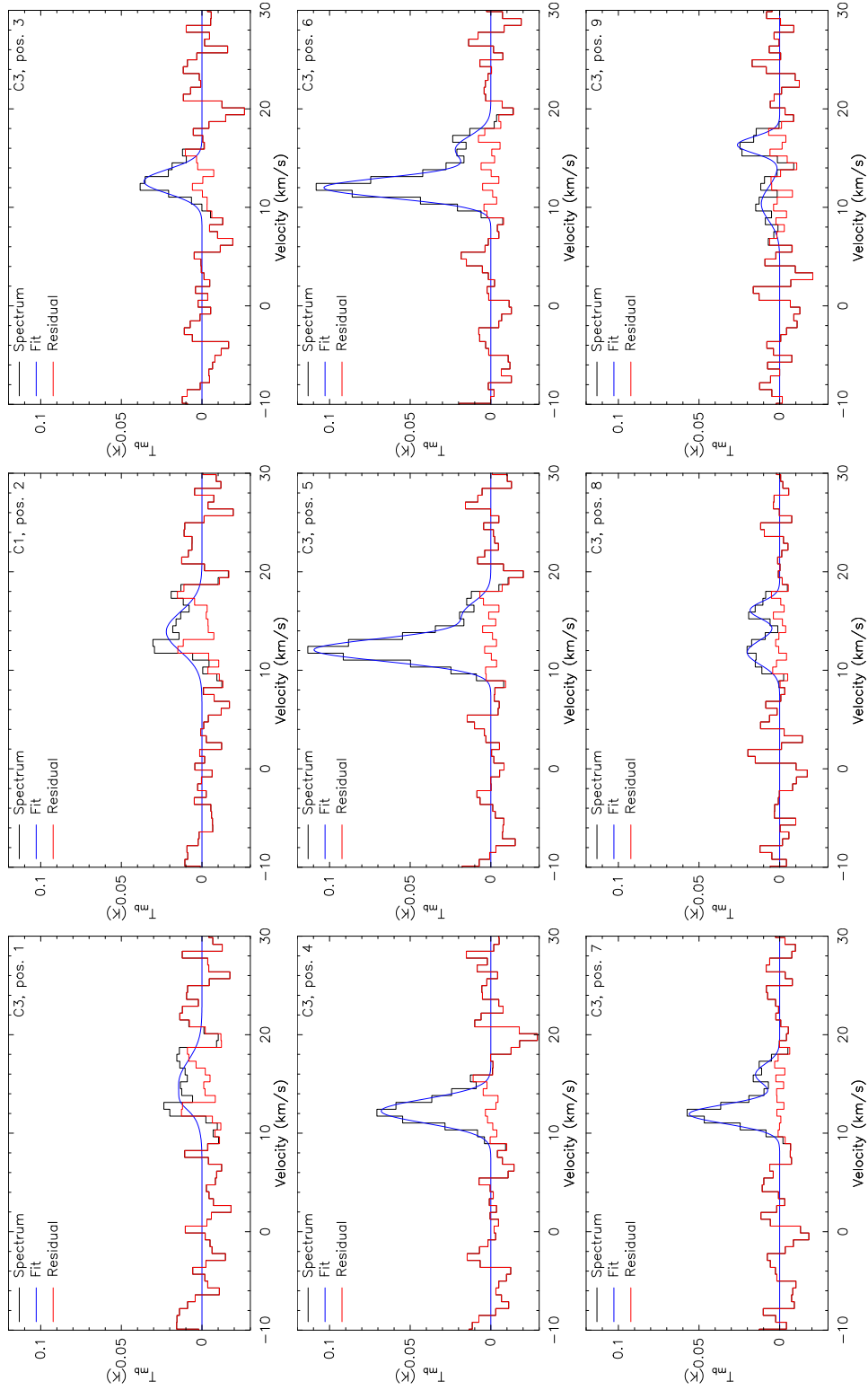


Figure D.9: Line fits of CS in C3 (toward MM2). Note: C1 pos. 2 = C3 pos. 2. Second velocity component appears from position 4.

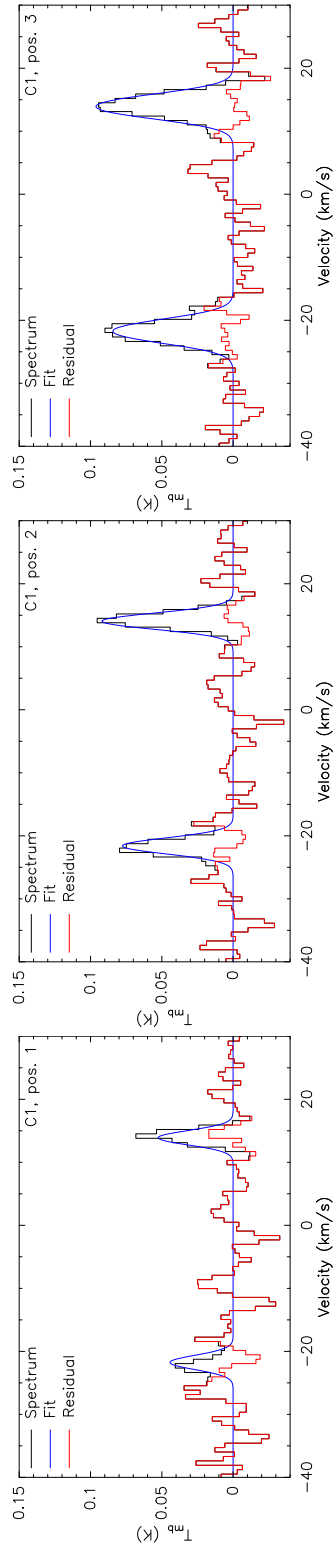


Figure D.10: Line fits of C_2H in C1 (toward MM1).

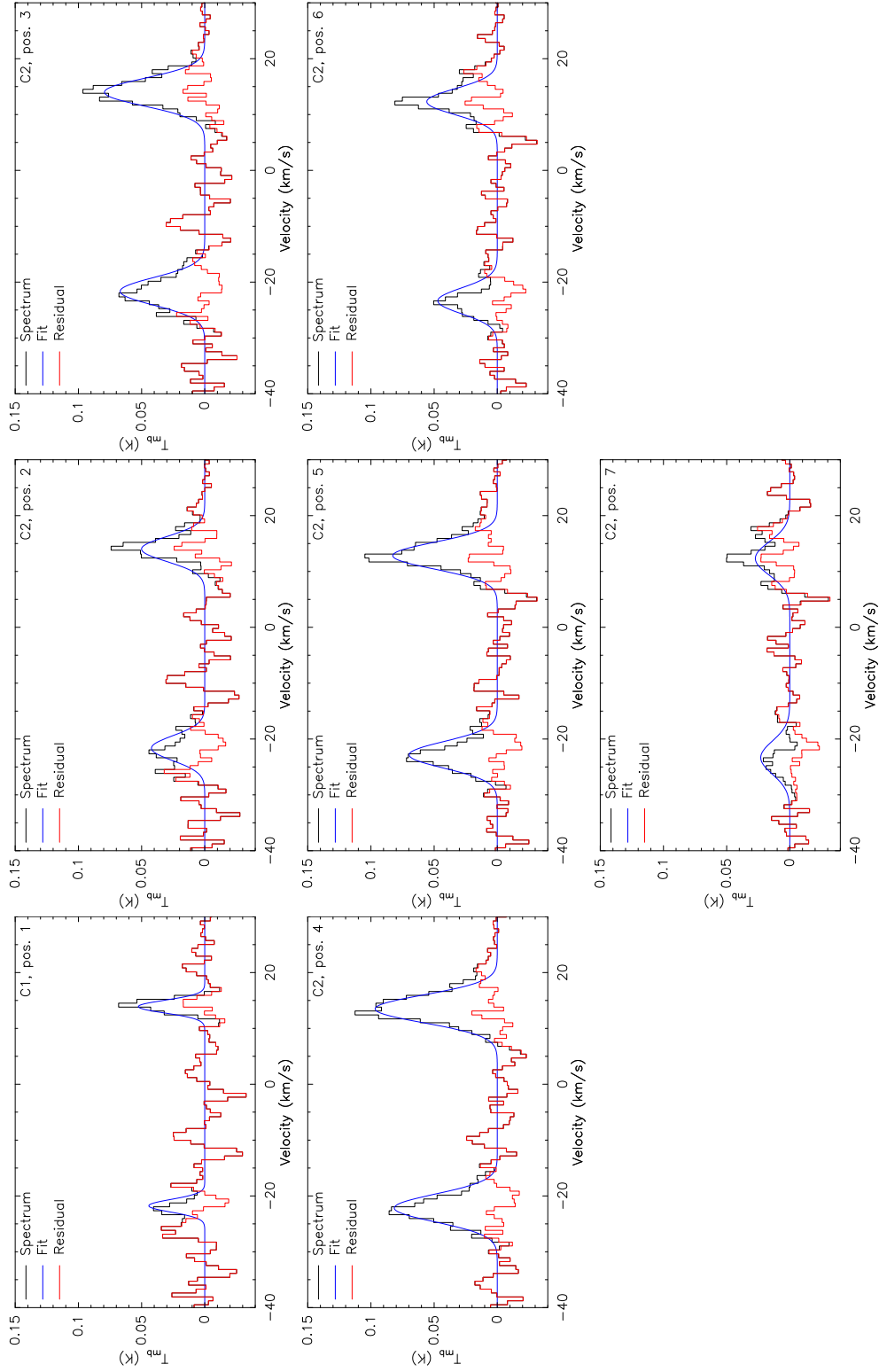


Figure D.11: Line fits of C_2H in C2 (toward MM2). Note: C1 pos. 1 = C2 pos. 1. Second velocity component appears from position 4.

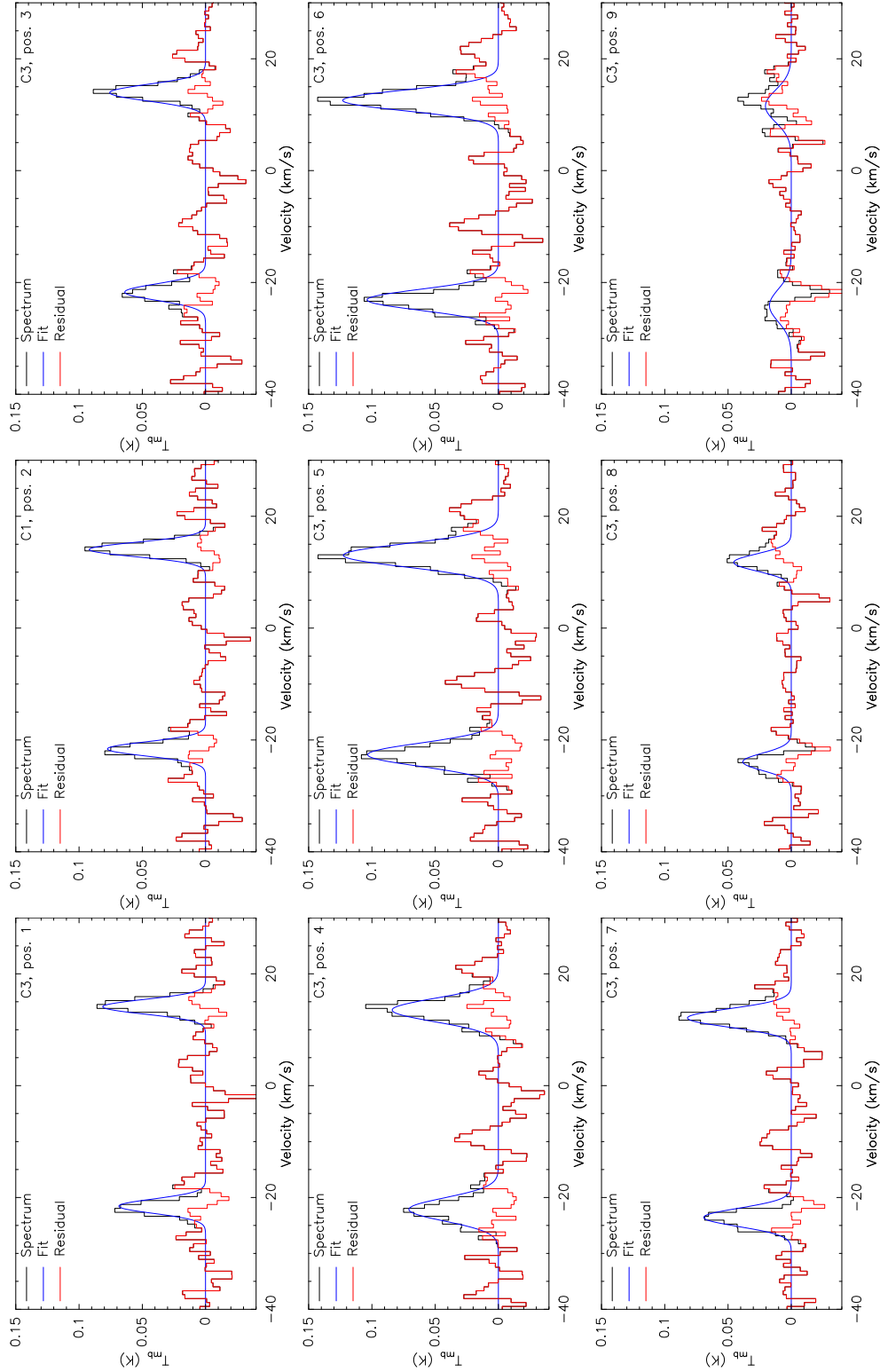


Figure D.12: Line fits of C_2H in C3 (toward MM2). Note: C1 pos. 2 = C3 pos. 2. Second velocity component appears from position 4.

Line fits of the observed species from the cut observations

E.1 1342201675 (o-H₂O — MM1)

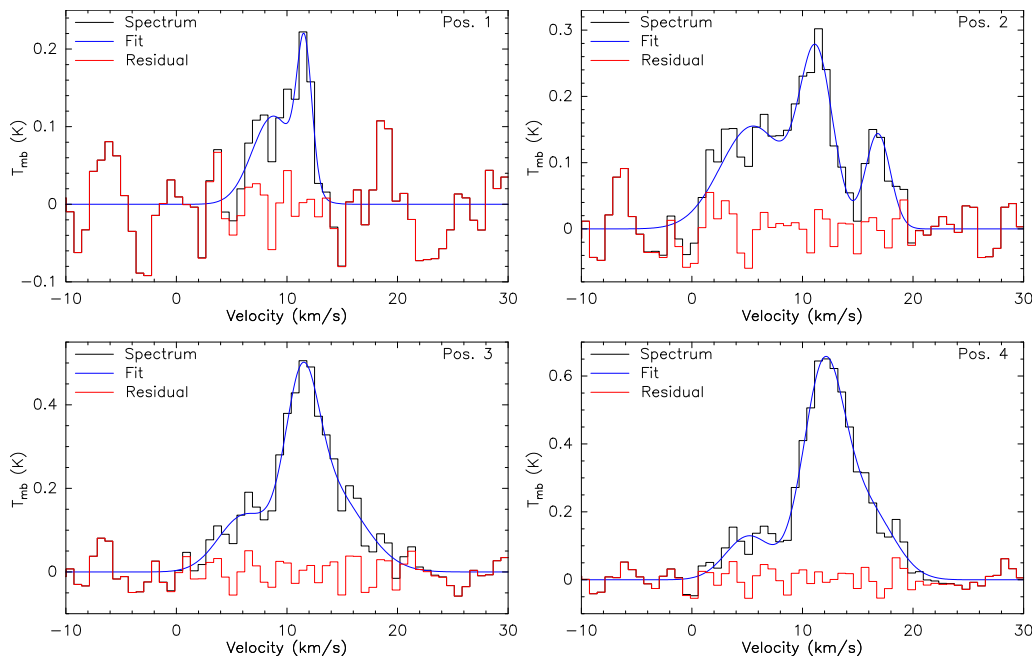


Figure E.1: Line fits of o-H₂O in MM1. The positions are indicated at the top right corner of plots.

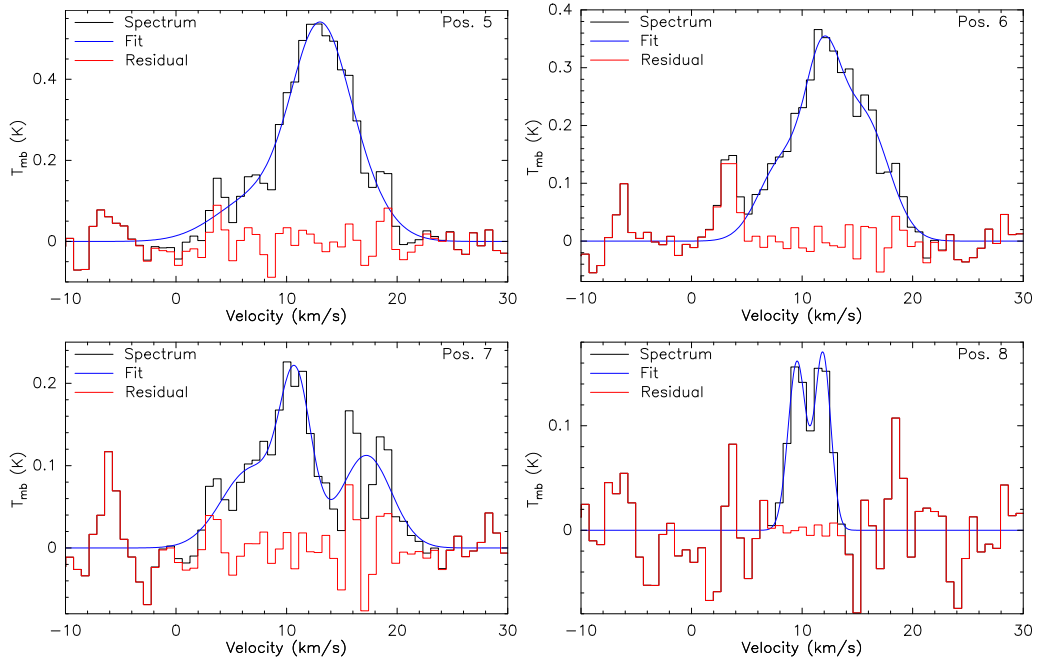


Figure E.2: Line fits of $o\text{-H}_2\text{O}$ in MM1 (cont.).

E.2 1342201676 ($o\text{-H}_2\text{O}$ — MM2)

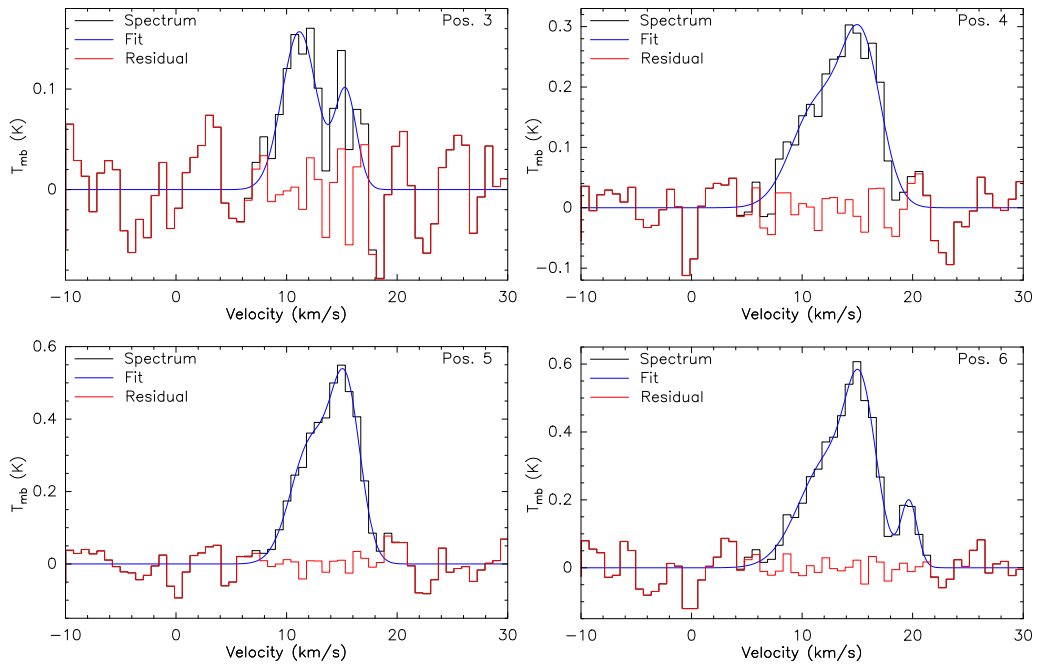


Figure E.3: Line fits of $o\text{-H}_2\text{O}$ in MM2.

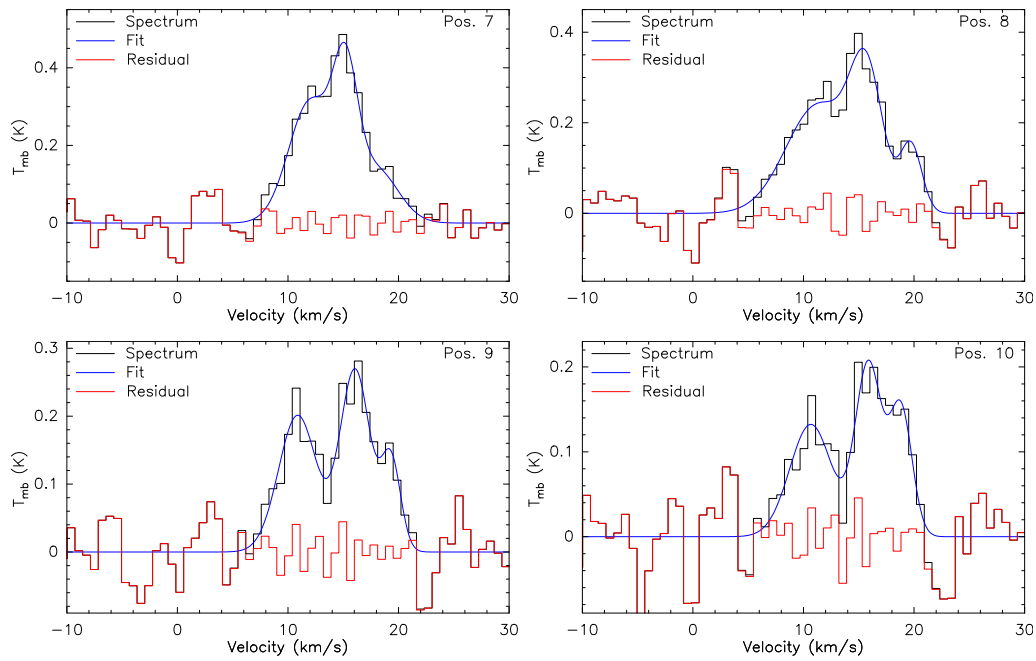


Figure E.4: Line fits of $o\text{-H}_2\text{O}$ in MM2 (cont.).

E.3 1342201750 (^{12}CO — MM1)

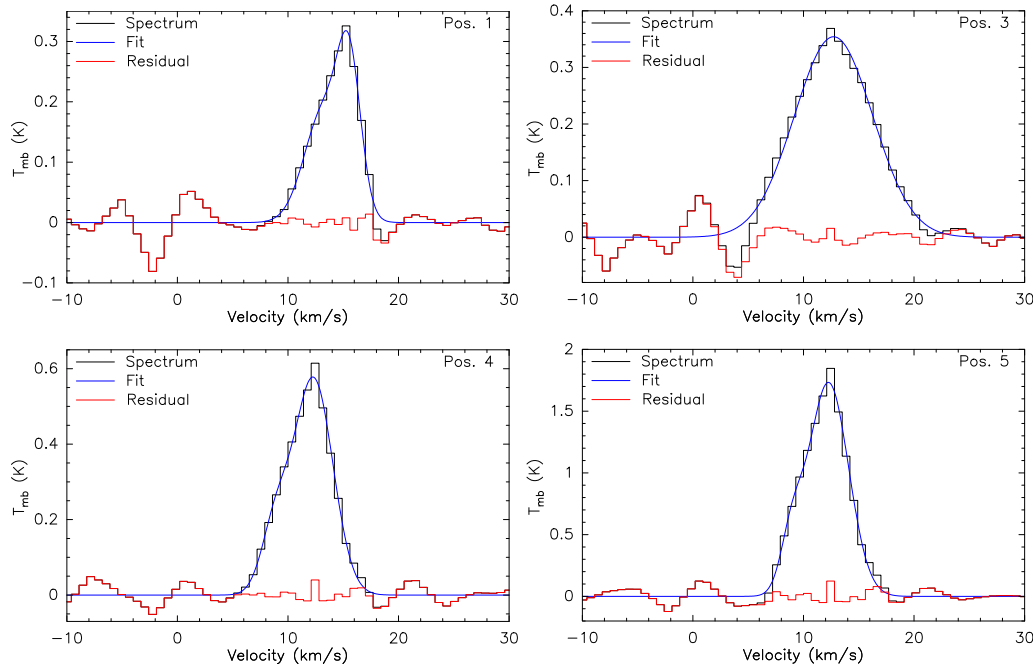


Figure E.5: Line fits of ^{12}CO in MM1.

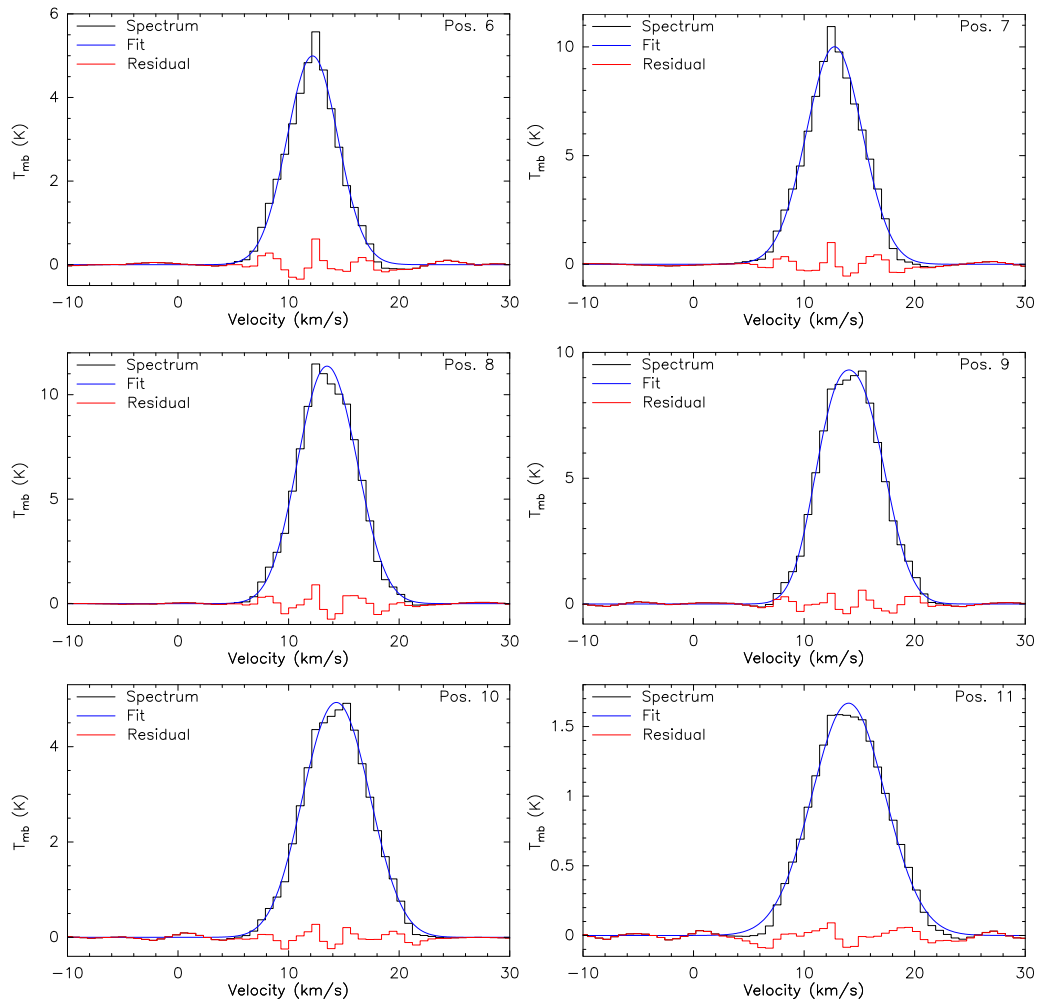


Figure E.6: Line fits of ^{12}CO in MM1 (cont.).

E.4 1342201752 (^{12}CO — MM2)

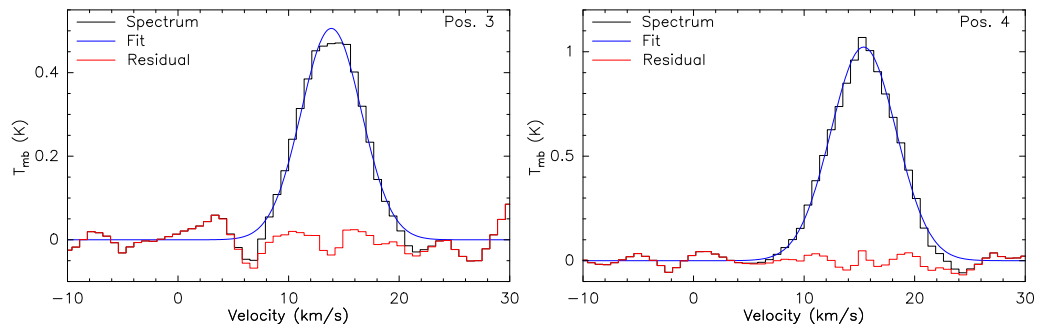


Figure E.7: Line fits of ^{12}CO in MM2.

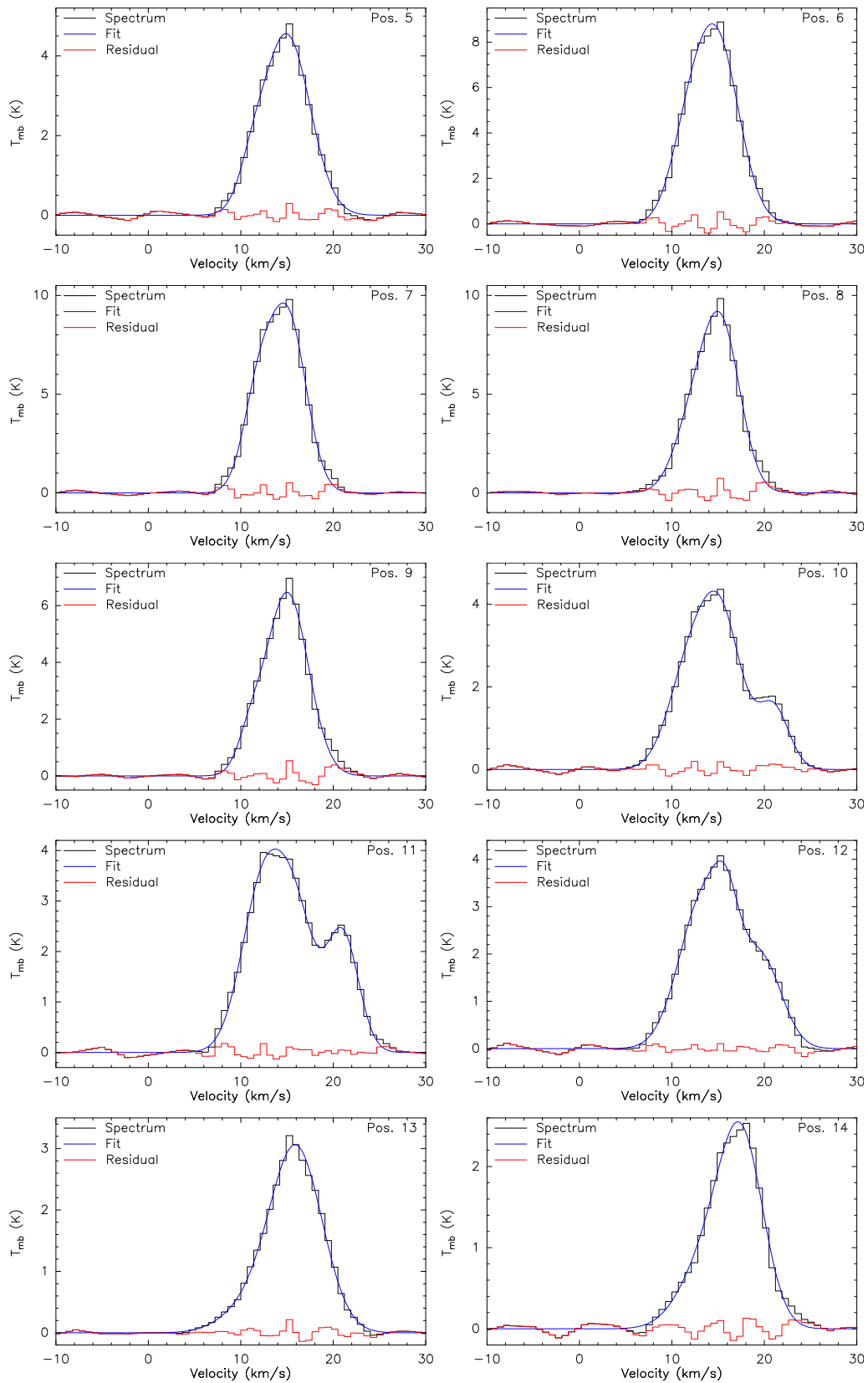
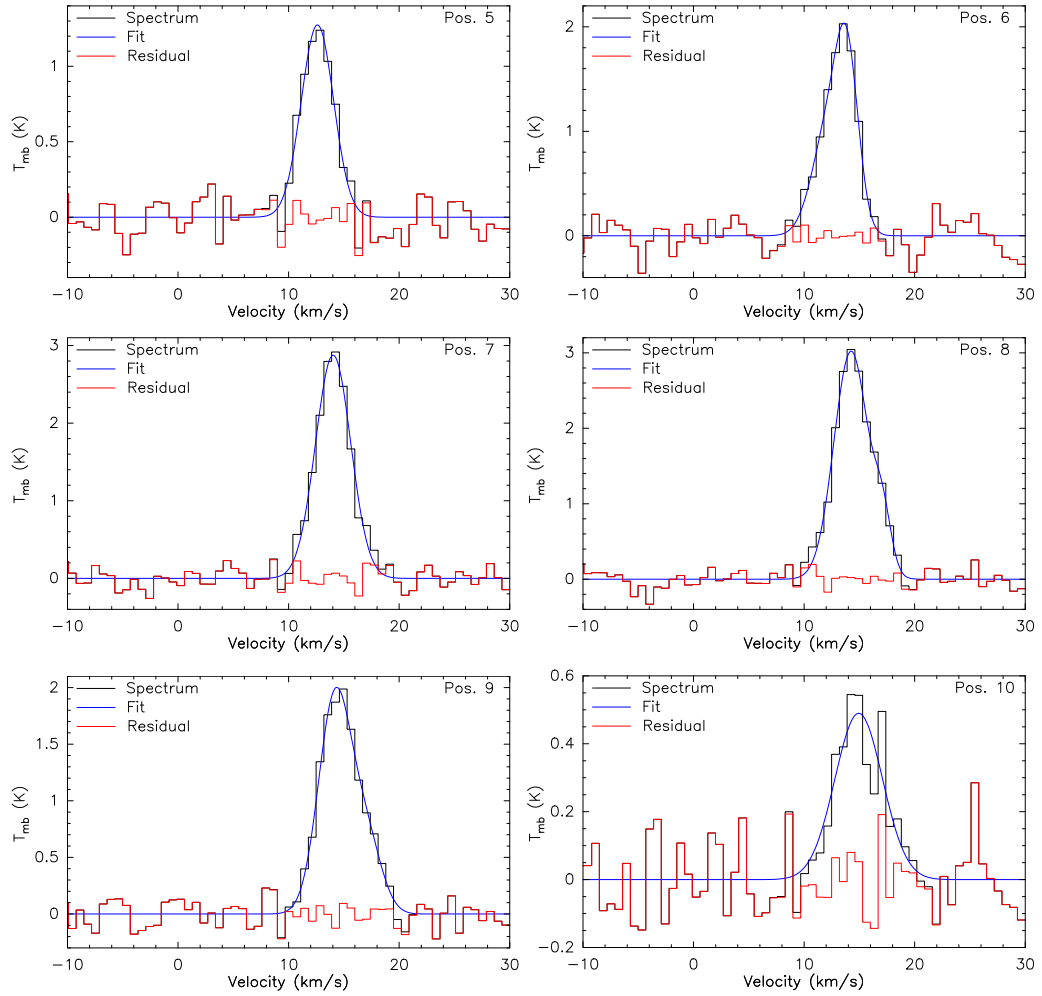
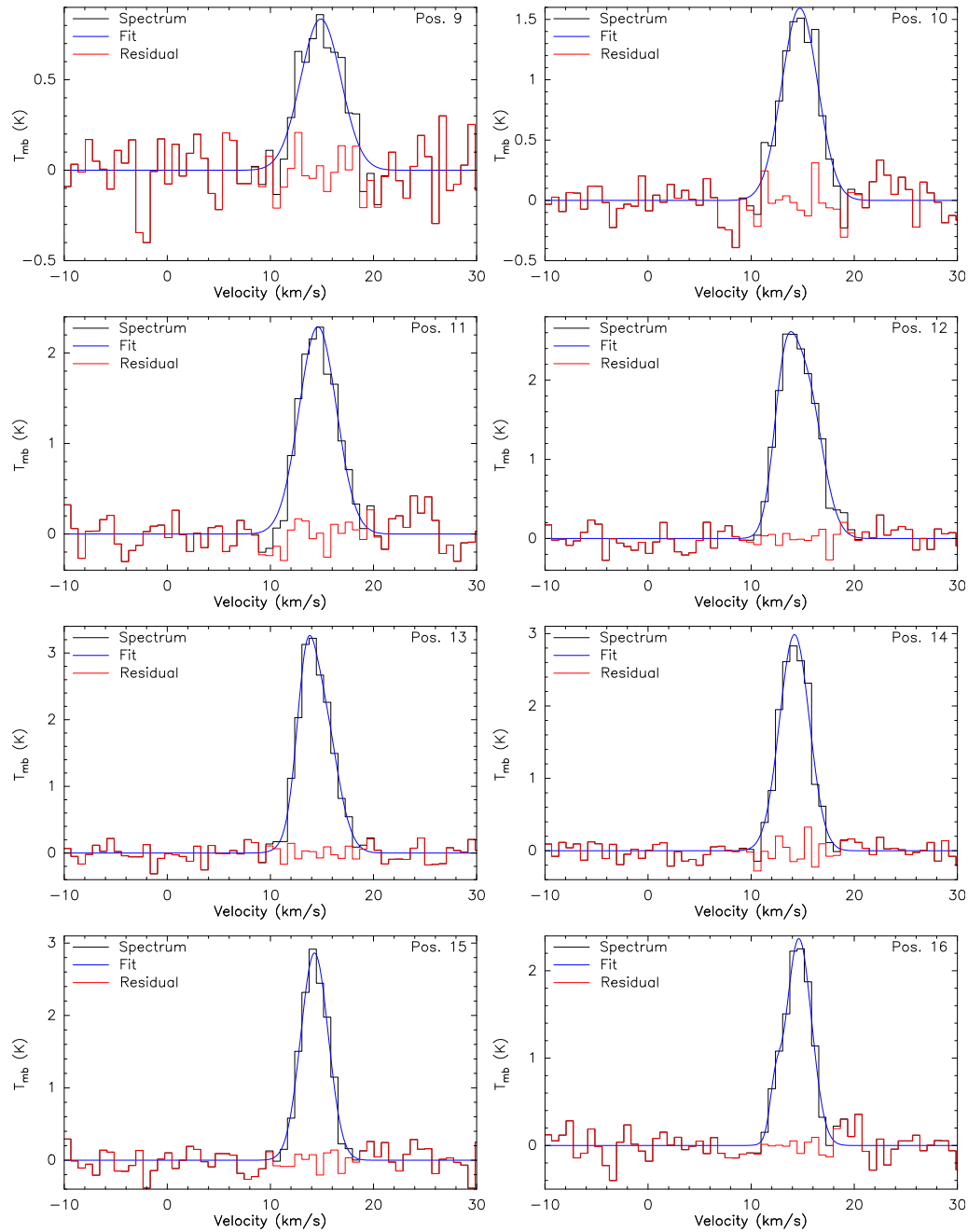


Figure E.8: Line fits of ^{12}CO in MM2 (cont.).

E.5 1342201809 (^{13}CO — MM1)**Figure E.9:** Line fits of ^{13}CO in MM1.

E.6 1342201810 (^{13}CO — MM2)**Figure E.10: Line fits of ^{13}CO in MM2.**

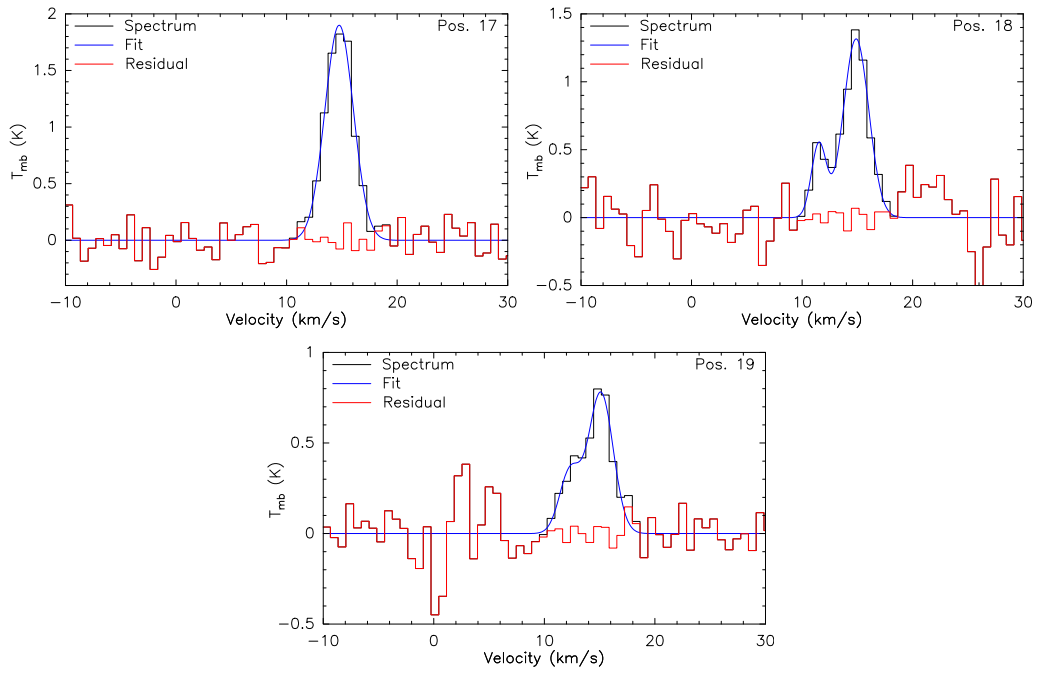


Figure E.11: Line fits of ^{13}CO in MM2 (cont.).

E.7 1342201818 ($^{12}\text{C}^+$ — MM1)

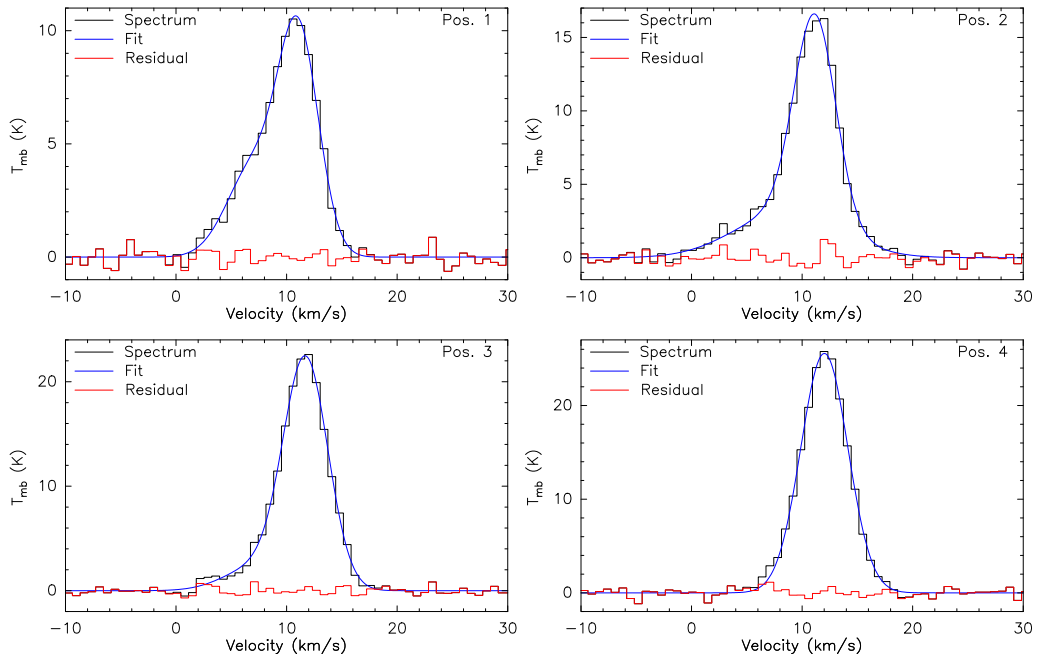


Figure E.12: Line fits of $^{12}\text{C}^+$ in MM1.

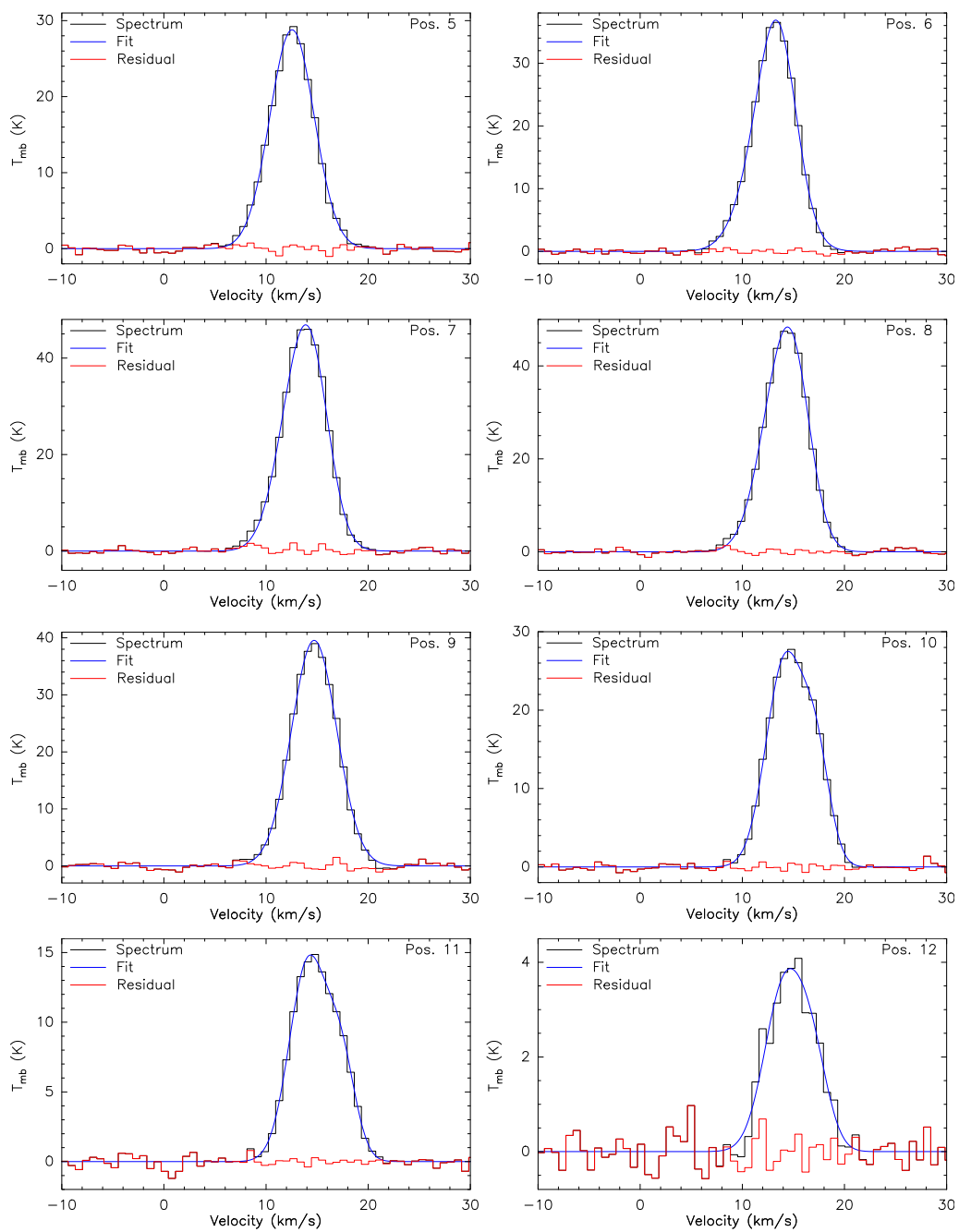
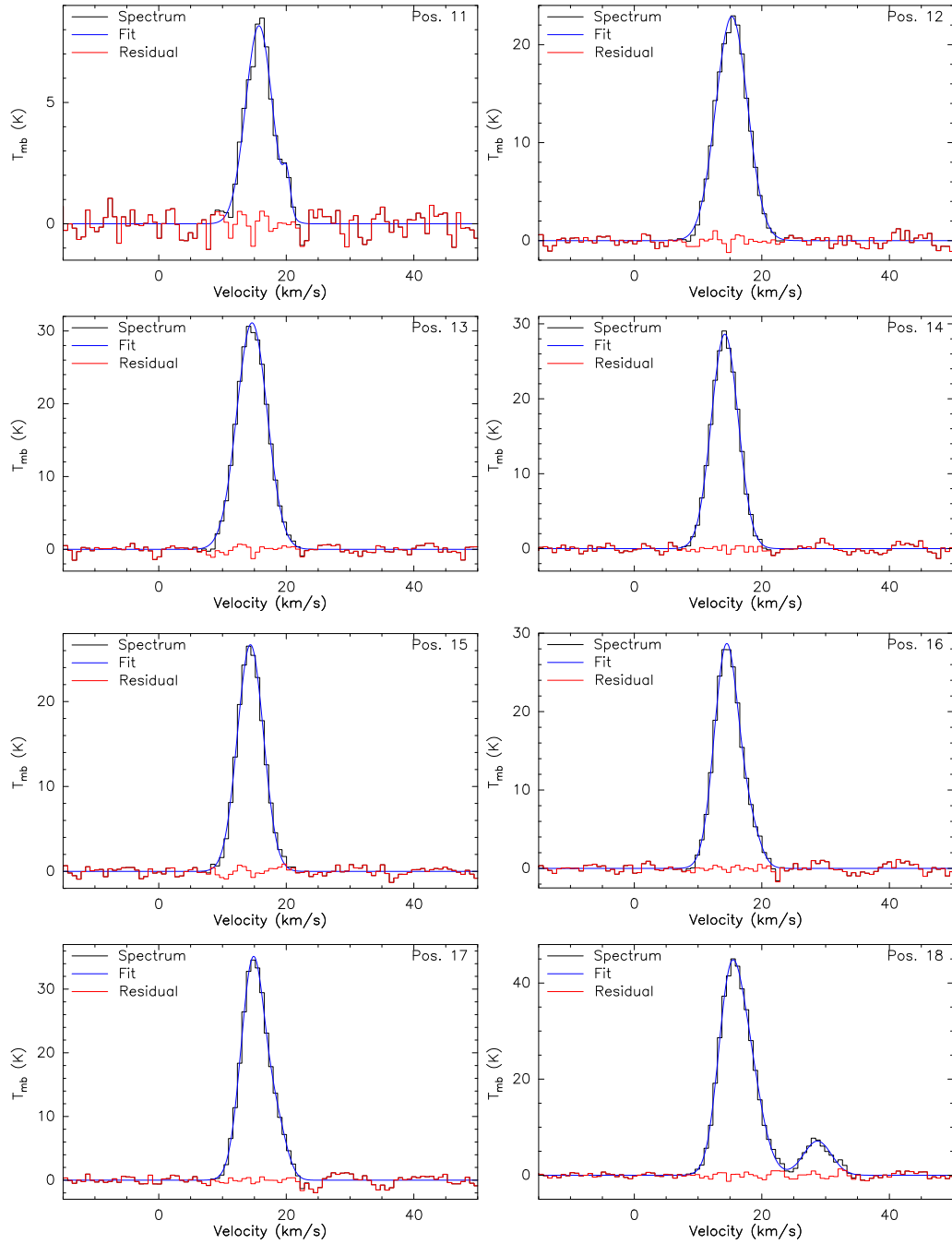


Figure E.13: Line fits of $^{12}\text{C}^+$ in MM1 (cont.).

E.8 1342201819 ($^{12}\text{C}^+$ — MM2)**Figure E.14:** Line fits of $^{12}\text{C}^+$ in MM2.

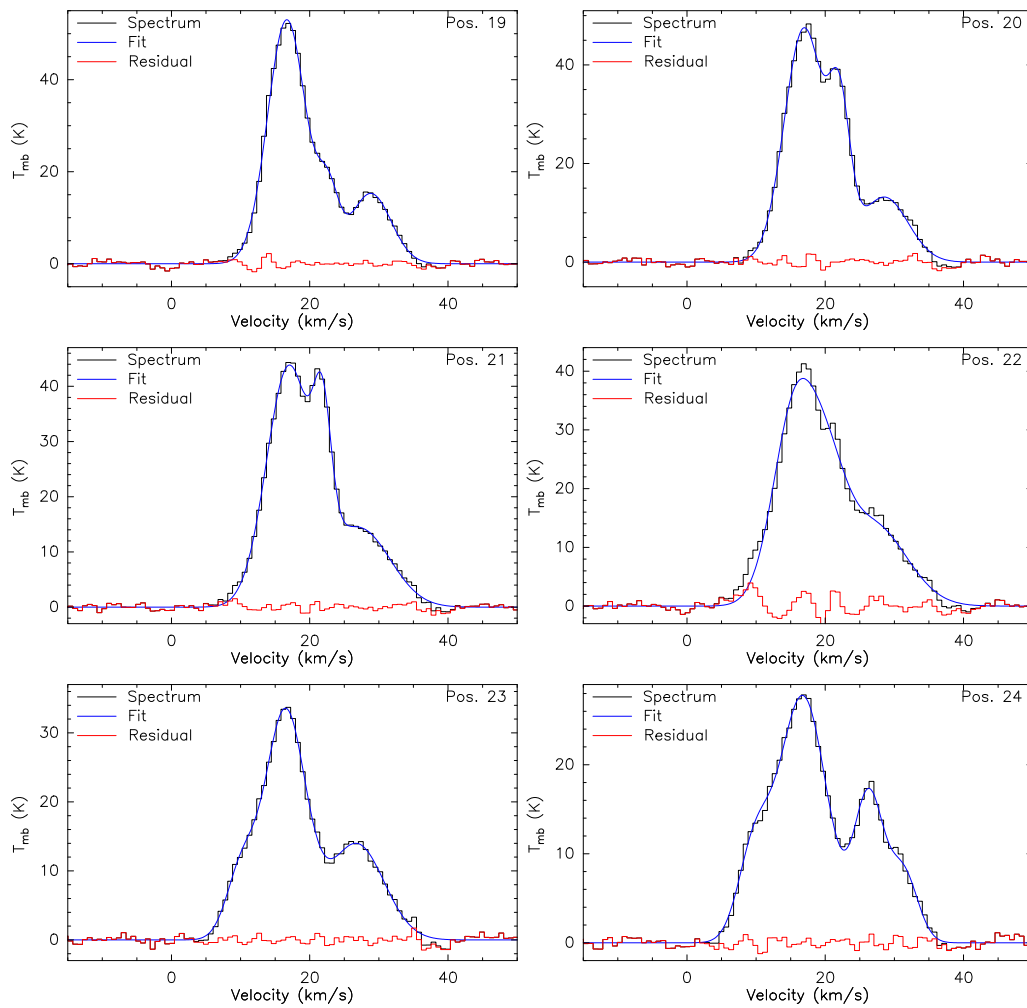


Figure E.15: Line fits of $^{12}\text{C}^+$ in MM2 (cont. 1).

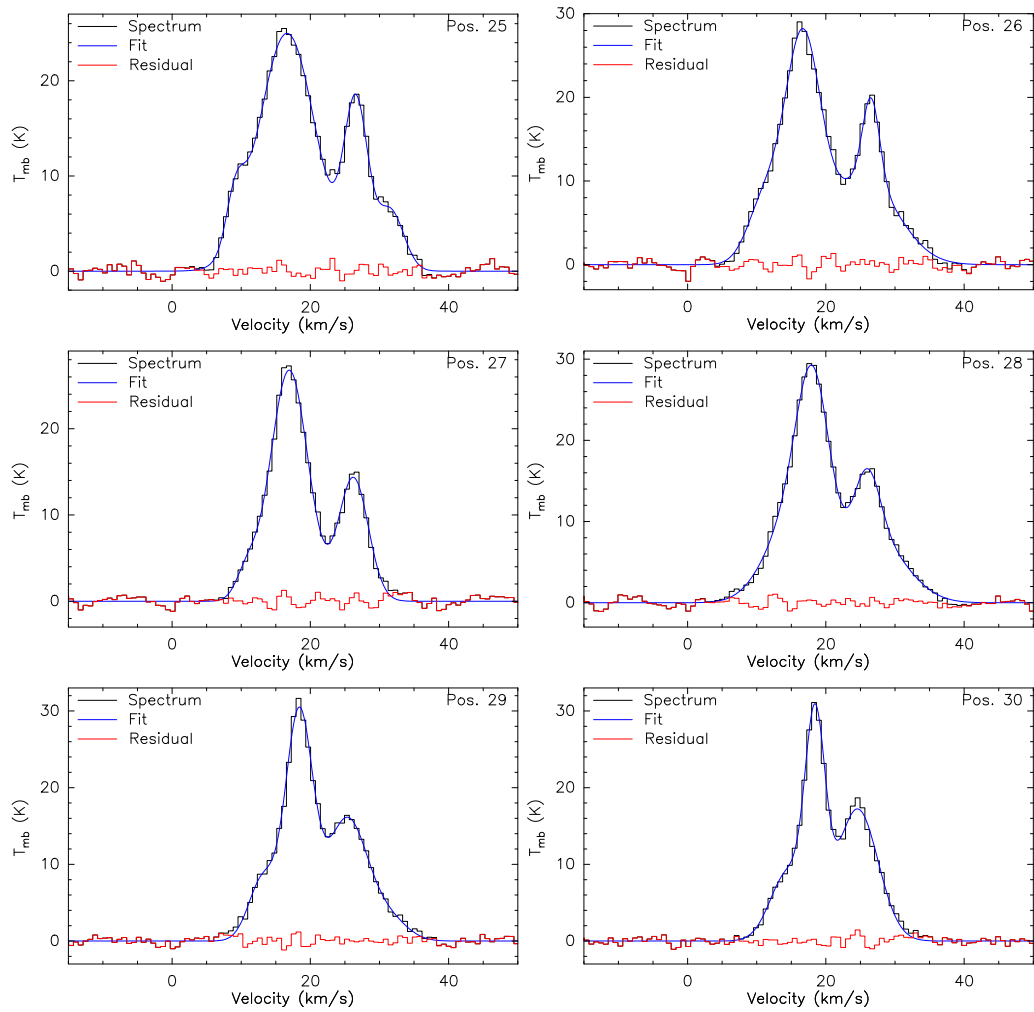


Figure E.16: Line fits of $^{12}\text{C}^+$ in MM2 (cont.2).

Line fits of the observed species from the point observations

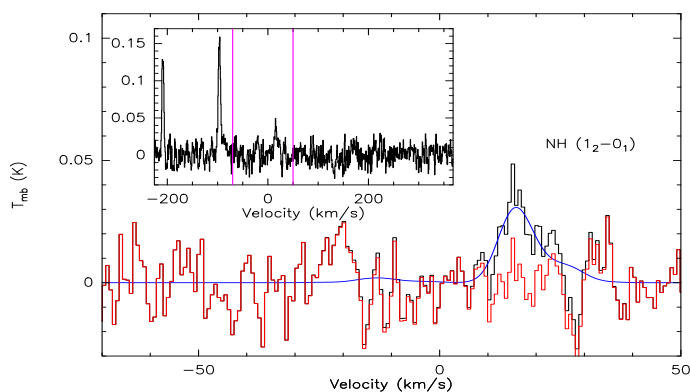


Figure F.1: Hyperfine line fit of the NH in MM2-IF.

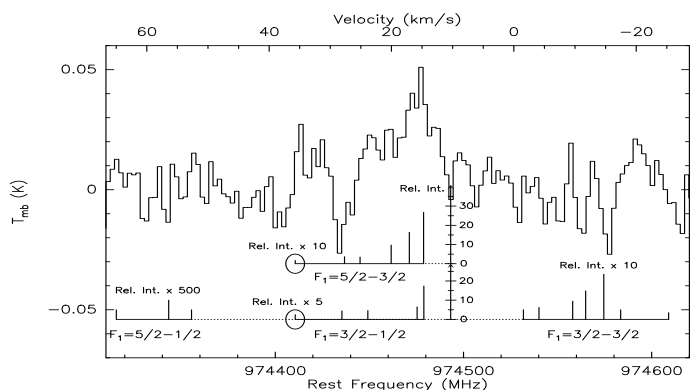


Figure F.2: Theoretical positions of the hf-components of the NH in MM2-IF. The line strengths are indicated in % of the total line strength. The scaling of the line strengths is indicated on the plot.

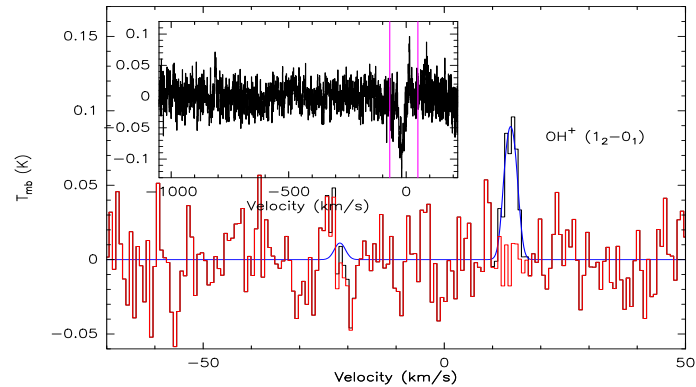


Figure F.3: Hyperfine line fit of the OH^+ in MM1-IF.

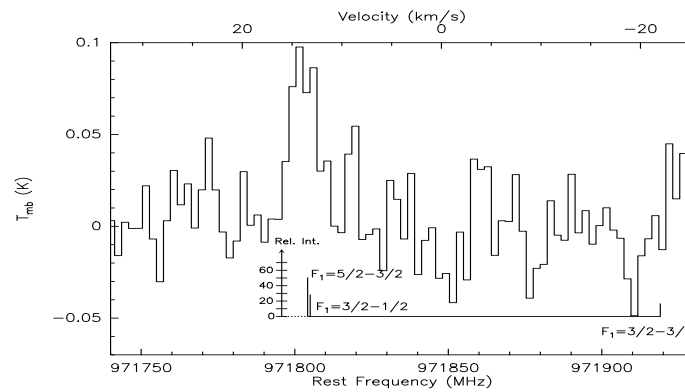


Figure F.4: Theoretical positions of the observed hyperfine components of the OH^+ in MM1-IF. The line strengths are indicated in % of the total line strength.

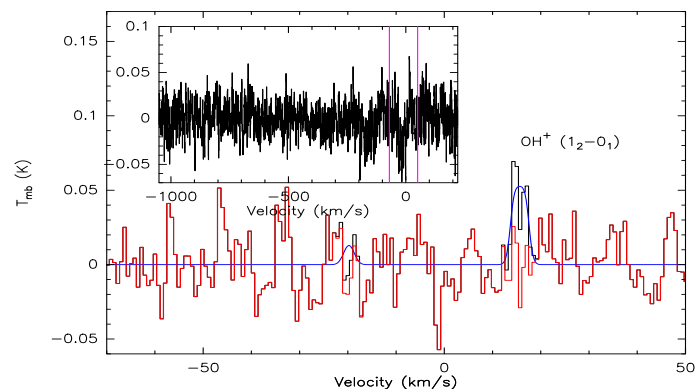


Figure F.5: Hyperfine line fit of the OH^+ in MM2-IF. The weak line, seen on the left side in the smaller plot on the upper panel, is NH (from LSB).

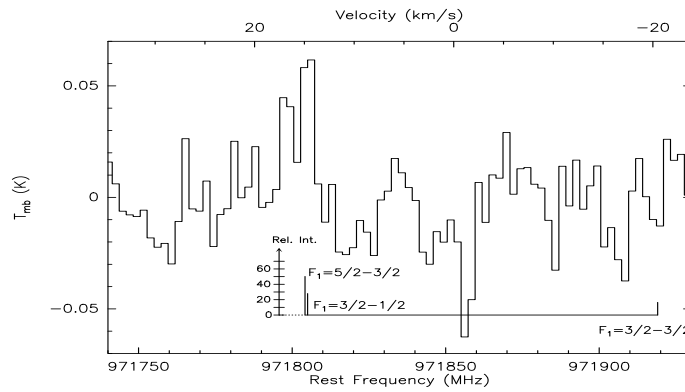


Figure F.6: Theoretical positions of the observed hyperfine components of the OH^+ in MM2-IF. The line strengths are indicated in % of the total line strength.

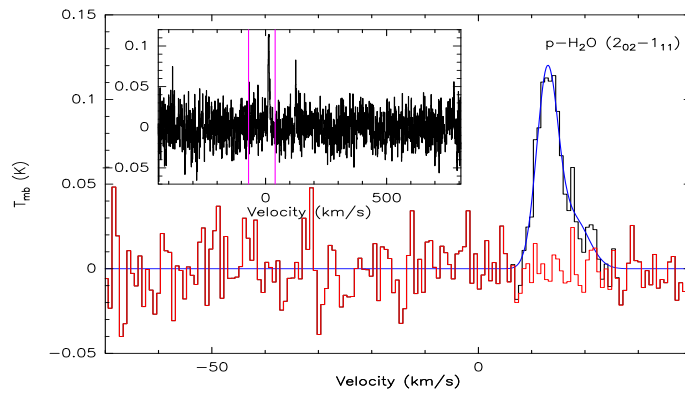


Figure F.7: Line fit of the $p\text{-H}_2\text{O}$ in MM2-peak.

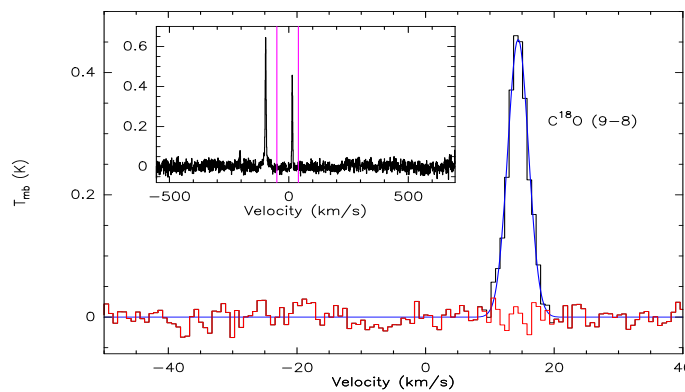


Figure F.8: Line fits of the C^{18}O in MM1. In the smaller plot of the top panel, the other two lines, from left to right, are NH (from LSB) and $p\text{-H}_2\text{O}$ (from USB), respectively.

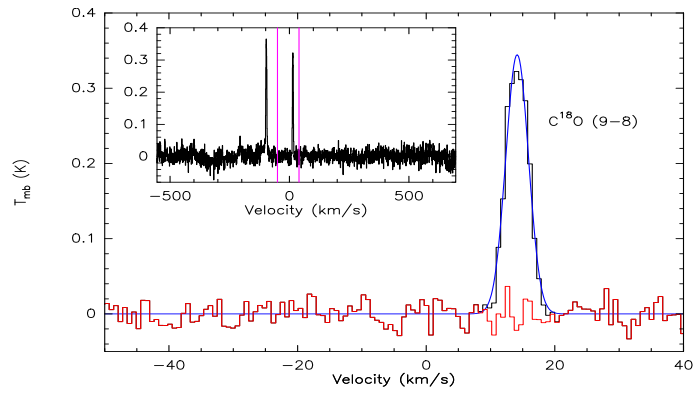


Figure F.9: Line fits of the $C^{18}O$ in MM2-IF.

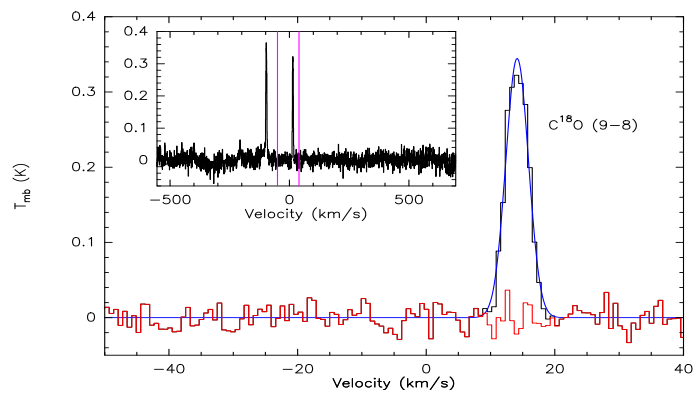


Figure F.10: Line fits of the $C^{18}O$ in MM2-peak.

Velocity channel maps

For all plots: the covered velocity range is roughly 7 to 20 km s⁻¹ (except Fig. G.1), the velocity resolution is 0.7 km s⁻¹ and the contours are from 10% to 90% of the peak values¹.

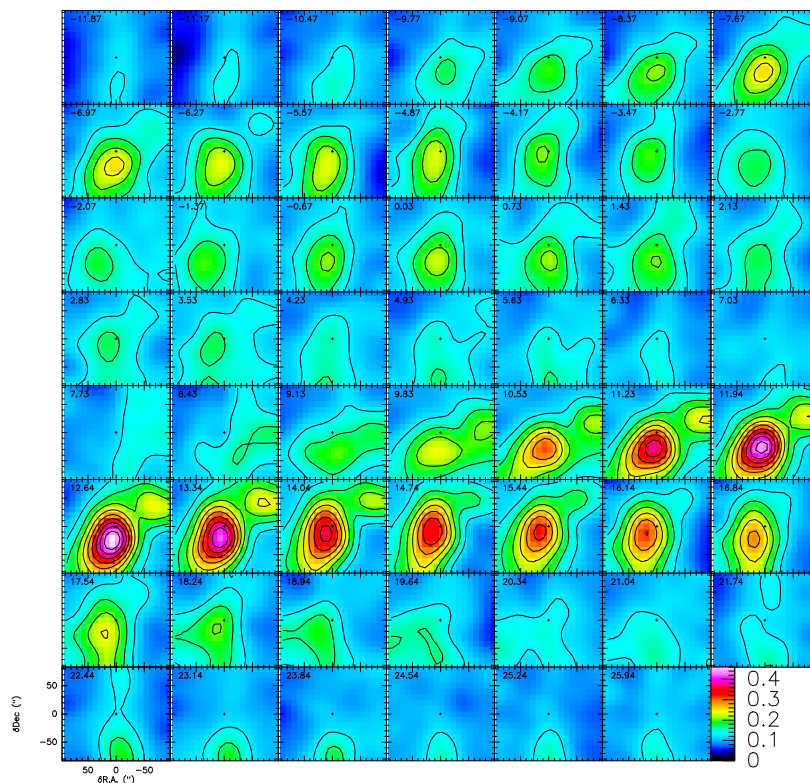


Figure G.1: This channel map shows all three observed hyperfine components of CH. The covered velocity range is roughly -12 to 26 km s⁻¹.

¹The peak values are 0.16 K, 0.2 K, 0.16 K and 0.46 K for CS ($11 \rightarrow 10$), C₂H ($F = 6 \rightarrow 5$), C₂H ($F = 5 \rightarrow 4$), and CH, respectively.

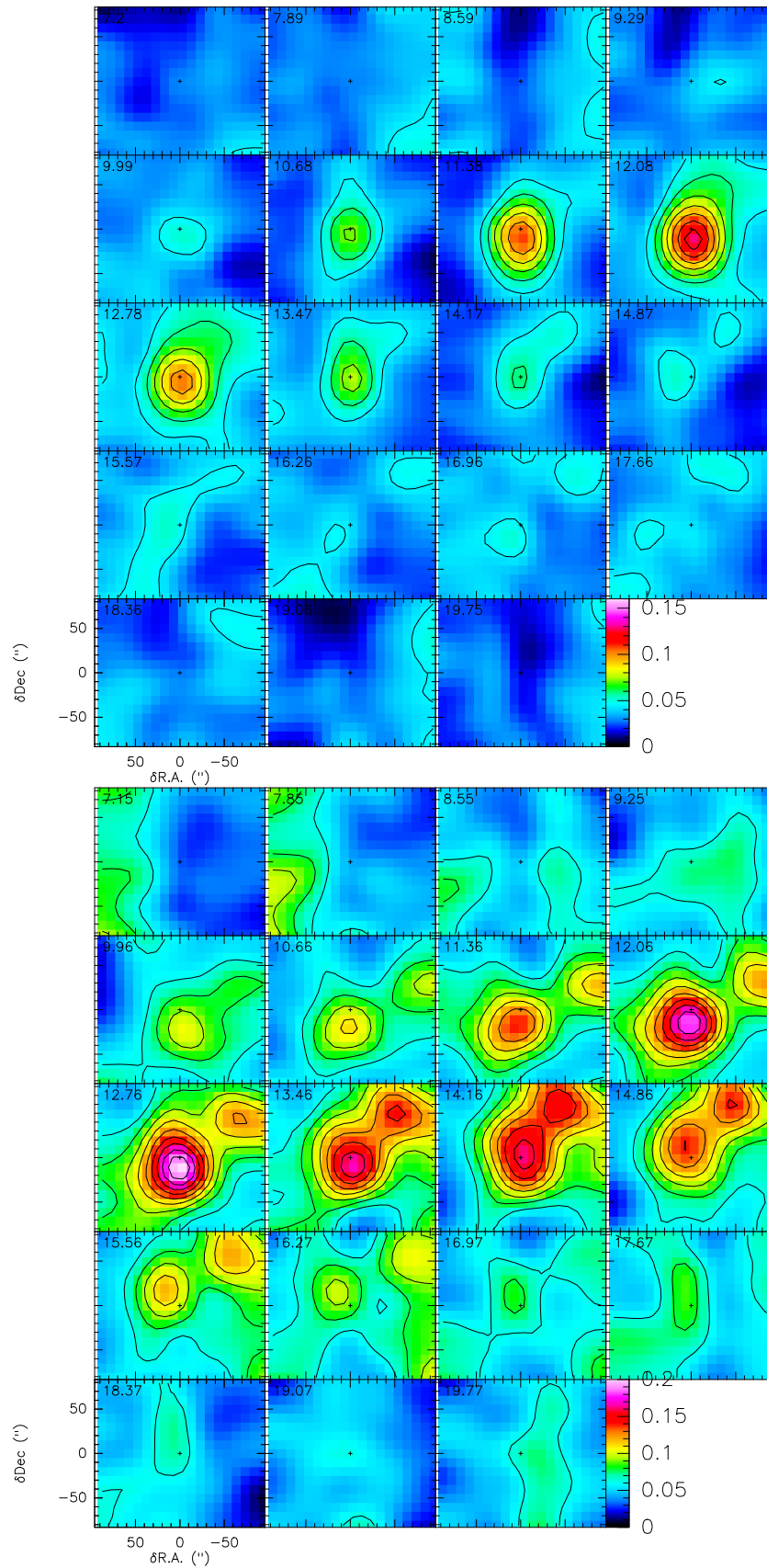


Figure G.2: Upper panel: $CS (11 \rightarrow 10)$. Lower panel: $C_2H (F = 6 \rightarrow 5)$.

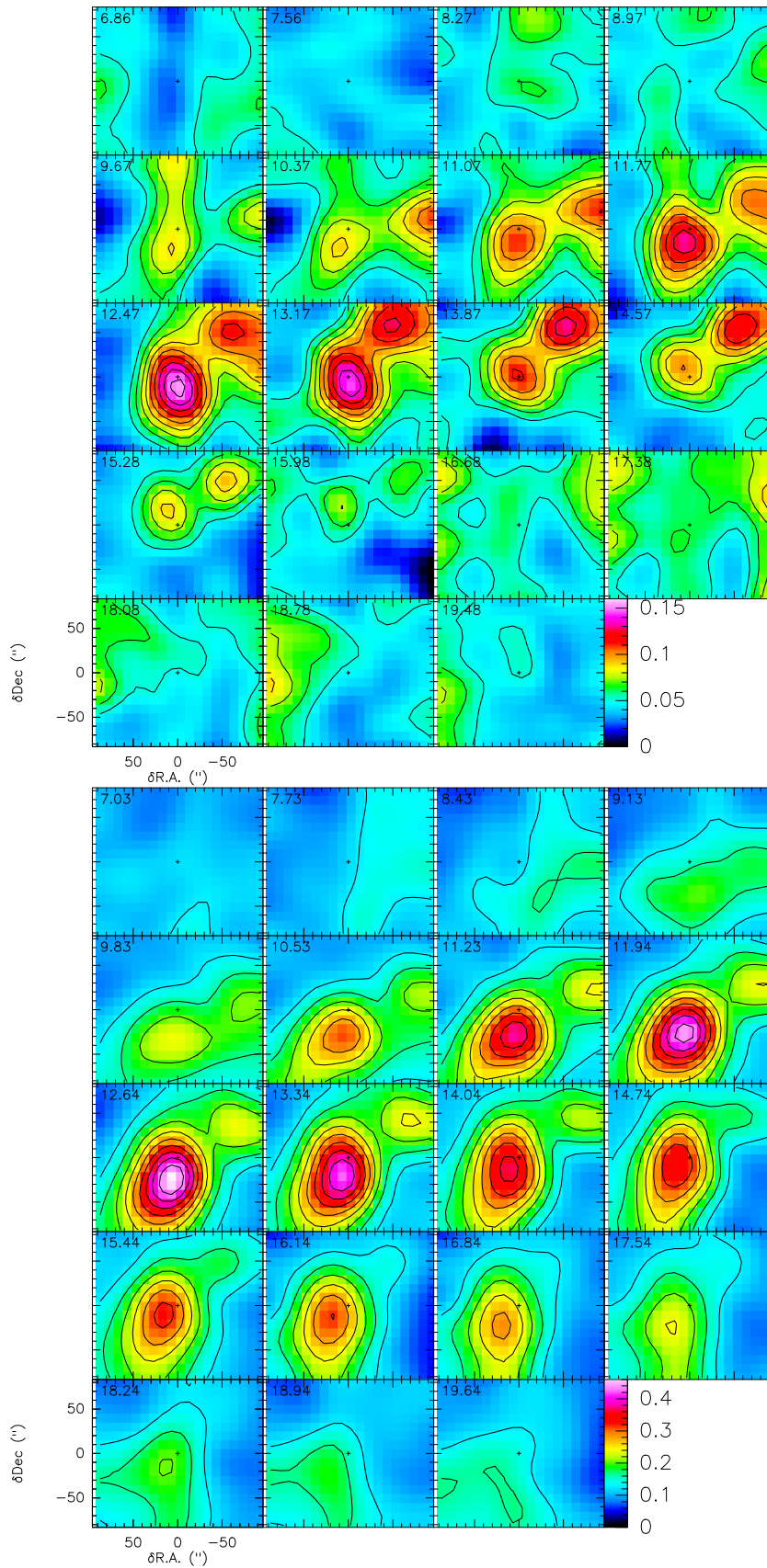


Figure G.3: Upper panel: C_2H ($F = 5 \rightarrow 4$). Lower panel: CH ($F = 2 \rightarrow 1$).

H

**Line shapes and their distributions in MM1
and MM2**

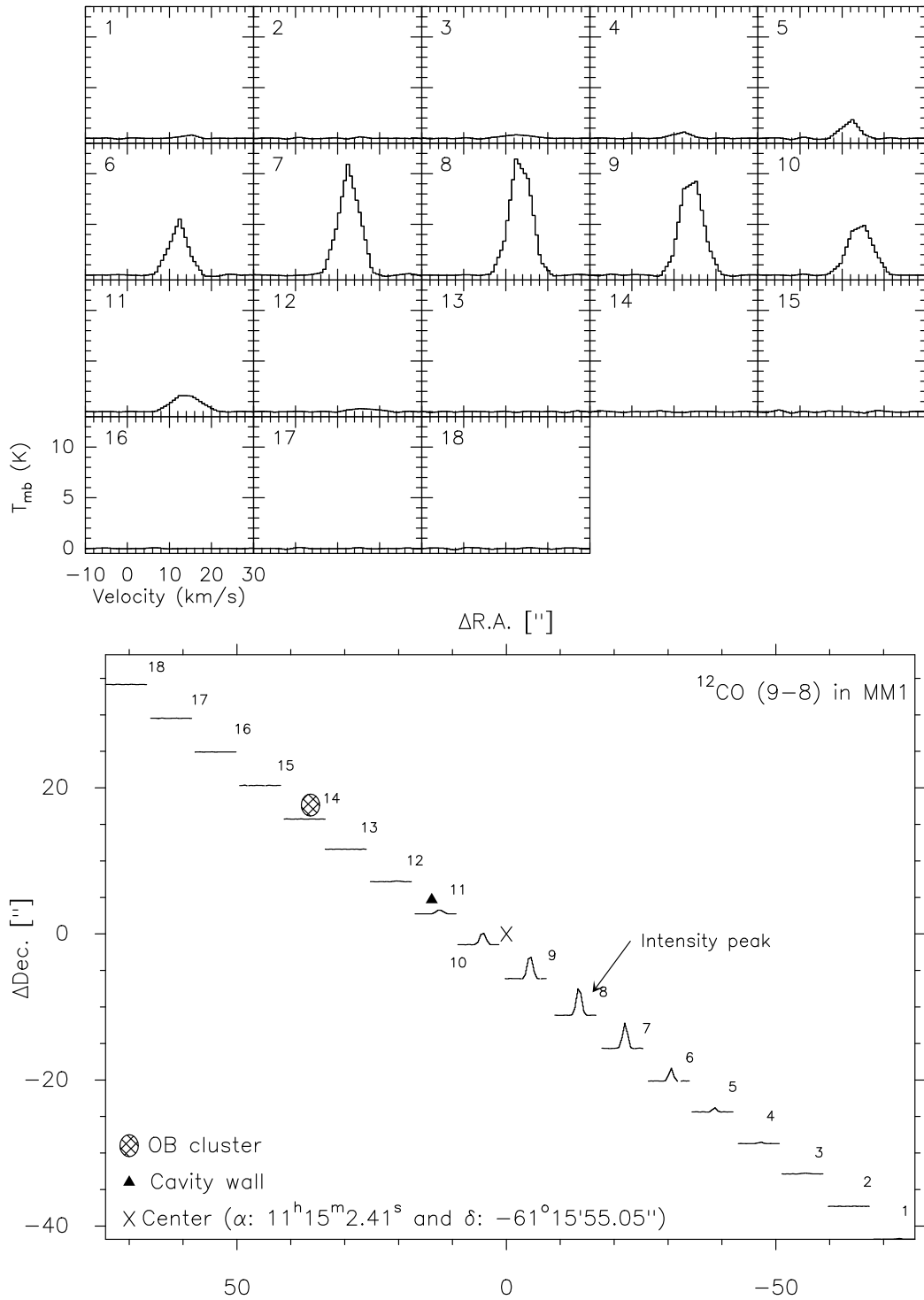


Figure H.1: The line shapes and distribution of ^{12}CO in MM1.

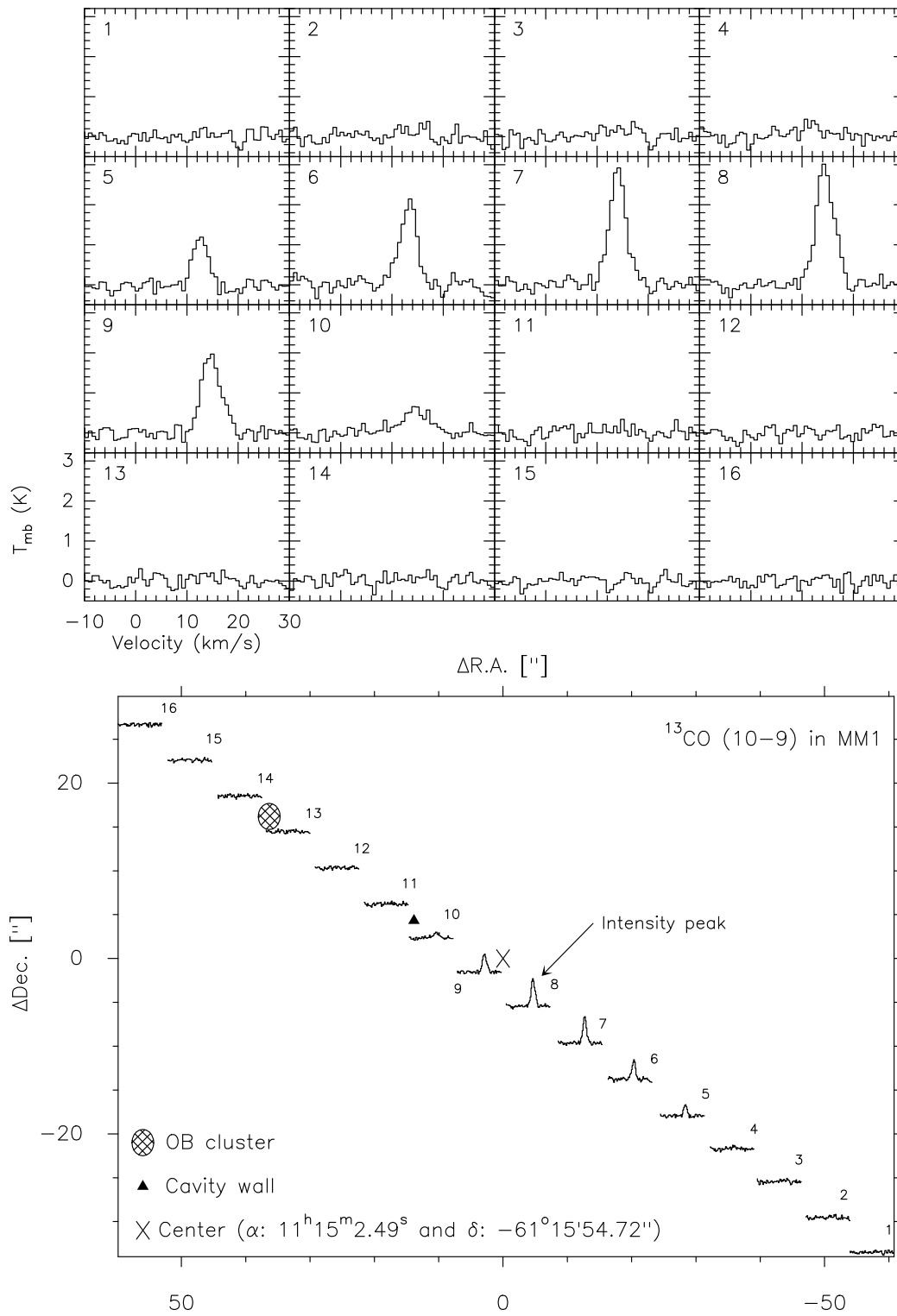


Figure H.2: The line shapes and distribution of ^{13}CO in MM1.

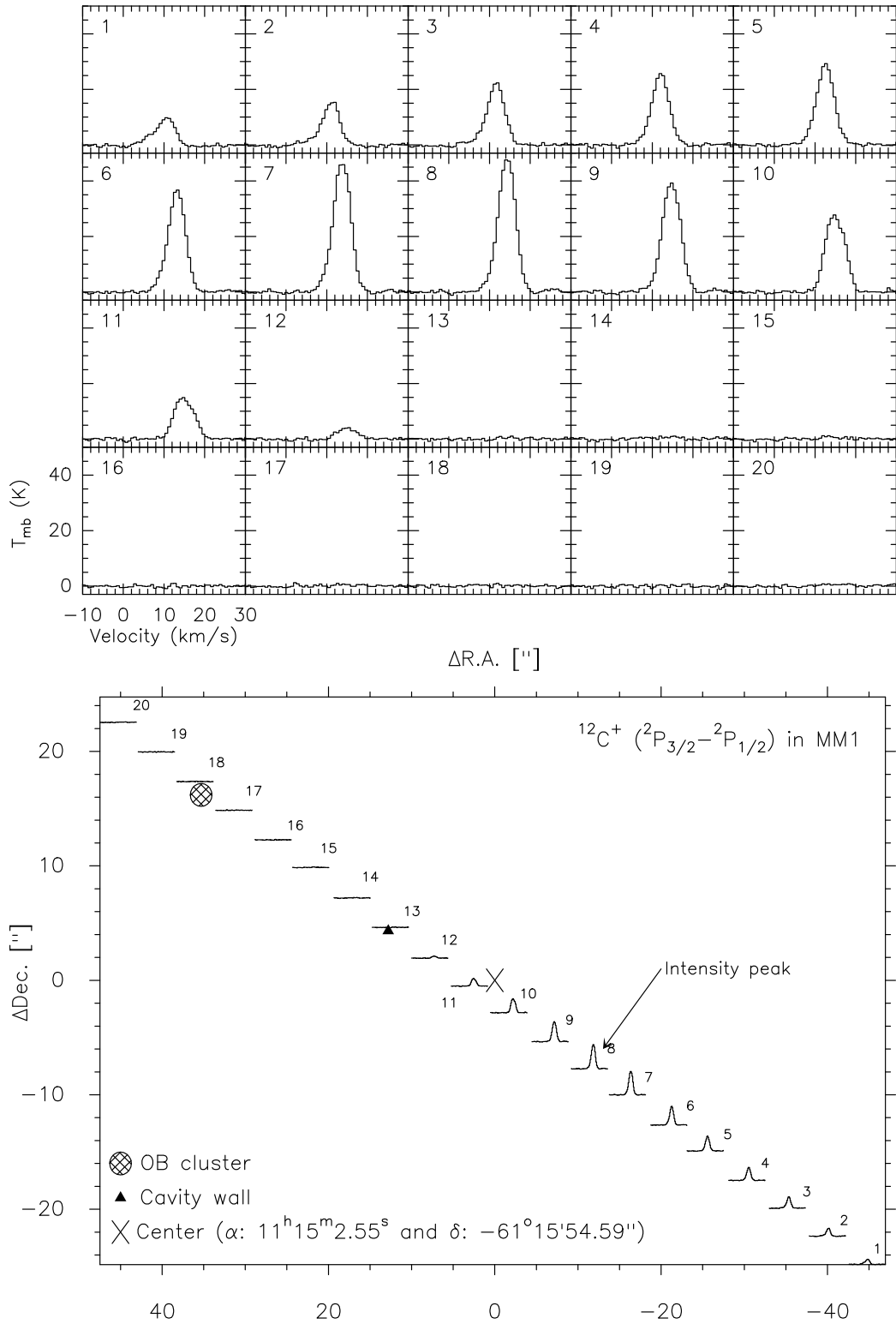


Figure H.3: The line shapes and distribution of $^{12}\text{C}^+$ in MM1.

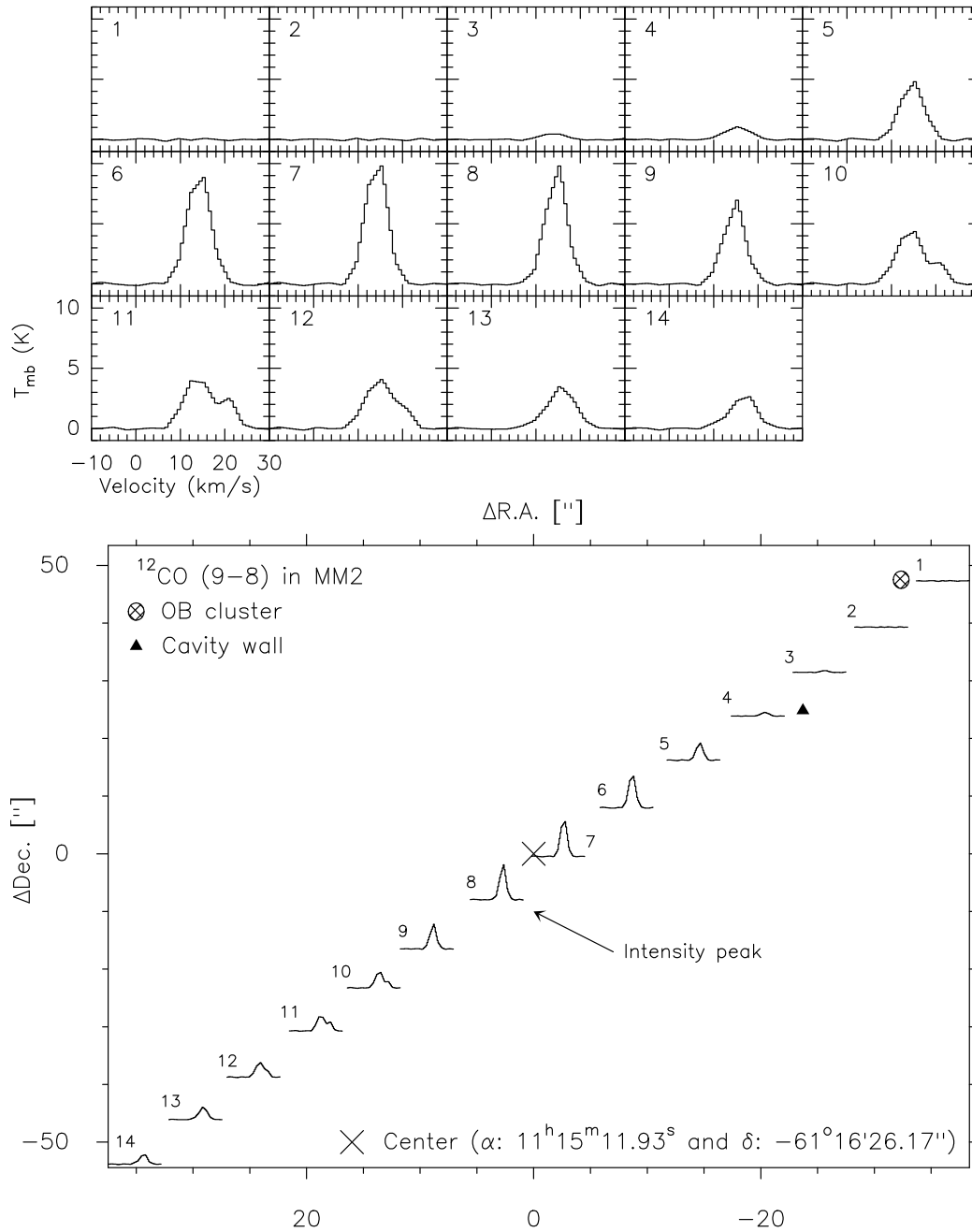


Figure H.4: The line shapes and distribution of ^{12}CO in MM2.

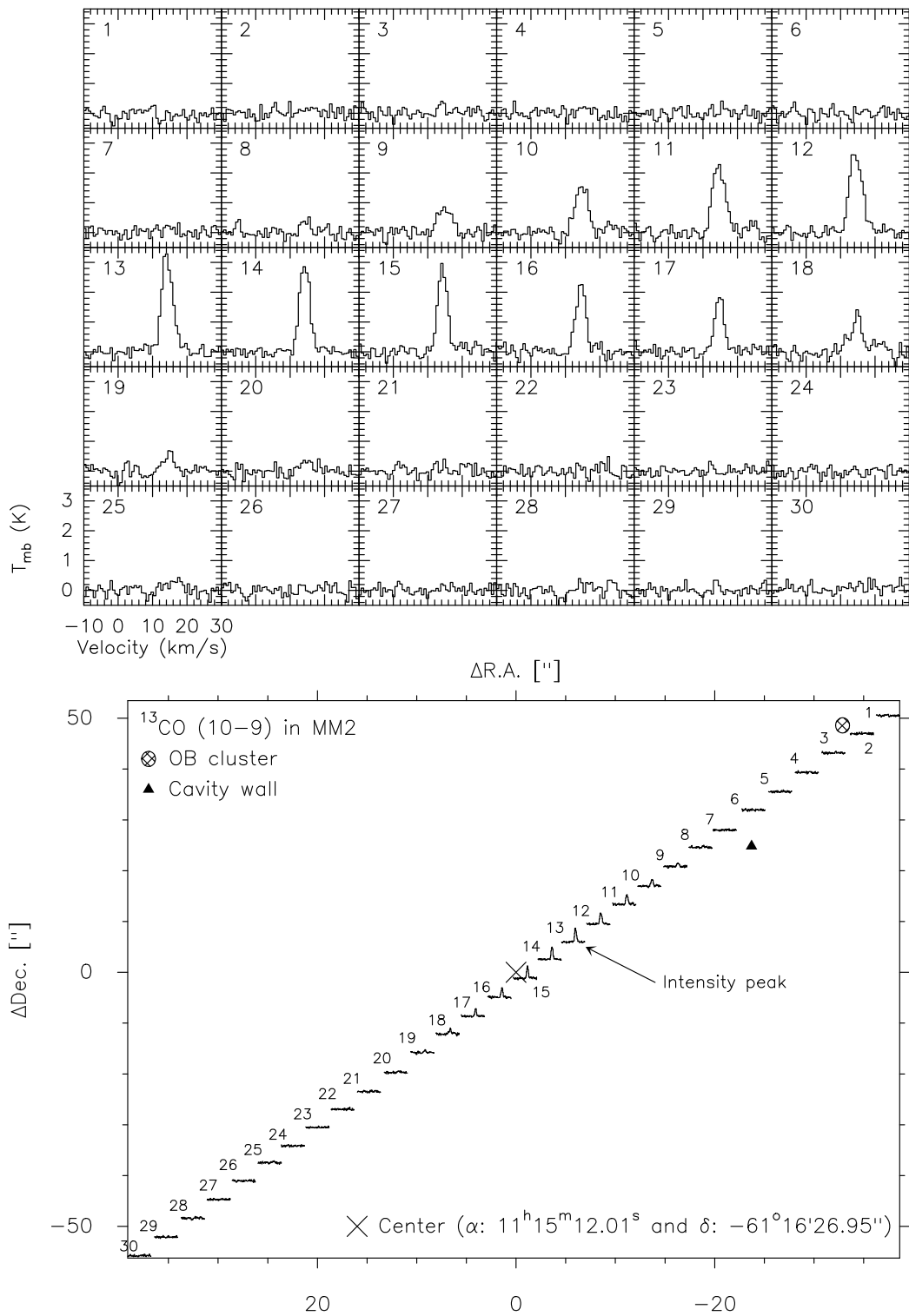


Figure H.5: The line shapes and distribution of ^{13}CO in MM2.

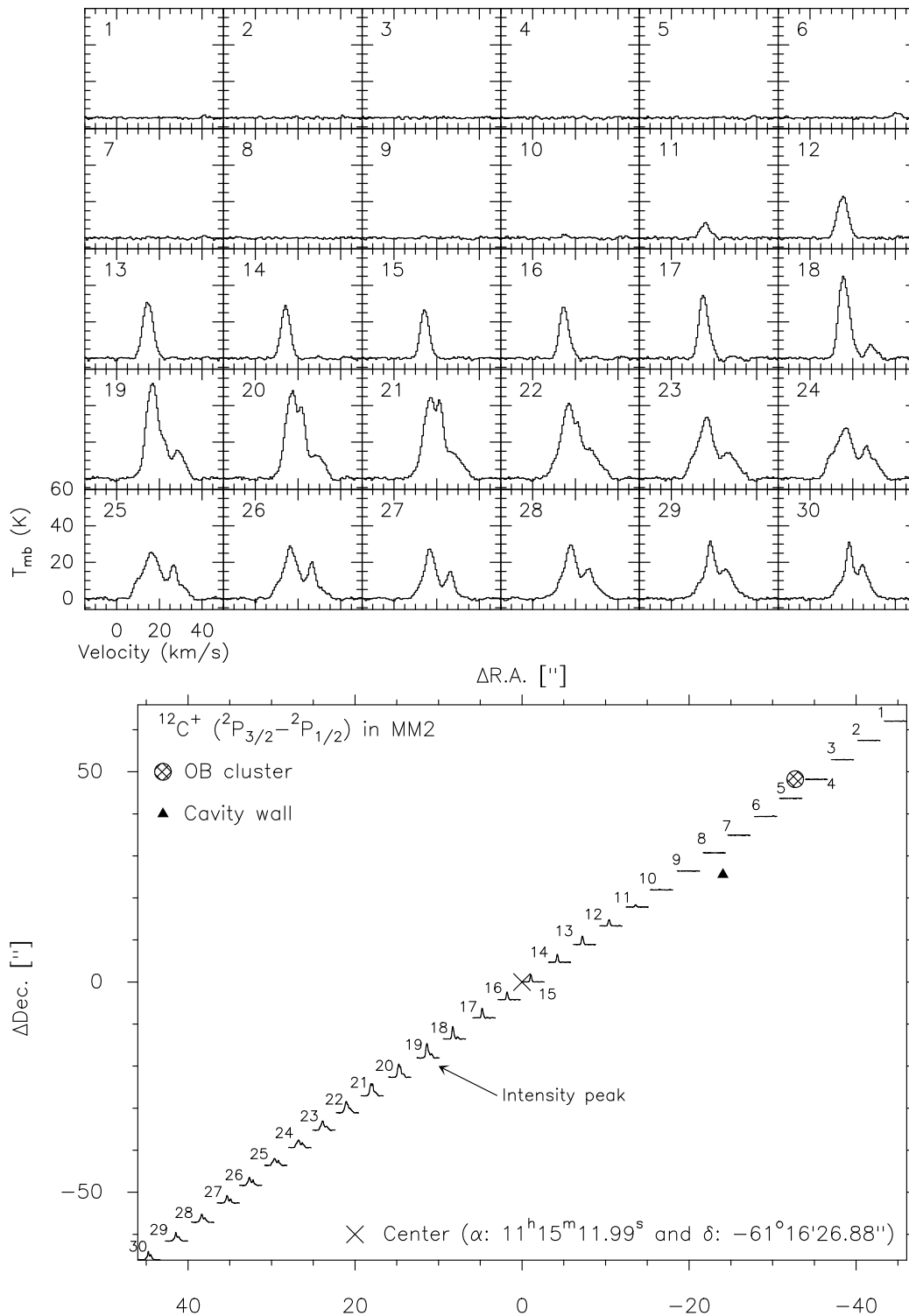


Figure H.6: The line shapes and distribution of $^{12}\text{C}^+$ in MM2.

Integrated intensity maps of the observed species from PACS observations

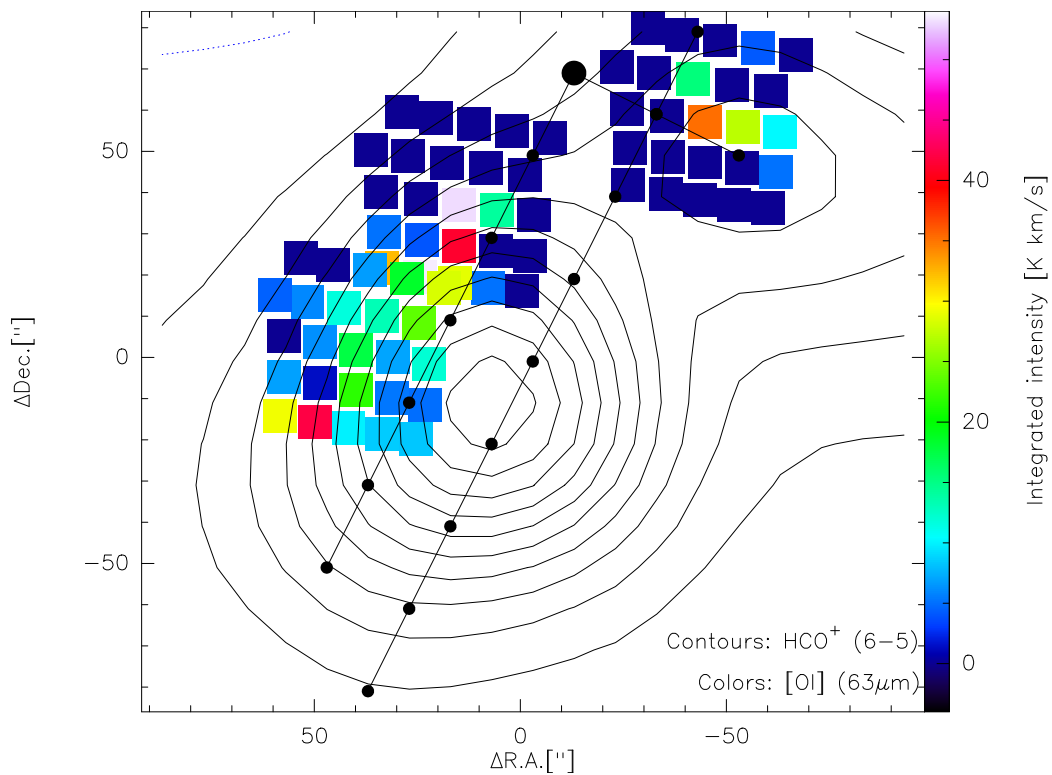


Figure I.1: Integrated intensity map of [OI] (63 μm) from range spectroscopy over plotted to HCO^+ (6 → 5) contours.

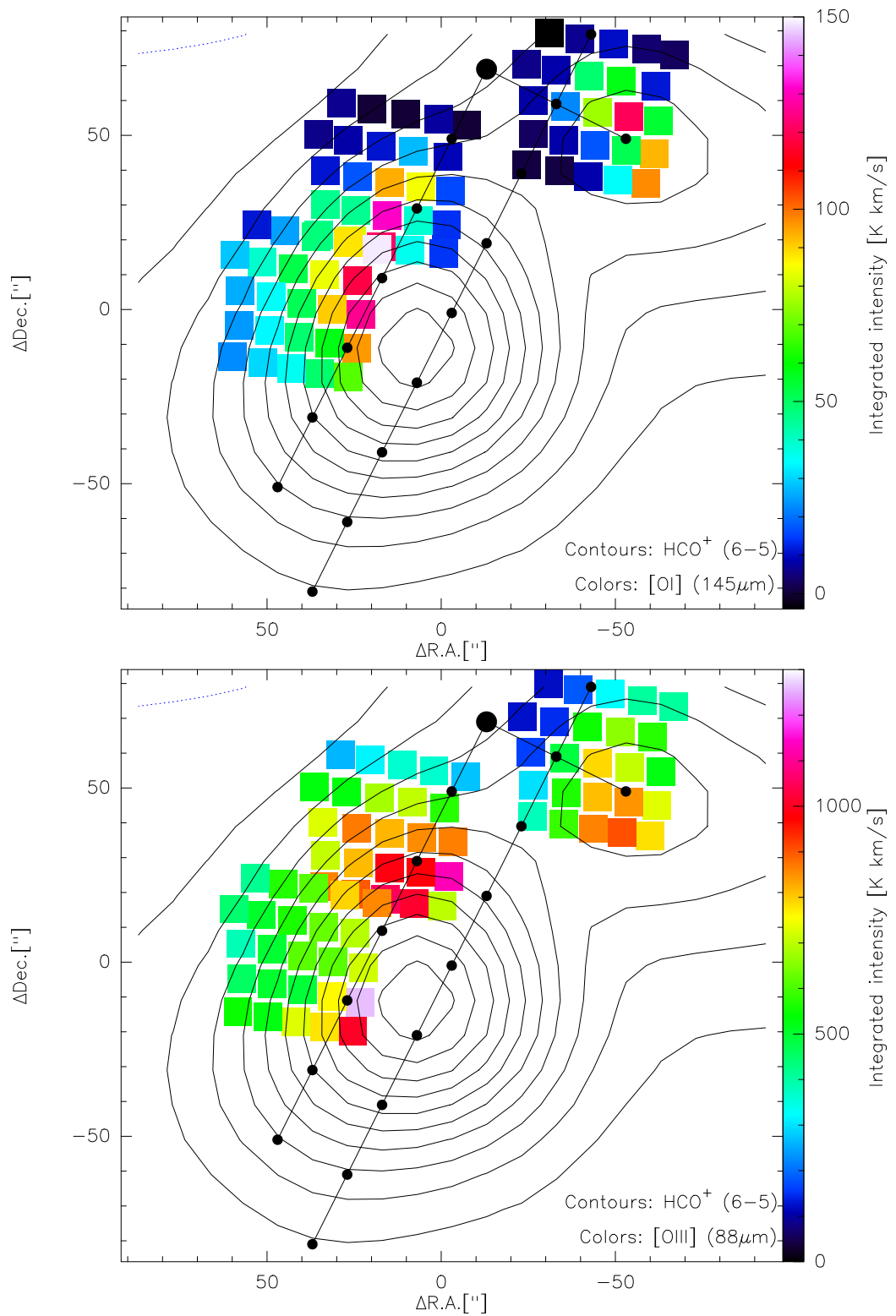


Figure I.2: Integrated intensity maps of $[OI] (145\mu m)$ and $[OIII] (88\mu m)$ from range spectroscopy over plotted to $HCO^+ (6 \rightarrow 5)$ contours.

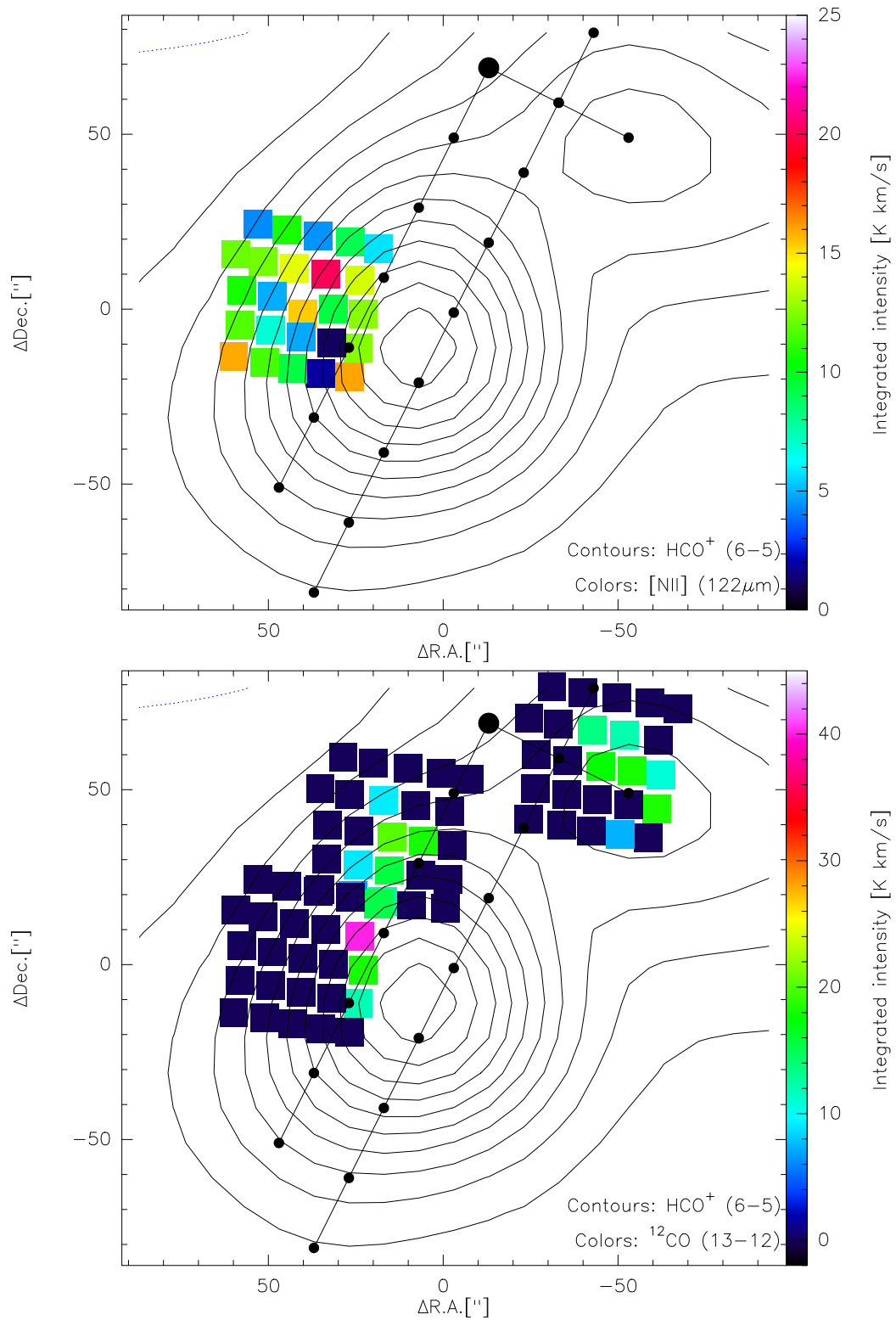


Figure I.3: Integrated intensity maps of [NII] ($122\mu m$) and CO ($13 \rightarrow 12$) from range spectroscopy over plotted to HCO^+ ($6 \rightarrow 5$) contours.

210 Integrated intensity maps of the observed species from PACS observations

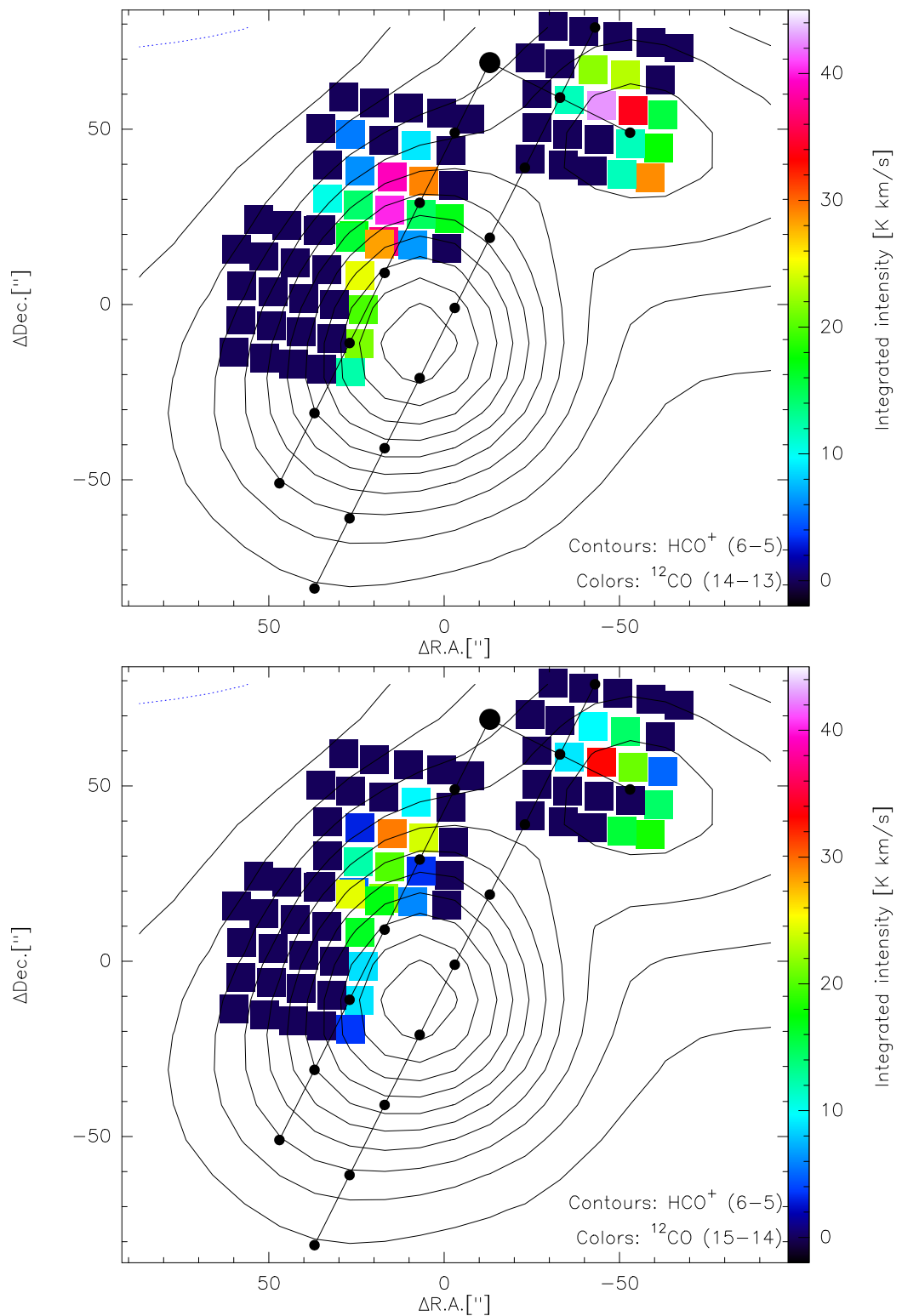


Figure I.4: Integrated intensity maps of ^{12}CO ($13 \rightarrow 12$ and $14 \rightarrow 13$) from range spectroscopy over plotted to HCO^+ ($6 \rightarrow 5$) contours.

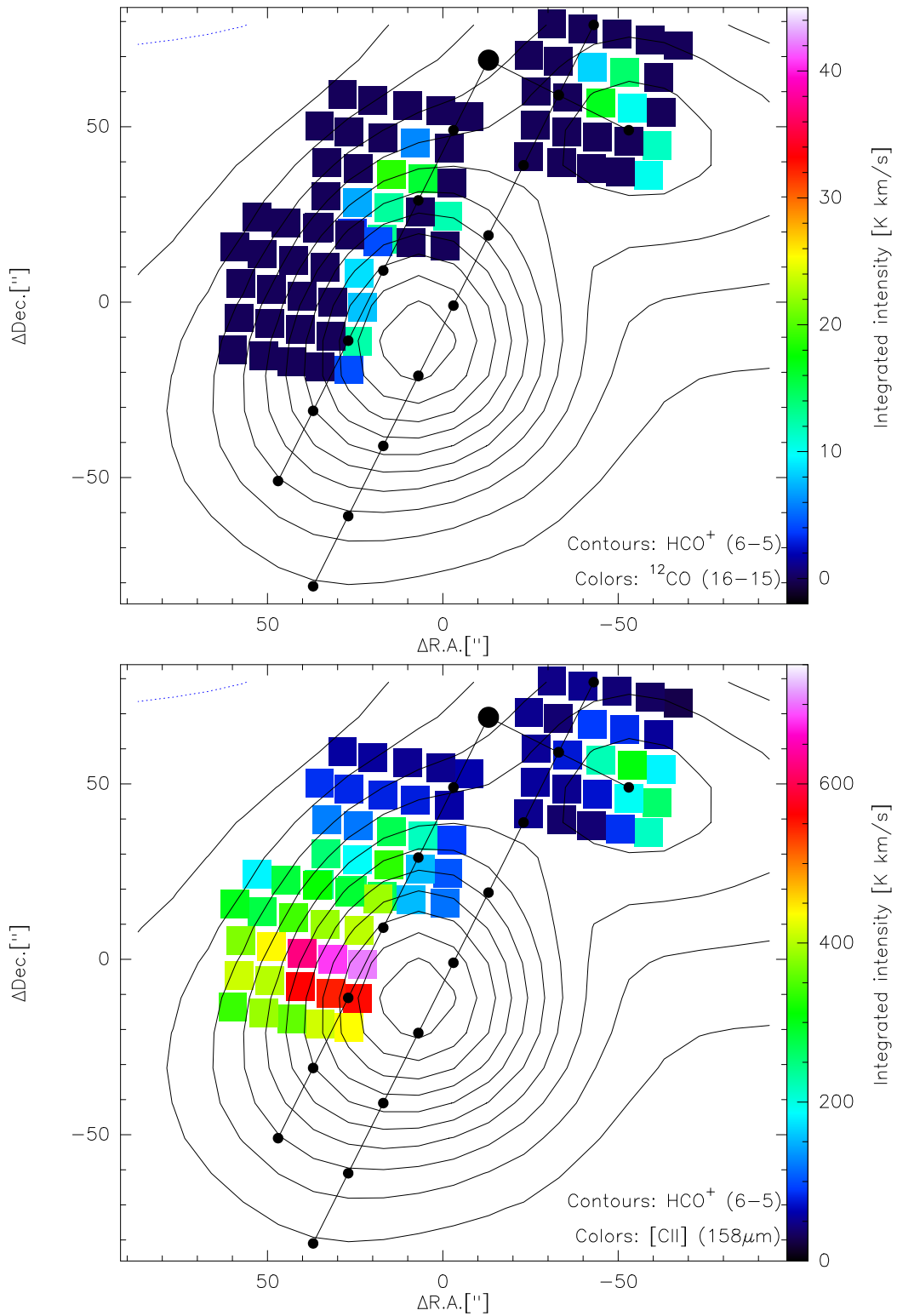


Figure I.5: Integrated intensity maps of ^{12}CO (16 \rightarrow 15) and $[\text{CII}]$ (158 μm) from range spectroscopy over plotted to HCO^+ (6 \rightarrow 5) contours.

212 Integrated intensity maps of the observed species from PACS observations



The derived physical parameters for Herschel observations

Table J.1: The determined physical parameters of HCO^+ and CS. The third column shows the offsets from 0,0 position ($\alpha_{J2000} = 11^{\text{h}}15^{\text{m}}8^{\text{s}}.85$ and $\delta_{J2000} = -61^{\circ}16'50''$). The central OB cluster is at the first position of C1 (hence C2, too).

Cut	$\Delta\alpha/\Delta\delta$ ["/"]	Vel. comp.	$\int T_{\text{mb}} dv$ [K km s ⁻¹]	V [km s ⁻¹]	FWHM [km s ⁻¹]	T_{peak} [K]
HCO^+						
C1	-13/69	1	0.73 ± 0.03	13.9 ± 0.10	4.74 ± 0.26	0.14
	-33/59	1	1.41 ± 0.03	13.7 ± 0.05	5.02 ± 0.13	0.26
	-53/49	1	1.95 ± 0.03	13.4 ± 0.04	5.20 ± 0.10	0.35
C2	-13/69	1	0.73 ± 0.03	13.9 ± 0.10	4.74 ± 0.26	0.14
	-3/49	1	1.23 ± 0.30	13.9 ± 0.06	4.86 ± 0.15	0.24
	7/29	1	2.31 ± 0.03	13.5 ± 0.04	5.27 ± 0.01	0.41
	17/9	1 st	2.76 ± 0.05	12.6 ± 0.01	4.59 ± 0.03	0.57
		2 nd	0.62 ± 0.04	15.5 ± 0.08	2.98 ± 0.22	0.20
	27/ - 11	1 st	0.37 ± 0.06	11.7 ± 0.07	2.12 ± 0.21	0.16
		2 nd	3.31 ± 0.07	13.2 ± 0.06	6.13 ± 0.09	0.51
	37/ - 31	1 st	1.66 ± 0.03	11.6 ± 0.01	4.45 ± 0.12	0.35
		2 nd	0.67 ± 0.01	15.8 ± 0.02	4.77 ± 0.29	0.13
	47/ - 51	1 st	1.19 ± 0.07	11.7 ± 0.12	4.74 ± 0.26	0.24
		2 nd	0.34 ± 0.07	16.6 ± 0.32	4.07 ± 0.63	0.08
	C3	-43/79	1	1.08 ± 0.03	13.8 ± 0.07	4.79 ± 0.17
-33/59		1	1.41 ± 0.03	13.7 ± 0.05	5.02 ± 0.13	0.26
-23/39		1	1.52 ± 0.03	13.5 ± 0.06	5.31 ± 0.13	0.27
-13/19		1 st	1.73 ± 0.01	12.5 ± 0.02	4.56 ± 0.38	0.36
		2 nd	0.62 ± 0.03	15.0 ± 0.20	4.86 ± 0.56	0.12
-3/ - 1		1 st	2.97 ± 0.20	12.2 ± 0.10	3.93 ± 0.18	0.41
		2 nd	0.81 ± 0.20	15.4 ± 0.20	3.16 ± 0.42	0.24

Table J.1 – *continued from previous page*

Cut	$\Delta\alpha/\Delta\delta$ ["/"]	Vel. comp.	$\int T_{\text{mb}} dv$ [K km s ⁻¹]	V [km s ⁻¹]	FWHM [km s ⁻¹]	T _{peak} [K]
	7/ – 21	1 st	3.28 ± 0.03	12.2 ± 0.01	4.39 ± 0.06	0.70
		2 nd	0.99 ± 0.03	15.6 ± 0.05	5.77 ± 0.24	0.16
	17/ – 41	1 st	2.13 ± 0.01	11.9 ± 0.01	4.00 ± 0.09	0.50
		2 nd	0.73 ± 0.14	15.7 ± 0.10	3.79 ± 0.35	0.18
	27/ – 61	1 st	1.13 ± 0.08	11.7 ± 0.01	4.11 ± 0.25	0.26
		2 nd	0.36 ± 0.08	16.0 ± 0.30	3.85 ± 0.75	0.09
	37/ – 81	1 st	0.18 ± 0.06	11.6 ± 0.20	2.55 ± 0.50	0.13
		2 nd	0.56 ± 0.07	16.3 ± 0.40	7.20 ± 0.88	0.05
CS						
C1	–13/69	1	0.04 ± 0.02	12.5 ± 0.30	1.38 ± 0.75	0.03
	–33/59	1	0.11 ± 0.02	13.9 ± 0.60	4.72 ± 1.05	0.02
	–53/49	1 st	0.06 ± 0.03	12.5 ± 0.30	1.73 ± 0.66	0.03
		2 nd	0.10 ± 0.03	16.3 ± 0.70	4.48 ± 1.46	0.02
C2	–13/69	1	0.04 ± 0.02	12.5 ± 0.30	1.38 ± 0.75	0.03
	–3/49	1	0.08 ± 0.02	12.4 ± 0.30	2.39 ± 0.64	0.03
	7/29	1	0.16 ± 0.02	12.4 ± 0.20	2.97 ± 0.46	0.03
	17/9	1 st	0.20 ± 0.03	12.6 ± 0.20	2.51 ± 0.29	0.08
		2 nd	0.09 ± 0.03	15.3 ± 0.60	3.22 ± 0.96	0.03
	27/ – 11	1 st	0.16 ± 0.03	12.0 ± 0.20	2.34 ± 0.35	0.07
		2 nd	0.09 ± 0.03	15.9 ± 0.70	3.72 ± 1.35	0.02
	37/ – 31	1 st	0.07 ± 0.02	12.0 ± 0.30	2.40 ± 0.58	0.03
		2 nd	0.04 ± 0.01	16.1 ± 0.40	2.23 ± 0.81	0.02
	47/ – 51	1 st	0.03 ± 0.01	12.6 ± 0.40	1.57 ± 0.73	0.02
2 nd		0.05 ± 0.01	16.3 ± 0.40	2.29 ± 0.77	0.02	
C3	–43/79	1 st	0.06 ± 0.01	13.1 ± 1.80	1.76 ± 20.3	0.03
		2 nd	0.09 ± 0.01	15.1 ± 0.50	5.33 ± 0.70	0.01
	–33/59	1	0.11 ± 0.02	13.9 ± 0.60	4.72 ± 1.05	0.02
	–23/39	1	0.11 ± 0.02	12.6 ± 0.30	2.83 ± 0.62	0.04
	–13/19	1	0.21 ± 0.02	12.3 ± 0.10	2.87 ± 0.32	0.07
	–3/ – 1	1 st	0.32 ± 0.03	12.1 ± 0.10	2.71 ± 0.27	0.11
		2 nd	0.06 ± 0.03	15.7 ± 0.90	3.06 ± 1.25	0.02
	7/ – 21	1 st	0.27 ± 0.03	12.0 ± 0.10	2.46 ± 0.25	0.10
		2 nd	0.07 ± 0.02	15.9 ± 0.60	3.20 ± 1.05	0.02
	17/ – 41	1 st	0.14 ± 0.01	11.9 ± 0.10	2.30 ± 0.30	0.06
		2 nd	0.04 ± 0.01	16.0 ± 0.50	2.50 ± 0.96	0.01
	27/ – 61	1 st	0.06 ± 0.01	11.8 ± 0.40	2.92 ± 0.72	0.02
		2 nd	0.04 ± 0.01	16.1 ± 0.30	2.04 ± 0.68	0.02
	37/ – 81	1 st	0.05 ± 0.02	10.4 ± 0.90	3.97 ± 1.68	0.01
2 nd		0.06 ± 0.01	16.3 ± 0.30	1.99 ± 0.45	0.03	

Table J.2: The determined physical parameters of CH and C₂H from hyperfine fitting method.

Cut	$\Delta\alpha/\Delta\delta$ ["'/"]	Vel. comp.	$\int T_{\text{mb}} dv$ [K km s ⁻¹]	V [km s ⁻¹]	FWHM [km s ⁻¹]	τ_{tot}
CH						
C1	-13/69	1	0.21 ± 0.47	13.7 ± 0.23	2.96 ± 0.47	0.10 ± 3.18
	-33/59	1	0.54 ± 0.61	13.6 ± 0.18	4.92 ± 0.61	1.26 ± 1.77
	-53/49	1	0.99 ± 0.36	13.1 ± 0.12	5.49 ± 0.36	1.32 ± 1.17
C2	-13/69	1	0.21 ± 0.47	13.7 ± 0.23	2.96 ± 0.47	0.10 ± 3.18
	-3/49	1	0.61 ± 0.42	14.1 ± 0.15	4.37 ± 0.42	1.22 ± 1.56
	7/29	1 st	1.06 ± 1.99	13.9 ± 0.41	3.77 ± 1.99	1.10 ± 5.61
		2 nd		15.4 ± 1.80	7.10 ± 1.80	1.10 ± 4.50
	17/9	1 st	1.81 ± 1.27	12.9 ± 1.08	4.32 ± 1.27	4.74 ± 6.17
		2 nd		14.6 ± 0.93	6.30 ± 1.64	5.12 ± 2.79
	27/ - 11	1 st	1.36 ± 1.14	11.7 ± 0.31	2.95 ± 1.14	7.51 ± 7.65
		2 nd		14.8 ± 0.85	6.19 ± 0.96	2.62 ± 1.40
	37/ - 31	1 st	1.25 ± 0.83	11.5 ± 0.23	3.20 ± 0.83	4.76 ± 3.51
		2 nd		15.1 ± 1.19	6.32 ± 1.48	1.56 ± 1.38
	47/ - 51	1 st	1.06 ± 0.85	11.6 ± 0.31	3.32 ± 0.85	2.44 ± 2.53
		2 nd		15.3 ± 1.42	6.07 ± 1.91	1.44 ± 1.83
C3	-43/79	1	0.29 ± 0.45	13.4 ± 0.20	3.27 ± 0.45	0.10 ± 1.56
	-33/59	1	0.54 ± 0.61	13.6 ± 0.18	4.92 ± 0.61	1.26 ± 1.77
	-23/39	1 st	0.96 ± 3.54	13.3 ± 1.42	7.37 ± 3.54	4.85 ± 3.50
		2 nd		14.6 ± 0.93	6.30 ± 1.64	5.12 ± 9.55
	-13/19	1 st	1.09 ± 3.04	11.7 ± 3.53	4.72 ± 3.04	2.69 ± 1.87
		2 nd		14.1 ± 2.21	4.74 ± 2.05	3.64 ± 3.77
	-3/ - 1	1 st	1.57 ± 0.68	12.0 ± 0.43	3.50 ± 0.68	2.55 ± 2.22
		2 nd		14.5 ± 0.43	2.33 ± 1.16	2.33 ± 2.23
	7/ - 21	1 st	1.62 ± 0.71	12.0 ± 0.24	2.84 ± 0.71	3.98 ± 3.54
		2 nd		14.4 ± 0.64	6.49 ± 0.74	2.67 ± 1.98
	17/ - 41	1 st	1.55 ± 0.55	11.9 ± 0.17	3.03 ± 0.55	3.28 ± 2.33
		2 nd		14.7 ± 0.59	6.89 ± 0.71	2.87 ± 1.62
27/ - 61	1 st	1.10 ± 0.61	11.7 ± 0.18	3.06 ± 0.61	5.68 ± 3.17	
	2 nd		14.9 ± 0.97	5.92 ± 1.17	3.41 ± 1.65	
37/ - 81	1 st	1.06 ± 0.70	12.8 ± 0.32	4.22 ± 0.70	7.16 ± 4.05	
	2 nd		17.1 ± 0.66	5.43 ± 0.76	4.90 ± 1.69	
C ₂ H						
C1	-13/69	1	0.25 ± 0.41	14.1 ± 0.18	2.62 ± 0.41	0.10 ± 2.42
	-33/59	1	0.50 ± 0.25	14.2 ± 0.10	2.95 ± 0.25	0.10 ± 4.05
	-53/49	1	0.71 ± 0.50	14.1 ± 0.11	3.97 ± 0.50	1.12 ± 1.75
C2	-13/69	1	0.25 ± 0.41	14.1 ± 0.18	2.62 ± 0.41	0.10 ± 2.42
	-3/49	1	0.46 ± 0.70	14.2 ± 0.24	5.15 ± 0.70	0.10 ± 0.53
	7/29	1	0.86 ± 0.36	14.2 ± 0.15	5.74 ± 0.36	0.10 ± 0.42
	17/9	1	1.04 ± 0.21	13.7 ± 0.10	5.78 ± 0.21	0.10 ± 0.21
	27/ - 11	1	0.83 ± 0.36	13.0 ± 0.13	5.54 ± 0.36	0.10 ± 0.22
	37/ - 31	1	0.56 ± 0.60	12.5 ± 0.18	5.34 ± 0.60	0.10 ± 0.21
	47/ - 51	1	0.38 ± 1.16	12.5 ± 0.47	6.86 ± 1.16	0.10 ± 0.49
-43/79	1	0.44 ± 0.27	14.3 ± 0.11	2.96 ± 0.27	0.10 ± 2.45	

Table J.2 – *continued from previous page*

Cut	$\Delta\alpha/\Delta\delta$ ["'"/''']	Vel. comp.	$\int T_{\text{mb}} dv$ [K km s ⁻¹]	V [km s ⁻¹]	FWHM [km s ⁻¹]	τ_{tot}
-33/59		1	0.50 ± 0.25	14.2 ± 0.10	2.95 ± 0.25	0.10 ± 4.05
-23/39		1	0.48 ± 0.43	14.1 ± 0.14	3.43 ± 0.43	0.10 ± 0.83
-13/19		1	0.70 ± 0.48	13.7 ± 0.17	4.81 ± 0.48	0.10 ± 0.61
-3/ - 1		1	1.05 ± 0.37	13.2 ± 0.13	4.79 ± 0.37	0.10 ± 0.44
7/ - 21		1	0.97 ± 0.32	12.7 ± 0.12	4.29 ± 0.32	0.10 ± 0.43
17/ - 41		1	0.57 ± 0.29	12.3 ± 0.12	3.78 ± 0.29	0.10 ± 0.69
27/ - 61		1	0.32 ± 0.49	11.9 ± 0.16	3.53 ± 0.49	0.10 ± 1.02
37/ - 81		1	0.27 ± 1.91	11.7 ± 0.69	6.72 ± 1.91	0.10 ± 0.78

Table J.3: *The output parameters of Gaussian-fitting for cut observations. This table contains only those positions where the given line was significantly visible.*

Position	Vel. comp.	$\int T_{\text{mb}} dv$ [K km s ⁻¹]	V [km s ⁻¹]	FWHM [km s ⁻¹]	T _{peak} [K]
1342201675 (MM1, o-H ₂ O)					
1	1 st	0.55 ± 0.27	8.8 ± 1.2	4.51 ± 1.61	0.11
	2 nd	0.31 ± 0.26	11.6 ± 0.3	1.59 ± 1.14	0.18
2	1 st	1.14 ± 0.19	5.5 ± 0.7	6.92 ± 1.15	0.16
	2 nd	0.96 ± 0.18	11.3 ± 0.2	3.53 ± 0.50	0.25
	3 rd	0.40 ± 0.07	11.6 ± 0.3	1.59 ± 1.14	0.18
3	1 st	0.71 ± 0.33	6.0 ± 1.0	5.31 ± 1.32	0.13
	2 nd	1.26 ± 0.69	11.4 ± 0.2	3.49 ± 0.63	0.34
	3 rd	1.58 ± 0.99	13.6 ± 0.2	7.41 ± 2.33	0.20
4	1 st	0.67 ± 0.15	5.2 ± 0.7	4.89 ± 0.70	0.13
	2 nd	2.85 ± 0.15	11.9 ± 0.7	4.39 ± 0.70	0.61
	3 rd	1.16 ± 0.15	16.0 ± 0.7	5.50 ± 0.70	0.20
5	1 st	0.83 ± 0.15	6.8 ± 0.7	8.17 ± 0.70	0.10
	2 nd	2.75 ± 0.15	12.7 ± 0.7	5.47 ± 0.70	0.51
	3 rd	2.45 ± 0.15	13.9 ± 0.7	7.68 ± 0.70	0.30
6	1 st	0.69 ± 0.08	8.1 ± 0.2	4.92 ± 0.58	0.13
	2 nd	1.29 ± 0.07	11.9 ± 0.1	3.82 ± 0.23	0.34
	3 rd	1.17 ± 0.04	15.6 ± 0.2	5.25 ± 0.36	0.21
7	1 st	0.64 ± 0.38	6.8 ± 2.0	6.33 ± 2.49	0.10
	2 nd	0.69 ± 0.38	10.8 ± 0.4	3.32 ± 0.94	0.21
	3 rd	0.64 ± 0.11	17.2 ± 0.5	5.34 ± 1.00	0.11
8	1 st	0.32 ± 0.10	9.5 ± 0.3	1.88 ± 0.70	0.16
	2 nd	0.30 ± 0.10	11.9 ± 0.3	1.69 ± 0.53	0.17
1342201676 (MM2, o-H ₂ O)					
3	1 st	0.61 ± 0.11	11.2 ± 0.3	3.68 ± 0.85	0.16
	2 nd	0.24 ± 0.08	15.3 ± 0.4	2.29 ± 0.66	0.10
4	1 st	0.95 ± 1.82	11.3 ± 5.5	5.37 ± 6.39	0.17
	2 nd	1.19 ± 2.10	15.4 ± 1.6	4.21 ± 2.34	0.26
5	1 st	1.48 ± 0.12	12.2 ± 0.7	4.24 ± 0.70	0.33
	2 nd	1.53 ± 0.12	15.4 ± 0.7	3.13 ± 0.70	0.46
6	1 st	2.09 ± 0.80	12.4 ± 1.1	6.20 ± 1.37	0.32
	2 nd	1.39 ± 0.73	15.4 ± 0.2	3.22 ± 0.71	0.40
	3 rd	0.36 ± 0.11	19.7 ± 0.2	1.75 ± 0.49	0.19

Table J.3 – *continued from previous page*

Position	Vel. comp.	$\int T_{\text{mb}} dv$ [K km s ⁻¹]	V [km s ⁻¹]	FWHM [km s ⁻¹]	T _{peak} [K]
7	1 st	1.55 ± 0.41	12.0 ± 0.6	4.65 ± 1.01	0.31
	2 nd	0.89 ± 0.94	15.2 ± 0.4	2.60 ± 0.98	0.32
	3 rd	0.70 ± 1.00	17.9 ± 3.2	4.76 ± 4.49	0.14
8	1 st	1.78 ± 0.67	11.4 ± 1.2	6.94 ± 2.38	0.24
	2 nd	1.00 ± 0.60	15.7 ± 0.3	3.45 ± 0.92	0.28
	3 rd	0.36 ± 0.13	19.7 ± 0.4	2.31 ± 0.72	0.15
9	1 st	0.87 ± 0.14	10.9 ± 0.3	4.06 ± 0.81	0.20
	2 nd	0.91 ± 0.17	16.0 ± 0.2	3.21 ± 0.68	0.27
	3 rd	0.29 ± 0.12	19.3 ± 0.4	2.07 ± 0.70	0.13
10	1 st	0.63 ± 0.13	10.7 ± 0.4	4.49 ± 1.11	0.13
	2 nd	0.60 ± 0.24	15.9 ± 0.6	2.77 ± 0.97	0.20
	3 rd	0.38 ± 0.23	18.8 ± 0.7	2.39 ± 1.08	0.15
1342201750 (MM1, ¹² CO)					
1	1 st	0.84 ± 0.07	13.3 ± 0.2	4.21 ± 0.48	0.19
	2 nd	0.58 ± 0.05	15.6 ± 0.1	2.45 ± 0.10	0.23
3	1	3.15 ± 0.10	12.7 ± 0.1	8.34 ± 0.29	0.35
4	1 st	0.57 ± 0.22	8.9 ± 0.3	2.99 ± 0.59	0.18
	2 nd	2.53 ± 0.22	12.3 ± 0.2	4.14 ± 0.29	0.57
5	1 st	1.08 ± 0.28	9.0 ± 0.2	2.36 ± 0.30	0.43
	2 nd	7.87 ± 0.32	12.3 ± 0.1	4.27 ± 0.18	1.73
6	1	28.91 ± 0.13	12.2 ± 0.0	5.44 ± 0.03	4.99
7	1 st	50.05 ± 0.18	12.6 ± 0.1	6.08 ± 0.05	7.73
	2 nd	13.73 ± 0.01	13.3 ± 0.3	5.47 ± 0.04	2.36
8	1 st	38.33 ± 0.09	12.3 ± 0.0	5.21 ± 0.01	6.91
	2 nd	36.33 ± 0.01	14.8 ± 0.0	5.28 ± 0.01	6.46
9	1 st	26.15 ± 0.15	12.3 ± 0.0	4.47 ± 0.05	5.50
	2 nd	38.67 ± 0.03	15.5 ± 0.0	5.14 ± 0.04	7.07
10	1 st	15.39 ± 1.23	12.7 ± 0.7	5.74 ± 0.70	2.52
	2 nd	21.22 ± 1.23	15.6 ± 0.7	6.03 ± 0.70	3.30
11	1 st	5.68 ± 0.44	13.5 ± 0.7	7.73 ± 0.70	0.69
	2 nd	8.14 ± 0.44	14.4 ± 0.7	7.68 ± 0.70	1.00
1342201752 (MM2, ¹² CO)					
3	1	3.46 ± 0.10	13.9 ± 0.1	6.42 ± 0.19	0.51
4	1	5.57 ± 0.08	15.4 ± 0.1	6.96 ± 0.08	1.02
5	1 st	2.46 ± 0.17	11.2 ± 0.1	3.31 ± 0.30	0.70

Table J.3 – *continued from previous page*

Position	Vel. comp.	$\int T_{\text{mb}} dv$ [K km s ⁻¹]	V [km s ⁻¹]	FWHM [km s ⁻¹]	T _{peak} [K]
	2 nd	28.92 ± 0.26	14.9 ± 0.0	5.99 ± 0.08	4.54
6	1 st	11.64 ± 3.68	11.5 ± 0.2	4.44 ± 0.25	2.47
	2 nd	49.44 ± 3.80	14.8 ± 0.2	5.69 ± 0.20	8.16
7	1 st	20.60 ± 0.24	11.9 ± 0.0	3.96 ± 0.06	4.88
	2 nd	41.69 ± 0.25	15.2 ± 0.0	4.56 ± 0.04	8.59
8	1 st	15.91 ± 0.22	12.2 ± 0.0	4.73 ± 0.16	3.16
	2 nd	41.82 ± 0.06	15.4 ± 0.0	4.82 ± 0.06	8.14
9	1 st	3.76 ± 0.38	11.0 ± 0.1	3.18 ± 0.14	1.11
	2 nd	36.95 ± 0.45	15.0 ± 0.0	5.38 ± 0.06	6.46
10	1 st	12.78 ± 1.15	11.8 ± 0.7	5.30 ± 0.70	2.26
	2 nd	19.27 ± 1.15	15.4 ± 0.7	5.20 ± 0.70	3.48
	3 rd	6.29 ± 1.15	21.0 ± 0.7	3.98 ± 0.70	1.49
11	1 st	18.09 ± 1.17	12.3 ± 0.7	5.37 ± 0.70	3.17
	2 nd	13.14 ± 1.17	16.0 ± 0.7	5.00 ± 0.70	2.47
	3 rd	9.97 ± 1.17	21.0 ± 0.7	4.06 ± 0.70	2.31
12	1 st	21.01 ± 0.24	13.5 ± 0.0	6.18 ± 0.10	3.21
	2 nd	4.51 ± 0.07	15.9 ± 0.1	3.20 ± 0.12	1.32
	3 rd	10.31 ± 0.21	19.7 ± 0.1	5.24 ± 0.04	1.85
13	1 st	2.50 ± 0.06	10.6 ± 0.0	6.79 ± 0.16	0.35
	2 nd	21.27 ± 0.09	15.5 ± 0.1	6.67 ± 0.03	3.00
14	1 st	6.57 ± 0.12	14.1 ± 0.1	6.94 ± 0.10	0.89
	2 nd	12.20 ± 0.03	17.6 ± 0.0	5.54 ± 0.06	2.07
1342201809 (MM1, ¹³ CO)					
5	1	4.68 ± 0.27	12.6 ± 0.1	3.45 ± 0.22	1.27
6	1 st	3.93 ± 0.31	12.3 ± 0.2	3.51 ± 0.08	1.05
	2 nd	3.57 ± 0.23	13.9 ± 0.1	2.40 ± 0.24	1.40
7	1	11.5 ± 0.31	14.0 ± 0.0	3.76 ± 0.12	2.88
8	1 st	11.72 ± 0.57	14.3 ± 0.1	3.64 ± 0.19	3.02
	2 nd	1.37 ± 0.48	17.1 ± 0.2	1.85 ± 0.36	0.69
9	1 st	7.24 ± 0.55	14.2 ± 0.1	3.53 ± 0.16	1.93
	2 nd	2.10 ± 0.49	17.2 ± 0.4	3.21 ± 0.50	0.61
10	1	2.64 ± 0.28	14.9 ± 0.3	5.06 ± 0.61	0.49
1342201810 (MM2, ¹³ CO)					
9	1	4.08 ± 0.38	14.9 ± 0.2	4.59 ± 0.44	0.84
10	1	6.97 ± 0.34	14.7 ± 0.1	4.11 ± 0.22	1.59

Table J.3 – *continued from previous page*

Position	Vel. comp.	$\int T_{\text{mb}} dv$ [K km s ⁻¹]	V [km s ⁻¹]	FWHM [km s ⁻¹]	T _{peak} [K]
11	1	10.42 ± 0.47	14.6 ± 0.1	4.27 ± 0.21	2.29
12	1 st	3.75 ± 1.21	13.1 ± 0.2	2.48 ± 0.32	1.42
	2 nd	8.31 ± 1.26	15.2 ± 0.3	3.83 ± 0.38	2.04
13	1 st	2.81 ± 1.65	13.4 ± 0.1	2.02 ± 0.47	1.31
	2 nd	9.73 ± 1.81	14.7 ± 0.3	3.76 ± 0.26	2.43
14	1	10.82 ± 0.24	14.2 ± 0.0	3.40 ± 0.08	2.99
15	1	9.56 ± 0.38	14.3 ± 0.1	3.14 ± 0.14	2.86
16	1 st	0.63 ± 0.36	12.3 ± 0.3	1.23 ± 0.48	0.48
	2 nd	7.35 ± 0.47	14.6 ± 0.1	2.92 ± 0.22	2.37
17	1	6.15 ± 0.29	14.8 ± 0.1	3.04 ± 0.17	1.90
18	1 st	0.91 ± 0.37	11.5 ± 0.3	1.58 ± 0.76	0.54
	2 nd	3.77 ± 0.47	14.9 ± 0.2	2.69 ± 0.44	1.32
19	1 st	0.81 ± 0.58	12.3 ± 0.7	2.24 ± 1.23	0.34
	2 nd	2.17 ± 0.67	15.1 ± 0.3	2.62 ± 0.86	0.78
1342201818 (MM1, ¹² C ⁺)					
1	1 st	23.63 ± 1.98	7.0 ± 0.3	5.68 ± 0.06	3.91
	2 nd	44.26 ± 2.28	11.1 ± 0.1	4.31 ± 0.16	9.64
2	1 st	36.29 ± 3.86	8.6 ± 0.7	11.0 ± 0.70	3.10
	2 nd	65.63 ± 3.86	11.2 ± 0.7	4.43 ± 0.70	13.92
3	1 st	16.03 ± 0.77	7.3 ± 0.3	6.84 ± 0.45	2.20
	2 nd	110.60 ± 1.21	11.7 ± 0.0	4.77 ± 0.06	21.80
4	1	136.40 ± 1.20	12.0 ± 0.0	5.01 ± 0.05	25.56
5	1	156.52 ± 1.12	12.5 ± 0.0	5.11 ± 0.04	28.80
6	1 st	107.10 ± 1.60	12.6 ± 0.0	5.64 ± 0.07	17.85
	2 nd	86.79 ± 1.35	13.6 ± 0.0	4.08 ± 0.02	19.99
7	1 st	206.63 ± 10.49	13.4 ± 0.7	5.00 ± 0.70	38.85
	2 nd	42.96 ± 10.49	14.9 ± 0.7	3.70 ± 0.70	10.91
8	1 st	183.36 ± 0.83	13.7 ± 0.0	4.91 ± 0.05	35.11
	2 nd	72.67 ± 0.51	15.3 ± 0.0	3.82 ± 0.07	17.87
9	1	219.51 ± 1.42	14.7 ± 0.0	5.21 ± 0.04	39.56
10	1 st	122.73 ± 7.00	14.2 ± 0.1	4.37 ± 0.14	26.41
	2 nd	41.43 ± 7.07	17.3 ± 0.1	3.16 ± 0.20	12.31
11	1 st	65.46 ± 5.12	14.1 ± 0.2	4.31 ± 0.24	14.27
	2 nd	23.52 ± 5.30	17.3 ± 0.2	3.32 ± 0.26	6.65

Table J.3 – *continued from previous page*

Position	Vel. comp.	$\int T_{\text{mb}} dv$ [K km s ⁻¹]	V [km s ⁻¹]	FWHM [km s ⁻¹]	T _{peak} [K]
12	1 st	16.51 ± 0.87	14.1 ± 0.1	4.52 ± 0.07	3.43
	2 nd	6.46 ± 0.47	16.9 ± 0.3	3.67 ± 0.09	1.65
1342201819 (MM2, ¹² C ⁺)					
11	1 st	42.73 ± 1.55	15.7 ± 0.1	4.92 ± 0.22	8.17
	2 nd	2.12 ± 0.86	20.1 ± 0.3	1.35 ± 0.48	1.47
12	1	142.81 ± 1.62	15.3 ± 0.0	5.86 ± 0.08	22.88
13	1	185.94 ± 1.47	14.6 ± 0.0	5.61 ± 0.05	31.12
14	1	150.99 ± 1.38	14.2 ± 0.0	4.95 ± 0.05	28.64
15	1	136.44 ± 1.30	14.4 ± 0.0	4.80 ± 0.05	26.70
16	1 st	136.17 ± 2.05	14.5 ± 0.0	4.49 ± 0.07	28.46
	2 nd	17.35 ± 1.64	18.3 ± 0.1	3.69 ± 0.33	4.41
17	1 st	165.98 ± 9.25	14.8 ± 0.1	4.48 ± 0.18	34.81
	2 nd	27.81 ± 8.82	18.6 ± 0.4	3.60 ± 0.51	7.25
18	1 st	93.84 ± 23.34	14.6 ± 0.1	4.07 ± 0.20	21.65
	2 nd	188.31 ± 24.09	16.9 ± 0.3	5.91 ± 0.19	29.94
	3 rd	39.13 ± 1.36	28.7 ± 0.1	5.16 ± 0.19	7.12
19	1 st	369.65 ± 3.39	16.7 ± 0.0	6.55 ± 0.07	53.04
	2 nd	52.24 ± 4.23	22.6 ± 0.1	3.61 ± 0.20	13.57
	3 rd	112.79 ± 3.19	28.8 ± 0.1	6.93 ± 0.22	15.29
20	1 st	340.61 ± 1.40	16.9 ± 0.0	6.75 ± 0.04	47.42
	2 nd	100.67 ± 0.85	22.1 ± 0.0	3.60 ± 0.03	26.28
	3 rd	114.47 ± 0.13	28.5 ± 0.1	8.15 ± 0.13	13.19
21	1 st	346.67 ± 3.76	16.9 ± 0.0	7.61 ± 0.08	42.82
	2 nd	126.91 ± 2.94	21.8 ± 0.0	3.00 ± 0.07	42.34
	3 rd	158.32 ± 2.28	27.2 ± 0.0	10.47 ± 0.16	14.20
22	1 st	273.83 ± 10.50	15.8 ± 0.7	7.56 ± 0.70	39.14
	2 nd	168.37 ± 10.50	20.6 ± 0.7	6.26 ± 0.70	27.96
	3 rd	171.85 ± 10.50	26.8 ± 0.7	11.53 ± 0.70	14.00
23	1 st	52.27 ± 6.97	10.1 ± 0.2	5.14 ± 0.36	9.56
	2 nd	244.12 ± 9.54	16.5 ± 0.1	6.96 ± 0.24	32.95
	3 rd	139.45 ± 4.34	26.8 ± 0.1	9.41 ± 0.30	13.93
24	1 st	56.42 ± 0.19	9.7 ± 0.1	5.48 ± 0.06	9.67
	2 nd	243.29 ± 1.86	16.7 ± 0.0	8.26 ± 0.09	27.68
	3 rd	85.54 ± 1.97	26.3 ± 0.0	5.01 ± 0.13	16.23
	4 th	40.80 ± 0.45	31.3 ± 0.0	4.90 ± 0.20	7.82
	1 st	18.10 ± 6.87	9.2 ± 0.7	3.16 ± 0.70	5.39

Table J.3 – *continued from previous page*

Position	Vel. comp.	$\int T_{\text{mb}} dv$ [K km s ⁻¹]	V [km s ⁻¹]	FWHM [km s ⁻¹]	T _{peak} [K]
	2 nd	255.58 ± 6.47	16.6 ± 0.7	9.61 ± 0.70	24.98
	3 rd	73.72 ± 6.51	26.6 ± 0.7	4.06 ± 0.70	17.04
	4 th	31.45 ± 6.51	31.5 ± 0.7	4.64 ± 0.70	6.37
26	1 st	42.73 ± 6.78	11.0 ± 0.7	5.64 ± 0.70	7.11
	2 nd	166.48 ± 6.78	16.6 ± 0.7	6.07 ± 0.70	25.78
	3 rd	30.61 ± 6.51	26.5 ± 0.7	2.88 ± 0.70	9.99
	4 th	12.46 ± 6.19	25.4 ± 0.7	11.48 ± 0.70	10.20
27	1 st	12.34 ± 2.18	10.8 ± 0.2	3.65 ± 0.47	3.17
	2 nd	183.78 ± 3.14	16.9 ± 0.0	6.44 ± 0.13	26.79
	3 rd	72.23 ± 1.96	26.2 ± 0.1	5.08 ± 0.16	14.29
28	1 st	97.42 ± 3.28	15.3 ± 0.2	9.24 ± 0.11	9.91
	2 nd	123.39 ± 3.08	18.1 ± 0.0	5.65 ± 0.07	20.52
	3 rd	41.75 ± 0.35	25.9 ± 0.1	4.42 ± 0.16	8.87
	4 th	85.38 ± 0.82	27.1 ± 0.0	10.65 ± 0.27	7.53
29	1 st	40.36 ± 0.80	13.1 ± 0.1	4.75 ± 0.07	7.98
	2 nd	145.00 ± 2.73	18.4 ± 0.0	4.67 ± 0.08	29.17
	3 rd	119.61 ± 2.87	25.3 ± 0.0	7.05 ± 0.20	15.94
	4 th	16.63 ± 1.25	31.5 ± 0.1	6.20 ± 0.11	2.52
30	1 st	57.06 ± 6.87	14.5 ± 0.7	6.00 ± 0.70	8.94
	2 nd	105.40 ± 6.47	18.4 ± 0.7	3.41 ± 0.70	31.10
	3 rd	128.97 ± 6.51	24.6 ± 0.7	7.03 ± 0.70	17.23

Table J.4: *The derived total column densities of cut observations.*

Position	Vel. comp.	N(o-H ₂ O) [10 ¹² cm ⁻²]	N(¹² CO) [10 ¹⁶ cm ⁻²]	N(¹³ CO) [10 ¹⁶ cm ⁻²]	N(¹² C ⁺) [10 ¹⁷ cm ⁻²]
MM1					
1	1 st	0.59	0.66	–	0.37
	2 nd	0.33	0.44	–	1.22
2	1 st	1.22	–	–	0.57
	2 nd	1.03	–	–	2.37
	3 rd	0.43	–	–	–
3	1 st	0.76	2.46	–	0.25
	2 nd	1.35	–	–	6.97
	3 rd	1.69	–	–	–
4	1 st	0.72	0.44	–	11.52
	2 nd	2.96	1.97	–	–
	3 rd	1.24	–	–	–
5	1 st	0.89	0.85	8.48	16.74
	2 nd	2.95	6.11	–	–
	3 rd	2.62	–	–	–
6	1 st	0.74	22.49	7.11	6.07
	2 nd	1.38	–	6.5	4.24
	3 rd	1.25	–	–	–
7	1 st	0.68	71.71	20.92	57.53
	2 nd	0.74	10.67	–	1.17
	3 rd	0.68	–	–	–
8	1 st	0.34	47.90	21.27	30.81
	2 nd	0.32	28.22	2.46	2.99
9	1 st	–	20.31	13.13	76.85
	2 nd	–	48.72	3.83	–
10	1 st	–	11.96	4.79	9.58
	2 nd	–	16.49	–	1.13
11	1 st	–	4.42	–	2.38
	2 nd	–	6.33	–	3.68
12	1 st	–	–	–	2.59
	2 nd	–	–	–	1.01
MM2					
3	1 st	0.65	2.67	–	–
	2 nd	0.27	–	–	–
4	1 st	1.02	5.87	–	–

Table J.4 – *continued from previous page*

Position	Vel. comp.	$N(\text{o-H}_2\text{O})$ [10^{12} cm^{-2}]	$N(^{12}\text{CO})$ [10^{16} cm^{-2}]	$N(^{13}\text{CO})$ [10^{16} cm^{-2}]	$N(^{12}\text{C}^+)$ [10^{17} cm^{-2}]
	2 nd	1.27	–	–	–
5	1 st	1.58	1.91	–	–
	2 nd	1.64	22.49	–	–
6	1 st	2.24	9.03	–	–
	2 nd	1.49	70.56	–	–
	3 rd	0.38	–	–	–
7	1 st	1.66	15.96	–	–
	2 nd	0.95	54.73	–	–
	3 rd	0.75	–	–	–
8	1 st	1.91	12.36	–	–
	2 nd	1.07	54.89	–	–
	3 rd	0.38	–	–	–
9	1 st	0.93	2.92	7.39	–
	2 nd	0.97	45.42	–	–
	3 rd	0.31	–	–	–
10	1 st	0.67	9.85	12.65	–
	2 nd	0.64	14.99	–	–
	3 rd	0.41	4.89	–	–
11	1 st	–	14.06	18.94	1.15
	2 nd	–	10.21	–	0.33
	3 rd	–	7.75	–	–
12	1 st	–	16.32	6.77	11.78
	2 nd	–	3.49	15.11	–
	3 rd	–	8.00	–	–
13	1 st	–	1.94	5.13	25.77
	2 nd	–	16.51	17.71	–
14	1 st	–	5.10	19.69	15.51
	2 nd	–	9.47	–	–
15	1	–	–	17.37	11.92
16	1 st	–	–	1.16	12.55
	2 nd	–	–	13.13	0.34
17	1 st	–	–	11.15	24.75
	2 nd	–	–	–	0.62
18	1 st	–	–	1.64	5.09
	2 nd	–	–	6.84	25.22
	3 rd	–	–	–	1.00

Table J.4 – *continued from previous page*

Position	Vel. comp.	N(o-H ₂ O) [10 ¹² cm ⁻²]	N(¹² CO) [10 ¹⁶ cm ⁻²]	N(¹³ CO) [10 ¹⁶ cm ⁻²]	N(¹² C ⁺) [10 ¹⁷ cm ⁻²]
19	1 st	–	–	1.50	46.38
	2 nd	–	–	3.97	1.63
	3 rd	–	–	–	6.41
20	1 st	–	–	–	66.24
	2 nd	–	–	–	6.50
	3 rd	–	–	–	6.37
21	1 st	–	–	–	121.32
	2 nd	–	–	–	18.84
	3 rd	–	–	–	12.06
22	1 st	–	–	–	124.38
	2 nd	–	–	–	20.81
	3 rd	–	–	–	14.17
23	1 st	–	–	–	1.57
	2 nd	–	–	–	48.28
	3 rd	–	–	–	9.41
24	1 st	–	–	–	1.77
	2 nd	–	–	–	38.89
	3 rd	–	–	–	3.93
	4 th	–	–	–	1.07
25	1 st	–	–	–	0.29
	2 nd	–	–	–	37.30
	3 rd	–	–	–	3.03
	4 th	–	–	–	0.49
26	1 st	–	–	–	1.14
	2 nd	–	–	–	17.23
	3 rd	–	–	–	0.48
	4 th	–	–	–	7.16
27	1 st	–	–	–	0.19
	2 nd	–	–	–	21.58
	3 rd	–	–	–	3.16
	4 th	–	–	–	4.52
28	1 st	–	–	–	4.52
	2 nd	–	–	–	8.32
	3 rd	–	–	–	1.11
	4 th	–	–	–	3.47
29	1 st	–	–	–	1.05
	2 nd	–	–	–	14.55

Table J.4 – *continued from previous page*

Position	Vel. comp.	N(o-H ₂ O) [10 ¹² cm ⁻²]	N(¹² CO) [10 ¹⁶ cm ⁻²]	N(¹³ CO) [10 ¹⁶ cm ⁻²]	N(¹² C ⁺) [10 ¹⁷ cm ⁻²]
	3 rd	–	–	–	7.24
	4 th	–	–	–	0.26
30	1 st	–	–	–	1.79
	2 nd	–	–	–	8.90
	3 rd	–	–	–	8.57

K

Energy level diagrams of the observed species

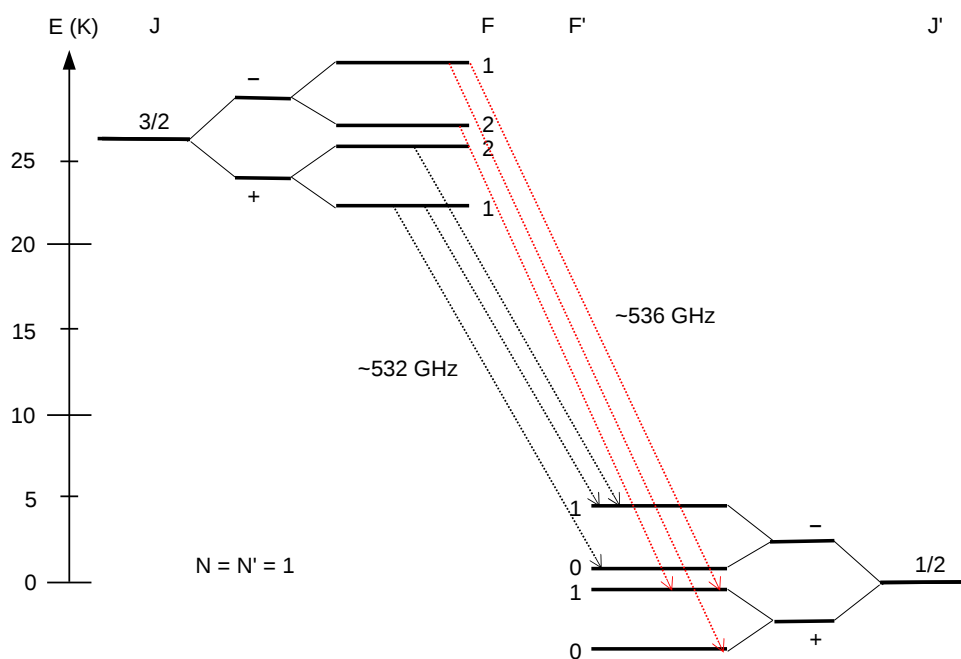


Figure K.1: Energy level diagram of CH. The observed three hyperfine-components are marked by red lines (at ~ 536 GHz). The other three hyperfine components (~ 532 GHz), which are related to the same rotational level ($N = N' = 1$), are also presented by black arrows. The hyperfine-structures are in arbitrary scales for better visibility.

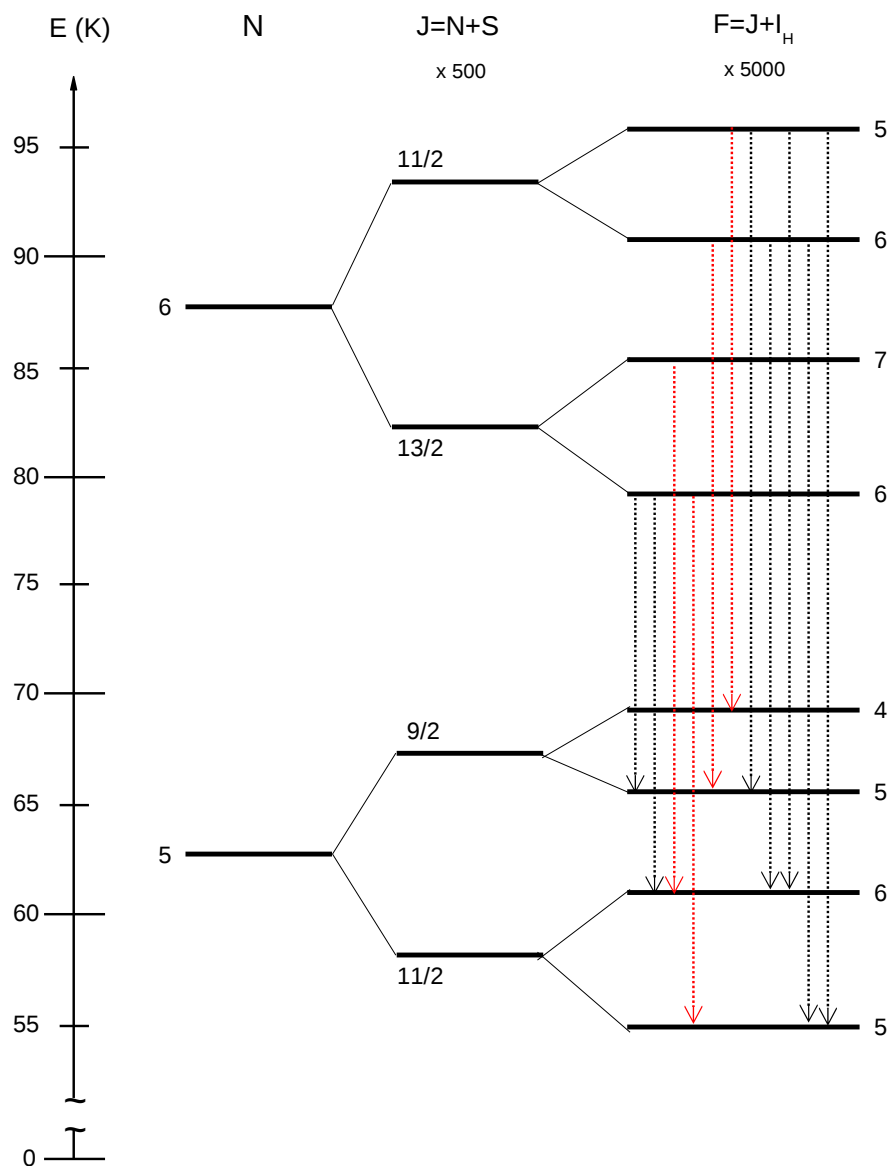


Figure K.2: Energy level diagram of C_2H at ground vibrational state ($v = 0$). All possible transitions are marked by dotted lines. The observed hyperfine components are showed by red lines. The fine and hyperfine-structures are scaled up for clarity.

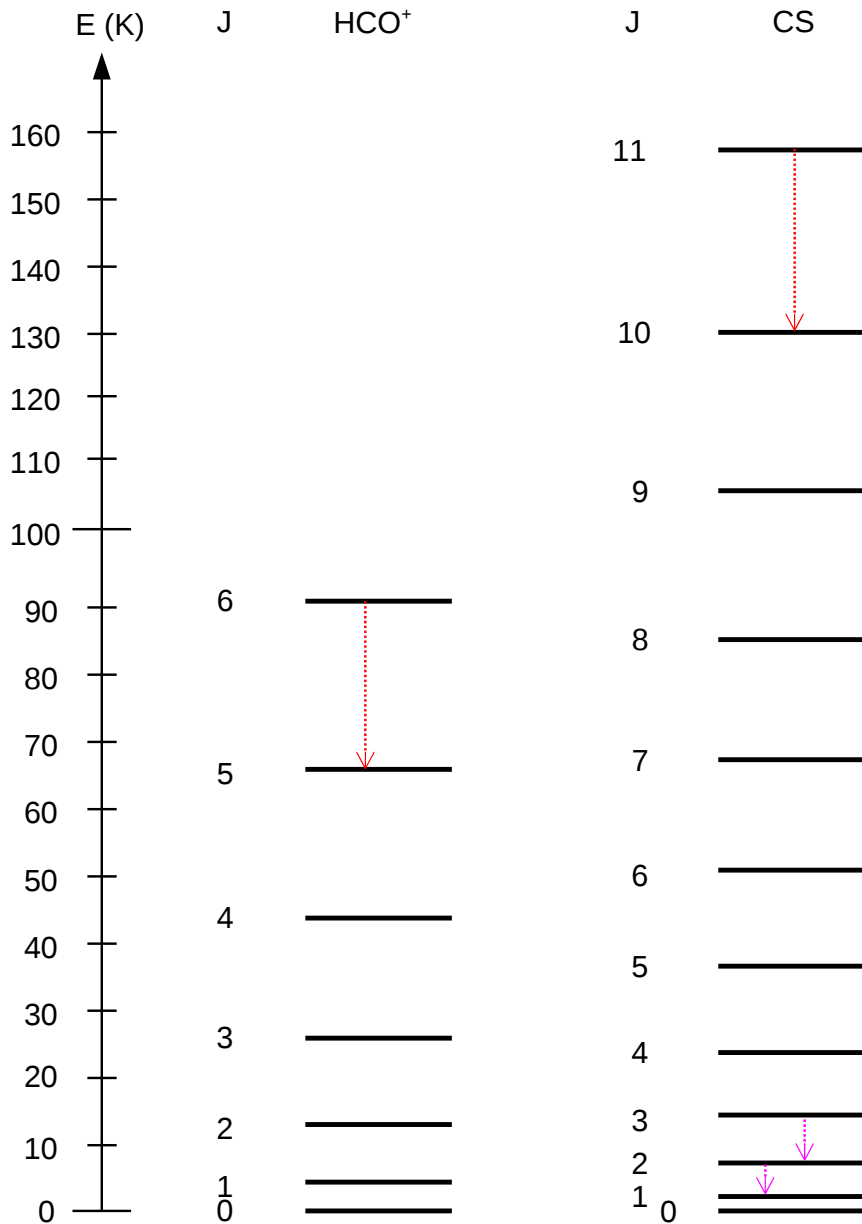


Figure K.3: Rotational energy level diagram of HCO^+ and CS at ground vibrational state ($v = 0$). The observed hyperfine components by Herschel are showed by red lines. Magenta arrows mark the observation by SEST telescope from [Nürberger et al. \(2002\)](#).

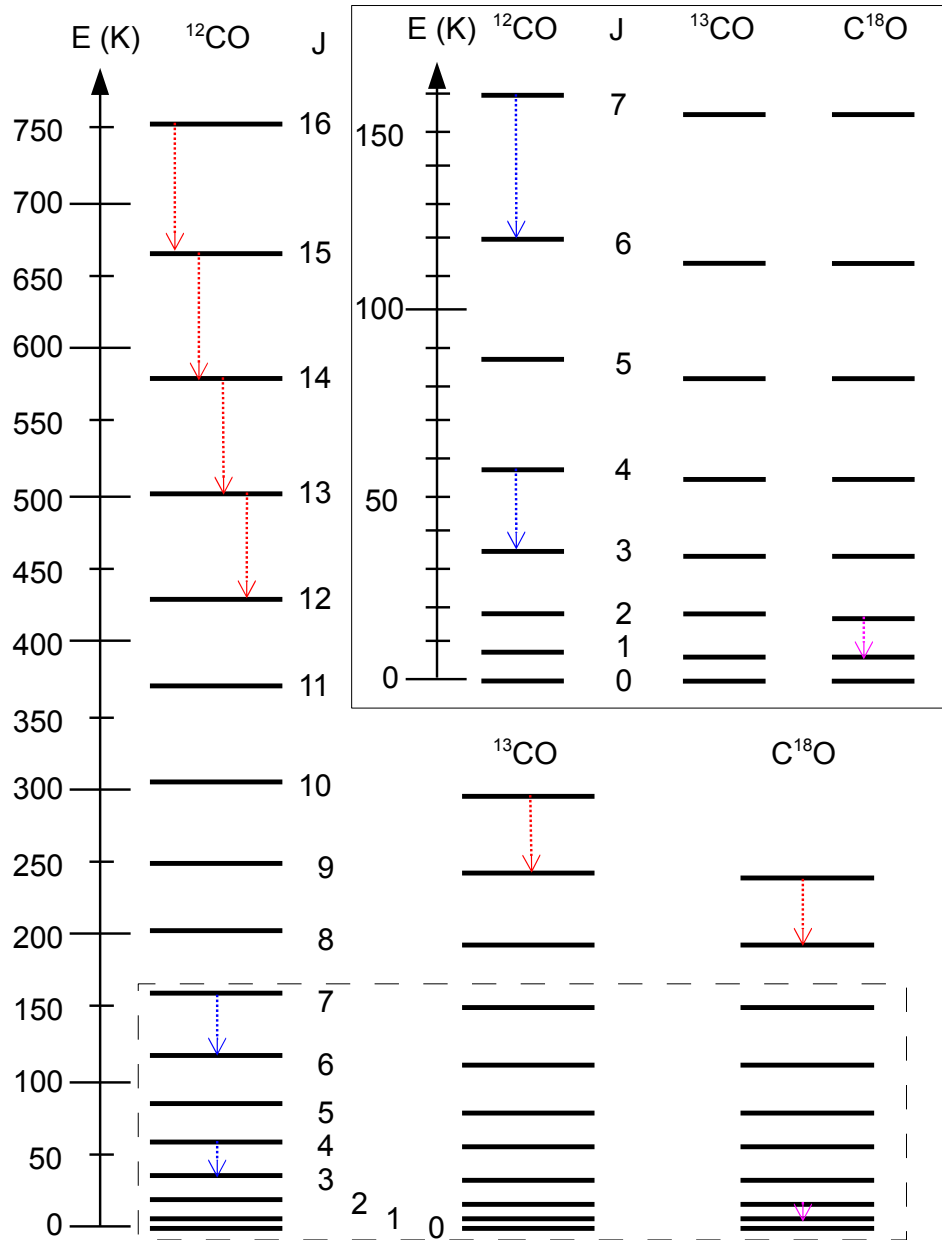


Figure K.4: Rotational “ladders” of ^{12}CO ($v = 0$), ^{13}CO and C^{18}O . The lowest 7 rotational transitions (within the dashed rectangle) are plotted in the smaller panel for better visibility. The transitions observed by Herschel are marked by the red dotted arrows. The blue arrows represent the observations by NANTEN2 telescope from Röllig et al. (2011). Magenta arrows from SEST observations from Nürnberger et al. (2002).

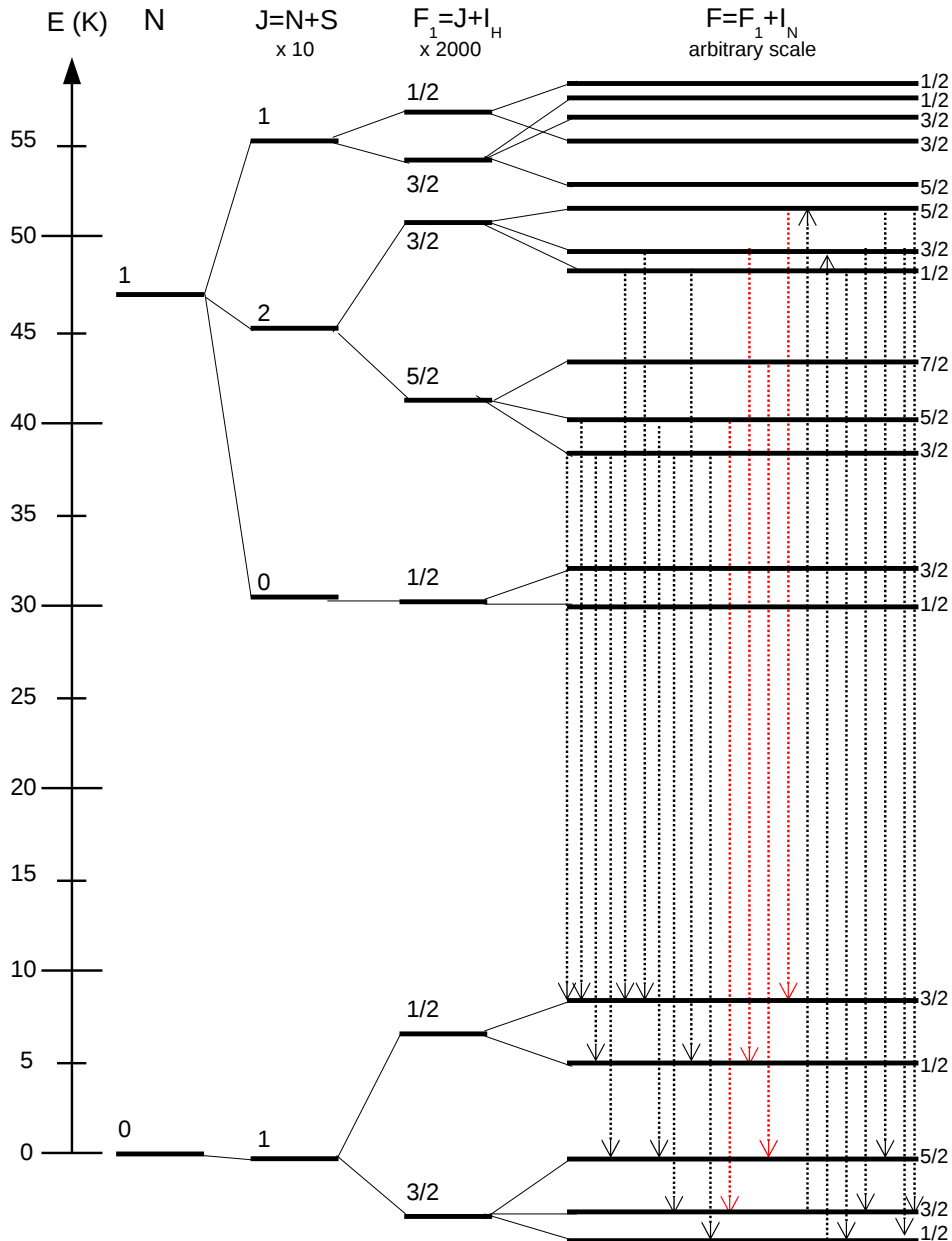


Figure K.5: Energy level diagram of NH $N = 1 \rightarrow 0$ rotational transition. The dotted lines with arrow show the transitions within the observed frequency range. The red dotted lines indicate transitions that we probably detected. The electric quadrupole-structures (F) are not properly scaled.

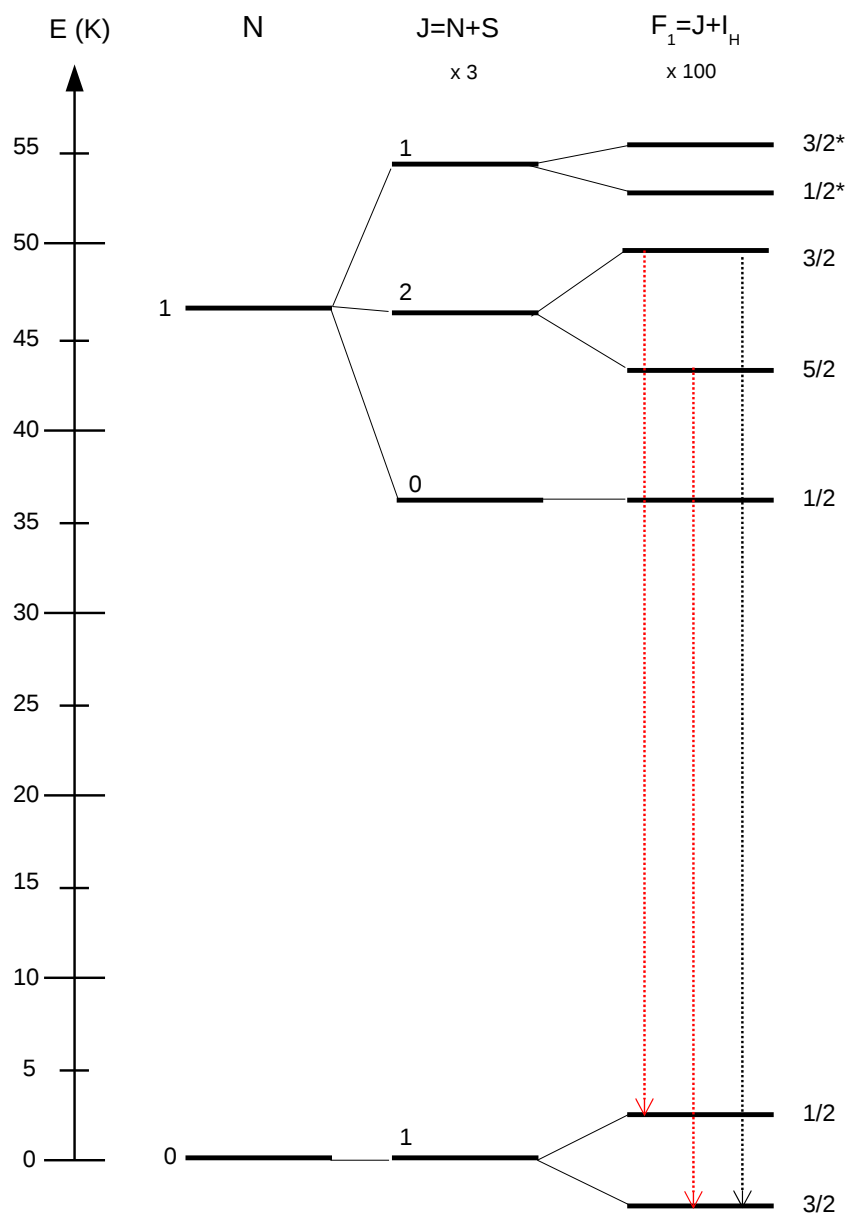


Figure K.6: Energy level diagram of OH^+ $N=1 \rightarrow 0$ rotational transition. The dotted lines with arrow show the transitions within the observed frequency range. The * sign marks hyperfine transitions with arbitrary scale.

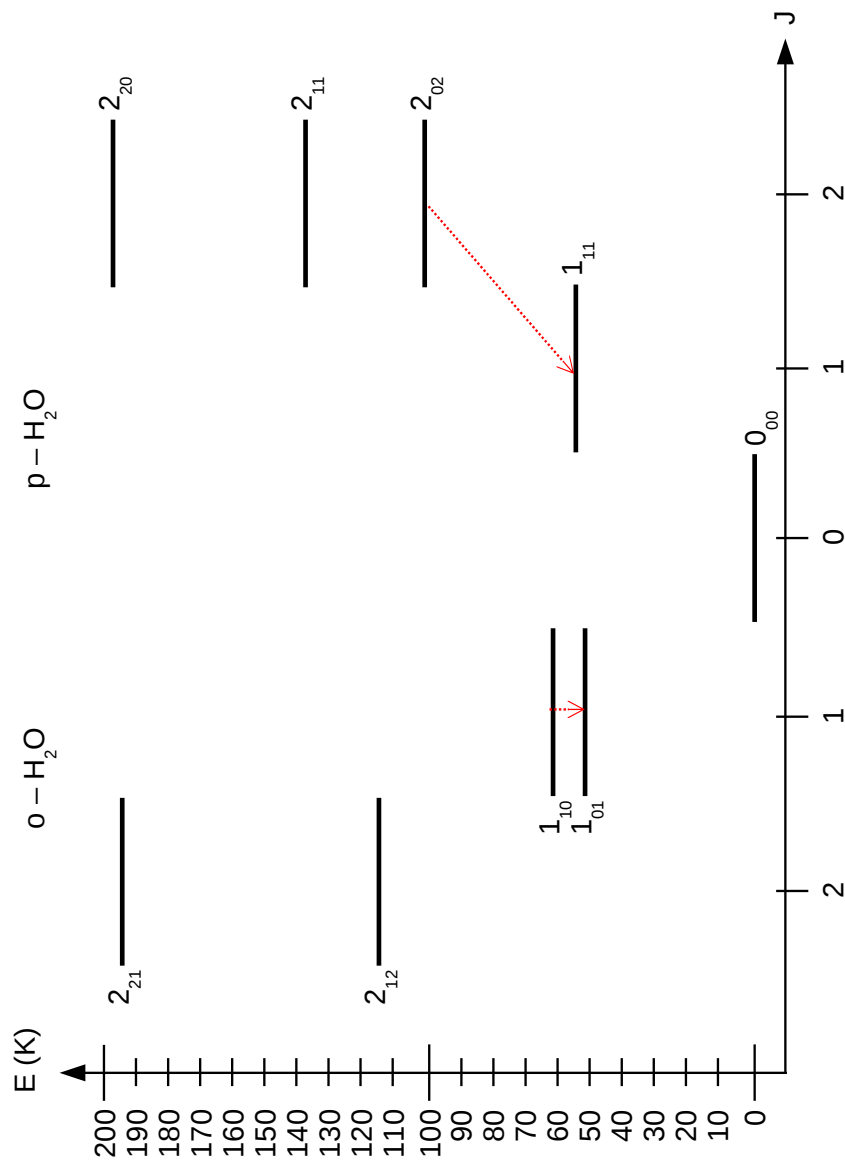


Figure K.7: Energy level diagrams of ortho- and para-water ($J < 3$). The red dotted lines mark the detected transitions.

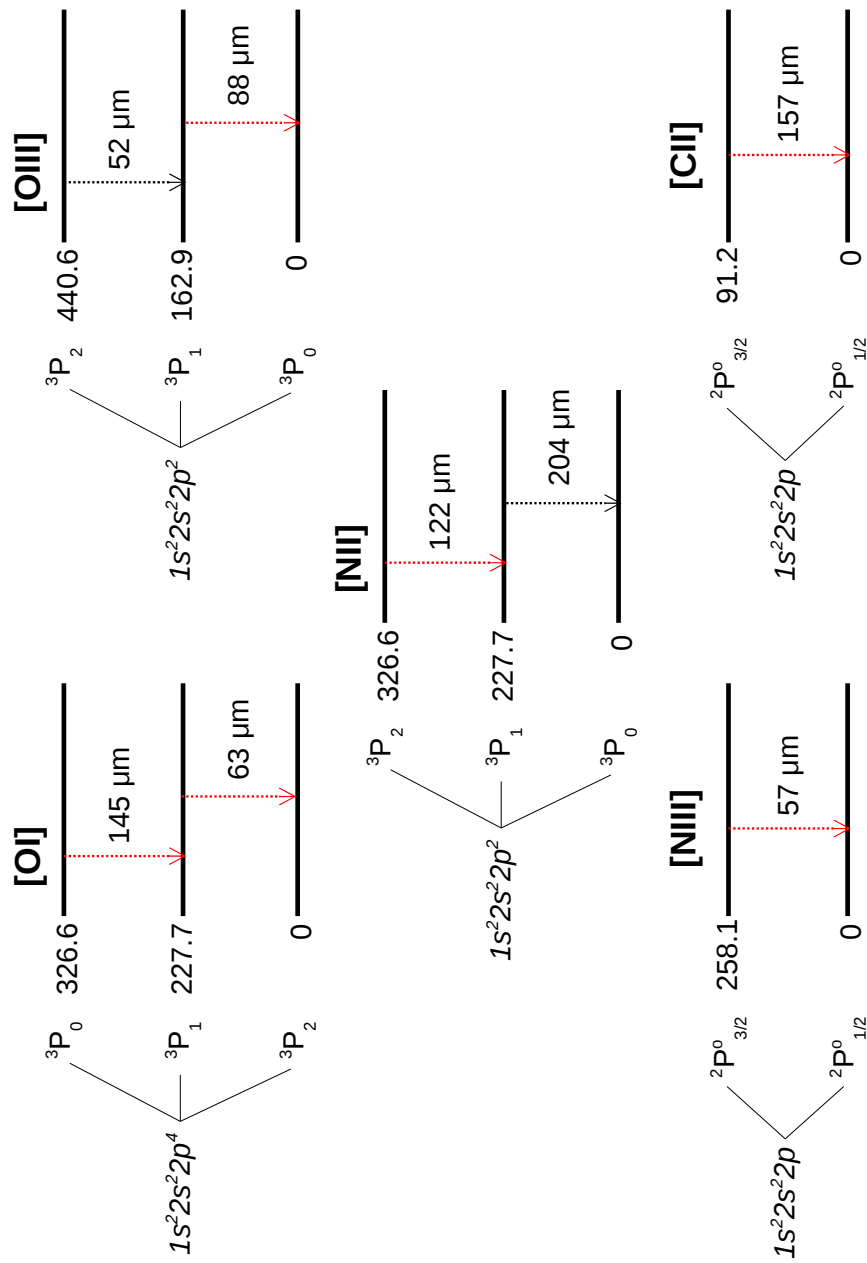


Figure K.8: Energy level diagrams of [NII], [NIII], [OII], [OIII] and [CII] (only the ground states are presented here). The red dotted lines mark the detected transitions (with the corresponding wavelengths). The energies of levels are in Kelvin.



Beam size correction

To be able to compare line intensities taken by different telescopes at different beam sizes, I converted all the line intensities to a common resolution. If all the lines had been observed as a full map, it would have been straightforward to resample them to a larger beam size (assuming that they are in finer resolution). On the other hand, most of the observations were not maps (we only have four HIFI full maps with $43''5$ beam size): HIFI cuts (from $12''2$ to $37''7$) and point observations ($22''5$). Moreover, I received previous ^{12}CO NANTEN2 observations smoothed to $38''$ and there are also PACS observations with beam size of $9''4$.

I chose, as a reference, the largest beam size ($43''5$). To calculate the scaling factors for the smaller beam sizes at given positions (red squares on Fig. 3.6), I assumed a certain geometry of the source. I also assumed that the observed species roughly follow the distribution of warm dust at the interface in both clumps (referred as MM1-IF and MM2-IF, Fig. L.1), while the species have roughly the same spatial distribution as the cooler dust deeper in MM2 (MM2-Peak). The scaling factors were determined by convolving dust maps to different beam sizes. The warm dust [> 45 K, (Xilouris et al., 2012)] can be traced by PAHs (Pahre et al., 2004), hence I used an averaged Spitzer IRAC (InfraRed Array Camera) map which was created by the combination of 3.6, 4.5, 5.8 and $8.0\ \mu\text{m}$ maps. All maps were re-projected and re-gridded to HCO^+ Herschel-map. Then, I convolved the averaged warm dust map to different beam sizes and picked the intensities from the desired positions (MM1-IF and MM2-IF). In case of MM2-peak, I used the averaged cold dust [< 20 K, (Xilouris et al., 2012)] map which was created by the combination of the 350 and $500\ \mu\text{m}$ SPIRE data. The NANTEN2 observations were directly convolved to $43''5$ beam size. The derived scaling factors are in Tab. L.2, while the result intensities are in Tab. L.1.

Table L.1: *The result intensities (scaled to 43''5 beam).*

Species	Intensity values [K km s ⁻¹]		
	MM1-IF	MM2-IF	MM2-Peak
o-H ₂ O (1 ₁₀ → 1 ₀₁) ^a	1.98	1.26	1.33
p-H ₂ O (2 ₀₂ → 1 ₁₁) ^b	0.41	0.39	0.20
¹² CO (4 → 3) ^c	90.59	138.71	228.46
¹² CO (7 → 6) ^c	54.33	78.25	132.81
¹² CO (9 → 8) ^a	17.76	11.00	8.73
¹² CO (13 → 12) ^d	0.35	0.80	–
¹² CO (14 → 13) ^d	0.85	1.56	–
¹² CO (15 → 14) ^d	0.66	1.17	–
¹² CO (16 → 15) ^d	0.33	0.75	–
¹³ CO (10 → 9) ^a	1.33	1.88	–
¹² C (1 → 0) ^c	8.16	15.69	27.96
¹² C (2 → 1) ^c	3.25	6.73	18.82
¹² C ⁺ (² P _{3/2} → ² P _{1/2}) ^a	3.90	9.57	32.04
HCO ⁺ (6 → 5) ^e	2.06	2.24	2.97
C ₂ H (6 → 5) ^e	1.04	1.11	0.90
CH (1 _{3/2} → 1 _{1/2}) ^e	1.82	2.46	3.28
NH (1 ₁ → 0 ₁) ^b	0.05	0.03	–
OH ⁺ (1 ₁ → 0 ₁) ^b	0.03	0.03	–
CS (11 → 10) ^e	0.21	0.15	0.17
[OI] (³ P ₁ → ³ P ₂) ^d	4.65	6.28	3.58
[OI] (³ P ₀ → ³ P ₁) ^d	1.52	3.74	2.05

^a Herschel cut observations (1 OTF–line).

^b Herschel point observations.

^c These transitions were observed by NANTEN2 telescope.

^d Herschel PACS observations.

^e Herschel OTF–maps.

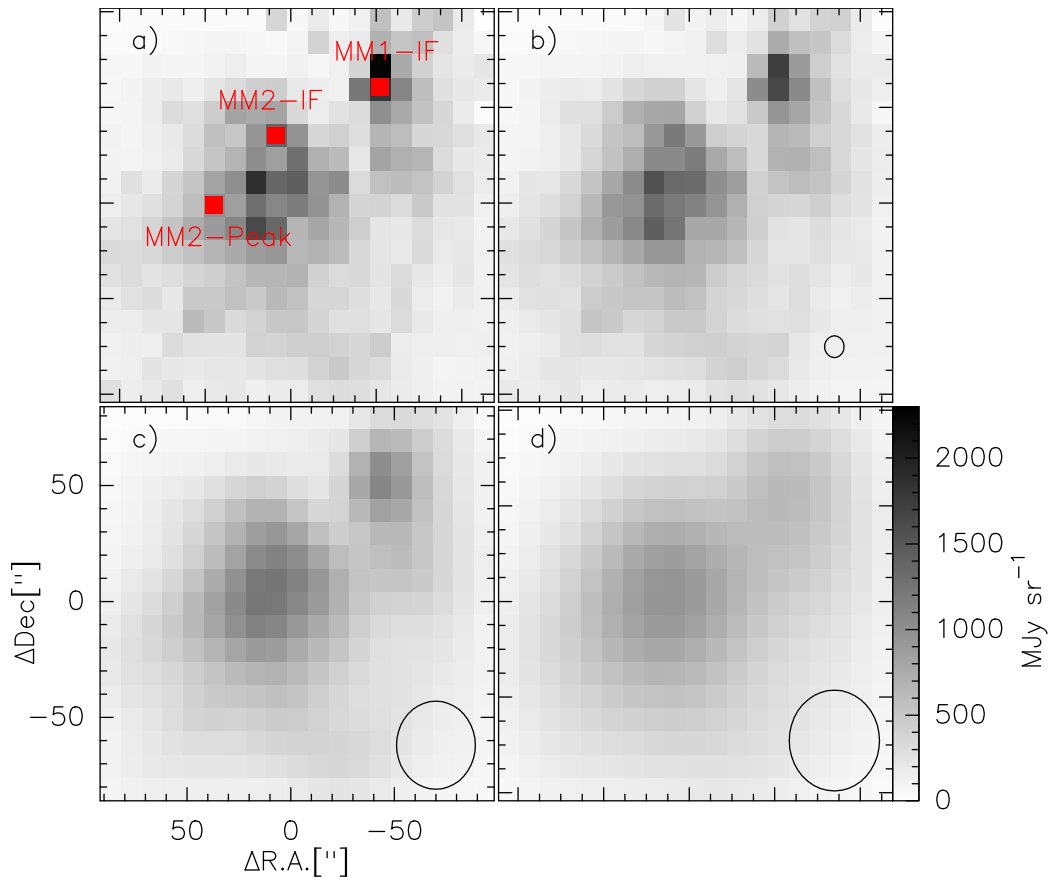


Figure L.1: The averaged Spitzer map (a), smoothed to $9''$ (b), to $26''$ (c) and to $43''$ (d) beam sizes (marked by circles). See explanation in the text. The red squares represent the positions where I took the observed intensities for modeling. All the panels have the same color scale.

Table L.2: The derived scaling factors.

Beam [']	Scaling factors		
	MM1-IF	MM2-IF	MM2-Peak
9.4	0.02	0.04	0.04
12.2	0.03	0.06	0.07
20.8	0.12	0.20	0.21
22.5	0.15	0.23	0.25
37.7	0.64	0.73	0.71
38.0	0.69	0.79	0.74
43.5	1.00	1.00	1.00



Example scripts

Note: The jython-scripts presented here as examples are working properly with HIPE version 5.1. There is no guarantee that the scripts will run with any other versions.

Listing M.1: *Export to CLASS script*

```
1 #import java
2 #import os, shutil
3 from herchel.hifi.scripts.users.share.all import *
4
5 # Define obsid, backends and sidebands
6 obsid = 1342218216
7 backend = ['WBS-H', 'WBS-V']
8 sideband = ['LSB', 'USB']
9 # Get the desired data from local pool
10 obs = getObservation(obsid, useHsa=False)
11 # Loop over backends and sidebands
12 for i in backend:
13     for j in sideband:
14         name = i + '-' + j
15         # Define the name of FITS-file
16         fitsname = '%s_%s_class.fits'%(obsid,name)
17         # Get the Level-2 data from the observation
18         htp = obs.refs["level2"].product.refs[name].product
19         # Call a task
20         hiclasstask = HiClassTask()
21         hiclassobj = None
22         # Loop over the datasets
23         dataset_iterator = htp.iterator()
24         while dataset_iterator.hasNext():
25             dataset = dataset_iterator.next()
26             # Here, you can do some processing on the dataset,
27             # like stitching the subbands, or setting to Double.
28             # the channels flagged as spurs. And then you
29             # continue:
```

```
29         sds = stitch(ds=dataset, variant="crossoverPoints",
30                     edgeTolerance=0.01, stepsize=0.0)
31         #fhf = FitHifiFringe()
32         #fds = fhf(sds1=sds, nfringes=2, plot=0, averscan=False
33                 , doglue=False)
34         # Re-inject the previous HiClass object
35         hiclassobj = hiclassobj
36         # We want to add this dataset
37         hiclassobj.dataset = sds
38         # Add it
39         hiclassobj = hiclassobj()
40         # Export to fits file
41         # We're not adding datasets anymore
42         hiclassobj.dataset = None
43         # We're exporting this result
44         hiclassobj.hiclassObj = hiclassobj
45         # We're exporting to this file
46         hiclassobj.fileName = fitsname
47         # Export the HiClass product into the FITS file
48         hiclassobj()
```

Listing M.2: Hyperfine fitting method for CH

```

1  !— Fit two velocity components in hyperfine structure of CH
2  GTVL\CLEAR ALL
3  LAS\FILE IN CH_CutMM2_Tmb.spec
4  LAS\FIND
5  LAS\GET 3
6  GREG1\PENCIL /we 2
7  LAS\SET PLOT hist
8  LAS\SET MODE x -60. 60.
9  LAS\SET MODE y -0.04 0.37
10 LAS\SET WINDOW -15. 25.
11 LAS\BASE 3
12 LAS\PLOT
13 SIC\DEFINE DOUBLE h k nu tbg voff1 voff2 a1 a2 a3 const1 fit1 [
    channels] fit2 [channels]
14 SIC\LET h = 6.626e-34
15 SIC\LET k = 1.381e-23
16 SIC\LET nu = 536761e6
17 SIC\LET tbg = 2.725
18 !— Velocity shifts of the weaker components relative to the
    main component
19 SIC\LET voff1 = 11.57
20 SIC\LET voff2 = 19.17
21 !— Intensity ratios of hyperfine components (including all
    components)
22 SIC\LET a1 = 0.3125
23 SIC\LET a2 = 0.0625
24 SIC\LET a3 = 0.125
25 !— Define functions
26 SIC\LET const1 0.5*sqrt(pi*log(2))
27 SIC\DEFINE FUNCTION g(x,a,b,c) exp(-pi*((x-a+c)|const1|b)**2)
28 SIC\DEFINE FUNCTION j(n,t) h*n|k*1|(exp(h*n|k|t)-1)
29 !— Define the fitting method (with two velocity components)
30 SIC\MFIT ry = (j(nu,&a)-j(nu,tbg))*(1-exp(-&b*(a1*g(rx,&c,&d,0)+
    a2*g(rx,&c,&d,voff1)+a3*g(rx,&c,&d,voff2))))+(j(nu,&e)-j(nu,
    tbg))*(1-exp(-&f*(a1*g(rx,&g,&h,0)+a2*g(rx,&g,&h,voff1)+a3*g(
    rx,&g,&h,voff2)))) /START 5 2 15 5 5 2 12 3 /STEP 0.1 0.01
    0.01 0.01 0.1 0.01 0.01 0.01
31 !— Draw the fit (blue), the residual (red)
32 GREG1\PENCIL /c 3
33 GREG1\HISTOGRAM rx mfit%fit
34 GREG1\PENCIL /c 1
35 GREG1\HISTOGRAM rx mfit%res
36 GREG1\PENCIL /DEFAULT
37 GREG1\DRAW TEXT -2 1 "T\Dmb\U_(K)" 0 90 /BOX 4
38 SIC\DELETE /function g j

```

Listing M.3: *Basic data reductions of a line spectroscopy*

```

1 # Initialization
2 mol = 0
3 line = 1
4 if mol == 0:
5     linen = 'OI'
6     x0 = 63.1837
7     s0 = 0.021/2.3
8 else:
9     linen = 'NIII'
10    x0 = 57.3432
11    s0 = 0.02/2.3
12 a0 = 2000
13 # Spaxel coordinates
14 posX = 4
15 posY = 4
16 # Define the initial input parameters for the fitting procedure
17 polyOrder = 2
18 initGuesses = []
19 for i in range(polyOrder+1):
20     initGuesses.append(0.0)
21 # Get the data cube and flux/wave infos
22 rbcube = obs.refs["level2"].product.refs["HPS3DRB"].product.refs
23     [mol].product
24 spec = extractSinglePixelSpectrum(simplecube=rbcube, posX=posX,
25     posY=posY)
26 flux = spec.getFlux()
27 wave = spec.getWave()
28 goodflux = flux[flux.where(IS_FINITE)]
29 goodwave = wave[goodflux.where(IS_FINITE)]
30 subSpectrum = Spectrum1d()
31 subSpectrum.setFlux(goodflux)
32 subSpectrum.setWave(goodwave)
33 #####
34 # Create the baseline subtracted plots #
35 #####
36 sf = SpectrumFitter(subSpectrum, False)
37 # Initialize the baseline fitting
38 sf.useFitter('lbn')
39 ModelBase = sf.addModel('poly', [polyOrder], initGuesses)
40 sf.setMask(min(goodwave), 63.159, 1.0)
41 sf.setMask(63.225, max(goodwave), 1.0)
42 # Do the baseline fit, calculate the residual
43 sf.doFit()
44 sf.residual()
45 # Plot original spectrum, baseline, residual
46 residualFlux = sf.getResidual()
47 baselineFlux = ModelBase.synthetic
48 p = PlotXY()
49 p.batch = 1
50 oriLayer = LayerXY(goodwave, goodflux, xrange=[min(goodwave), max
51     (goodwave)], color=Color.green)
52 oriLayer.style.chartType = Style.HISTOGRAM

```



```

50 resiLayer = LayerXY(goodwave, residualFlux , xrange=[min(goodwave
    ),max(goodwave)], color=Color.blue)
51 resiLayer.style.chartType = Style.HISTOGRAM
52 resiLayer.xaxis.visible=0
53 baseLayer = LayerXY(goodwave, baselineFlux , xrange=[min(goodwave
    ),max(goodwave)],color=Color.red)
54 baseLayer.xaxis.visible=0
55 p.addLayer(oriLayer)
56 p.addLayer(resiLayer)
57 p.addLayer(baseLayer)
58 p.setXtitle('Wavelength_[$\mu$m]')
59 p.setYtitle('Flux_[Jy]')
60 p.batch = 0
61 pName = '%s_blue_BspX%s%s_%.eps'%(pn[5:], posX, posY, linen)
62 p.saveAsEPS(pName)
63 if line == 1:
64     # Do the Gaussian fit , calculate the residual
65     sf.setMask(min(goodwave),63.159,0.0)
66     sf.setMask(63.1,63.3,1.0)
67     sf.setMask(63.225,max(goodwave),0.0)
68     ModelGauss = sf.addModel('gauss',[a0,x0,s0])
69     # Do the fit , calculate the residual
70     sf.doGlobalFit()
71     sf.residual()
72     # Get the results of the Gaussian fit
73     gaussianFlux = ModelGauss.getResultData()
74     # Get the fit parameters and their standard deviations (
        Gaussian)
75     fitParamsGauss = sf.getResult()["Parameters"].data
76     fitErrorsGauss = sf.getResult()["StdDev"].data
77     # Create plots about the baseline subtracted , Gaussian-
        fitted spectra
78     spxPlot = PlotXY()
79     spxPlot.batch = 1
80     spxResidLayer = LayerXY(goodwave, residualFlux , xrange=[min(
        goodwave),max(goodwave)], color=Color.blue)
81     spxResidLayer.style.chartType = Style.HISTOGRAM
82     spxPlot.addLayer(spxResidLayer)
83     spxGaussLayer = LayerXY(goodwave, gaussianFlux , xrange=[min(
        goodwave),max(goodwave)], color=Color.red)
84     spxGaussLayer.xaxis.visible=0
85     spxPlot.addLayer(spxGaussLayer)
86     vline = LineAnnotation (LineAnnotation.XLINE, x0)
87     vline.setColor(Color.green)
88     spxResidLayer.addLineAnnotation(vline)
89     # Setting dashes of length 2.0 with gaps of length 1.0
90     vline.dashArray = [2.0, 1.0]
91     spxResidLayer.setLineAnnotation(0, vline)
92     spxPlot.setXtitle('Wavelength_[$\mu$m]')
93     spxPlot.setYtitle('Flux_[Jy]')
94     spxPlot.batch = 0
95     print '%2d_%.2d_%.10.4f_%.7.4f_%.9.4f_%.7.4f_%.8.4f_%.7.4f_%.7.4f_
        %.7.4f'%(posX, posY, fitParamsGauss[0], fitErrorsGauss[0],
        fitParamsGauss[1], fitErrorsGauss[1], fitParamsGauss[2],

```

```
        fitErrorsGauss [2], fitParamsGauss [3], fitErrorsGauss [3])
96     spxPlotName = '%s_blue_spx%s%s_%.eps'%(pn[5:], posX, posY,
        linen)
97     spxPlot.saveAsEPS(spxPlotName)
98     elif line == 0:
99         spxPlot = PlotXY()
100        spxPlot.batch = 1
101        spxResidLayer = LayerXY(goodwave, residualFlux, xrange=[min(
            goodwave), max(goodwave)], color=Color.blue)
102        spxResidLayer.style.chartType = Style.HISTOGRAM
103        spxPlot.addLayer(spxResidLayer)
104        spxPlot.setXtitle('Wavelength_[$\mu$m]')
105        spxPlot.setYtitle('Flux_[Jy]')
106        spxPlot.batch = 0
107        print '%2d_%.2d'%(posX, posY)
108        spxPlotName = '%s_blue_spx%s%s_%.eps'%(pn[5:], posX, posY,
            linen)
109        spxPlot.saveAsEPS(spxPlotName)
110    #del(rbcube)
```

Listing M.4: *Creating integrated flux maps and other plots*

```

1 # Import necessary tasks
2 import java
3 import os, shutil
4 from java.awt import Color
5 from herschel.ia.toolbox.image import TransposeTask
6 from herschel.ia.toolbox.image import AutomaticContourTask
7 from herschel.ia.gui.plot.renderer import ChartFitMode
8 from herschel.ia.numeric.toolbox.basic import Floor
9 # Define obsid and pool name
10 obsid = '1342214684'
11 pn = '1342214684'
12 # Get the observation from local pool
13 obs = getObservation(obsid, verbose=True, poolName=pn)
14 # Start a loop because we have two lines
15 for i in range(2):
16     # Get the Level-2 cube
17     rbcube = obs.refs["level2"].product.refs["HPS3DRB"].product.
        refs[i].product
18     # Get the dimensions of the dataset
19     naxis1 = rbcube.dataset.meta.get('naxis1').long
20     naxis2 = rbcube.dataset.meta.get('naxis2').long
21     naxis3 = rbcube.dataset.meta.get('naxis3').long
22     if i == 0:
23         # The rest wavelength of line in micron
24         lineFreq = 63.1837
25         # Subtract the baseline from the whole cube
26         baselineSubtractedCube = subtractBaselineFromCube(cube=
            rbcube, startOfRanges=Double1d([62.94,63.225]),
            endOfRanges=Double1d([63.159,63.44]), polyDegree=2)
27         # Do integration of line
28         integratedCube = integrateSpectralMap(cube=
            baselineSubtractedCube, startArray=Double1d([63.159])
            , endArray=Double1d([63.225]))
29         # Define a file where the results will be written
30         myFile = open('/home/zoltan/WORK/NGC3603/PACS_data/%
            s_blue_fitpar_OI.txt' %(pn[5:]), 'w')
31     else:
32         lineFreq = 57.3432
33         baselineSubtractedCube = subtractBaselineFromCube(cube=
            rbcube, startOfRanges=Double1d([57.052,57.371]),
            endOfRanges=Double1d([57.3,57.618]), polyDegree=2)
34         integratedCube = integrateSpectralMap(cube=
            baselineSubtractedCube, startArray=Double1d([57.3]),
            endArray=Double1d([57.371]))
35         myFile = open('/home/zoltan/WORK/NGC3603/PACS_data/%
            s_blue_fitpar_NIII.txt' %(pn[5:]), 'w')
36     # The output is a SimpleImage
37     myImage = integratedCube.getSimpleImage(0)
38     # Need to flip and rotate the image to be consistent with
        the footprint
39     flippedImage1 = transpose(image=myImage, type=TransposeTask.
        FLIP_HORIZONTAL)

```

```

40     flippedImage2 = transpose(image=flippedImage1 ,type=
        TransposeTask.ROTATE_90)
41     #####
42     ##### Start to create the integrated intensity map #####
43     #####
44     # Need an 'image' for a layer
45     imageForLayer = flippedImage2.getImage()
46     integratedMap = PlotXY()
47     # Create an empty layer
48     dummyX = Double1d(range(0))
49     dummyY = Double1d(range(0))
50     dummylayer = LayerXY(dummyX,dummyY,xrange=[0,5], yrange
        =[0,5], visible=0)
51     # Create the another layer and put the image into it
52     laylma = LayerImage(imageForLayer,xrange=[0,5], yrange
        =[0,5])
53     # Manage the x and y axis of the layers
54     laylma.xaxis.title.visible=0
55     laylma.yaxis.title.visible=0
56     laylma.xaxis.tick.visible=0
57     laylma.yaxis.tick.visible=0
58     laylma.xaxis.tick.label.visible=0
59     laylma.yaxis.tick.label.visible=0
60     laylma.getXaxis().setInverted(True)
61     laylma.getYaxis().setInverted(True)
62     dummylayer.getXaxis().setInverted(True)
63     dummylayer.getYaxis().setInverted(True)
64     dummylayer.xaxis.tick.autoAdjustNumber=0
65     dummylayer.xaxis.tick.number=10
66     dummylayer.xaxis.tick.minorNumber=0
67     dummylayer.xaxis.titleText = dummylayer.yaxis.titleText = '
        Spaxel_numbers'
68     dummylayer.yaxis.tick.autoAdjustNumber=0
69     dummylayer.yaxis.tick.number=10
70     dummylayer.yaxis.tick.minorNumber=0
71     # Need to change the tick labels , so create a new one and
        put it to the layer
72     labellist = [ "", "4", "", "3", "", "2", "", "1", "", "0", "" ]
73     newLabels = String1d(labellist).toArray()
74     dummylayer.xaxis.tick.label.setFixedStrings(newLabels)
75     dummylayer.yaxis.tick.label.setFixedStrings(newLabels)
76     integratedMap.addLayer(dummylayer)
77     integratedMap.addLayer(laylma)
78     # Get the max and min intensities to create the color bar
        for the plot
79     levels = cutLevels(image = flippedImage2 , method =
        CutLevelsTask.PERCENT, percent = 100.0)
80     lowcut = levels[0]
81     highcut = levels[1]
82     # Keep the square shape for the main plot
83     integratedMap.setChartFitMode(ChartFitMode.FIXED_SIZE)
84     # Create the color bar and add to the plot
85     colorbar = PlotOverlayLayout(marginRight=1.0)
86     integratedMap.setLayout(colorbar)

```

```

87  # Create a subplot where the color bar will be
88  spBar = SubPlot(SubPlotBoundsConstraints(0.0, 1.02, 0.0,
      -0.23))
89  # Create an image that includes the color bar and add to the
      plot
90  lenBar=2561
91  barIma=Float2d(lenBar,1)
92  barIma[:,0]=(Float1d.range(lenBar)*(highcut-lowcut)/lenBar)+
      lowcut
93  layBar = LayerImage(barIma)
94  layBar.colorTable=integratedMap[1].colorTable
95  layBar.intensityTable=integratedMap[1].intensityTable
96  layBar.setHighCut(highcut)
97  layBar.setLowCut(lowcut)
98  layBar.ycdelt = (highcut-lowcut)/lenBar
99  layBar.ycrval = lowcut
100 layBar.ycrpix = +0.5
101 layBar.yrange = [lowcut, highcut]
102 layBar.xrange = [0,1]
103 spBar.addLayer(layBar)
104 integratedMap.addSubPlot(spBar)
105 # Manage the x and y axis of the color bar and subplot
106 xaxis=spBar.baseLayer.xaxis
107 xaxis.titleText=""
108 xaxis.tick.label.visible = 0
109 xaxis.tick.autoAdjustNumber = 0
110 xaxis.tick.number = 0
111 xaxis.tick.minorNumber = 0
112 xaxis.tick.height = 0.0
113 xaxis.getAuxAxis(0).tick.height = 0.0
114 xaxis.getAuxAxis(0).tick.minorNumber = 0
115 yaxis=spBar.baseLayer.yaxis
116 yaxis.titleText=""
117 yaxis.tick.label.visible=0
118 yaxis.tick.autoAdjustNumber=0
119 yaxis.tick.number=5
120 yaxis.tick.minorNumber=0
121 yaxis.tick.height=0.04
122 yaxis.getAuxAxis(0).tick.label.visible=1
123 yaxis.getAuxAxis(0).titleText="Integrated_flux_(Jy_$$\mu$m)"
124 yaxis.getAuxAxis(0).title.visible = 1
125 yaxis.getAuxAxis(0).tick.height = 0.04
126 yaxis.getAuxAxis(0).tick.number = 5
127 yaxis.getAuxAxis(0).tick.minorNumber = 0
128 integratedMap.width = integratedMap.height = 1000
129 if i == 0:
130     integratedMapName = '%s_blue_iMap_OI.eps'%(pn[5:])
131 else:
132     integratedMapName = '%s_blue_iMap_NIII.eps'%(pn[5:])
133 # Save the integrated map and close the plot window
134 integratedMap.saveAsEPS(integratedMapName)
135 integratedMap.close()
136 #####
137 #### Integrated map is done ####

```

```

138 #####
139 #####
140 #### Create subplots corresponding to footprint ####
141 #####
142 # Create a dummy dataset to make the main window plot
143 dummyX = Double1d(range(0))
144 dummyY = Double1d(range(0))
145 # Define the range of the main plot
146 if pn[5:] == '14681':
147     xCoords = [168.776, 168.745]
148     yCoords = [-61.273, -61.257]
149 elif pn[5:] == '14684':
150     xCoords = [168.814, 168.786]
151     yCoords = [-61.282, -61.266]
152 elif pn[5:] == '14687':
153     xCoords = [168.824, 168.795]
154     yCoords = [-61.288, -61.272]
155 X = xCoords[0]-xCoords[1]
156 Y = abs(yCoords[0]-yCoords[1])
157 # Define the size of the subplots
158 sizeBoxX = sizeBoxY = 0.15
159 # Start to create the main plot
160 footprintPlot = PlotXY()
161 footprintPlot.batch=1
162 footprintPlot.setLayout(PlotOverlayLayout())
163 fpPLayer = LayerXY(dummyX,dummyY, xrange=[xCoords[0],xCoords
    [1]], yrange=[yCoords[0],yCoords[1]], visible=1)
164 footprintPlot.addLayer(fpPLayer)
165 footprintPlot.setXtitle('Right_Ascension_[\u00B0]')
166 footprintPlot.setYtitle('Declination_[\u00B0]')
167 comboPlot = PlotXY()
168 comboPlot.batch = 1
169 # Loop over the spaxels
170 for j in range(naxis1):
171     for k in range(naxis2):
172         # Get the spectra and its flux and wave values
173         spec = extractSinglePixelSpectrum(simplecube=rbcube,
            posX=j, posY=k)
174         flux = spec.getFlux()
175         wave = spec.getWave()
176         goodflux = flux[flux.where(IS_FINITE)]
177         goodwave = wave[goodflux.where(IS_FINITE)]
178         normsubSpectrum = Spectrum1d()
179         # Normalize the flux data for the better
            visualization
180         nfluxarr = Double1d()
181         for l in goodflux:
182             nflux = (l-min(goodflux))/(max(goodflux)-min(
                goodflux))
183             nfluxarr.append(nflux)
184         normsubSpectrum.setFlux(nfluxarr)
185         normsubSpectrum.setWave(goodwave)
186         # The coordinates of the observed datapoints (same
            as the footprint plot)

```

```

187     xc = MEAN(NAN_FILTER(rbcube["ra"].data[:,j,k]))
188     yc = MEAN(NAN_FILTER(rbcube["dec"].data[:,j,k]))
189     # Define the positions of the subplot within the
        main plot
190     top = (((yCoords[1]-yc)*100)/Y)/100-sizeBoxY/2
191     left = (((xCoords[0]-xc)*100)/X)/100-sizeBoxX/2
192     bottom = (1.0-top)-sizeBoxY
193     right = (1.0-left)-sizeBoxX
194     # Define the subplot
195     subfootprintPlot = SubPlot(SubPlotBoundsConstraints(
        top, left, bottom, right))
196     subfpPLayer = LayerXY(goodwave, nfluxarr, xrange=[min(
        goodwave), max(goodwave)], yrange=[-1,2], color=
        Color.blue)
197     # Manage the outlook of the subplots
198     subfpPLayer.getXAxis().getTick().setHeight(0.02)
199     subfpPLayer.getYAxis().getTick().setHeight(0.02)
200     subfpPLayer.getXAxis().getTick().setMinorNumber(0)
201     subfpPLayer.getYAxis().getTick().setMinorNumber(0)
202     subfpPLayer.setXtitle('')
203     subfpPLayer.setYtitle('')
204     subfpPLayer.getXAxis().getTick().getLabel().
        setFontSize(0.0000001)
205     subfpPLayer.getYAxis().getTick().getLabel().
        setFontSize(0.0000001)
206     subfpPLayer.style.chartType = Style.HISTOGRAM
207     # Creating a vertical line at the rest wavelengths
        of the lines
208     vline = LineAnnotation (LineAnnotation.XLINE,
        lineFreq)
209     vline.setColor(Color.red)
210     subfpPLayer.addLineAnnotation(vline)
211     # Setting dashes of length 2.0 with gaps of length
        1.0
212     vline.dashArray = [2.0, 1.0]
213     subfpPLayer.setLineAnnotation(0, vline)
214     # Put information about the spaxel number into the
        subplots
215     subfpPLayer.addAnnotation(Annotation(min(goodwave)
        +0.07, 1.3, '%s,%s'%(j,k), fontSize=3.0))
216     subfootprintPlot.addLayer(subfpPLayer)
217     footprintPlot.addSubPlot(subfootprintPlot)
218     # Create a comboplot which includes the spaxels
219     comboPlotLayer = LayerXY(goodwave, goodflux, xrange=[
        min(goodwave), max(goodwave)], yrange=[min(goodflux
        )-20,max(goodflux)+20], color=Color.blue)
220     #comboPlotLayer.addAnnotation(Annotation(min(SPXW)
        +0.1,max(SPXF), 'Spaxel %s,%s'%(k,l)))
221     comboPlotLayer.setXtitle('Wavelength_[$\mu$m]')
222     comboPlotLayer.setYtitle('Flux_[Jy]')
223     comboPlotLayer.style.chartType = Style.HISTOGRAM
224     comboPlotLayer.addLineAnnotation(vline)
225     comboPlot.addLayer(comboPlotLayer,-j,k)
226     values = '%10.5f_%.10.5f_%.2d_%.2d'%(xc,yc,j,k)

```

```
227         # Write out the results to previously created file
228         myFile.write(values + '\n')
229     footprintPlot.getXaxis().setInverted(True)
230     if i == 0:
231         footprintPlotName = '%s_blue_fpPlot_OI.eps'%(pn[5:])
232     else:
233         footprintPlotName = '%s_blue_fpPlot_NIII.eps'%(pn[5:])
234     footprintPlot.batch=0
235     footprintPlot.saveAsEPS(footprintPlotName)
236     footprintPlot.close()
237     if i == 0:
238         comboPlotName = '%s_blue_comboPlot_OI.eps'%(pn[5:])
239     else:
240         comboPlotName = '%s_blue_comboPlot_NIII.eps'%(pn[5:])
241     comboPlot.batch=0
242     comboPlot.saveAsEPS(comboPlotName)
243     comboPlot.close()
244     myFile.close()
245 #del(barlma, baselineSubtractedCube, bottom, colorbar, comboPlot
, comboPlotLayer, comboPlotName, dummylayer, dummyX, dummyY,
flippedImage1, flippedImage2, flux, footprintPlot,
footprintPlotName, fpPLayer, goodflux, goodwave, highcut,
imageForLayer, integratedCube, integratedMap,
integratedMapName, i, j, k, l, labellist, layBar, laylma,
left, lenBar, levels, lineFreq, lowcut, myFile, myImage,
naxis1, naxis2, naxis3, newLabels, nflux, nfluxarr,
normsubSpectrum, obsid, rbcube, right, sizeBoxX, sizeBoxY,
spBar, spec, subfootprintPlot, subfpPLayer, top, values,
vline, wave, X, xaxis, xCoords, Y, yaxis, yCoords)
```


List of Figures

1.1	The Earth's atmospheric transmission.	6
1.2	The position of NGC 3603 in the Carina constellation	7
2.1	A schematic figure about the structure of a PDR	19
2.2	Photoelectric heating and photo-pumping	20
2.3	Possible reaction types of two species on grain surface	23
3.1	Schematic figure on the DBS observing mode	28
3.2	Schematic figure on the OTF observing mode	28
3.3	How the integral-field spectrometer works	29
3.4	Real PACS footprint on the sky	31
3.5	The NGC 3603	36
3.6	Visualization of all the Herschel observations	37
4.1	Baseline subtraction and line fitting (PACS)	41
4.2	Observed lines in PACS range spectroscopy	42
4.3	Spaxel distribution on the sky and integrated flux map of [OI] (63 μm)	45
5.1	CS ($2 \rightarrow 1$) map of NGC 3603	48
5.2	C ¹⁸ O ($2 \rightarrow 1$) map of NGC 3603	49
5.3	NANTEN2 integrated intensity maps	50

5.4	$N(\text{H}_2)$ and dust temperature map of NGC 3603	52
5.5	UV-flux of NGC 3603	53
6.1	Comparison of Herschel OTF–maps	56
6.2	Integrated intensity maps of [OI] (63 μm) and [NIII]	59
6.3	PV–diagrams of HCO^+ vs CS and CH vs C_2H	63
6.4	PV–diagrams from Herschel cut observations	64
6.5	Velocity channel map of HCO^+ (6 \rightarrow 5)	66
6.6	Comparison of line profiles in C1, C2 and C3	68
6.7	Hyperfine fitting for CH and C_2H	70
6.8	Normalized T_{int} of the observed species along C1, C2 and C3	71
6.9	o- H_2O in MM1	72
6.10	o- H_2O in MM2	73
6.11	Hfs line fitting for NH (MM1-IF) and the positions of hyperfine components	76
6.12	Line fitting for p- H_2O (MM1-IF and MM2-IF)	77
6.13	Total column densities versus excitation temperature	80
6.14	The derived total column densities along C1, C2 and C3	82
6.16	Rotational diagrams of ^{12}CO	84
6.17	The derived abundances along C1, C2 and C3	89
6.18	Correlation between the virial parameter and mass	92
7.1	The commonly used geometries in PDR-modelling	96
7.2	RADEX model fitting (MM1-IF and MM2-IF)	103
7.3	RADEX model fitting (MM1-IF and MM2-IF, cooling lines)	104
7.4	KOSMA- τ clumpy model fitting (MM1-IF and MM2-IF)	105
7.5	KOSMA- τ clumpy model fitting (MM1-IF and MM2-IF, cooling lines)	106
8.1	Shock fronts in NGC 3603	112
8.2	Visualization of emission rotation HCO^+	113
8.3	Visualization of emission rotation in MM2.	114
8.4	IRS sources in NGC 3603	118

8.5	The $^{12}\text{CO}/^{13}\text{CO}$ integrated line intensity ratios as a function of rotational quantum number	123
8.6	The projected distance of the peak integrated line intensities	125
8.7	Abundances as a function of visual extinction	128
C.1	Integrated intensity map of CH and HCO^+	162
C.2	Integrated intensity map of CS and C_2H	163
C.3	Comparison of Herschel, Spitzer and NANTEN2 maps (I)	164
C.4	Comparison of Herschel, Spitzer and NANTEN2 maps (II)	165
D.1	Line fits of CH in C1	167
D.2	Line fits of CH in C2	168
D.3	Line fits of CH in C3	169
D.4	Line fits of HCO^+ in C1	170
D.5	Line fits of HCO^+ in C2	171
D.6	Line fits of HCO^+ in C3	172
D.7	Line fits of CS in C1	173
D.8	Line fits of CS in C2	174
D.9	Line fits of CS in C3	175
D.10	Line fits of C_2H in C1	176
D.11	Line fits of C_2H in C2	177
D.12	Line fits of C_2H in C3	178
E.1	Line fits of o- H_2O in MM1	179
E.2	Line fits of o- H_2O in MM1 (cont.)	180
E.3	Line fits of o- H_2O in MM2	180
E.4	Line fits of o- H_2O in MM2 (cont.)	181
E.5	Line fits of ^{12}CO in MM1	181
E.6	Line fits of ^{12}CO in MM1 (cont.)	182
E.7	Line fits of ^{12}CO in MM2	182
E.8	Line fits of ^{12}CO in MM2 (cont.)	183
E.9	Line fits of ^{13}CO in MM1	184
E.10	Line fits of ^{13}CO in MM2	185

E.11	Line fits of ^{13}CO in MM2 (cont.)	186
E.12	Line fits of $^{12}\text{C}^+$ in MM1	186
E.13	Line fits of $^{12}\text{C}^+$ in MM1 (cont.)	187
E.14	Line fits of $^{12}\text{C}^+$ in MM2	188
E.15	Line fits of $^{12}\text{C}^+$ in MM2 (cont.1)	189
E.16	Line fits of $^{12}\text{C}^+$ in MM2 (cont.2)	190
F.1	Hyperfine line fit of the NH in MM2-IF (I)	191
F.2	Hyperfine line fit of the NH in MM2-IF (II)	191
F.3	Hyperfine line fit of the OH^+ in MM1-IF (I)	192
F.4	Hyperfine line fit of the OH^+ in MM1-IF (II)	192
F.5	Hyperfine line fit of the OH^+ in MM2-IF (I)	192
F.6	Hyperfine line fit of the OH^+ in MM2-IF (II)	193
F.7	Line fit of the p- H_2O in MM2-peak	193
F.8	Line fits of the C^{18}O in MM1-IF	193
F.9	Line fits of the C^{18}O in MM2-IF	194
F.10	Line fits of the C^{18}O in MM2-peak	194
G.1	Velocity channel map of CH (all)	195
G.2	Velocity channel map of CS ($11 \rightarrow 10$) and C_2H ($F = 6 \rightarrow 5$)	196
G.3	Velocity channel map of C_2H ($F = 5 \rightarrow 4$) and CH ($F = 2 \rightarrow 1$)	197
H.1	^{12}CO in MM1	200
H.2	^{13}CO in MM1	201
H.3	$^{12}\text{C}^+$ in MM1	202
H.4	^{12}CO in MM2	203
H.5	^{13}CO in MM2	204
H.6	$^{12}\text{C}^+$ in MM2	205
I.1	Integrated intensity map [OI] ($63 \mu\text{m}$)	207
I.2	Integrated intensity maps of [OI] ($145 \mu\text{m}$) and [OIII] ($88 \mu\text{m}$)	208
I.3	Integrated intensity maps of [NII] ($122 \mu\text{m}$) and CO ($13 \rightarrow 12$)	209
I.4	Integrated intensity maps of ^{12}CO ($14 \rightarrow 13$ and $15 \rightarrow 14$)	210
I.5	Integrated intensity maps of ^{12}CO ($16 \rightarrow 15$) and [CII] ($158 \mu\text{m}$)	211

K.1	Energy level diagram of CH	227
K.2	Energy level diagram of C ₂ H ($v = 0$)	228
K.3	Energy level diagrams of HCO ⁺ and CS ($v = 0$)	229
K.4	Energy level diagrams of ¹² CO, ¹³ CO and C ¹⁸ O	230
K.5	Energy level diagram of NH	231
K.6	Energy level diagram of OH ⁺	232
K.7	Energy level diagram of H ₂ O ($J < 3$)	233
K.8	Energy level diagrams of [NII], [NIII], [OI], [OIII] and [CII] . .	234
L.1	Convolved Spitzer maps	237

List of Tables

3.1	The main parameters of the HSO	26
3.2	Summary of the observed molecules (HIFI)	34
3.3	Summary of the observed molecules (PACS)	35
4.1	Observational parameters for HIFI	43
6.1	The derived excitation temperatures in MM1 and MM2	80
6.2	Summary of HIFI point observations	86
6.3	The calculated column densities of OTF observations	87
6.4	The calculated abundances from OTF observations	88
6.5	The results of Jeans mass derivations	91
6.6	The derived masses and virial parameter along C1, C2 and C3	92
7.1	Output parameters from RADEX code	101
7.2	Line intensities of the selected lines for KOSMA- τ model	102
7.3	Output parameters from KOSMA- τ model	107
8.1	Derived thermal line-broadening for OTF observations	111
8.2	The calculated turbulent velocities	111
8.3	The derived pressures in NGC 3603	122
J.1	Physical parameters of HCO ⁺ and CS	213

J.2	Physical parameters of CH and C ₂ H	215
J.3	Output parameters of line fits for cut observations	217
J.4	Derived column densities for Herschel cut observations	223
L.1	The scaled intensity values	236
L.2	The derived scaling factors	237

Acknowledgements

When I started my graduate studies 6 years ago, I thought that this day would never come. I had a long and rugged journey but, at the end, I did it. I came to Cologne to learn more and to make new acquaintances. With astronomy, which is a unique and interesting occupation, all these aspirations could be met. The Santa Claus of Jürgen Stutzki's group would like to give thanks with the following lines for the countless opportunities and experiences that I had during my time in Cologne.

First of all, I would like to say many, many thanks for my principal supervisor Prof. Dr. Jürgen Stutzki. He offered a great opportunity to do high level scientific research on his team at the University of Cologne. Even though most of the time he has been amazingly busy, he always found time to shepherd me on the appropriate track. I am truly thankful for his support and guidance.

I received a lot of help from PD. Dr. Markus Röllig too. Except the last few months, we were sat next to each other in our office. Therefore, I was literally able to turn him any time (except Wednesdays) with different questions. Based on his best knowledge and patience, he always tried to help me. If needed, very critical and harsh comments were given by him about my PhD-thesis. I believe that his (and Prof. Stutzki's) strict comments made my thesis better.

I also would like to thank to PD. Dr. Volker Ossenkopf for his professional help. He composed his opinions and advice, related to my thesis and paper, in concise ways. I have learned a lot from him and I am thankful for the experience (as well as for the surprisingly good cakes that he made :-)).

Dr. Robert Simon ... what can I say about my German brother? I clearly remember the day when our friendship started. The location: San Pedro de Atacama, the time: October, 2009. After my very first trip to Chile and

my absolutely first kidnapping by a fake cab driver in Santiago de Chile, we were sitting in a restaurant in the middle of nowhere and having a conversation. During that talk, I think we received the first impressions that we share mutual range of interests: the same taste in music (we also play instruments), liking badminton etc. In addition, our ways to think about many things and life were quite close to each other. At that time, we did not know that the next day will be the longest and hardest day of my entire life and that he would save my life. Although that day was not so pleasant for me and for him (I think), it brought something else, something very valuable: a hopefully lifelong friendship.

A tons of discussions and meetings meant a lot and really helped me to get through the harder periods of my life and of my "Beer-hD" (hehe ... I put it in, I told you). Of course, I should mention the usual "badminton-Mondays", the parties together with André ("aber hallo??") which were always so funny. I do not even say anything about the Dream Theater concerts, ice-hockey games (especially the very last Play-off game) and soccer games that we watched together. Because if I did in details, I would write another hundred pages :-)

I am very glad that I met and know a very gracious person, namely PD. Dr. Nicola Schneider. We had so many substantial conversations which were helpful in both professional and personal ways (I hope we shall meet in France :-)).

I had several interesting and fruitful professional/personal discussions with Dr. Yoko Okada (Domo arigatou gozaimasu Yoko). I also had very good times and talks with Dr. Ronan Higgins ("slainte man") and Dr. Edward Chambers (Sir, yes Sir!...by the way, it was good to watch, together with Robert, the XLVII Super Bowl...am I remembering correctly that the Baltimore Ravens won?:-P) who became real fathers during my PhD-period. I wish them a very happy and long life together with their families. Likewise, as with the aforementioned people, I had very nice moments with my fellow sufferers whom I hereby wish an endless supply of power, patience and persistence to finish their theses: Pablo (I really hope that, at the end, you will be very happy with your family. ¡Vamos amigo y Vamos Chile!), Silke, Philipp, Christian, Cristian, Norma and all the others ...

I should not forget the young and international team in Groningen [Dr. Mihkel Kama, Dr. Umut Yildiz, Dr. Zsófia Nagy (with whom had valued professional/personal conversations in Cologne too and I hope her life will be happy, and successful), Dr. Per Bjerke, Ian Avruch (Max) and the others ...). We have been trying to mine deeply into HIPE and receive the most from it which is not an easy task even nowadays :-P

I also would like to say thanks to Bettina and Steffi. They know the German administration and bureaucracy much better than I. Thus, I am sure, my life in Germany would have been harder without them. There was a person

who tried to dive with me into the very deep lake of programming and of Linux world. It was a more or less successful project because of him and not me . . . thank you for everything Dr. Frank Schlöder (do not worry, I won't tell anybody about your secret place, which is located in your drawer, where you store all your sweets :-)).

In any case, I would like to bring attention to a name which belongs to a very good, intelligent and kind person who launched me on a long and cragged pathway. He always believed in me and supported me, and he's had a great influence on my life. His name is András Horkai and I bless my fate that we met, and that he became my mentor and a very good friend. To receive a PhD-degree could be an important station of anybody's life but the path that I am walking on is the road of turning into a human being. He helped me get a lot closer to this goal!

I think it is not a secret that once we live in abroad, we are isolated from our family and friends even in such a modern world. Therefore, I would like to mention the great times we had when our friends/family members are visited us in Cologne: Szabolcs (we should play some heavy stuff, don't you think?!) and Feca (if you were not an alcoholic, it would be good . . . but I am afraid it does not really matter now :-)), Indi and Zsolti (do you already have rubber glove? do you make shunt?:-)), Tüdi and Krisztián (it is quite strange that we first met in Szeged then both of us are living in Germany, isn't?; anyway all conversations and times we spent together were really good and I hope that we shall continue in the future in France). Nonetheless, family was always the first priority for me. Even before we came to Cologne my wife, Andrea, has been the most important person in my life. During my PhD-period when, unfortunately, both my mother and father died (thank you for everything; but many thanks to my stepfather István, too) and I can only see my younger brother rarely (I hope this will change in the near future), the definition of family is concentrated on two people: Andrea and I. All of my deepest respect and love are yours! You were able to endure innumerable problems, you supported me and stuck with me! We went through so many difficulties so far but we are stronger and better! I love you more than my life!

I truly apologize from everybody who was not mentioned here!
To sum up, I deeply thank everybody for all the years I have spent here in University of Cologne, for all experiences and for everything! I wish you all a long, successful, peaceful and happy life!

I shall miss you, Köln, very much, but new opportunities and discoveries are waiting for us in France. Kölle Alaaf!!!

HIFI has been designed and built by a consortium of institutes and university departments from across Europe, Canada and the United States under the leadership of SRON Netherlands Institute for Space Research, Groningen, The Netherlands and with major contributions from Germany, France and the US. Consortium members are: Canada: CSA, U. Waterloo; France: CESR, LAB, LERMA, IRAM; Germany: KOSMA, MPIfR, MPS; Ireland, NUI Maynooth; Italy: ASI, IFSI-INAF, Osservatorio Astrofisico di Arcetri-INAF; Netherlands: SRON, TUD; Poland: CAMK, CBK; Spain: Observatorio Astronómico Nacional (IGN), Centro de Astrobiología (CSIC-INTA). Sweden: Chalmers University of Technology - MC2, RSS & GARD; Onsala Space Observatory; Swedish National Space Board, Stockholm University - Stockholm Observatory; Switzerland: ETH Zurich, FHNW; USA: Caltech, JPL, NHSC.

PACS has been developed by a consortium of institutes led by MPE (Germany) and including UVIE (Austria); KU Leuven, CSL, IMEC (Belgium); CEA, LAM (France); MPIA (Germany); INAF-IFSI/OAA/OAP/OAT, LENS, SISSA (Italy); IAC (Spain). This development has been supported by the funding agencies BMVIT (Austria), ESA-PRODEX (Belgium), CEA/CNES (France), DLR (Germany), ASI/INAF (Italy), and CICYT/MCYT (Spain).

The Herschel spacecraft was designed, built, tested, and launched under a contract to ESA managed by the Herschel/Planck Project team by an industrial consortium under the overall responsibility of the prime contractor Thales Alenia Space (Cannes), and including Astrium (Friedrichshafen) responsible for the payload module and for system testing at spacecraft level, Thales Alenia Space (Turin) responsible for the service module, and Astrium (Toulouse) responsible for the telescope, with in excess of a hundred subcontractors.

HCSS / HSpot / HIPE is a joint development (are joint developments) by the Herschel Science Ground Segment Consortium, consisting of ESA, the NASA Herschel Science Center, and the HIFI, PACS and SPIRE consortia.

Erklärung

Ich versichere, dass ich die von mir vorgelegte Dissertation selbstständig verfasst angefertigt, die Benutzten Quellen und Hilfsmittel vollständig angegeben und die Stellen der Arbeit - einschliesslich Tabellen, Karten und Abbildungen -, die anderen Werken im Wortlaut oder dem Sinn nach entnommen sind, in jedem Einzelfall als Entlehnung kenntlich gemacht habe; dass diese Dissertation noch keiner anderen Fakultät oder Universität zu Prüfung vorgelegen hat; dass sie - abgesehen von unten angegebenen Teilpublikationen - noch nicht veröffentlicht worden ist sowie, dass ich eine solche Veröffentlichung vor Abschluss des Promotionsverfahrens nicht vornehmen werde.

Die Bestimmungen dieser Promotionsordnung sind mir bekannt. Die von mir vorgelegte Dissertation ist von Prof. Dr. Jürgen Stutzki betreut worden.

Ich versichere, daß ich alle Angaben wahrheitsgemäß nach bestem Wissen und Gewissen gemacht habe und verpflichte mich, jedmögliche, die obigen Angaben betreffenden Veränderungen, dem Dekanat unverzüglich mitzuteilen.

Köln, den 26. Mai 2014

Zoltán Makai

CURRICULUM VITAE

PERSONAL

Name: Zoltán Sándor Makai
Address: Windmühlenstrasse 139, 51063 Köln, Germany
Date of birth: March 25th, 1975
Place of birth: Budapest, Hungary
Nationality: Hungarian

SCHOOLS & UNIVERSITIES

12/2008–05/2014 Graduate studies at the I. Physics Institute, University of Cologne, Germany. The title of Ph.D. thesis: *The physics and chemistry of photon-dominated clouds in NGC 3603*
09/2001 – 05/2006 Undergraduate studies for master thesis in astrophysics at Optics and Quantum Electronics Department, University of Szeged, Hungary. The title of the thesis: *Photometric studies of Galactic open clusters*
1995–1999 General secondary school, Budapest
1989–1992 Vocational school, Budapest, Hungary
1981–1989 Elementary school, Budapest, Hungary

PROFESSIONAL EXPERIENCE

12/2008–06/2014 Graduate research at the University of Cologne, Germany
08/2006–08/2008 Data analyst at the Rochester Institute of Technology, Rochester,
06/2005–08/2005 Summer student research within the special program of *Space Astronomy Summer Program (SASP)* at the Space Telescope Science Institute, Baltimore, MD, USA (topics: infrared photometry)
2002–2006 Undergraduate research at the University of Szeged, Hungary